

https://dspace.org/

Optimisation of a novel trailing edge concept for a high lift device

Botha, Jason Daniel Michael

2015-05-14
http://hdl.handle.net/10539/17760

Downloaded from a DSpace repository. https://dspace.org/

Optimisation of a Novel Trailing Edge Concept for a High Lift Device

by Jason Daniel Michael Botha

A dissertation submitted to the Faculty of Engineering and the Built Environment, University of the Witwatersrand, in fulfilment of the requirements for the degree of Master of Science in Engineering.

Johannesburg, August 29, 2014

Declaration

I declare that this dissertation is my own unaided work. It is being submitted to the Degree of Master of Science in Engineering to the University of the Witwatersrand, Johannesburg. It has not been submitted before for any degree or examination to any other University.

.....
Jason Daniel Michael Botha

Signed on this the ..... day of .....,.....

Abstract

This research aims to improve aerodynamic performance of a high lift system by means of implementing a novel concept (referred to as the flap extension) on the leading edge of the flap of a three element high lift device. The concept is optimised using two optimisation approaches based on Genetic Algorithm optimisations. A zero order approach which makes simplifying assumptions to achieve an optimised solution: and a direct approach which employs an optimisation in ANSYS DesignXplorer using RANS calculations. The concept was seen to increase lift locally at the flap. The solution to the zero order optimisation showed a decreased stall angle and decreased maximum lift coefficient due to early stall onset at the flap. The DesignXplorer optimised solution matched that of the baseline solution very closely. Computational Aeroacoustic simulations were performed using the DES model in 2D on the baseline and DesignXplorer optimised solution. The DesignXplorer optimised concept steadied the shear layer that bounds the spoiler cove thus reducing noise from this vicinity by 10dB at frequencies over 7 000Hz.

Acknowledgements

What am I doing with my life?
– M.C. Meijer

Thank you to my supervisor, Professor Laurent Dala. Without his support and motivation I would have never believed myself to achieve the results I have. His guidance and assistance was well received and I am grateful for the assistance he has provided relating to both studies and my future career aspirations.

Thank you to the National Aerospace Centre and Airbus for funding the second year of my research.

I extend my thanks to my family whom, whilst they have no idea what I've really been doing for the past year and a half, have given their unending support nevertheless.

To my long-suffering friends who are also part of the post-graduate engineering community: MC, Pierre, Hans. I'm sure you can all relate to the endless struggle of academic research. Thanks!

Finally I would like to extend thanks to an additional inspiration in my life; Mr B. Wayne for always reminding me that, through the good and bad, to always accept that there are "greys" in every situation. We may not like them, but it's part of what we do.

Contents

1 Introduction **16**
1.1 Research Background . . . 16

2 Literature Review **19**
2.1 High Lift Aerodynamics . . . 19
2.1.1 Physics of High Lift . . . 19
2.1.2 Limits of High Lift . . . 20
2.2 High Lift System Design . . . 20
2.2.1 High Lift Components . . . 20
2.3 High Lift System Simulations . . . 25
2.3.1 Computational Studies . . . 25
2.3.2 Optimisation Studies . . . 27
2.4 Aircraft Noise . . . 28
2.4.1 Airfoil Noise . . . 29
2.4.2 High Lift System Noise . . . 30
2.5 Aeroacoustics . . . 34
2.5.1 Lighthill's Analogy . . . 34
2.5.2 Ffowcs-Williams & Hawkings Acoustic Analogy . . . 36
2.5.3 Computational Aeroacoustics . . . 38
2.5.4 Optimisations . . . 39
2.6 Summary . . . 39

3 Methodology **40**
3.1 Research Motivation . . . 40
3.1.1 Limitations of Research . . . 40
3.2 Research Problem . . . 41
3.2.1 Aims and Objectives . . . 41
3.3 Method . . . 41
3.4 TC12 Profile . . . 42
3.5 Prior Work on the TC12 Profile . . . 44
3.6 Optimisation Procedure . . . 45
3.7 Definition of Error and Percentage Increase . . . 46

4 Validation **47**
4.1 Experimental Data . . . 47
4.1.1 Clean Configuration . . . 47
4.1.2 High Lift Configuration . . . 48
4.2 MSES Validation . . . 49
4.2.1 Conclusion of MSES Validation . . . 57
4.3 ESDU Validation . . . 57
4.3.1 Calculations . . . 57
4.3.2 Conclusion of ESDU Validation . . . 63
4.3.3 Modification of Methods to Analyse Novel Modifications . . . 64
4.4 ANSYS Fluent Validation . . . 66
4.4.1 Initial Conditions . . . 67
4.4.2 Solver Settings . . . 70

4.4.3 Clean Configuration Validation . . . 71
4.4.4 Meshing Strategy (Clean Configuration) . . . 71
4.4.5 Results (Clean Configuration) . . . 78
4.4.6 High Lift Configuration Validation . . . 83
4.4.7 Meshing Strategy (High Lift Configuration) . . . 83
4.4.8 Results (High Lift Configuration) . . . 96
4.5 Conclusion . . . 100

5 Aerodynamic Investigation 1 **101**
5.1 Flap Optimisation Routine . . . 101
5.1.1 Genetic Algorithm . . . 102
5.1.2 Geometry Function . . . 102
5.1.3 Aerodynamic Solver . . . 104
5.1.4 Objective Function . . . 105
5.2 Solution . . . 106
5.2.1 XFoil Result . . . 107
5.2.2 MSES Result . . . 108
5.2.3 Fluent Result . . . 112
5.3 Smoothed Geometry . . . 118
5.4 Slotted Geometry . . . 121
5.5 Findings . . . 124

6 Aerodynamic Investigation 2 **125**
6.1 Optimisation Routine . . . 125
6.1.1 Multi Objective Genetic Algorithm . . . 126
6.1.2 Geometry Tool . . . 127
6.1.3 Meshing Tool . . . 128
6.1.4 Aerodynamic Solver . . . 129
6.2 Solution . . . 130
6.3 Findings . . . 137

7 Aeroacoustic Investigation **138**
7.1 Initial Conditions . . . 138
7.2 Solver Settings . . . 139
7.3 Mesh Set up . . . 140
7.4 SA Based Acoustic Simulations . . . 142
7.4.1 Solution . . . 143
7.5 DES Based Acoustic Simulations . . . 144
7.5.1 Solution . . . 146
7.6 Acoustics of the DesignXplorer Optimised TC12 Profile . . . 148
7.7 Findings . . . 151

8 Design Investigation **153**
8.1 Predesign Concepts . . . 153
8.2 Concept Down Selection . . . 157
8.3 Conclusion . . . 161

9 Conclusion **162**
9.1 Summary and Conclusions . . . 162
9.2 Recommendations for Future Work . . . 163

References **165**

10 Appendix **170**

A ESDU Tables **170**

B MSES Grids **173**

C Additional MSES Results **178**

D Clean Airfoil Mesh in Ansys Mesher **182**

E Validation of Tools for Zero Order Optimisation **184**
E.1 MATLAB Genetic Algorithm Toolbox . . . 184
E.2 Validation Solutions . . . 184

F Down Selection Process Data **185**

List of Figures

1.1 Effect of flaps and slats on lift *ESDU 85033: Increments in Aerofoil Maximum Lift Coefficient due to Deployment of Various High Lift Devices* (1992) . . . 16
2.1 Drawings of various trailing edge high lift devices . . . 21
2.2 Advanced drooped hinge flap lift compared to a conventional fowler flap (*The ADHF "advanced dropped hinge flap" patented by Airbus onboard the A350 XWB*, 2013) . . . 22
2.3 Development of trailing edge high lift systems on airliners (Reckzeh, 2003) . . . 22
2.4 Drawings of various leading edge high lift devices . . . 24
2.5 Challenges inherent in multi-element flow field prediction (Rumsey and Ying, 2002) 26
2.6 Aircraft noise levels by component during approach (Dobrzynski, 2008) . . . 29
2.7 Five different types of airfoil self noise . . . 30
2.8 Suspected slat noise sources (Choudhari et al., 2012) . . . 31
2.9 Slat setting results summary for TIMPAN project (*Technologies to IMProve Airframe Noise* , 2013) . . . 33
2.10 Noise sources examined during the VALIANT project . . . 33
2.11 Source surfaces as implemented in ANSYS Fluent for FWH solutions (*ANSYS Fluent online user guide*, 2013) . . . 37
2.12 Schematic drawing of a RANS-LES simulation (Nebenfuhr, 2012) . . . 38
3.1 Schematic of TC12 profile in high lift configuration . . . 43
3.2 Slat motion of TC12 profile in high lift configuration . . . 43
3.3 Fowler flap motion of TC12 profile in high lift configuration . . . 43
3.4 Optimised concept as implemented by Vitale (2010) . . . 44
3.5 Optimisation region of TC12 airfoil in high lift configuration . . . 45
3.6 Betz flap, *Modification De La Forme Dun Profil* (1980) . . . 45

4.1 Coefficient of lift against angle of attack for TC12 profile in clean configuration, KKK experiments . . . 48
4.2 Coefficient of lift against angle of attack for TC12 profile in high lift configuration, KKK experiments . . . 49
4.3 Cl vs. alfa for TC12 profile in clean configuration at Re 2.94 Million, MSES . . . 50
4.4 Pressure distribution of TC12 profile in clean configuration at Re 2.94 million, angle of attack 8.11 degrees in MSES . . . 51
4.5 Pressure distribution (peak) of TC12 profile in clean configuration at Re 2.94 million, angle of attack 8.11 degrees . . . 51
4.6 Pressure distribution of TC12 profile in clean configuration at Re 9.06 million, angle of attack 8.1 Degrees . . . 52
4.7 Pressure distribution (peak) of TC12 profile in clean configuration at Re 9.06 million, angle of attack 8.1 Degrees . . . 52
4.8 Comparison of inviscid MSES results with wind tunnel Re 2.9 million . . . 54
4.9 Pressure distribution for TC12 high lift at matched Cl 2.879 . . . 55
4.10 Cl vs. alfa for TC12 profile in high lift configuration at Re 2.95 Million, MSES . . . 56
4.11 Cd vs. alfa for TC12 profile in high lift configuration in MSES . . . 56
4.12 ESDU definitions associated with basic airfoil geometry . . . 58
4.13 ESDU definitions associated with slats . . . 59
4.14 ESDU definitions associated with slotted flaps . . . 60
4.15 Diagram explaining conventions in equations (4.14) and (4.15) . . . 66
4.16 Initial blocking of TC12 profile clean configuration . . . 72
4.17 Close up of blocking of TC12 profile clean configuration mesh . . . 72
4.18 Boundary layer mesh of TC12 profile clean configuration . . . 73
4.19 Boundary layer mesh close to surface of TC12 profile clean configuration . . . 73
4.20 Boundary layer mesh at the trailing Edge of TC12 profile clean configuration . . . 74
4.21 TC12 profile clean configuration airfoil mesh (full view) . . . 75
4.22 TC12 profile clean configuration airfoil mesh close Up on airfoil . . . 75
4.23 Mesh adaptations for TC12 profile clean configuration . . . 77
4.24 Mesh adaptations of TC12 profile clean configuration within the boundary layer at the leading edge . . . 77
4.25 Second Order Convergence of Fluent Results for the TC12 Clean Airfoil at 8.1051 degrees . . . 79
4.26 Coefficient of Drag convergence for the TC12 profile in clean configuration at 8.1051 degrees . . . 79
4.27 Separations at the leading edge of TC12 profile in clean configuration . . . 80
4.28 Cl vs. alfa for TC12 in clean configuration compared to experiments, Re 2.95 Million, transition-SST turbulence model . . . 81
4.29 Cd vs. alfa for TC12 in clean configuration compared to experiments, Re= 2.95 Million, transition-SST turbulence model . . . 81
4.30 Pressure distributions of TC12 profile in clean configuration at 8.1 degrees, Fluent vs. Experiments . . . 82
4.31 Pressure Distributions of TC12 profile in clean configuration zoomed in at separation bubble, Fluent vs. experiments . . . 83
4.32 Mesh at the region between TC12 profile in high lift configuration, slat trailing edge and main element leading edge . . . 84
4.33 Mesh at the cove region of the slat TC12 profile high lift configuration . . . 85

4.34 Mesh at the cove region of the main element TC12 profile in high lift configuration 85
4.35 Mesh between the spoiler and the flap TC12 profile in high lift configuration . . 86
4.36 Close up of flap trailing edge mesh TC12 profile in high lift configuration 86
4.37 Mesh outer block for TC12 profile in high lift configuration 88
4.38 Mesh close up of airfoil for TC12 profile in high lift configuration 88
4.39 Adapted region of mesh for TC12 profile in high lift configuration 90
4.40 Scaled residuals for TC12 high lift configuration mesh, SA turbulence model . . . 91
4.41 Convergence of drag coefficient residuals for TC12 high lift configuration mesh, SA turbulence model 92
4.42 Pressure contours for TC12 profile in high lift configuration, SA turbulence model, 8.09 degree, Re 2.95 million 92
4.43 Recirculation at slat cove of TC12 profile in high lift configuration, SA turbulence model, 8.09 degrees, Re 2.95 million 93
4.44 Scaled residuals of TC12 profile in high lift configuration, k-omega SST turbulence model, 8.09 degrees, Re 2.95 million 94
4.45 Excerpt of value of drag residuals for TC12 profile in high lift configuration, k-omega SST turbulence model, 8.09 degrees, Re 2.95 million 94
4.46 Pressure distribution for TC12 profile in high lift configuration, k-omega SST turbulence model, 8.09 degrees, Re 2.95 million 95
4.47 Velocity contours for TC12 profile in high lift configuration, k-omega SST turbulence model, 8.09 degrees, Re 2.95 million 95
4.48 Cl vs. alfa for TC12 profile in high lift configuration, Re 2.95 million vs. KKK windtunnel data 96
4.49 Cl vs. alfa showing stall for TC12 profile in high lift configuration, Re 2.95 million vs. KKK windtunnel data 97
4.50 Cd vs. alfa for TC12 profile in high lift configuration, Re 2.95 million 97
4.51 Pressure distribution for TC12 profile in high lift configuration, SA Turbulence Model vs. Windtunnel Data, 8.09 degrees, Re 2.95 Million 98
4.52 Pressure distribution at slat for TC12 profile in high lift configuration, SA turbulence model vs. windtunnel data, 8.09 degrees Re 2.95 million 99
4.53 Pressure distribution peak for TC12 profile in high lift configuration, SA turbulence model vs. windtunnel data, 8.09 degrees Re 2.95 million 99
4.54 Pressure distribution for TC12 profile in high lift configuration, k-omega SST turbulence model, 8.09 degrees, Re 2.95 million 99
4.55 Pressure Distribution at slat for TC12 profile in high lift configuration, k-omega SST turbulence model vs. windtunnel data, 8.09 degrees, Re 2.95 million 100
4.56 Pressure peak at slat for TC12 profile in high lift configuration, k-omega SST turbulence model vs. windtunnel data, 8.09 degrees, Re 2.95 million 100
5.1 System diagram of the optimisation routine 102
5.2 Selected design variables for optimisation 103
5.3 Constrained optimisation variables 104
5.4 Pareto front of optimised solutions 106
5.5 Geometry of solution of zero order flap optimisation 107
5.6 Cl vs. alfa of TC12 flap optimised solution vs baseline in XFOIL 108
5.7 Cd vs. alfa of TC12 flap optimised solution vs baseline in XFOIL 108
5.8 Gridding at the flap for the zero order optimised extension 109

5.9 Cl vs. alfa of TC12 profile in high lift configuration optimised solution vs baseline in MSES . . . 110
5.10 Cd vs. alfa of TC12 profile in high lift configuration optimised solution vs baseline in MSES . . . 110
5.11 Pressure distribution of TC12 profile in high lift configuration optimised solution vs. baseline in MSES, baseline matched Cl, Re 2.95 Million . . . 111
5.12 Pressure distribution of TC12 high lift configuration flap at 8.09 degrees optimised solution vs. baseline in MSES, baseline matched Cl, Re 2.95 million . . . 112
5.13 Mesh at the leading edge of the TC12 flap showing the implementation of the new concept . . . 113
5.14 Cl vs. alfa of TC12 high lift configuration zero order optimised solution vs. baseline in Fluent SA turbulence model, Re 2.95 Million . . . 114
5.15 Cl vs. alfa of TC12 high lift configuration at stall zero order optimised solution vs. baseline in Fluent SA turbulence model, Re 2.95 Million . . . 114
5.16 Cd vs. alfa of TC12 high lift configuration zero order optimised solution vs. baseline in Fluent SA turbulence model, Re 2.95 Million . . . 115
5.17 Pressure distribution of tc12 high lift configuration optimised solution vs. baseline in Fluent SA turbulence model, 8.09 degrees, Re 2.95 million . . . 116
5.18 Pressure distribution at flap of TC12 high lift configuration optimised solution vs. baseline in Fluent SA turbulence model, 8.09 degrees, Re 2.95 million . . . 117
5.19 Streamlines around trailing edge of zero order optimised flap extension showing the Coanda effect . . . 118
5.20 Pressure coefficient along span at the trailing edge of the main element of the TC12 profile comparing zero order optimised solution to the baseline . . . 118
5.21 Mesh at the leading edge of the TC12 flap showing the meshing around the smoothed concept . . . 119
5.22 Pressure distribution of TC12 high lift configuration optimised solution with smoothed geometry vs. baseline at 8.09 degrees in Fluent, SA turbulence model, Re 2.95 Million . . . 120
5.23 Pressure distribution of TC12 high lift configuration optimised solution with smoothed geometry vs. baseline at 8.09 degrees in Fluent, SA turbulence model, Re 2.95 Million . . . 120
5.24 Mesh at the leading edge of the TC12 flap showing the meshing around the slotted concept . . . 121
5.25 Pressure distribution of TC12 high lift configuration optimised solution with slot vs. baseline at 8.09 degrees in Fluent, SA turbulence model, Re 2.95 Million . . . 122
5.26 Pressure distribution of TC12 high lift configuration optimised solution with slot (flap alone) at 8.09 degrees vs. baseline in Fluent, SA turbulence model, Re 2.95 Million . . . 123
5.27 Recirculation regions on new concept extension with slot . . . 123
6.1 System diagram of MOGA optimisation in Ansys DesignXplorer . . . 126
6.2 Parameterisation of flap extension concept in DesignXplorer . . . 128
6.3 Example of an automatically generated mesh for DesignXplorer optimisation of TC12 high lift profile . . . 129
6.4 Boundary layer sizing of mesh for DesignXplorer optimisation of TC12 high lift profile . . . 129
6.5 Convergence history of DesignXplorer MOGA optimisation of TC12 profile . . . 131

6.6 Sensitivity analysis of input parameters to output parameters of DesignXplorer MOGA optimisation of TC12 profile . . . 132
6.7 Geometry of DesignXplorer MOGA optimised solution . . . 132
6.8 Mesh of DesignXplorer MOGA optimised solution . . . 133
6.9 Cl vs. alfa of TC12 profil in high lift configuration DesignXplorer optimised solution vs. baseline in fluent sa turbulence model, Re 2.95 million . . . 133
6.10 Cl vs. alfa at stall of TC12 profile in high lift configuration DesignXplorer optimised solution vs. baseline in Fluent, SA turbulence model, Re 2.95 million . . . 134
6.11 Cd vs. alfa of TC12 profile in high lift configuration DesignXplorer optimised solution vs. baseline in Fluent SA turbulence model, Re 2.95 million . . . 134
6.12 Pressure distribution of TC12 high lift configuration at 8.09 degrees DesignXplorer optimised solution vs. baseline in Fluent, Re 2.95 million, SA turbulence model . . . 135
6.13 Pressure distribution of TC12 high lift configuration flap at 8.09 degrees DesignXplorer optimised solution vs. baseline in Fluent, Re 2.95 million, SA turbulence model . . . 136
6.14 Pressure distribution of TC12 high lift configuration main element at 8.09 degrees DesignXplorer optimised solution vs. baseline in Fluent, Re 2.95 million, SA turbulence model . . . 136
6.15 Streamlines showing recirculation region of the DesignXplorer optimised concept 137
7.1 Integration region around TC12 profile in high lift configuration for acoustic calculations . . . 141
7.2 Integration region around TC12 profile in high lift configuration for acoustic calculations at slat . . . 141
7.3 Integration region around TC12 profile in high lift configuration for acoustic calculations at flap . . . 142
7.4 Mesh refinements for SA turblence model acoustic simulations . . . 142
7.5 Directivity of sound for the TC12 profile in high lift configuration at 8.09 degrees angle of attack using the SA turbulence model . . . 143
7.6 Sound spectrum for the TC12 profile in high lift configuration at 8.09 degrees angle of attack using the SA turbulence model . . . 144
7.7 Fluctuation of drag during last 1 000 iterations of the TC12 profile in high lift configuration at 8.09 degrees angle of attack using the DES turbulence model . . . 145
7.8 Courant numbers at each cell at the trailing edge of the TC12 profile in high lift configuration at 8.09 degrees angle of attack using the DES turbulence model . . . 145
7.9 Vorticity between 0 - 1 000 near the trailing edge of the TC12 profile in high lift configuration at 8.09 degrees angle of attack using the DES turbulence model . . . 146
7.10 Directivity of sound for the TC12 profile in high lift configuration at 8.09 degrees angle of attack using the DES turbulence model . . . 147
7.11 Sound spectrum for the TC12 profile in high lift configuration at 8.09 degrees angle of attack using the DES turbulence model . . . 148
7.12 Vorticity between 0 - 1 000 near the trailing edge of the DesignXplorer optimised TC12 profile in high lift configuration at 8.09 degrees angle of attack using the DES turbulence model . . . 149
7.13 Vorticity between 0 - 1 000 near the trailing edge comparing the TC12 profile in high lift configuration compared to the DesignXplorer optimised solution at 8.09 degrees angle of attack using the DES turbulence model . . . 149

7.14 Directivity of sound for the optimised TC12 profile in high lift configuration against the baseline at 8.09 degrees angle of attack using the DES turbulence model 150
7.15 Sound spectrum for the optimised TC12 profile in high lift configuration against the baseline at 8.09 degrees angle of attack using the DES turbulence model . . . 151
7.16 Filtered sound spectrum for the optimised TC12 profile in high lift configuration against the baseline at 8.09 degrees angle of attack using the DES turbulence model 151
8.1 Vitale predesign concept . . . 154
8.2 Betz track predesign concept . . . 154
8.3 Unpowered Krueger flap predesign concept . . . 155
8.4 Powered Betz predesign concept . . . 156
8.5 Fixed position predesign concept . . . 156
8.6 Bullnose predesign concept . . . 157
8.7 Example of DSP selection . . . 160
8.8 Results of concept DSP . . . 160
A.1 Figure 1 from ESDU 85033 . . . 170
A.2 Figure 2 from ESDU 85033 . . . 171
A.3 Figure 7 from ESDU 85033 . . . 171
A.4 Figure 9 from ESDU 85033 . . . 172
A.5 Figure 10 from ESDU 85033 . . . 173
B.1 Full view of grid for the TC12 profile in high lift configuration in MSES . . . 174
B.2 View of grid close to airfoil for the TC12 in profile high lift configuration in MSES 174
B.3 Grid at slat cove for the TC12 profile high lift configuration in MSES . . . 175
B.4 Grid at spoiler cove for the TC12 profile high lift configuration in MSES . . . 175
B.5 Grid at leading edge of flap for the TC12 profile in high lift configuration in MSES 176
B.6 Slat panelling for the TC12 profile in high lift configuration in MSES . . . 176
B.7 Main element panelling for the TC12 profile in high lift configuration in MSES . 177
B.8 Flap panelling for the TC12 profile high lift configuration in MSES . . . 177
C.1 Cl vs. alfa for TC12 profile in clean configuration, inviscid, MSES . . . 178
C.2 Cl vs. alfa for TC12 profile in clean configuration, Re 5.94 million, MSES . . . 178
C.3 Cl vs. alfa for TC12 profile in clean configuration, Re 9.06 million, MSES . . . 179
C.4 Cl vs.alfa for TC12 profile in clean configuration, Re 12.25 million, MSES . . . 180
C.5 Cl vs. alfa for TC12 profile in clean configuration, Re 14.44 million, MSES . . . 181
D.1 Mesh for the TC12 profile clean configuration in ANSYS mesher . . . 182
D.2 Mesh for the TC12 profile in clean configuration, ANSYS mesher (zoomed in) . . 183
D.3 Mesh for TC12 profile clean configuration leading edge, ANSYS mesher . . . 183
D.4 Mesh for TC12 profile clean configuration trailing edge, ANSYS mesher . . . 183
E.1 GA results for toolbox validation . . . 185
F.1 Comparison criterion Vitale baseline . . . 186
F.2 Comparison criterion Betz baseline . . . 187
F.3 Comparison criterion Krueger baseline . . . 188
F.4 Comparison criterion Powered Betz baseline . . . 189
F.5 Comparison criterion Fixed baseline . . . 190
F.6 Comparison criterion Bullnose baseline . . . 191
F.7 Scenario weightings . . . 192
F.8 Scenario weightings for Vitale Concept and Betz Track . . . 192
F.9 Scenario weightings for Krueger and Powered Betz . . . 193
F.10 Scenario weightings for Fixed Position and Bullnose . . . 193

F.11 Averaged results of the Down Selection Process 193

List of Tables

1.1 Explanation of European Commission high lift projects to date 18
3.1 Summary of TC12 slat and flap translations and rotations 44
4.1 Discrepancies Between Cl of TC12 Profile in Clean Configuration for MSES and Wind Tunnel Experiments 50
4.2 Grid Parameters for TC12 High Lift Configuration Simulations in MSES 53
4.3 Data for ESDU calculations for the TC12 main element airfoil 58
4.4 Data for ESDU calculations for TC12 profile slat 59
4.5 Data for ESDU calculations for TC12 profile flap 60
4.6 List of available options for ESDU method modification 65
4.7 Initial conditions for CFD calculations 67
4.8 Summary of required boundary conditions from calculations 70
4.9 Summary of solver settings used for Fluent validation simulations 70
4.10 Convergence criteria for Fluent simulations 70
4.11 Summary of TC12 profile clean configuration blocking parameters for meshing . 71
4.12 TC12 Clean Configuration Mesh Element Summary 74
4.13 Grid convergence study of the TC12 profile mesh in clean configuration 76
4.14 Turbulence model selection for Fluent simulations for the TC12 profile clean configuration 78
4.15 TC12 high lift configuration boundary layer mesh parameters 84
4.16 Mesh node and element information for TC12 profile in high lift configuration . . 87
4.17 Grid convergence study for TC12 profile in high lift configuration 89
4.18 Turbulence model selection TC12 profile in high lift configuration 90
7.1 Initial conditions for CAA simulations 138
7.2 Summary of solver settings used for Fluent CAA simulations 140
8.1 Down Selection Process disciplines and criteria part 1 158
8.2 Down Selection Process disciplines and criteria part 2 159
D.1 Mesh information for tri mesh of TC12 profile in clean configuration, ANSYS mesher 182
D.2 Discrepancies between quad mesh and tri mesh for TC12 profile in clean configuration 184

List of Symbols

c'_{ti}	Extended chord of element i [non dimensional to c]
c_{ti}	Chord of element i [non dimensional to c]
$(a_1)_0$	Slope of lift coefficient curve with incidence for basic airfoil in incompressible flow
C_D	Coefficient of Drag
C_{L0B}	Lift coefficient at zero incidence of basic airfoil based on c
C_{L_0}	Lift coefficient at zero incidence including high lift devices
C_{L_m}	Maximum lift coefficient of airfoil including high lift devices
C_{LmB}	Maximum lift coefficient of basic airfoil, based on c
C_L	Coefficient of Lift
C_f	Skin Friction Coefficient
$H(f)$	Heaviside function
H_l	Height of trailing edge of leading edge device above basic airfoil chord line [non dimensional to c]
K_l	Correlation factor for effect of deflection of leading edge devices
L_l	Overlap between trailing edge of deflected edge device and fixed airfoil nose [non dimensional to c]
L	Airfoil Chord Length [m]
M	Free stream Mach Number [M]
M	Free stream Mach Number [m/s]
P'	Pressure Fluctuations [N/m^3]
Re	Reynolds Number
R	Ideal Gas Constant [287 Jkg^1K^{-1}]
T	Temperature [K]
U^*	Friction Velocity [m/s]
U	Free Stream Velocity [m/s]
$\Delta C'_{L0l}$	$\Delta C'_{L0}$ for leading edge device
$\Delta C'_{Lml}$	$\Delta C'_{Lm}$ for leading edge device
ΔC_{L0t}	ΔC_{L0} for trailing edge devices
ΔC_{Lmt}	ΔC_{Lm} for trailing edge devices
Δc_l	Increment in chord due to leading edge device [non dimensional to c]
Δc_{ti}	Increment in chord of element i [non dimensional to c]
Δt	Timestep [s]
α	Angle of attack [degrees]
δ_L	Deflection of leading edge device [degrees]
δ_{ij}	Kronecker delta
δ_{ti}	Deflection of trailing edge device [degrees]
δ	Boundary Layer Length [m]
μ	Kinematic Viscosity [m^2/s]
μ	Dynamic Viscosity [N.s/m^2]
ω	Vorticity [1/s]
ϕ°_{te}	Lift Angle between basic airfoil datum chord at trailing edge and upper surface [degrees]
ρ'	Density Fluctuations [kg/m^3]
ρ_L	Leading edge radius [non dimensional to c]
ρ	Density [kg/m^3]
τ_w	Shear Stress at the wall [N/m ^{2}]

θ_l	Angular trailing edge flap chord length parameter [non dimensional to c]
θ	Deflection Angle of Flap Extension [degrees]
a_l	Rate of change of lift coefficient with leading edge device deflected
a_{ml}	Rate of change of $\Delta C'_{Lml}$ with leading edge device deflection
a	Speed of sound [m/s]
c'_l	Extended chord of leading edge device [non dimensional to c]
c'	Extended chord [non dimensional to c]
c_l	Chord of leading edge device [non dimensional to c]
c	Chord of basic airfoil [m]
f	Frequency [Hz]
k	Heat capacity ratio [dimensionless]
t	Thickness of airfoil [non dimensional to c]
x_n	Chordwise position of fixed airfoil nose [non dimensional to c]
x_{ts}	Chordwise position of trailing edge of shroud [non dimensional to c]
y^+	Dimensionless wall distance
y	Wall distance [m]
he	Height of Maximum Camber at 0.5c of Flap Extension [non dimensional to c]
le	Chord Length of Flap Extension [non dimensional to c]
pt	Point Along Leading Edge of Flap Extension that Extension Passes Through
SPL	Sound Pressure Level [dB]

Nomenclature

CAA	Computational Aeroacoustic
CFD	Computational Fluid Dynamics
CFL	Courant-Friedrichs-Lewy
DES	Detached Eddy Simulation
DNS	Direct Numerical Simulation
DSP	Down Selection Process
EASN	European Aeronautics Science Network
ESDU	Engineering Sciences Data Unit
FAA	Federal Aviation Administration
FAR	Federal Aviation Regulations
FWH	Ffowcs-Williams & Hawkings
HAK	High Lift Concepts 2
KKK	Kryo-Kanal Köln (Cryogenic Wind Tunnel, Cologne)
LBL	Laminar Boundary Layer

LES Large Eddy Simulation

MDO Multidisciplinary Design Optimisations
MOGA Multi Objective Genetic Algorithm

RANS Reynolds Averaged Navier Stokes

SA Spalart-Allmaras
SPL Sound Pressure Level

TBL Turbulent Boundary Layer
TE Trailing Edge

UWE University of the West of England, Bristol

VS Vortex Shedding

1 Introduction

1.1 Research Background

In order for a commercial aircraft to fulfil its primary requirement of efficient flight, it needs a wing that is designed to minimise drag at cruise conditions. A conventional clean wing, however, results in an aircraft with unreasonable short field performance. To provide a compromise between efficient cruise and acceptable airfield performance (in terms of take off and approach speed and distance) the high lift system is introduced.

High lift systems refer to all the components on an aircraft that have the intention of increasing the lift of that aircraft during certain flight conditions. The system generally comprises of: leading edge devices, trailing edge flaps and sometimes a boundary layer influencing device (Primarily in military aircraft.) These devices are covered in more detail within the literature review. Figure 1.1 shows the effect of the two main high lift devices, in various combinations, on a generic lift against angle of attack graph. The figure aims to show the importance of trailing edge devices in increasing C_L,and of leading edge devices in delaying stall when compared to an airfoil without these devices.

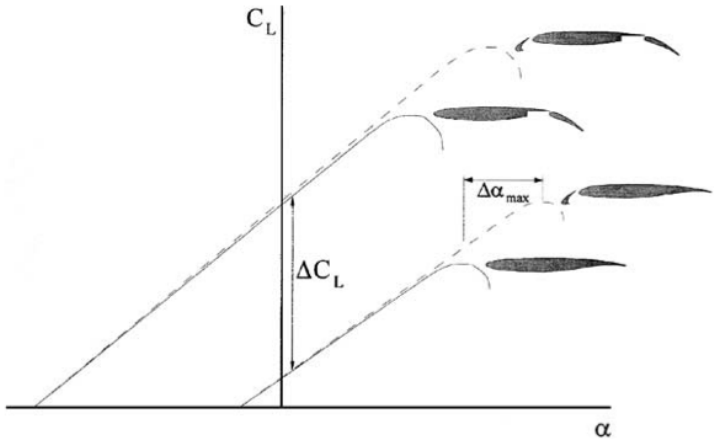


Figure 1.1: Effect of flaps and slats on lift *ESDU 85033: Increments in Aerofoil Maximum Lift Coefficient due to Deployment of Various High Lift Devices* (1992)

High lift systems are used in different configurations for take off and landing. A high L/D_{max} ratio configuration is favourable for take off whilst a high drag configuration is favourable for landing, with emphasis on a high $C_{L_{max}}$.

Take off and landing distances are regulated by the Federal Aviation Administration (FAA) and any design of related high lift systems has to maintain adherence to FAA requirements, Federal Aviation Regulations (FAR) 23.51 (Fed, 1996a) and FAR 25.105, 25.107 and 25.345 (Fed, 1996b) related to high lift devices as well as take off and landing.

The Need for High Lift Systems Research

Currently there is a need for an improved high lift system. There are numerous requirements for the systems and multiple areas in which improvements can be made. Three areas marked for improvement, for high lift devices, are aerodynamics, noise and cost. It is seen that there is a feasible opportunity for advances in the development of these categories.

High lift devices contribute a large portion to the overall cost of the aircraft. Rudolph (1996a) estimates that, in general, the trailing edge (along with all moving surfaces) amounts to 10% of the total cost of the entire aircraft. He adds that a reduction from a triple slotted to a double slotted flap design leads to a flap cost reduction of about a third.

Meredith (1993) lists the following trade-off factors for a generic large twin engine aircraft in order to illustrate the need for high lift system improvements:

- An increase in lift coefficient of 0.10 at constant angle of attack results in a reduction in approach attitude of one degree. This results in a shortening of landing gear due to lower ground clearance requirements and thus a weight saving of 1400 lb (635 kg).
- A 1.5% increase in maximum lift coefficient is equivalent to a 6600 lb (2994 kg) increase in payload at a fixed approach speed.
- A 1% increase in take off L/D is equivalent to a 2800 lb (1270 kg) increase in payload or a 150 nm increase in range.

Aircraft range is empirically calculated by the commonly used Breguet range equation, equation (1.1):

$$R = \frac{\eta}{c}\frac{C_L}{C_D} ln \frac{W_0}{W_1} \tag{1.1}$$

where η is the efficiency of the propulsion, c is the specific fuel consumption, C_L and C_D are lift and drag coefficients respectively and W_0 and W_1 are the take off and landing weights respectively.

Van Dam (2002) puts together a compelling thought experiment which compares two aircraft, one with high lift devices and one instead with a larger wing surface area. He explains that, due to the L/D term of equation (1.1), it is impossible for the aircraft without high lift devices to achieve the same range as that of the aircraft with high lift devices. He concludes that high lift devices will remain necessary for years to come.

European Vision 2020

The European Framework FP-7 highlights a European Vision for the year 2020 with regards to development within numerous research disciplines, one of these being transport, and, on a deeper level, air transport.

According to the European vision for 2020, ACARE (Advisory Council for Aeronautics Science in Europe) has highlighted some research challenges for the 2020 vision (Busquin, 2001). Related to high lift systems (amongst other aircraft subsystems) are the following:

- Drag reduction through conventional and novel shapes.
- Noise Reduction:
  - Reduction in perceived noise to one half of current average levels (10 dB).
- Emission Reduction:
  - 50% cut in CO_2 emissions per passenger kilometre (which means a 50% cut in fuel consumption in the new aircraft of 2020) and an 80% cut in nitrogen oxide emissions.
- Environmentally friendly production, maintenance and disposal.

The European Aeronautics Science Network (EASN) further backs the European Commission's Vision for 2020 by aiming to bring university activities into an integrated network. This online community aims to enable communication between members of specific research fields. The high lift research group falls under the category of flight physics and according to their website (*EASN : Aeronautical Research and Technology Areas*, 2013) has the following primary objectives relating specifically to high lift:

- To reduce take off and landing distances.
- To get simpler and lighter high lift systems (typically 3 airfoils) with the same efficiency than more complex systems.
- To reduce aerodynamic noise.

Up to now, there have been a number of European projects related to the European Vision 2020 high lift research group. Some of them are summarised in the table below.

Project	**Date**	**Contributions**
Eurolift	2000 - 2004	Reduce time and cost of high lift system production by means of better understanding of flow, account for flow effects early on, increase design accuracy, improve correlation between wind tunnel data and flight conditions (Thiede, 2001)
Eurolift II	2004 - 2007	Improvement on Eurolift, realistic new high lift configurations, advanced high lift configurations, flow control(*European High Lift Programme II*, 2006)
SADE	2008 - 2012	Morphing leading edge devices, single slotted flaps, wind tunnel tests for verification(*SADE Public Web Site*, 2009)

Table 1.1: Explanation of European Commission high lift projects to date

2 Literature Review

A Literature survey was conducted on literature related to aerodynamics and aeroacoustics of high lift systems. To introduce the reader to the topic of high lift some time is spent defining necessary terms and explaining the physics thereof. The reader is directed towards the computational studies and prediction of high lift as well as the design of such systems.

For aircraft noise: an introduction to the topic, particularly pertaining to high lift systems, is provided, detailing the noise generating mechanisms and the prediction and suppression thereof. Studies on the reduction of noise are cited in both an experimental and computational environment.

2.1 High Lift Aerodynamics

2.1.1 Physics of High Lift

High lift systems are designed to increase low speed performance of aircraft by increasing lift production of commercial aircraft. The physical reasons for an increase in lift by high lift systems was mathematically formulated and collated by Smith (1975). Smith is considered as one of the first researchers to understand and document the flow physics relating to high lift systems. His paper is widely cited throughout high lift research and no high lift research is complete without an understanding of his observations.

Smith comments on slots saying that a slot is, contrary to understanding at the time, not a device that adds energy to the flow. He states that if anything, a slot gives flow a lower velocity with a maintained total head.

Smith made five key observations related to gaps. As follows:

1. *Slat effect*: Pressure peaks are lowered due to the velocities of individual airfoil elements running counter to each other. By simulating a slat as a vortex at the leading edge of a conventional airfoil he showed that the C_L of the total system was higher than the clean configuration.

2. *Circulation effect*: By increasing circulation, lift is increased. Similar to the slat effect adding a vortex at the trailing edge of an airfoil increases total circulation around an airfoil (unlike before where a leading edge vortex decreased circulation due to counter running velocities).

3. *Dumping effect*: As an individual fluid element leaves the trailing edge it is effectively 'dumped' overboard. At the trailing edge of a multi-element airfoil there is effectively a vortex (as stated earlier) which increases circulation at the trailing edge. This increased velocity accelerates a boundary layer over the edge faster than what would be normal thus relieving pressure quicker and minimising the adverse pressure gradient.

4. *Off-the-surface pressure recovery*: At high angles of attack a pressure gradient may become large enough to encourage separation. With the addition of a gap between airfoils in a multi-airfoil configuration the adverse pressure gradient is able to recover more efficiently than it would if it were in continuous contact with a wall.

5. *Fresh boundary layer effect*: Each element receives a new, thin, boundary layer giving the fluid elements better resistance to separation.

Smith concludes that an airfoil having $n+1$ elements will always perform better than an airfoil with only n elements. He proves this by means of mathematical formulations which will not be included here. Van Dam (2002) on the other hand disagrees with the theory stating that the confluent boundary layer, which is a combination of the fresh boundary layer on every $n+1$ element and the dumped boundary layer from the n^{th} element, is much thicker than a conventional boundary layer hence increasing risk of separation. Van Dam concludes the argument by saying that an optimisation of the gap size requires a balance of the viscous and inviscid effects.

2.1.2 Limits of High Lift

The maximum possible lift coefficient that can be achieved, in a theoretical case, is that of the lifting cylinder. A lifting cylinder, as experimented on by Prandtl and Tietjens (1957) can be theoretically seen to provide a maximum lift coefficient of $C_{L_{max}}=4\pi$. In real world applications, due to viscous effects, there will always be separation on a lifting cylinder which will hamper it from producing the maximum possible lift. Smith (1975) also provides a detailed argument about lifting limits in relation to Mach numbers. His observations are interesting yet, due to their purely fundamental nature, are not necessary for clarification within this dissertation.

2.2 High Lift System Design

Design of high lift systems revolves around design of components to provide sufficient aerodynamic performance of aircraft at lower speeds than cruise for reasonable airfield performance. Apart from the aerodynamic limits of high lift other limits must also be considered; namely: tail strike angle, aircraft moment balancing, structural limits, passenger comfort, optimal take off distance and second segment climb angle. Proper design of a high lift system accounts for as many known variables as possible.

2.2.1 High Lift Components

The high lift system comprises of three primary components, namely the leading edge device (slat, Krueger flap, etc.), trailing edge device and possibly flow control devices. All these devices aid in increasing lift of the aircraft using their own unique methods. What follows is a brief explanation of trailing edge devices and flow control as well as some basic information relating to the physics thereof.

Mason (2007) provides a fairly extensive summary of high lift devices in their current form. Dick Kita, of Grumman, made the following drawings (Figure 2.1) of various conventional configurations of high lift systems (Kita, Feb. 1985). These drawings can form a starting point in the design or understanding of a high lift system.

Trailing Edge Devices

Figure 2.1 shows a series of trailing edge devices used to increase lift. The most basic of these devices is the plain flap which is a hinged section near the trailing edge of a clean airfoil. The plain flap introduces an increased camber to the clean airfoil providing additional aerodynamic loading towards the trailing edge. Lift produced by the airfoil is increased at the expense of higher drag.

In commercial aircraft, the primary type of device used is the Fowler flap. The actuation of this flap allows the flap to translate and rotate into a position that provides optimum aerodynamic efficiency for increased lift. Many commercial aircraft have multi-slotted flaps whereby the Fowler flap is split into multiple sections (each with their own translations and rotations). These multiple slots work on the *slot effect* (put forth by Smith (1975)) to increase lift production.

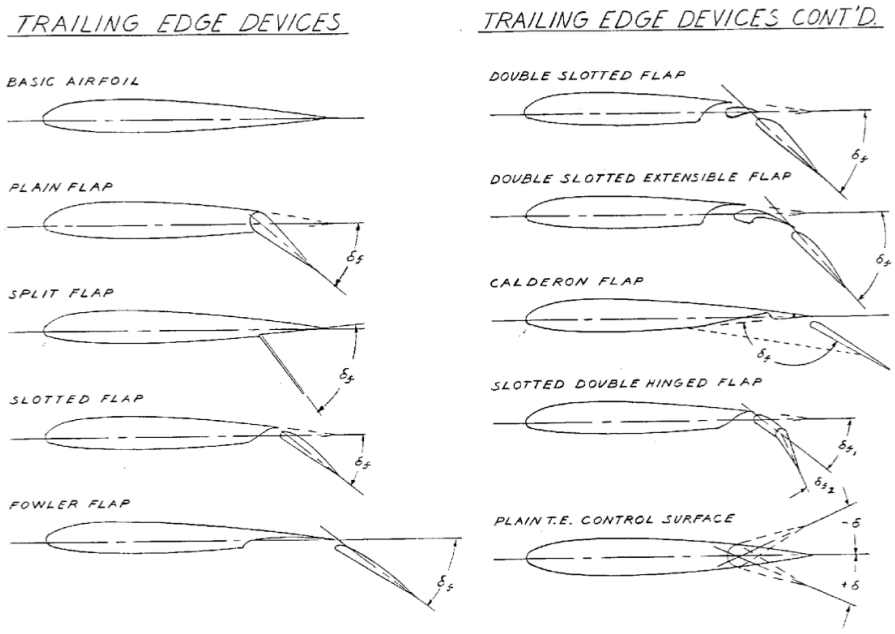


Figure 2.1: Drawings of various trailing edge high lift devices

A particularly novel trailing edge device is showcased on the new Airbus A350XWB in the form of a dropped-hinge flap (*The ADHF "advanced dropped hinge flap" patented by Airbus onboard the A350 XWB*, 2013). This design sees the spoiler employed with a two direction hinge which, firstly, allows regular operation of the spoiler as an airbrake during landing, but also allows the spoiler to optimise the gap between itself and a single slotted flap at different flap settings as well as slightly increasing aft camber of the overall airfoil. Figure 2.2 shows a schematic of the design as well as an illustration of the lift improvements by means of the implemented concept.

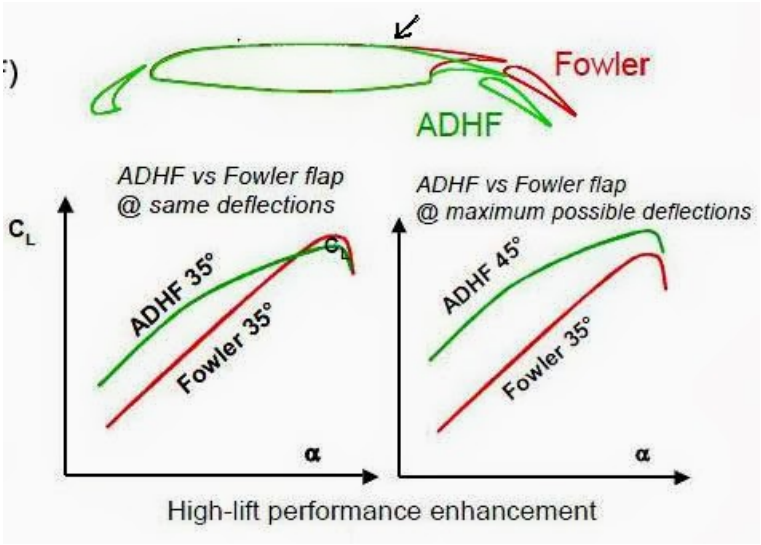


Figure 2.2: Advanced drooped hinge flap lift compared to a conventional fowler flap (*The ADHF "advanced dropped hinge flap" patented by Airbus onboard the A350 XWB*, 2013)

The general trend in trailing edge device design has been to become mechanically simpler. Figure 2.3, as compiled by Reckzeh (2003) shows how both Airbus and Boeing have simplified the number of elements of their trailing edge devices since their inception. Although the Airbus A350 XWB and Boeing 787 are not included in the diagram they would still follow the same trend, the 787 employs two sets of single slotted flaps (inboard and outboard) and the A350 is on par with previous development.

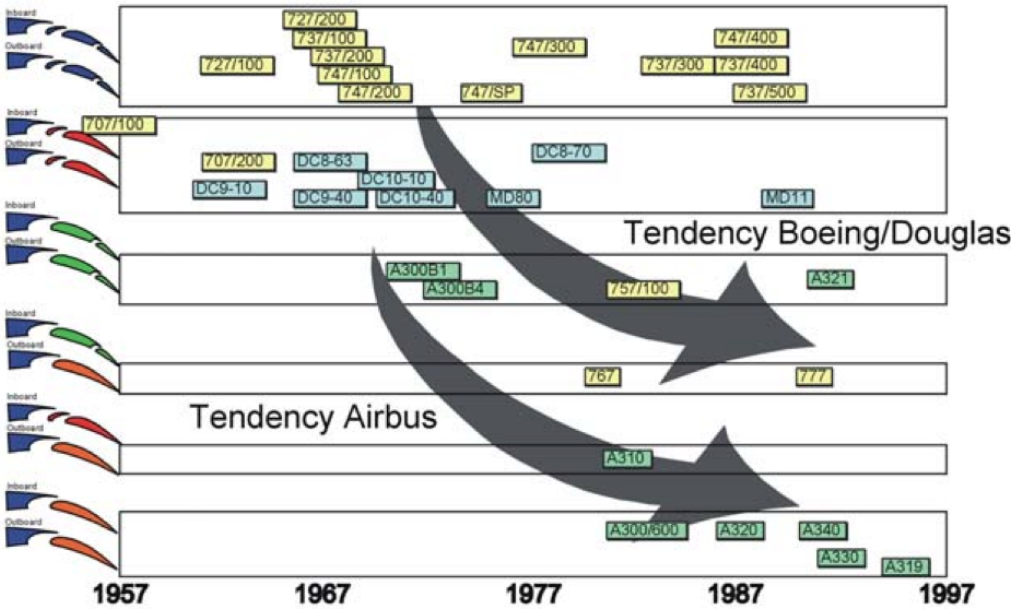


Figure 2.3: Development of trailing edge high lift systems on airliners (Reckzeh, 2003)

Trailing edge device design is also well documented by Smith (1975). An important observation of his is the optimum position of a cylinder at the trailing edge of an airfoil which will provide maximum lift. Smith concludes, by means of experiments, that a cylinder placed at approximately 60 degrees from the trailing edge will provide the best increase in circulation for the system. This is a good fundamental starting place for any trailing edge device design.

Rudolph (1996b) discusses out a number of roadblocks for single slotted flaps. He explains that there are two major obstacles, the first is that a single slotted flap produces a lower maximum lift coefficient than that of flaps with additional slots- this may be insufficient for landing. Secondly the single slotted flap could allow for unnecessarily high airplane attitude at landing. He adds that a single slotted flap should not provide problems during take off.

Rudolph suggests a number of possible solutions and design directions for future single slotted flap design (his suggestions are all backed with a series of observations which are not included here). His suggestions are summarised as follows:

- Maximize the flap deflection angle.
- Increase the wing incidence angle.
- Maximize the flap span.
- Minimize flap discontinuities.
- Use drooped spoilers.
- Increase flap chord and wing area.
- Minimize leading-edge discontinuities.
- Compromise on wing leading-edge contour.
- Optimize slat taper.
- Decrease slat deployment angle.
- Trade slat chord for an increase in flap chord.
- Use a more efficient flap mechanism.

Leading Edge Devices

Figure 2.4 shows a series of leading edge high lift devices. The role of these devices is typically to delay stall to higher angles. When coupled with a trailing edge device the leading edge device can be seen to delay stall so that the trailing edge device can increase lift more effectively at higher angles.

The effectiveness of the leading edge devices in figure 2.4 typically ranges from top to bottom with the *increased leading edge radius* being least effective and the *slat* being the most effective.

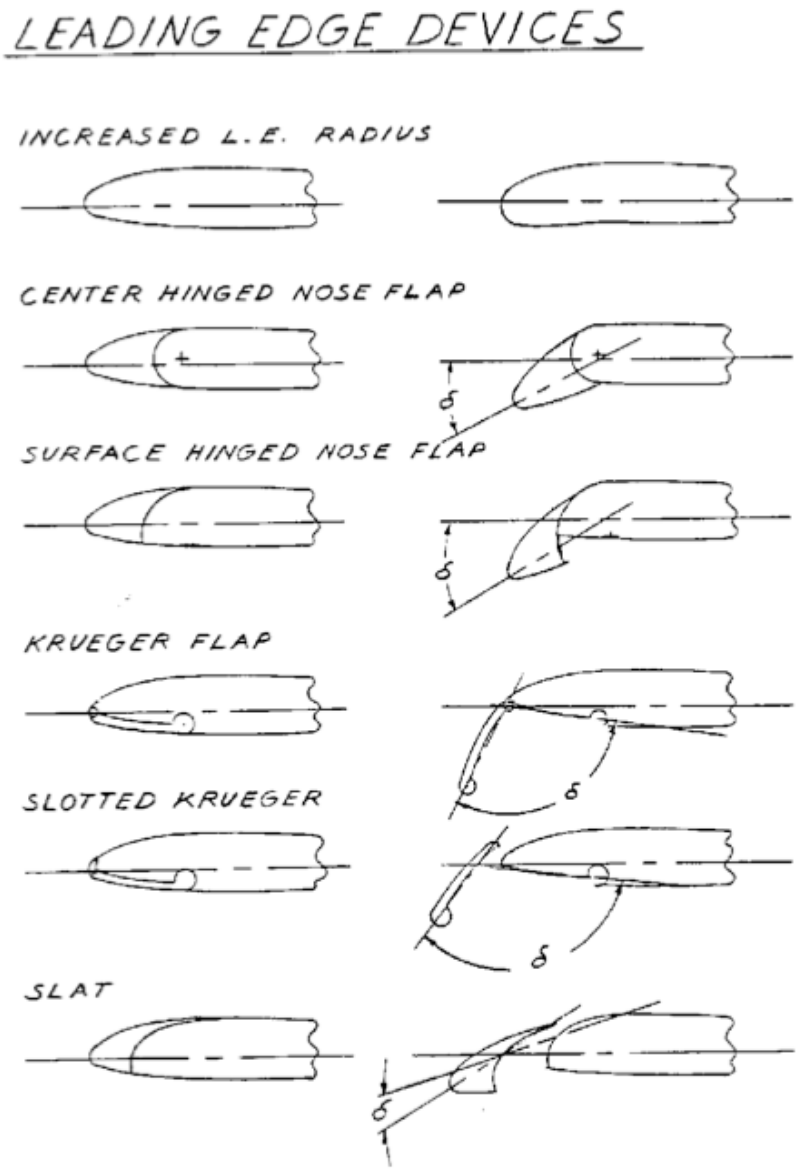


Figure 2.4: Drawings of various leading edge high lift devices

F. and Fullmer (1947) writes a fundamental NACA report which discusses the effectiveness of two different types of Krueger flaps- one intended to slide forward along the upper surface and another hinged on the lower surface of the airfoil. Both models were tested with a trailing edge split flap and a combination of results were found. The most effective design was that of the upper surface flap which provided an increase in maximum lift of 30% over the plain airfoil. The lower surface flap, by comparison, provided an 8.5% increase in maximum lift.

Actuation Devices

In order for flaps and slats to extend and retract an actuation system is used. High lift devices extend and retract by means of geared tracks or linkage systems. There is a contradictory constraint put forth by the available range of motion of the linkage system and the aerodynamically

optimal position required by the high lift device.

Flow Control Devices

Flow control is any way of adjusting flow over a wing to achieve a desired effect. The following is a list of flow control strategies:

- *Power Augmented Lift:* By blowing air from the aircraft jet engine over a flap the circulation around a wing can be increased dramatically, allowing for very short take off. The technology is primarily for military transport aircraft use (Campbell, 1964).
- *Blowing and Suction:* Boundary layer length can be controlled by either blowing to add energy to the boundary layer thus delaying stall or, by sucking, to remove the onset of turbulent flow and also, hence, delaying stall (Schlichting, 2000).
- *Vortex Generation:* (Patzold, 2008) By tripping a boundary layer to transition from laminar to turbulent flow at the predicted transition point, separation can be minimised because of the addition of a high energy turbulent boundary layer. This increases the stall angle at a cost of increased drag in all flight configurations. Vortex generation can be performed passively by means of turbulators or actively with flow control strategies.
- *Magnus Effect:* (Seifert, 2012) The effect that a rotating cylinder can provide lift is a commonly noted fundamental aerodynamic case. Experiments have been conducted on full scale flying magnus effect aircraft and, while they may be aerodynamically efficient in terms of L/D they are not efficient from a power generation point of view. Additional power is needed to maintain the correct circulation needed for lift.
- *Plasma Actuation:* This mechanism of flow control is to maintain flow attachment by means of electrical current (Shang and Huang, 2014).

2.3 High Lift System Simulations

2.3.1 Computational Studies

Rumsey and Ying (2002) provides one of the broadest papers detailing the CFD capabilities in predicting high lift aerodynamics in 2002. Within his paper he assesses 10 - 15 years of research within the field and draws trends based on the computations.

MSES (*MSES Multi-element Airfoil Design/Analysis Software*, 2013) is a coupled full potential/euler flow solver written by Dr. Drela of MIT. The code has been shown to provide good results but does, however, have a tendency to over-predict lift (Van Dam, 2002). Mason (2010) explains how MSES can lead to inaccurate predictions due to the coupling of viscous and inviscid effects within the code. He provides a method which can be used in order to get calculations to agree with test data- the idea is to change the properties, α, M_∞ or C_L in order to match pressure distributions between experimental and computational results. Instead of running a simulation at a specific angle of attack (to solve for C_L) a better approach is to run the simulation at a certain lift coefficient and to solve for angle of attack.

Within the prediction of high lift a number of challenges are faced. Current CFD methods, particularly the design of turbulence models, related to external aerodynamics struggle to correctly predict the complex flow fields around high lift airfoils. Figure 2.5 from Rumsey and Ying (2002) provides a detailed look at the challenges inherent in the CFD predictions. Many of the issues are related to merging boundary layers which are not handled well in conventional RANS CFD equations. Another issue is the large number of separations along the elements- the complex flow fields around multi element airfoils has made stall points hard to predict.

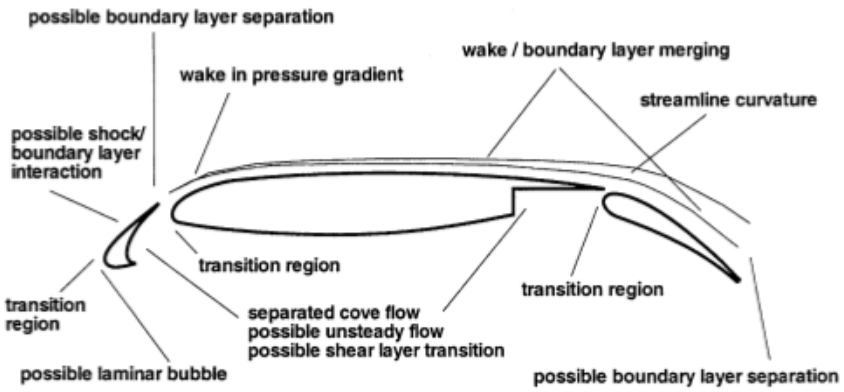


Figure 2.5: Challenges inherent in multi-element flow field prediction (Rumsey and Ying, 2002)

Rumsey provides a set of conclusions on high lift prediction from his paper:

- In both 2-D and 3-D flows, surface pressures, skin friction, lift, and drag can generally be predicted with reasonably good accuracy at angles of attack below stall.
- In 2-D flows, computed velocity profiles (with the exception of slat wakes) generally follow experiment reasonably well. Misprediction of the slat wake does not appear to have a significant influence on integrated quantities below stall. Not enough comparisons have been made yet in 3-D to know if the same trend regarding slat wake holds there.
- In 2-D flows, trends due to Reynolds number can usually be predicted. However, analysis to date has only been performed at relatively low (Re 10 million) Reynolds numbers at which wind tunnel measurements have been available. Trends due to geometry changes (e.g. gap, overhang) can some- times be predicted, but in general CFD is unreliable in this regard.

Rumsey also includes a series of guidelines for predicting high lift with regards to gridding guidelines and solver settings. These are not included here but can be found in his paper (Rumsey and Ying, 2002).

The High Lift Prediction Workshop (*AIAA CFD High Lift Prediction Workshop*, 2014) has been active since 2010 and has, since then, hosted two workshops on CFD prediction of high lift. There is a large amount of experimental data for the profile available for validation.

The second workshop (HiLiftPW-2, June 2013) provided a standard geometry and set of grids for participants to "Assess the numerical prediction capability (meshing, numerics, turbulence modelling, high-performance computing requirements, etc.) of current-generation CFD technology/codes for swept, medium-to-high-aspect ratio wings for landing or take-off configurations" (*AIAA CFD High Lift Prediction Workshop*, 2014). The geometry tested is the EUROLIFT DLR F-11 profile (as used by Thiede (2001))- a three dimensional half wing model which represents a typical high lift system as would be seen on a commercial aircraft.

The most recent High Lift Prediction Workshop is inconclusive with regards to submitted results. There were 48 submitted cases, a majority of which (about 80%) used the SA turbulence model. Areas of concern uncovered within the study were:

- There is a large scatter of results close to stall. All the grids tested either over, under or correctly predicted lift. No trend was observed.
- Many of the grids had convergence issues where residuals would 'hang'.
- The addition of slat and flap tracks as well as bundles of pressure tubes affected results.
- CFD mostly mispredicted drag and pitching moments at any angle of attack above 7 degrees.

2.3.2 Optimisation Studies

Duddy (1949) explains that for take off and landing there are certain optimum values of $C_{L_{max}}$ for best efficiency. He explains that during take off it is favourable to have a slightly lower value for maximum lift coefficient than for landing. The reason for this is that a higher lift coefficient provides a shorter take off but an extended second segment climb. It is important to note that due to the age of the paper not much attention is given to swept transonic wings or aircraft with jet propulsion.

Modern optimisations have shifted towards Multidisciplinary Design Optimisations (MDO) whereby a number of different parameters are optimised in order to fulfil a list of requirements in a number of different fields.

Wild (2008) provides a review of a CFD based optimisation that couples an aerodynamic and kinematic optimisation into its MDO environment. The result is an optimised trailing edge flap with a number of different operating points as well as a kinematic system that is able to extend the flaps close to the necessary operating points.

Reckzeh (2004) gives an insight into how Airbus designed a high lift wing for the Airbus A380. He explains the different sets of requirement based on aerodynamic performance required for take off and landing. Slat geometry was optimised and the clean wing slightly compromised in order to achieve acceptable high lift performance. After the 2D design was finalised, the 3D design was analysed using multiple slat and flap configurations as well as *quasi-3D* methods to predict performance. Wind tunnel tests were conducted. The wind tunnel test data was compared with the computational predictions to aid in the design process.

Mamo (2010) uses a house of quality analysis to analyse a number of unique concepts for high lift. The analysis leads to a serrated leading edge device being analysed and tested in a wind tunnel to confirm the initial hypothesis.

An example of a modern high lift system design employing an MDO approach is that of the system designed for the A400M. Reckzeh (2008), states that in the design of the A400M high lift system there were a number of mission requirements which were different to requirements of commercial transport. To optimise a solution a balance of aerodynamic performance, weight, kinematics and other aspects need to be considered. This balance of requirements is required for all modern high lift systems.

Kania et al. (n.d.) presents a novel concept which covers the spoiler cove during take off and landing. This trailing edge modification sees gains aerodynamic performance for take off. Landing performance is worse than the baseline with the new concept.

2D airfoil methods are widely used in high lift optimisation. Soulat et al. (2012) performs a multi objective optimisation on a typical three element high lift airfoil, the author parameterises the gap and overlap as well as the rotation angle of the flap and slat. Improvements in lift are found. Wild (2008) states that the optimisation process took five weeks turn-around time, showing the slow turn around times for such projects. Faster processing times are possible but require high computational resources, effort has been directed towards faster CFD optimisations (Brezillon et al., 2008).

Chen et al. (2012) run a 2D optimisation with a Genetic Algorithm to optimised slat and flap positioning in order to maximise aerodynamic performance. The optimisation uses a human in the loop which can add or remove design points to aid in rapid convergence. The objective function is to optimise maximum lift near stall. This was performed successfully.

2.4 Aircraft Noise

Modern aircraft are aiming to become quieter for both passengers as well as those living near airports, as noise is both a nuisance and a health risk. In the past few decades there has been a shift in focus within aircraft design and operations which has aimed to determine noise sources and find ways in which to minimise or alleviate their effects.

Figure 2.6 shows the EPN (Effective Perceived Noise) generated by different aircraft components for two different types of aircraft (Herr, 2012). Dobrzynski (2008) explains that for the same air speed; an aircraft in the landing configuration will produce 10dB more noise due to deployment of high lift systems. It is broadly perceived that an increase of 10 dB is perceived to be a doubling of loudness. From the diagram it is shown that for a long range air transport flap noise accounts for 4% of the total aircraft noise which is in total about 7% of overall airframe noise. Likewise for a short range transport these figures are raised to 6% of total noise which leads to a contribution of 10% of overall airframe noise.

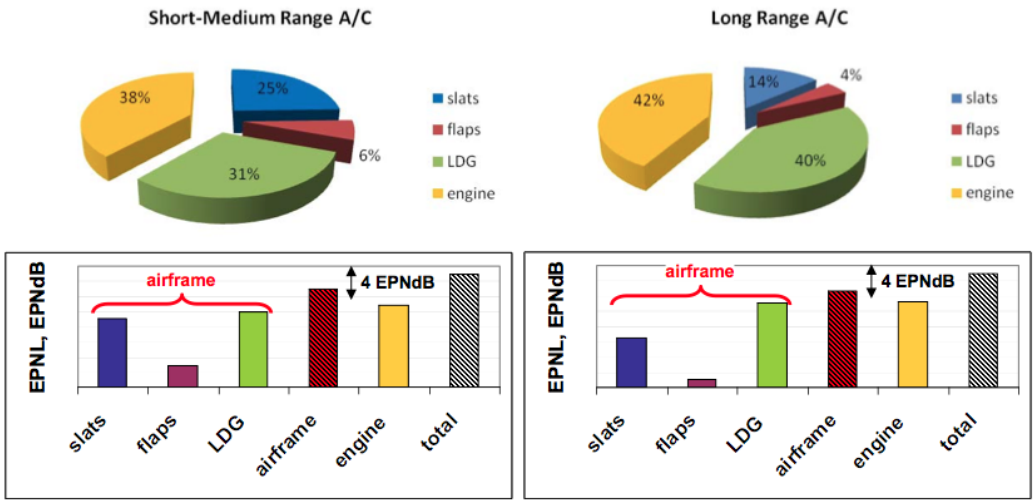


Figure 2.6: Aircraft noise levels by component during approach (Dobrzynski, 2008)

Noise generated by aircraft is generally measured by its Sound Pressure Level (SPL) (2.1):

$$SPL = 20log_{10}(\frac{P'_{RMS}}{P_{ref}}) \tag{2.1}$$

where P'_{RMS} is the Root Mean Square of the pressure fluctuations and P'_{ref} is the reference pressure which is generally $2e{-}5$ Pa (equivalent to the pressure generated by a mosquito in a room).

2.4.1 Airfoil Noise

Brooks et al. (1989) is a fundamental NASA research paper that collects data related to airfoil noise generation mechanisms as well as the prediction thereof.

According to Brooks et al. (1989), airfoil self-noise occurs due to interactions between an airfoil blade and the turbulence produced in its own boundary layer and near wake. It is the total noise produced when an airfoil encounters smooth non-turbulent inflow. Six specific flow conditions are cited as being fundamental noise producers.

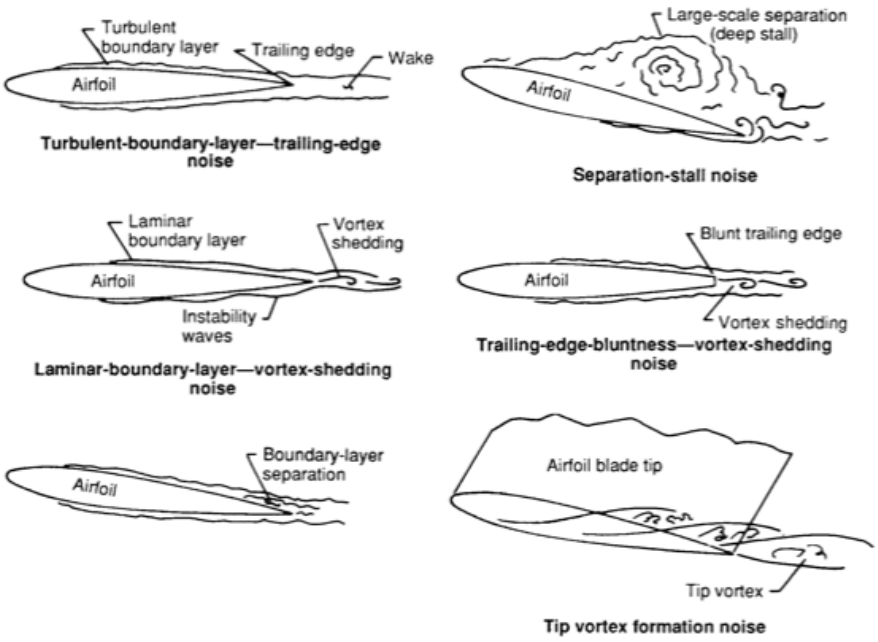


Figure 2.7: Five different types of airfoil self noise

Brooks et al. (1983) explains the noise mechanisms for airfoil self noise seen in figure 2.7 as follows:

- At high Reynolds number, there is a Turbulent Boundary Layer (TBL) along most of the airfoil. Noise is produced as turbulence passes over the Trailing Edge (TE).
- At low Re, there is mostly a Laminar Boundary Layer (LBL) along the airfoil. The instability of this boundary layer results in Vortex Shedding (VS) and noise from the TE.
- At angles of attack greater than zero, flow can separate near the TE on the upper surface to produce TE noise due to the shed turbulent vorticity.
- At angles of attack post stall large scale separation causes low frequency noise.
- A blunt TE can produce vortex shedding and associated noise.
- Tip vortices from flap edges (or propeller blades) produces aerodynamically generated noise.

2.4.2 High Lift System Noise

High lift systems are identified as a major source of noise during take off and landing. The complex design of high lift systems thus far has purely been from an aerodynamic point of view. Lately various studies and research efforts have been directed to minimising noise related to high lift systems. Research has concentrated on better predicting this noise and understanding primary noise generators by means of fly over tests (Gibson (1974), Sijtsma and Stoker (2004)). Zhang (2010) and Casalino et al. (2008) identify primary noise sources within high lift devices. The four primary noise generators are as follows:

Slat Noise

Figure 2.8 shows a schematic of the suspected major slat noise sources as researched by Choudhari et al. (2012). Zhang (2010) explains that slat noise is a result of various sources. The edge cusp provides a separation of flow on the lower surface of the slat, this produces an unsteady shear layer that bounds a recirculation region within the cove. The impact of the unsteady shear layer on the main element causes additional impingement on the unsteady shear layer this produces a tonal noise feedback loop. These unsteady structures are a source of broadband noise.

The finite thickness trailing edge of the slat leads to vortex shedding which produces high frequency and low to middle frequency noise sources.

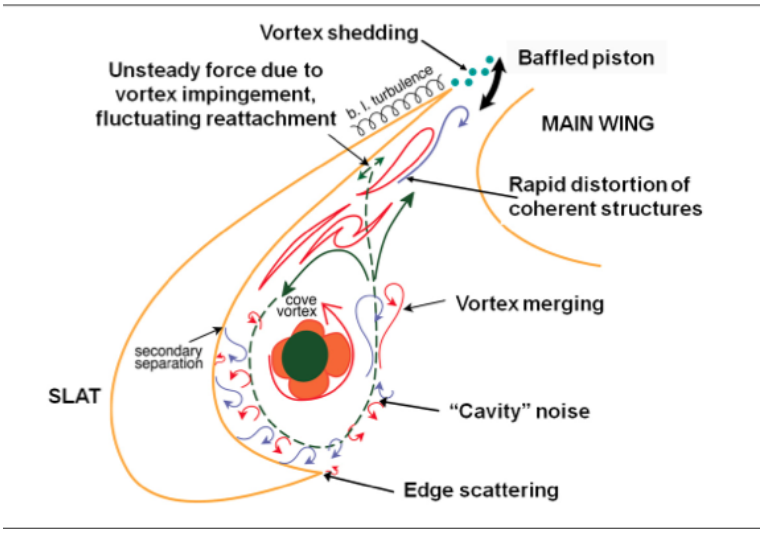


Figure 2.8: Suspected slat noise sources (Choudhari et al., 2012)

Singer et al. (1999) observes that, for a slat, there is significant sensitivity to slat position, moving the slat in their experiment by 20 degrees caused an increase in SPL by 20dB. They conclude that vortex shedding from the trailing edge of the slat is responsible for high-frequency noise.

Flap Side Edge Noise

Angland (2008) performed experimental and computational studies on flap side edge noise, identifying three potential acoustic sources. The first two sources were the turbulent shear layers that rolled up to form the flap side-edge vortex. A mid-frequency broadband hump was measured by an on-surface microphone at the point of reattachment of the turbulent shear layer on the flap side-edge. The third source was a low frequency instability in the off-surface vortex due to non-linear vortical interactions upstream of the flap.

Slat Track and Flap Track Fairing

Dobrzynski et al. (1998) performed studies comparing a high lift wing model that included a

set of slat and flap tracks with a model without these included devices. They found that these fairings and tracks are a source of noise, increasing overall noise of a configuration by about 8dB.

Trailing Edge Noise

As discussed in the section on airfoil self noise, trailing edge noise is a source of aerodynamically generated noise. Within a high lift system this is also a primary noise generator. There is a large amount of separation on the flap, particularly during landing, as the flap is generally positioned at a high angle of attack (beyond 20 degrees). This separation, as a turbulent flow, is a source of noise.

Noise Reduction Methods

There have been a number of projects specifically related to the reduction of sound from high lift devices. Some projects have worked on minimising sound at the source by means of altered geometries which would remove sound generating mechanism; whilst other projects have attempted to damp existing sound. A list of the European FP-7 (and prior) projects related to high lift noise reduction can be found on the X-NOISE[1] website.

Below is an excerpt of some European aeroacoustic projects related to the second generation work. The list is specifically geared towards summarising projects related to noise from high lift systems.

- *TIMPAN* (2006–2009): Technology to IMProve Airframe Noise, had a focus on landing gear and high lift systems. The projects high lift focus was threefold:
  - *Slatless configurations:* these would eliminate sound from slats and make use of the Coanda effect from engines to improve circulation instead.
  - *Acoustic treatment:* this process applies sound dampening material to a sound source to dampen its effect. Possible implementations are wing leading edge liner, slat wire meshes and slat trailing edge treatments.
  - *Slat settings:* Setting slat gaps to achieve optimum acoustic properties whilst minimising aerodynamic losses. This was seen as the most effective solution with an overall decrease of 3.5 dB from the baseline configuration. Figure 2.9 highlights the successful results for this component of the project.

[1] According to their website (www.xnoise.eu) "X-NOISE is a collaborative network project in the area of aeroacoustics. To lower the exposure of community to aircraft noise. We strive to coordinate research activities, disseminate results, and contribute to an aeroacoustical knowledge base. X-NOISE is made possible by the European Union."

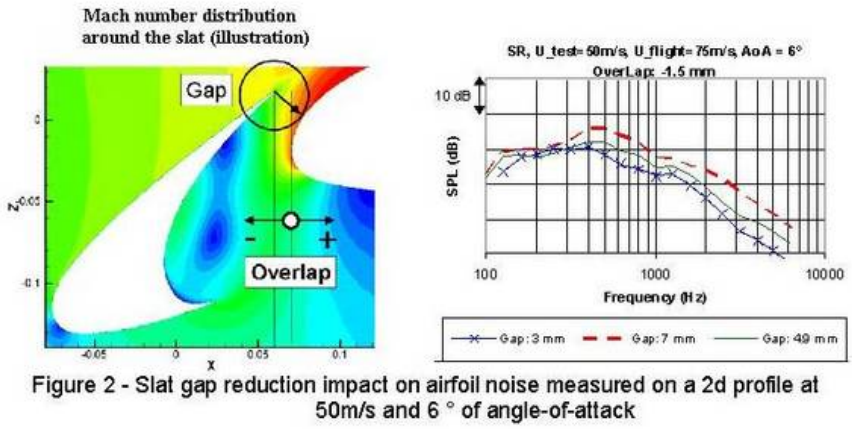


Figure 2.9: Slat setting results summary for TIMPAN project (*Technologies to IMProve Airframe Noise* , 2013)

- *VALIANT* (2009–2012): VALidation and Improvement of Airframe Noise prediction tools (*VALidation and Improvement of Airframe Noise prediction Tools*, 2009). The project was performed in a number of smaller work packages. Figure 2.10 shows the airfoil noise sources examined in the project. The project focussed on four generic test cases:
  - Turbulent flow over a gap
  - Flow past airfoil with flap
  - Flow past airfoil with slat
  - Flow past two-struts (landing gear)

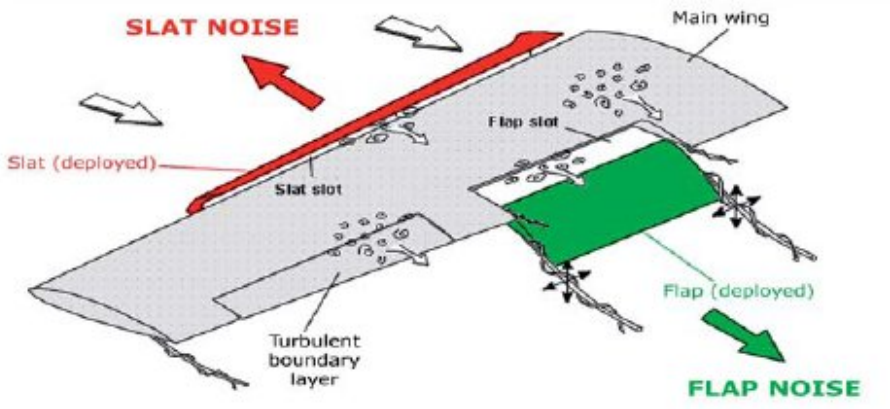


Figure 2.10: Noise sources examined during the VALIANT project

- *OPENAIR* (2009–2013): The primary aim of OPENAIR (OPtimisation for low Environmental Noise impact) *OPtimisation for low Environmental Noise impact* (2009) is a reduction of 2.5 dB towards ACARE goals. For the high lift section of the project further

work is done to optimise the high lift slat gap and overlap (as in TIMPAN) for maximum decreases in noise levels. Further work was also done on flap side edge treatments, as well as minimisation of spoiler noise by means of fractal shapes on the underside of spoilers to minimise recirculation. Emphasis was placed on successfully validated CAA cases being run.

2.5 Aeroacoustics

Aeroacoustics is the study of noise caused by aerodynamic forces. Aeroacoustic noise is generated by time dependent pressure fluctuations. Turbulent flow is a primary source of the fluctuations but other sources are, recirculations (as in separation bubbles or in slat coves) and vortices.

2.5.1 Lighthill's Analogy

Lighthill is attributed with defining modern day aeroacoustics by solving the Lighthill analogy- an analogy to describe sound production derived from rearranging the RANS equations into a form similar to that of the 'classical' wave equation for conventional acoustics (Lighthill (1952), Lighthill (1954)). Lighthill's theory is an analogy which means that, although the equation is exact and derived without approximation, it is only one in which the acoustic terms are replaced by representative fluid terms. Because of this the Lighthill analogy can only solve for certain aspects of the full acoustic solution. The analogy is less computationally intensive than a direct computation. Lighthill describes sound sources in terms of three different sound sources: *monopole, dipole and quadrupole* sources.

Wagner et al. (2007) describes the different sound sources as people jumping up and down in a boat. According to the authors a monopole is described as a single person jumping up and down in a boat. The boat generates waves in the water which radiate outwards. A dipole is described as two people in a boat passing a ball to eachother. The exchange produces oscillations due to the force required to throw or catch the ball. A quadropole is described as a chaotic motion of two people fighting in a boat.

In deriving the Lighthill analogy the first step is to assume that the listener is at a farfield location away from the sound source. That is to say the listener is sufficiently far away enough that the fluid in the vicinity of the listener is uniform and stagnant. Thus the acoustic field around the listener can be described by the wave equation:

$$\frac{\partial^2 \rho'}{\partial t^2} - C_0^2 \nabla^2 \rho' = 0 \tag{2.2}$$

where ρ' is the fluctuating component of density ($\rho = \rho_{mean} + \rho'$), t is time and C_0 is the speed of sound in the farfield. The derivation of equation (2.2) can be found in any acoustics textbook and is not included here.

Any part of the fluid not described by the behaviour of a uniform stagnant flow as described by the wave equation is considered to be a source term. The Lighthill analogy is a collection of

these source terms.

To begin the derivation of the analogy the mass and momentum equations of a fluid need to be defined. These are equations (2.3) and (2.4) respectively.

$$\frac{\partial \rho}{\partial t} + \nabla \cdot (\rho \bar{v}) = m \tag{2.3}$$

where $\bar{v}$ is the velocity vector and m is mass.

$$\frac{\partial}{\partial t}(\rho \bar{v}) + \nabla \cdot (\bar{P} + \rho \bar{v} \bar{v}) = \bar{f} + m\bar{v} \tag{2.4}$$

where $\bar{f}$ is an external force density, $\bar{P}$ is the negative of the fluid stress tensor.

Taking the time derivates of the mass conservation equation ((2.3)) and including a volume fraction, β as well as eliminating $\partial m/\partial t$ we find equation (2.5):

$$\frac{\partial^2}{\partial t \partial x_i}(\rho v_i) = \frac{\partial m}{\partial t} - \frac{\partial^2 \rho}{\partial t^2} = -\frac{\partial^2 \rho_f}{\partial t^2} + \frac{\partial^2 \beta \rho_f}{\partial t^2} \tag{2.5}$$

where v_i is the fluid velocity, ρ_f is $\rho_f = \rho_0 + \rho'$ which is the density terms of the steady (ρ_0) and unsteady (time dependant) (ρ') fluctuations combined and β is the volume fraction appended due to properties of mass injection.

Performing the divergence of (2.4) yields (2.6):

$$\frac{\partial^2}{\partial t \partial x_i}(\rho v_i) = -\frac{\partial^2}{\partial x_i \partial x_j}(P_i j + \rho v_i v_j) + \frac{\partial f_i}{\partial x_i} \tag{2.6}$$

Combining equations (2.5) and (2.6), equation (2.7) is obtained:

$$\frac{\partial \rho_f}{\partial t^2} = \frac{\partial^2}{\partial x_i \partial x_j}(P_i j + \rho v_i v_j) + \frac{\partial^2 \beta \rho_f}{\partial t^2} - \frac{\partial f_i}{\partial x_i} \tag{2.7}$$

Using this solution a wave equation can now be constructed by introducing the term $-C_0^2(\partial^2 \rho')/(\partial x_i^2)$ to both sides of (2.6) to obtain:

$$\frac{\partial^2 \rho'}{\partial t^2} - C_0^2 \frac{\partial \rho'}{\partial x_i} = \frac{\partial^2 T_{ij}}{\partial x_i \partial y_i} + \frac{\partial^2 \beta \rho_f}{\partial t^2} - \frac{\partial f_i}{\partial x_i} \tag{2.8}$$

Where:

$$T_{ij} = P_{ij} + \rho v_i v_j - (C_0^2 \rho' + P_0)\delta_{ij} \tag{2.9}$$

Equations (2.8) and (2.9) are simplified to:

$$C_0^2 \frac{\partial^2 \rho'}{\partial x_i^2} = \frac{\partial^2 \rho' \delta_{ij}}{\partial x_i \partial x_j} \tag{2.10}$$

And;

$$T_{ij} = \rho v_i v_j - \tau_{ij} + (p' - C_0^2 \rho')\delta_{ij} \tag{2.11}$$

Equation (2.10) is the usual form of the Lighthill's analogy as seen in literature. The left hand side is the wave equation ((2.2)) whilst the right hand side is the source term which includes equation (2.11) which is the Lighthill stress tensor; this explains three aeroacoustic processes on production of sound (Hirschberg, 2004)- namely:

- Non linear convective forces described by the Reynolds stress tensor $\rho v_i v_j$
- The viscous forces τ_{ij}
- The deviation from a uniform sound velocity C_0 or the deviation from an isentropic behaviour $(p' - C_0^2 \rho')$

Equation (2.9) is exact and still hard to solve; in practice an integral formulation of this equation is used. This equation and its derivation are not included but can be found in Hirschberg (2004).

2.5.2 Ffowcs-Williams & Hawkings Acoustic Analogy

Ffowcs-Williams and Hawking (1969) derived the Ffowcs-Williams & Hawkings (FWH) equation; a rearrangement of the exact continuity and Navier Stokes equations. The time histories of which are required for calculation. To solve the FWH equation a surface and volume integral are required, this surface is arbitrary but should be defined sufficiently close to acoustic sources (eg: turbulence) in order to capture noise from these locations. ANSYS Fluent has a built in FWH solver which deals with this integration region requirement by allowing the user to create meshes with multiple fluid domains joined with a permeable surface between them (see figure 2.11).

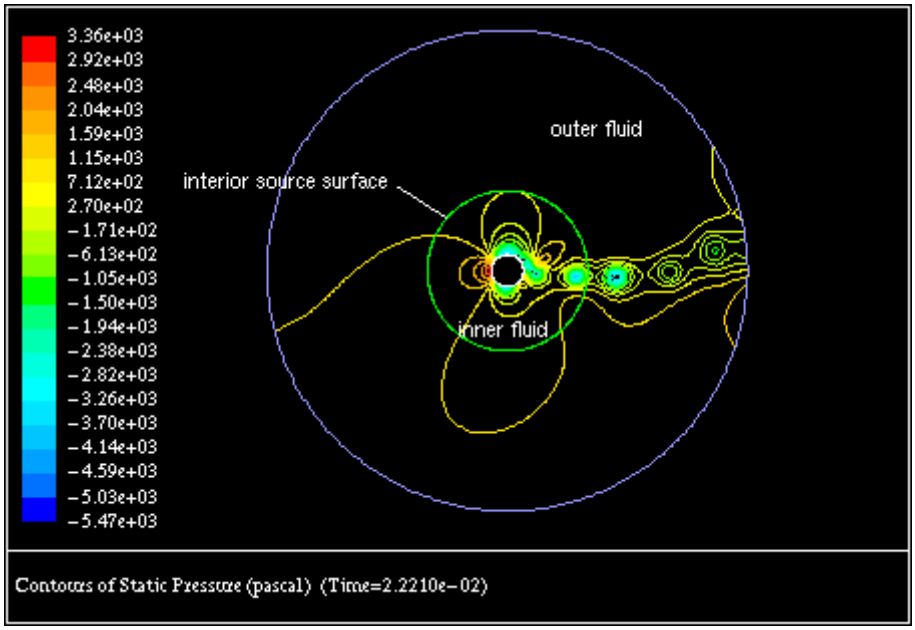


Figure 2.11: Source surfaces as implemented in ANSYS Fluent for FWH solutions (*ANSYS Fluent online user guide*, 2013)

The FWH equation in differential form is written as equation (2.12):

$$(\frac{\partial^2}{\partial t^2} - C_0^2 \frac{\partial^2}{\partial x_i \partial x_i})(H(f)\rho') = \frac{\partial^2}{\partial x_i \partial x_i}(T_{ij}H(f)) - \frac{\partial}{\partial x_i}(F_i\delta(f)) + \frac{\partial}{\partial x_i}(Q\delta(f)) \tag{2.12}$$

where

$$T_{ij} = \rho u_i u_j + P_{ij} - C_0^2 \rho' \delta_{ij} \tag{2.13}$$

$$F_i = (P_{ij} + \rho u_i(u_j - v_j))\frac{\partial f}{\partial x_i} \tag{2.14}$$

$$Q = (p_0 v_i + \rho(u_i v_i))\frac{\partial f}{\partial x_i} \tag{2.15}$$

T_{ij} in (2.13) is the previously defined Lighthill stress tensor which, in this equation, is known as the quadropole term. The dipole term is expressed as F_i (equation (2.14)) and Q (equation (2.15)) is the monopole term. These additional terms describe all possible sources of sound; unlike the Lighthill analogy which negates dipole and monopole sound production assuming negligibility. δ_{ij} is the Kronecker delta function which is 1 when $i = j$ and 0 otherwise. $H(f)$ is the Heaviside function which is 1 for $f > 0$ and 0 for $f < 0$

2.5.3 Computational Aeroacoustics

Computational Aeroacoustic (CAA) consists of the process of modelling those unsteady aerodynamic processes which generate aerodynamic noise. Since only a small fraction of the flow energy generates noise these schemes are either very computationally expensive or (when using an acoustic analogy) not entirely accurate. In order to simulate aeroacoustics, a number of methods are available which will be laid out here.

Direct Method

Two primary sets of direct methods exist: the Direct Numerical Simulation (DNS) (Orszag, 1970) and Large Eddy Simulation (LES) (*ANSYS Fluent online user guide Large Eddy Simulation (LES) Model*, 2013). The DNS method directly solves the Navier Stokes equations without any simplification (no turbulence model is used). With sufficiently high order differencing, and correct boundary treatments, the small scale acoustic energies can be calculated directly. With current computing power the feasibility of such simulations is very low. LES simulations on the other hand are *filtered* simulations which only take into account a windowed portion of turbulent eddies. LES simulations are performed using unsteady 3D computations with applied filtering; the solutions of which can provide acoustic data to the user.

Hybrid Method

A less computationally expensive approach to CAA is that of hybrid methods. One such method is a hybrid RANS-LES method in which a mesh is split into different regions depending on what type of data is required. (Nebenfuhr, 2012). Figure 2.12 is an example of where such a hybrid method would be used. A RANS model is used within the free stream flow and until the separation point of the airfoil, up until this point no specific turbulent length scales need be resolved as flow is relatively uniform and free of large vortical structures. After separation flow becomes highly vortical and a LES approach works better to resolve the data. The overall effect of the hybrid approach is a reduction in computational cost by means of minimising wasted computational time in regions that do not require a higher order model. Fluent contains the Detached Eddy Simulation (DES) method as one of the turbulence models available for 2D and 3D calculations. The DES model uses RANS calculations near walls, where LES is computationally expensive, and LES where turbulent length scales are large enough to be resolved quickly.

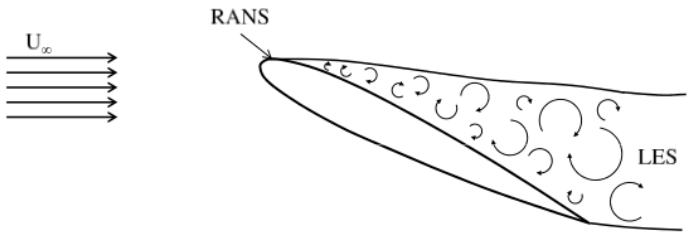


Figure 2.12: Schematic drawing of a RANS-LES simulation (Nebenfuhr, 2012)

Semi-Empirical Method

Semi-Empirical prediction methods make use of engineering data and standard airfoil configurations to predict how changes in an airfoil geometry will affect noise production. These methods make use of accurately measured noise data. One such example was the experimental work done by Brooks et al. (1989) to produce one of the first semi-empirical noise prediction codes. A more modern code, named NAFnoise (*NREL AirFoil Noise*, 2006), has been written to predict noise output by turbine blades from the five primary sources of airfoil noise. The code couples empirical data and analysis from XFoil to predict acoustics. The accuracy of the code is yet to be determined

2.5.4 Optimisations

A number of geometric optimisations have been performed that have the objective of minimising noise by means of changing the geometry of an airfoil.

Bizzarrini et al. (2011) performs an airfoil multi disciplinary optimisation for a power generating wind turbine which couples an airfoil flow solver with a noise prediction tool (NAFnoise). The result is a series of airfoils which exhibit a decrease in A-weighted noise of up to just over 1 dB and an increase in L/D of up to 14. Kuo and Sarigul-Klijn (2012) studies the effect of using micro tabs to minimise noise. Overall a decrease in noise of 2.4dB is achieved.

2.6 Summary

This review provides an overview of topics related to high lift validation, experimentation, design and optimisation as well as an introduction to aerodynamically generated noise, aerodynamically generated noise within high lift devices, the simulation thereof and the optimisation of airfoils for noise reduction.

High lift devices, particularly those of a single slotted design, have not yet reached their full potential for aerodynamic optimums. Various optimisation studies and designs have been undertaken to fulfil specific design criteria. There are also promising new concepts being developed.

Previous work in prediction of high lift has been erratic and not many trends have been found with regards to computations of high lift aerodynamics. Workshops have been held but accurate prediction across the board, particularly close to stall, is yet to be achieved.

Current work related to high lift device noise has been related to assessing primary noise sources. Work at reducing these noise sources has been successful but has not yet seen inclusion in current commercial aircraft. A lot of high lift noise reduction has been in applying preventative measures. Geometric optimisations have been limited to single element airfoils.

Previous work as highlighted in this review shows a wide range of tools related to aerodynamics and a separate set related to aeroacoustics. This present study will contribute a computational insight into improving high lift performance by means of a new concept and observing the changes to the noise generated by implementation of the new concept.

3 Methodology

THE topic of this dissertation is an aeroacoustic and aerodynamic optimisation of the multi-element high lift airfoil profile, TC12, provided by Airbus Germany GmbH. The basis of the work is a continuation of prior work performed at the University of the West of England, Bristol (UWE).

This chapter will provide:

- Research motivation. This explains why the research is relevant and in which direction this research will be taken. The limitations to the research are also added.
- Research problem. This is the problem statement which explains what the purpose of the study is. The specific aims and objectives of the dissertation are given which explain the measures of success of the research.
- Method. The procedure of the investigation is presented and highlights what needs to be done in order to fulfil the aims. This is a thorough explanation of the steps taken within the research to achieve the aims and objectives.
- Background. Following the method there are two background sections. The first explains the profile that will be investigated and the second summarises previous work pertaining to this particular profile.
- Optimisation procedure. This explains the general optimisation procedure, highlighting a novel concept that will be implemented throughout the course of the dissertation.
- Error. A mathematical equation is provided that defines how the percentage error is calculated for the duration of the dissertation.

3.1 Research Motivation

According to Rudolph (1996b) there are still a number of roadblocks for aerodynamic performance of single slotted flaps. Numerous design directions are suggested for further development of the systems. Increases in the performance of high lift systems have direct correlation with increases in range, payload and approach attitude (Meredith, 1993). It is also observed that there has been success in employing numerical optimisations to improve aerodynamic performance of high lift systems (Brezillon et al., 2008; Wild, 2008; Soulat et al., 2012; Chen et al., 2012). There is also great demand for less noisy aircraft- one area marked for noise reduction being high lift systems (Dobrzynski, 2008).

3.1.1 Limitations of Research

The computational prediction of high lift aerodynamics is seen as a rather complex field due to the intricate flow fields around the profiles. Numerous studies and workshops have been performed yet, currently, all known CFD methods provide no consistency across the board (Rumsey et al., 2003). To account for this there will be a focus on data trends rather than absolute data. Computational comparisons will be made to baselines as opposed to direct comparison with experimental data.

3.2 Research Problem

At present there is still scope to improve high lift systems' aerodynamics. Within this field numerical optimisations have been implemented successfully to improve aerodynamic performance. As well as aerodynamic improvements there is also scope for minimising noise produced by the systems in lieu of the European FP-7 framework. Methods to improve a high lift profile for aerodynamics and aeroacoustics will be investigated.

3.2.1 Aims and Objectives

The aim of this research will be to successfully optimise a high lift system by implementing a novel concept. This dissertation will have the following objectives:

- Minimise noise from the flap region. The measured SPL is to be minimised as much as possible in order to reduce the A-weighted SPL of the TC12 profile in high lift configuration and effectively reduce the total noise emitted by the entire aircraft in accordance with the ACARE targets for the European 2020 vision.
- Increase aerodynamic performance of the TC12 profile in high lift configuration, keeping in mind observations from Meredith (1993) relating to aircraft range due to high lift system improvements. This can be done using a figure of merit such as the lift-to-drag ratio.

Success will be measured by validation and verification of the new design by means of computational studies.

3.3 Method

This dissertation will focus on a series of studies pertaining to the Airbus TC12 research profile. In order to investigate the research problem a number of tools will be used. To improve aerodynamic performance of high lift systems two separate computational investigations will be performed in which Genetic Algorithms will be employed to numerically optimise the profile. Aerodynamic optimisation will be performed by means of finding the best numerical solutions for the implementation of a novel concept. The research will also have a focus on the noise generated by the TC12 profile - comparing noise from the baseline results to those of the optimised solution.

Due to limitations in the field of computational prediction of high lift systems the data of optimised solutions needs to be compared to validated aerodynamic data (chapter 4). Thus a large portion of the work presented will be to produce a set of aerodynamic data for the TC12 profile with which to compare any modifications in the work to. Throughout the course of this dissertation the baseline profile and boundary conditions will be kept consistent in order to draw conclusions from trends observed in results.

The first aerodynamic investigation will be a 'zero order' optimisation approach (chapter 5). This approach will attempt to improve aerodynamic performance of the TC12 profile in high lift configuration by using zero order modelling that does not account for the effects of a full system approach. Optimisation will be handled within MATLAB and will employ a Genetic Algorithm to achieve an optimised solution. Findings of this investigation will be compared to the validated data produced.

The second aerodynamic investigation will be a direct optimisation method (chapter 6). This optimisation approach will also have the outcome of improving aerodynamic performance of the TC12 profile in high lift configuration. The approach will be to perform a direct optimisation which uses an automatic mesh generation method and ANSYS Fluent as an aerodynamic solver in order to improve aerodynamic performance of the profile. Findings of this investigation will be compared to the validated data produced.

An aeroacoustic investigation will be performed (chapter 7) to understand the sound production of the TC12 profile. Comparisons will be made between sound production of the baseline profile and the best performing profile from the aerodynamic investigation. This chapter will be self contained as a validation and comparison. Findings will be presented based on a comparison of the change in noise with different profiles.

A design investigation is performed (chapter 8) which will investigate future options for realistic implementation of the concept suggested. This chapter will use an MDO approach to compare numerous suggested and arrive at a reasonable solution.

The dissertation is concluded and recommendations for future work are given.

3.4 TC12 Profile

The TC12 profile, which is the basis for the work of this dissertation, is a research airfoil profile designed by Airbus. The profile is a supercritical transonic airfoil designed for efficient transonic cruise. The profile also has a high lift configuration designed for take off and landing (in two separate configurations).

This high lift configuration consists of a *slat*, *main element* and *Fowler flap* (referred to from here on simply as 'the flap'). These airfoil elements are shown in figure 3.1 which shows a comparison of the clean and high lift configurations of the TC12 profile on a non-dimensionalised plot. The high lift configuration shown (with slat and flap extended) is set to the landing configuration.

For the duration of this dissertation *'clean configuration'* will refer to the TC12 profile in the clean configuration as shown by the black dotted lines of fig. 3.1, whilst *'high lift configuration'* will refer to the TC12 profile in high lift landing configuration as shown in fig. 3.1 as the Slat, Main Element and Flap. Also shown is the spoiler, spoiler cove and slat cove.

The thin trailing edge on the main element is the spoiler used as an airbrake during landing.

Figures 3.2 and 3.3 along with table 3.1 below detail the slat and flap rotations and translations, as required for the *landing configuration*, as well as their non dimensional chord lengths.

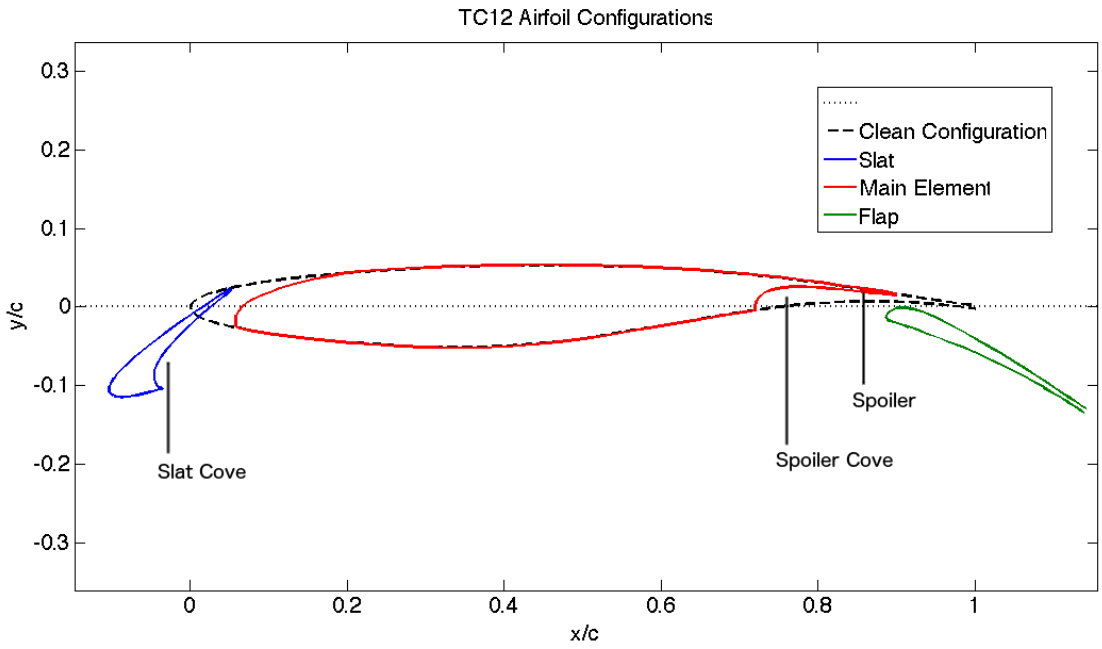


Figure 3.1: Schematic of TC12 profile in high lift configuration

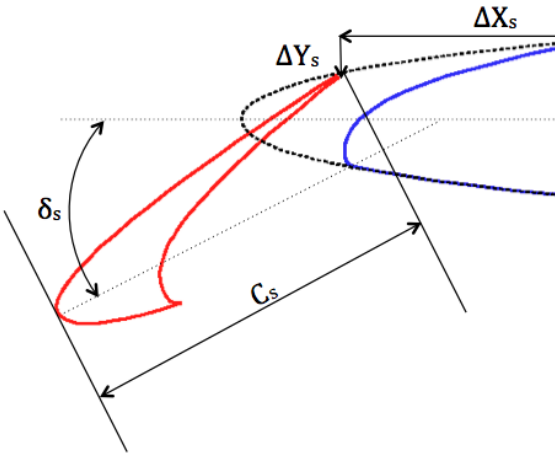


Figure 3.2: Slat motion of TC12 profile in high lift configuration

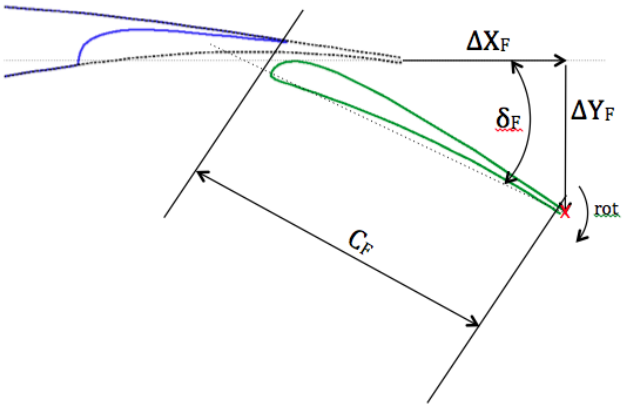


Figure 3.3: Fowler flap motion of TC12 profile in high lift configuration

Parameter	**Slat**		**Flap**	
Chord length	c_s/c	0.1982	c_F/c	0.2800
Rotation angle	δ_s	28.00°	δ_F	25.36°
Pivot location	$X_{rot,s}/c$	0.198117	$X_{rot,F}/c$	1
	$Y_{rot,s}/c$	0.043233	$Y_{rot,F}/c$	0
X-Translation	$\Delta X_s/c$	-0.146415	$\Delta X_F/c$	0.139933
Z-Translation	$\Delta Y_s/c$	-0.020459	$\Delta Y_F/c$	-0.131644

Table 3.1: Summary of TC12 slat and flap translations and rotations

3.5 Prior Work on the TC12 Profile

Wolkensinger

Wolkensinger (2008) performed experimental work on the TC12 profile in high lift configuration. The idea behind his project was to create a wind tunnel model that could be easily modified to experiment on future modifications to the profile at UWE. The model was produced by means of layering laser cut wooden panels side by side along the span. Pressure taps were added at key locations along the chord within all three elements. The model was experimented on in the UWE low speed wind tunnel; pressure data along the chord was measured as well as flow angularity by means of hot-wire anemometry.

Pätzold

Patzold (2008) focussed on numerical optimisation of the TC12 profile in high lift configuration by application of various flow control devices (Gurney flaps and vortex generators). He conclusively increased overall lift produced by the profile, by 7.7% and increased the lift to drag ratio at the higher end of the lift range by an unspecified amount.

Vitale

Vitale (2010) conducted a numerical optimisation of the TC12 profile in high lift configuration by means of implementing a novel concept- a Krueger flap within the flap of the TC12 profile (figure 3.4). The concept's position with respect to the flap was optimised, to provide increases in aerodynamic performance. Lift was increased by 3.5%.

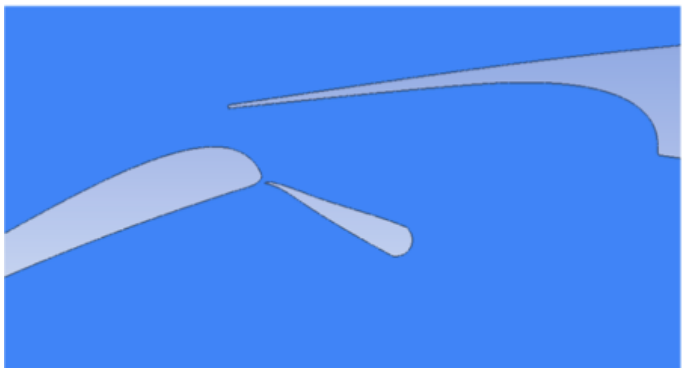


Figure 3.4: Optimised concept as implemented by Vitale (2010)

3.6 Optimisation Procedure

The approach to optimise the TC12 profile for landing configuration is to implement a novel concept at the leading edge of the flap. Figure 3.5 shows the region in which the optimisation will occur. Most diagrams in this dissertation related to the optimisation will be zoomed in to show modifications in this region. The novel concept to be implemented is a 'betz flap' (*Modification De La Forme Dun Profil*, 1980) (see figure 3.6). The concept, thus referred to as the *'flap extension'* will act similar to an upper surface krueger flap (F. and Fullmer, 1947). Increases in lift should be achieved because of an increase in the camber and area of the TC12 flap: increasing local lift in this vicinity. An increase in lift at the flap should increase circulation around the entire high lift system. This should not only locally increase flap lift but also increase lift upstream at the main element and the slat.

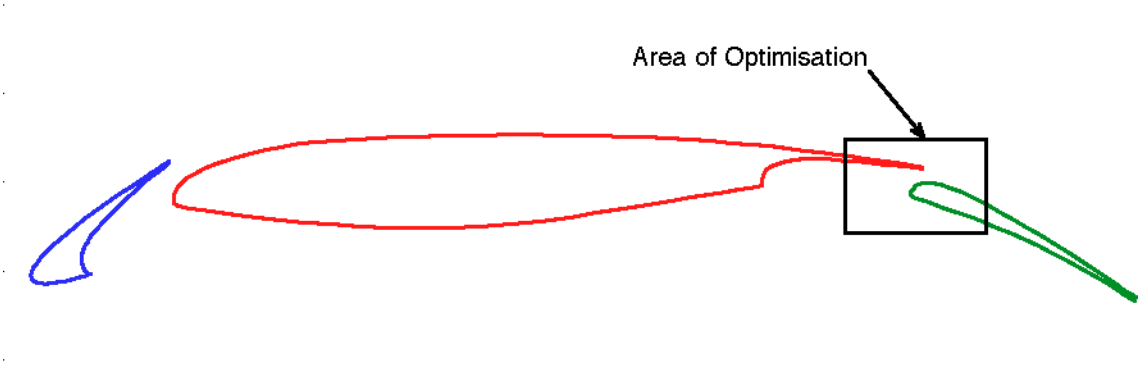


Figure 3.5: Optimisation region of TC12 airfoil in high lift configuration

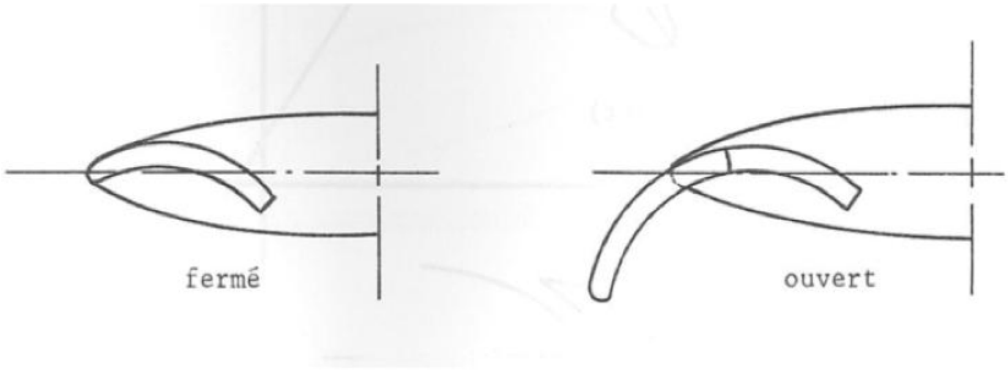


Figure 3.6: Betz flap, *Modification De La Forme Dun Profil* (1980)

The flap extension should also have an effect on the recirculation region within the spoiler cove. This should bring stability to the shear layer of fluid flow that borders the recirculation region. Stability of the unsteady pressure fluctuations should minimise noise produced in this vicinity.

3.7 Definition of Error and Percentage Increase

For the duration of this dissertation error calculations will be defined by equation (3.1).

$$\%_{\text{error}} = \frac{|\text{exact value} - \text{estimated value}|}{\text{exact value}} * 100\% \tag{3.1}$$

where exact value is the value of the desired data point based on experiments and estimated value is the value of the desired data point based on computational simulations.

When comparing optimised solutions to each other equation (3.2) will be used:

$$\%_{\text{increase}} = \frac{|\text{original value} - \text{new value}|}{\text{original value}} * 100\% \tag{3.2}$$

where original value is the value of the desired data point based on baseline solutions and new value is the value of the desired data point based on optimised simulations.

4 Validation

THIS chapter describes the validation of various aerodynamic tools used throughout the course of this dissertation. Experimental data for the TC12 airfoil profile is presented for the high lift and clean airfoil case. The validation is performed to have baseline data with which to compare future results to because of the limitations in the field of high lift prediction.

MSES, a full potential flow solver code, is used to validate the experimental data. Following this an Engineering Sciences Data Unit (ESDU) method is used to confirm the maximum lift and lift at zero angle of attack of the TC12 profile in high lift configuration when compared to the clean airfoil. Finally a Reynolds Averaged Navier Stokes (RANS) computation is performed, using ANSYS Fluent, in 2D, to confirm experimental data for the profile in high lift and clean configuration.

4.1 Experimental Data

The experimental data presented was obtained at the Kryo-Kanal Köln (Cryogenic Wind Tunnel, Cologne) (KKK) wind tunnel under the research programme High Lift Concepts 2 (HAK). Experimentation was done to determine aerodynamic characteristics of the TC12 profile during takeoff and landing, these characteristics were used to determine the most effective slat setting position for the TC12 profile.

4.1.1 Clean Configuration

Clean configuration results for the TC12 profile were obtained by Hansen and Szabo (1998), their study was an in depth experimental investigation of the stall characteristics of the TC12 profile at a range of Reynolds numbers (defined by (4.1)). According to the research, the profile exhibits a leading edge stall at lower Reynolds numbers (characterised by a sudden loss of lift at a critical angle of attack) which gradually changes to a combined leading- and trailing-edge stall at higher Reynolds numbers (this type of stall being seen as a change in the gradient of the lift curve slope at a critical angle of attack followed by a gradual loss of lift at high angles of attack). Only lift was measured during experiments.

$$Re = \frac{\rho U L}{\mu} \tag{4.1}$$

where ρ is density in kg/m^3, U is freestream velocity in m/s, L is airfoil chord length in m and μ is kinematic viscosity in m^2/s.
Figure 4.1 shows the wind tunnel data for the clean configuration TC12 profile. This data was obtained at the given Reynolds numbers and with a Mach number of 0.2. Conditions were strictly controlled to maintain constant pressure, temperature and velocity. This was made possible by running experiments within a cryogenic wind tunnel.

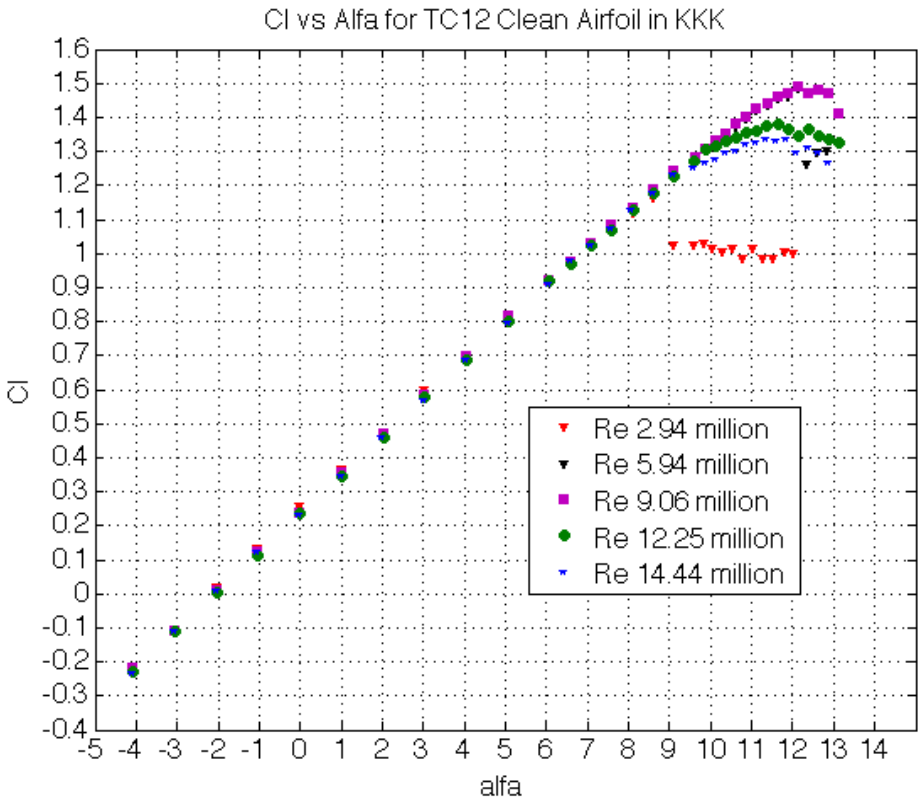


Figure 4.1: Coefficient of lift against angle of attack for TC12 profile in clean configuration, KKK experiments

4.1.2 High Lift Configuration

Figure 4.2 shows the wind tunnel data for the high lift configuration. The experiments were performed at various Reynolds numbers as shown and at a Mach number of 0.2.

The high lift configuration improves the lift generated by the profile at the same Reynolds numbers and angles of attack when compared to the clean configuration. Lift is increased due to the deployment of the flap and slat. The slat delays stall to higher angles of attack due to the *fresh boundary layer* effect (Smith, 1975); whilst the flap increases circulation around the airfoil body thus increasing lift. The stall characteristics with increasing Reynolds numbers follow the same trend as that of the clean configuration.

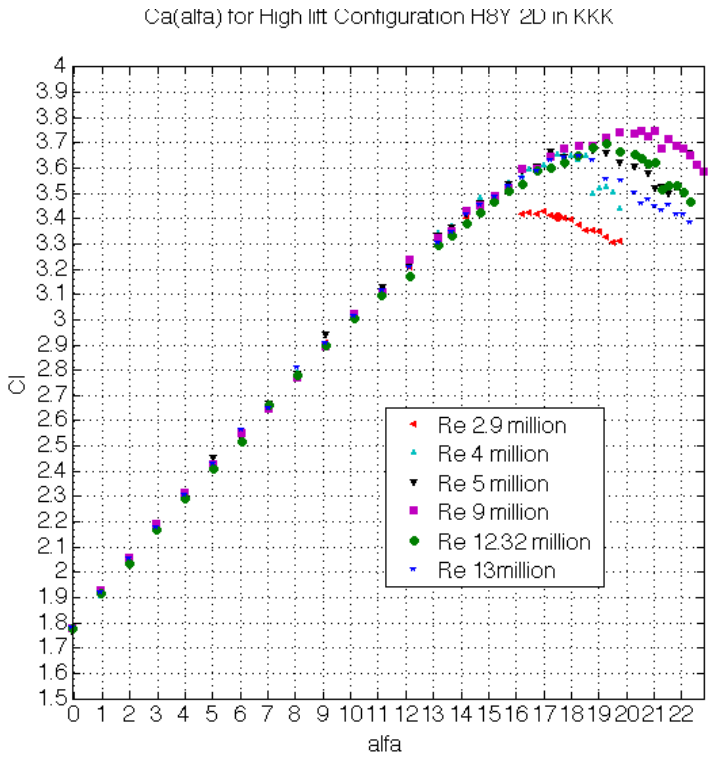


Figure 4.2: Coefficient of lift against angle of attack for TC12 profile in high lift configuration, KKK experiments

4.2 MSES Validation

Using MSES, a series of results was obtained for both the clean configuration as well as the high lift configuration of the TC12 profile.

Clean Configuration

MSES was used to obtain lift against angle of attack for the clean configuration TC12 profile at a range of Reynolds numbers. The data obtained is compared to experimental data.

Figure 4.3 shows the lift coefficient against angle of attack for the TC12 profile in clean configuration at a Reynolds number of 2.94 million. Additional results for higher Reynolds number as well as an inviscid solution are shown in the appendix.

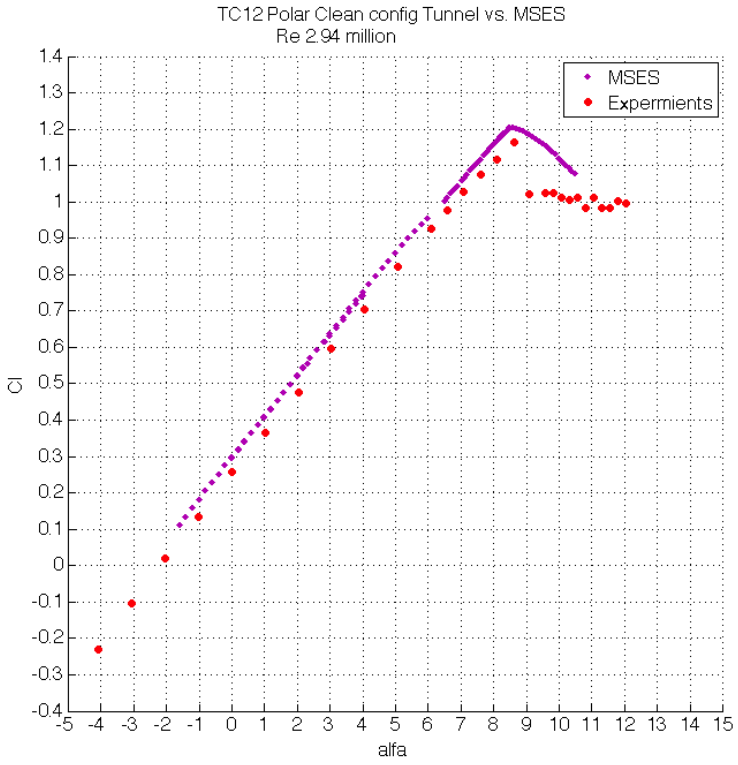


Figure 4.3: Cl vs. alfa for TC12 profile in clean configuration at Re 2.94 Million, MSES

Table 4.1 summarises the numerical error of the MSES computations for the TC12 profile, in clean configuration, at a series of Reynolds numbers, when compared to the experimental data. Agreement is best at Re 2.94 million due to the lowest errors and best prediction.

Reynolds Number	**% error** α_{stall}	**% error** C_{Lmax}	**% error** $\partial C_l/\partial\alpha$	**% error** $C_{L\alpha=0}$
2.94e6	0.13 %	3.44 %	18.38 %	15.88 %
5.94e6	37.45 %	-23.57 %	14.22 %	27.95 %
9.06e6	30.9 %	-16.44%	73.75 %	26.7 %
12.25e6	0.34 %	12.88 %	10.49 %	25.96 %
14.44e6	7.41 %	10.92 %	11.32 %	28.22 %

Table 4.1: Discrepancies Between Cl of TC12 Profile in Clean Configuration for MSES and Wind Tunnel Experiments

Figures 4.4 and 4.5 show a comparison of the pressure distributions as computed by MSES (for the TC12 profile), at a Reynolds number of 2.94 million, with the experimental data. In order to obtain a reasonably similar pressure distribution the C_L was fixed and the angle of attack was solved for. By looking at figure 4.5 it is noted that the separation bubble, characterised by the constant spanwise pressure, is predicted at the correct location but not at the correct pressure. The trend observed is accurate.

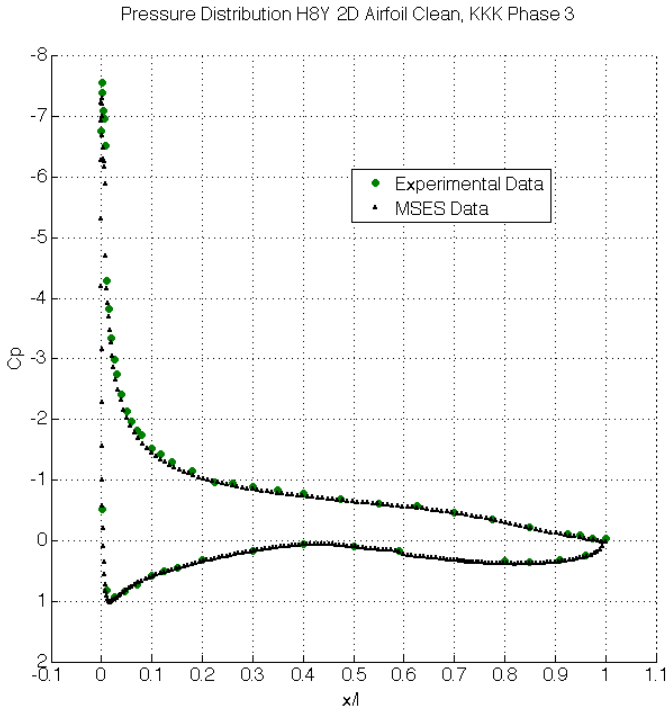


Figure 4.4: Pressure distribution of TC12 profile in clean configuration at Re 2.94 million, angle of attack 8.11 degrees in MSES

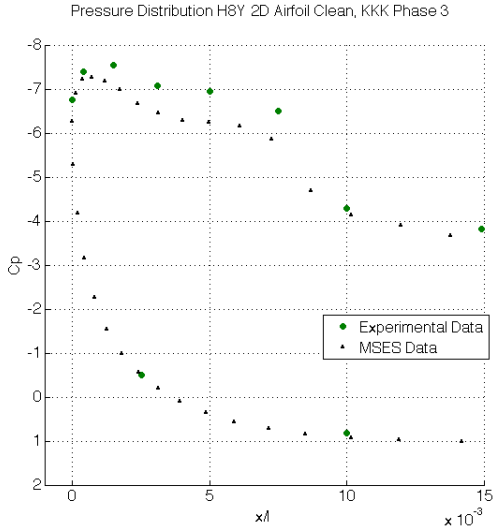


Figure 4.5: Pressure distribution (peak) of TC12 profile in clean configuration at Re 2.94 million, angle of attack 8.11 degrees

Figures 4.6 and 4.7 show a comparison of the pressure distribution as computed by MSES (for the TC12 profile), at a Reynolds number of 9.06 million, with the experimental data. The pressure distributions have an equal c_l value. MSES predicts a separation bubble which, according to experimental data at this angle of attack, does not exist.

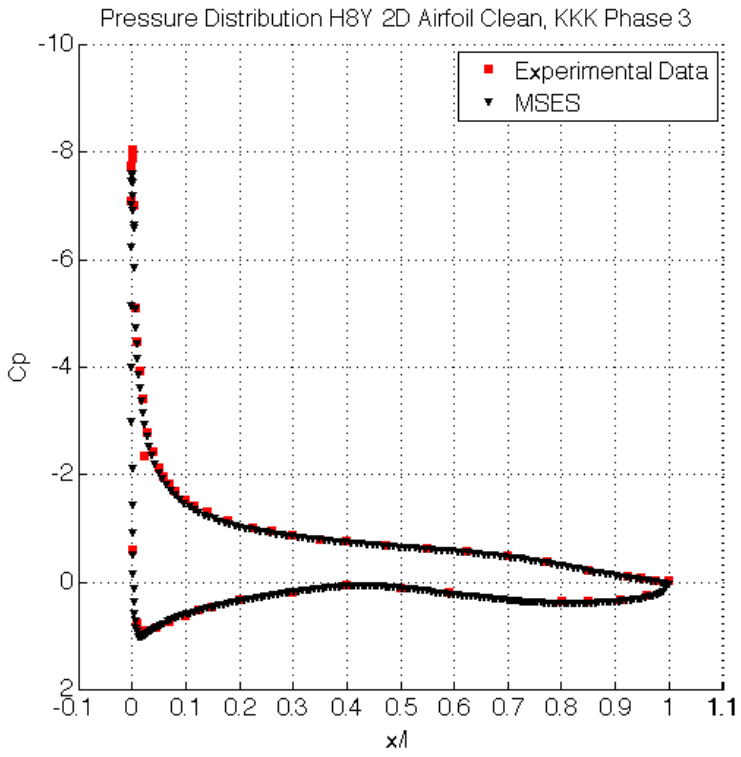


Figure 4.6: Pressure distribution of TC12 profile in clean configuration at Re 9.06 million, angle of attack 8.1 Degrees

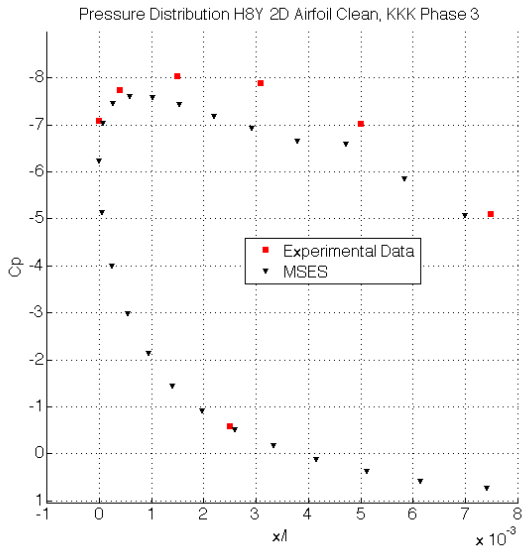


Figure 4.7: Pressure distribution (peak) of TC12 profile in clean configuration at Re 9.06 million, angle of attack 8.1 Degrees

Upon inspection, the data at varying Reynolds numbers is very inconsistent- stall is not predicted accurately nor consistently. MSES predicts a sharp leading edge stall for all Reynolds numbers as opposed to the experimental observation of a combined leading- and trailing-edge stall. The cases evaluated were particularly difficult cases to converge and thus a simplifying assumption for the momentum-entropy conservation had to be made. The standard momentum-conservation for a Euler solver was used.

MSES is sensitive to upstream changes in streamwise pressure gradient. When entropy conservation is used errors near stall are minimised but convergence of the overall solution becomes much harder to achieve- the balance of correct gridding, parameters and conditions to achieve a converged solution was not possible.

MSES provided the most accurate results for the TC12 profile in clean configuration at a Reynolds number of 2.94 million. Reynolds number effects were not well accounted for, and hence data from MSES did not correlate well with experimental data from Hansen and Szabo (1998) over the full range of experimental Reynold numbers. The limitations of the full potential/euler coupled solver are exposed here.

High Lift Configuration

MSES was used to obtain aerodynamic data for the high lift configuration TC12 profile at a range of Reynolds numbers. The data obtained is compared to experimental data for the configuration.

Multi-element airfoils as used for high lift have two large separation regions. One in the slat cove and one beneath the spoiler. These regions are accounted for within MSES by means of approximating a separation region in these 'deadzones'. Even with reasonable separation approximations MSES does not obtain converged solutions very easily. The solver is very insensitive to grid sizes (*MSES Multi-element Airfoil Design/Analysis Software*, 2013) but finding a set of grid parameters that leads to convergence is time consuming.

Table 4.2 shows the grid parameters used within MSES to obtain converged results. The parameters are related to the size of the grid in relation to the airfoil. Images of the grids and panelling on individual elements are included in appendix B.

Grid Parameter	**Value**
Airfoil side points	121
Left inlet points	32
Right outlet points	32
Number of streamlines on top of domain	21
Number of streamlines on bottom of domain	17
Maximum streamlines between two airfoils	13
X-spacing parameter	0.85
Aspect ratio of each cell at stagnation point	1.8
Grid boundaries	-2.18 3.42 -2.50 3.10

Table 4.2: Grid Parameters for TC12 High Lift Configuration Simulations in MSES

Figure 4.8 shows a comparison of the lift coefficient against angle of attack for the high lift configuration TC12 profile against the experimental data at Re 2.95 million. As expected the inviscid results largely over-predict lift and negate stall because of exclusion of friction in the calculations. This simulation is performed as an initial proof of concept to confirm that the software was installed correctly. The data provided is meaningless to this study which will need to account for viscous effects to compare performance.

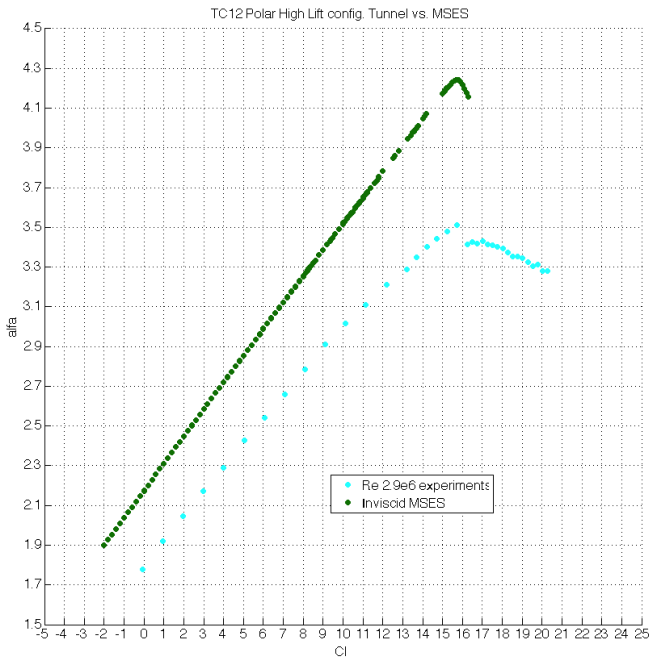


Figure 4.8: Comparison of inviscid MSES results with wind tunnel Re 2.9 million

Figure 4.9 shows a comparison of the pressure distributions as computed by MSES (for the high lift TC12 profile), at a Reynolds number of 2.95 million, with the experimental data. In order to obtain a reasonably similar pressure distribution the C_L was fixed and the angle of attack was solved for - from here on further this is referred to as the *'matched Cl'* value. The pressure distribution is presented differently to that of a single element airfoil; where each enclosed region represents a separate element of the high lift system. From left to right; between x/c -0.1 to 0.05 the pressure coefficient against span along the slat is shown; from 0.05 to 0.9 the main element pressure distribution is shown; from x/c 0.9 to 1.1 the flap pressure distribution is shown.

The pressure distribution shows good agreement by means of predicting major flow features on the high lift airfoil. At the main element the pressure peak is predicted at an accurate location and trend, a separation bubble on the leading edge at around x/c 0.2 is predicted. Likewise the data at the flap as well as a down stream separation at x/c 1.05 is predicted accurately. The pressure on the lower surface of the slat (within the slat cove) is predicted accurately but the upper surface pressure distribution is not predicted accurately.

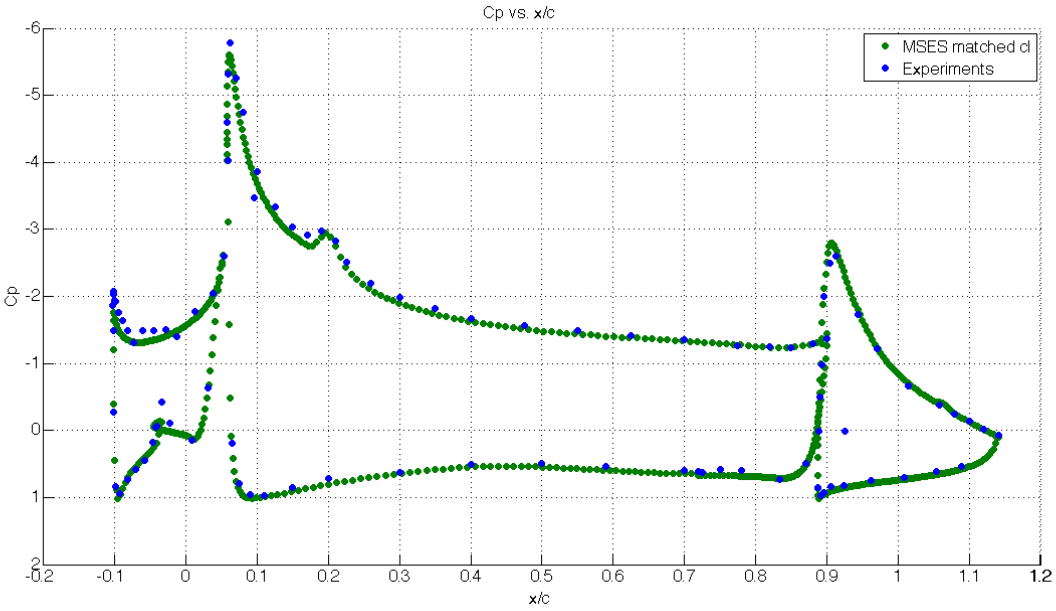


Figure 4.9: Pressure distribution for TC12 high lift at matched Cl 2.879

Figure 4.10 and 4.11 show lift and drag data obtained for the TC12 profile in high lift configuration by means of using the MSES code. Lift is overpredicted, yet still follows the same trend as the experiments to exhibit a slight trailing edge stall (as seen by the change in the lift curve slope in figure 4.10 at around 9 degrees). Stall is not predicted. No comments can be made over the validity of drag data as there is no experimental data available for comparison. This data is used as the *baseline* data when used in comparing any future modifications to the TC12 profile in high lift configuration.

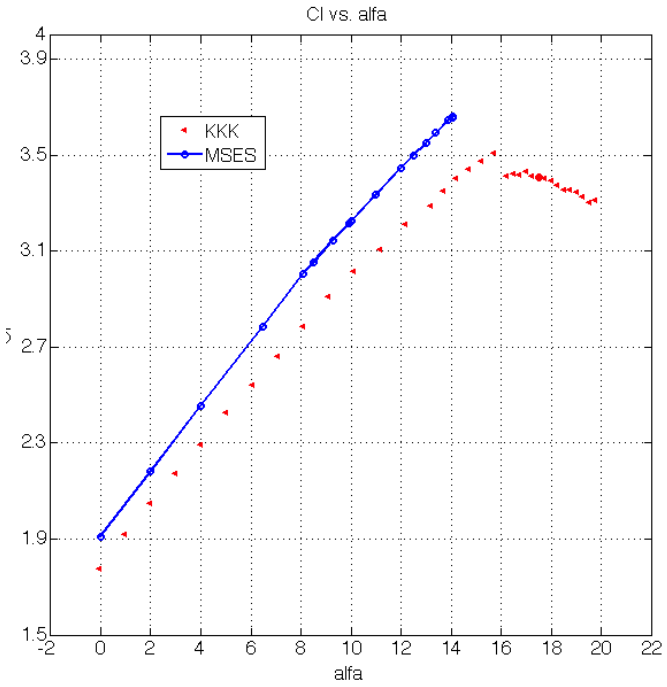


Figure 4.10: Cl vs. alfa for TC12 profile in high lift configuration at Re 2.95 Million, MSES

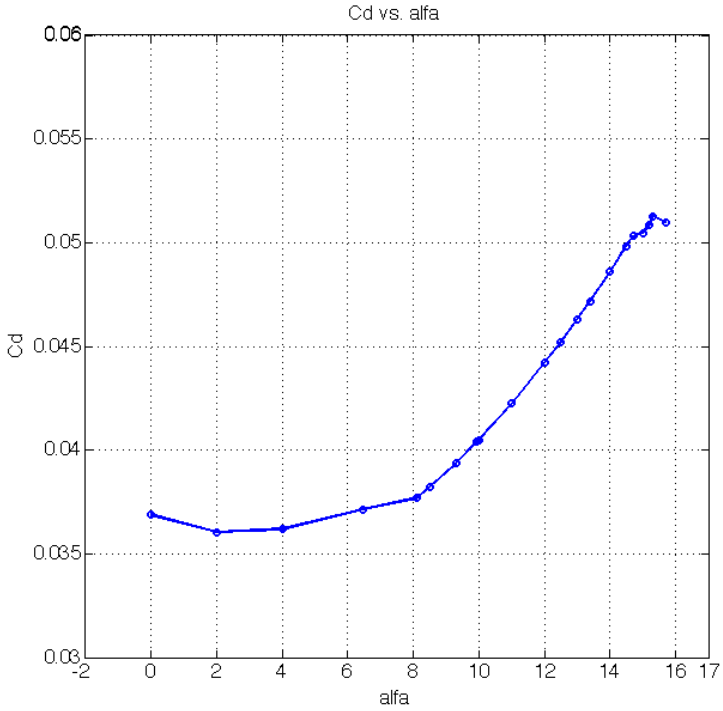


Figure 4.11: Cd vs. alfa for TC12 profile in high lift configuration in MSES

4.2.1 Conclusion of MSES Validation

MSES was successful in predicting the lift of the TC12 profile in clean configuration at the Reynolds number 2.95 million. In predicting the lift of the TC12 profile in high lift configuration, the tool was unable to predict any stall and rather failed to converge at very high angles of attack. The computations can be used to look at trends that will arise due to modifications to the TC12 profile provided that future computations employ the same set of conditions used during the validation.

4.3 ESDU Validation

As an additional validation of the high lift configuration, the ESDU empirical methods (*ESDU 85033: Increments in Aerofoil Maximum Lift Coefficient due to Deployment of Various High Lift Devices*, 1992) were employed to provide a good validation of the existing data. The methods rely on accurate data for the airfoil clean configuration as well as information about the geometry of the slat and flap.

By using ESDU 85033, two values can be obtained for the high lift system. The maximum lift coefficient (C_{L_m}) unbound to an angle of attack and the lift coefficient at zero incidence (C_{L_0}). In order to obtain the solution, the effect on the lift curve slope of the slat and flap at both zero incidence and maximum lift coefficient are found. These values are then used to calculate the estimated change in parameters.

The method assumes that all flap and slat gaps and overlaps are well designed for maximum efficiency. Another assumption is that the trailing edge flap has a lift curve slope of 2π because it should be sufficiently thin.

4.3.1 Calculations

To ease the calculations the flap was non-dimensionalised to a clean airfoil chord length of 1 and moved into a CAD package to measure all the necessary information. All formulae used in this section are from the equations in the ESDU 85033 method and follow the steps of Example 8.3 (*ESDU 85033: Increments in Aerofoil Maximum Lift Coefficient due to Deployment of Various High Lift Devices*, 1992).

Tables 4.3, 4.4 and 4.5 as well as figures 4.12, 4.13 and 4.14 detail the required geometric information required to perform the ESDU 85033 calculations. Figures A.1 to A.5 in appendix A are tables used to find certain values as required in the calculations.

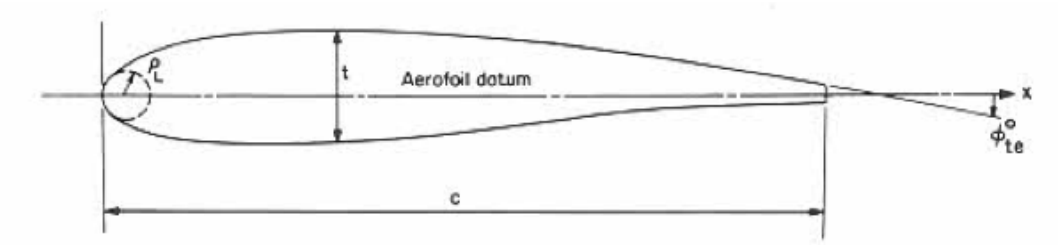


Figure 4.12: ESDU definitions associated with basic airfoil geometry

Main Element		
Parameter	**Symbol**	**Value**
Reynolds Number (according to chord)	Re	2.9e6
Chord	c	1
Leading Edge Radius	ρ_L	0.01249471
Trailing Edge Angle	ϕ_{te}°	8.49787°
Airfoil Thickness	t	0.104775
Chordwise Position of Trailing Edge of Shroud	x_{ts}	0.84350244
Slope of Lift Coefficient Curve	$(a_1)_0$	0.11411/degree
Maximum Lift Coefficient of Basic Airfoil	C_{LmB}	1.164049 @ 8.11 ° (from experiments)
Lift Coefficient at Zero Incidence of Basic Airfoil	C_{L0B}	0.257544 (from experiments))

Table 4.3: Data for ESDU calculations for the TC12 main element airfoil

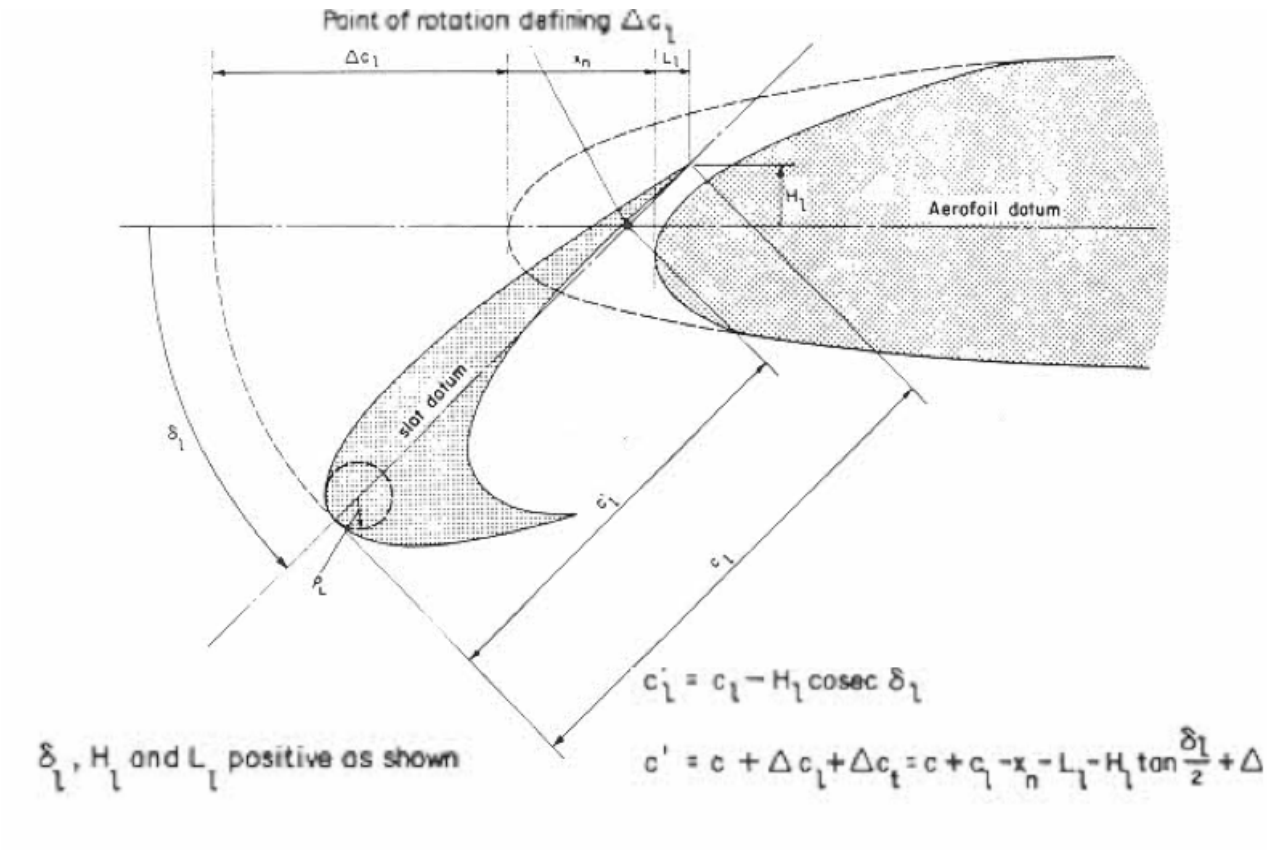


Figure 4.13: ESDU definitions associated with slats

Slat		
Parameter	**Symbol**	**Value**
Slat Deflection Angle	δ_L	40.67986°
Extended Chord of Leading Edge Device	c_l'	0.19195851
Slat Chord	c_l	0.20288924
Incremement in Chord due to Leading Edge Device	Δc_l	0.14720798
Chordwise Position of Fixed Airfoil Nose	x_n	0.05711756
Overlap Between Trailing Edge of Deflected Edge Device and Fixed Airfoil nose	L_l	-0.00407756
Height of Trailing Edge of Leading Edge Device Above Basic Airfoil Chord Line	H_l	0.007125

Table 4.4: Data for ESDU calculations for TC12 profile slat

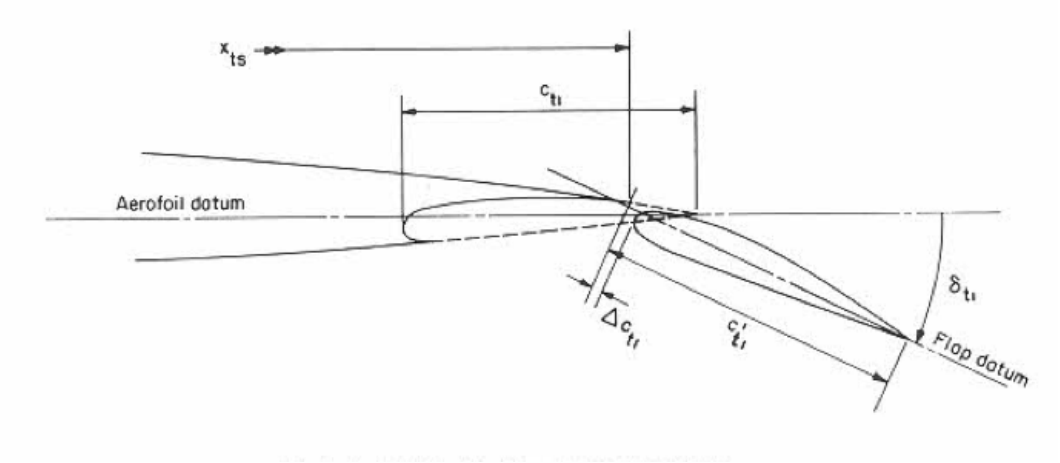


Figure 4.14: ESDU definitions associated with slotted flaps

Flap		
Parameter	**Symbol**	**Value**
Chord of Element i	c_{ti}	0.27997022
Extended Chord of Element i	Δc_{ti}	0 (negligible)
Increment in Chord of Element i	δ_{ti}	25.29171795 °

Table 4.5: Data for ESDU calculations for TC12 profile flap

Calculation steps:

1. Calculate c'_l

As measured: $c'_l = 0.19195851$

2. Calculate Δc_l

As measured: $\Delta c_l = 0.14720798$

3. Calculate c'_{ti}

$$c'_{ti} = c_{ti} + \Delta c_{ti} \tag{4.2}$$

c'_{ti}=c_{ti} (single slotted flap)
$c'_{ti} = 0.27997022$

4. Calculate c'_l and $\frac{c'}{c}$

$$c'_l = \Delta c_l + x_{ts} + \sum_{i=1}^{n} c'_{ti} \tag{4.3}$$

$c' = 0.14720798 + 0.90062 + 0.27997022$
$c' = 1.3277982$

$c'/c = 1.3277982/1$

$c'/c = 1.3277982$

5. Element equivalent chords and chord ratios

slat

$c'_l/c' = 0.19195851/1.3277982$

$c'_l/c' = 0.1445690392$

flap

$c_{et1} = c'_{ti} = 0.27997022$

$c'_{ti}/c' = 0.27997022/1.3277982$

$c'_{ti}/c' = 0.21085299$

6. Calculate θ_l

$$\theta_l = cos^{-1}(1 - 2\frac{c'_l}{c'}) \tag{4.4}$$

$\theta_l = cos^{-1}(1 - 2 * (0.1445690392/1))$
$\theta_l = 0.780073545$ rad

7. Calculate $\Delta C'_{L0l}$

$$a_l = -2(\theta_l - sin\theta_l) \tag{4.5}$$

a_l = -2*(0.780073545 - sin(0.780073545))
a_l = -0.153483687

(From figure A.2 for $\delta_L = 40.67986$):
$K_l = 0.95$

$\delta_l = 40.67986°$
= 0.709997 rad

$$\Delta C'_{L0l} = a_l \frac{\delta_l}{K_l} \tag{4.6}$$

$\Delta C'_{L0l}$ = -0.153483687*(0.709997/0.95)
$\Delta C'_{L0l}$ = -0.114708376

8. Calculate ΔC_{L0t}

$c_{et1}/c' = \ c'_{t1}/c' = \ 0.27997022/1.3277982$

$c_{et1}/c' = 0.2108529896$

(From figure A.3 for $\delta_{t1} = 25.29171795°$ and $\frac{c_{et1}}{c'} = 0.2108529896$):

$C'_{L1} = 1.03$
$J_{t1} = 1.17$

$$\Delta C'_{L0t} = J_{t1} \Delta C'_{L1} \frac{(a1)_0}{2\pi} \tag{4.7}$$

$\Delta C'_{L0t}$ = 1.17* 1.03* 6.3099/(2π)
ΔC_{L0t} = 1.21022382

9. Calculate $\Delta C'_{Lml}$

$$a_{ml} = 2 sin\theta_l \tag{4.8}$$

a_{ml} = 2 sin (0.789973545)
a_{ml} = 1.406663403

(From figure A.1 for $\rho_L/t = 0.119253$ (slat and flap)):
$K_g = 1.54$

(From figure A.2 for $\delta = 40.67986$ ° (slat and flap)):
$K_l = 0.95$

$$\Delta C'_{Lm} = K_g K_l a_{ml} \delta_l \tag{4.9}$$

$\Delta C'_{Lml}$ = 1.54 *0.95* 1.406663403* 0.709997
$\Delta C'_{Lml}$ = 1.461137303

10. Calculate ΔC_{Lmt}

(From figure A.4 $\delta_t = 25.29171795$ °):
$K_{t1} = 0.35$

(From figure A.5 for $\rho_L/t = 0.119253$):
$K_{T1} = 1.875$

$$\Delta C'_{Lmt} = K_{T1} K_{t1} \Delta C'_{L0t1} \tag{4.10}$$

$\Delta C'_{Lmt} = 1.875 * 0.35 * 1.21022382$
$\Delta C'_{Lmt} = 0.79420938$

11. Calculate C_{L_m}

$$F_R = 0.153 log(Re) \tag{4.11}$$

$F_R = 0.153 log(2.9e6)$
$F_R = 0.98875$

$$C_{lm} = C_{lmB} + F_R(\frac{c'}{c})(\Delta C'_{Lml} + \Delta C'_{Lmt}) \tag{4.12}$$

$C_{lm} = 1.164049 + 0.98875 * 1.3277982(1.461137303 + 0.79420938)$
$C_{lm} = 4.125005$

12. Calculate C_{L_0}

$$C_{L0} = C_{L0B} = (\frac{c'}{c})(\Delta C_{L0l} + \Delta C'_{L0t} \tag{4.13}$$

$C_{L0} = 0.257544 + 1.3277982(-0.114708376 + 1.21022382)$
$C_{L0} = 1.7121674$

4.3.2 Conclusion of ESDU Validation

Error on C_{L_m}

$\%_{error_{Clm}} = |4.125005 - 3.509845018|/3.509845018$

$\%_{error_{Clm}} = 17.53\%$

Error on C_{L_0}

$\%error_{Clm} = |1.776178956 - 1.7121674|/1.776178956$

$\%error_{Clm} = 3.6\%$

It is noted that the error percentage of the prediction of the maximum lift falls out of the range of the empirical method (which suggests a maximum error of around 10 %). This error can be decreased by performing the analysis at a higher Reynolds number as the analysis is not so sensitive to Reynolds number changes but, as seen in the experiments, the configuration itself does lend itself to sensitivity to changes in Reynolds number. The low error at zero angle of attack is reasonable.

4.3.3 Modification of Methods to Analyse Novel Modifications

As part of the optimisation process that follows in subsequent chapters; an additional method of analysis would be favourable. One option would be to modify or extend the ESDU methods employed for the TC12 profile in high lift configuration to be used to predict small geometric changes akin to those researched by Vitale (2010). Using the Vitale concept as a modification a number of options are explored in table 4.6 below.

Option	Pro	Con
Option 1		
Model the concept flap and the main flap as a single longer flap.	The entire flap effectively becomes longer providing a larger flap chord for the calculations.	The method will not account for any extension into the flap cove as this is subtracted from the flap chord extension. To get around this, the new combined flap could be repositioned completely exposed which would increase the total airfoil effective length. The angle of attack would also be adversely affected throwing off results.
Option 2		
Find the lift curve slope of the novel concept flap and the main flap together and modify equation (4.7) to get a better result. The effect of the new flap can be seen in isolation and superimposed into the formulae.	The equation is a function of an empirical value J_{t1}. In order to accurately find the effect of the concept a new empirical data bank would need to be found or created.	
Option 3		
Model the concept flap and main flap as a double slotted flap.	This option would be able to use unmodified methods and accurate representations of the flap geometry.	The angle of attack of the concept flap is negative, which will cause worse results. The flap also sits inside the cove causing the same overlap issues as in *Option 1*.
Option 4		
Model the concept flap as a slat.	Slat modelling will properly account for any boundary layer effects on the main airfoil. The deflection angle of the slat will also be properly accounted for.	The method non-dimensionalises all values thus analysis as a slat will place a small slat at the leading edge of the main airfoil.

Table 4.6: List of available options for ESDU method modification

Conclusion of ESDU Method Modifications

The ESDU methods are designed with very specific set of assumptions backed up by numerous empirical studies. The methods are designed to get a good first approximation of a high lift configuration. One such problem here is that a flap is assumed to have a certain lift curve slope when, more recently, lots of research has been done to improve the aerodynamic performance of flaps. Modifications to these assumptions will cause solutions to fall out of the scope of the methods Thus these methods cannot be used to quantify aerodynamic performance increases from the small uncharacteristic modifications to high lift geometries.

4.4 ANSYS Fluent Validation

A CFD validation of the TC12 profile in clean and high lift configuration was performed using ANSYS Fluent. Fluent is a commercial Computational Fluid Dynamics (CFD) program used to solve fluid problems such as external flow over airfoils by means of solving the RANS equations. Meshes were created and exported to the CFD solver where they were solved with a number of different turbulence models in order to obtain several sets of results. Fluent was used in 2D mode with steady calculations applied along with the application of various turbulence models in order to find a series of aerodynamic results for the TC12 profile. A 2D method was selected as it is computationally less expensive than a 3D method. A 2D method also provides more flexibility in preliminary design when a designer does not yet know the constraints of the 3D configuration. The data found in this section will later be compared to that of optimised geometries to see whether there are changes in aerodynamic performance of new configurations.

In order to perform the simulations, a number of steps are followed for both the clean and high lift configurations of the TC12 profile. Firstly, a mesh is generated- to achieve an acceptable mesh a number of hand calculations are performed to obtain estimates for the required geometry sizes and mesh settings. Next the meshes are created within the meshing tools, boundary conditions are applied. These meshes are exported to Fluent and then solved for - a number of different turbulence models are tested in order to achieve acceptable results. Grid convergence is analysed to confirm whether the solution obtained by Fluent is independent of the mesh used. The Fluent calculations are compared to experimental results and then used as the baseline results for comparing future optimisations to.

Lift and Drag conventions

The meshes generated are non-moving, thus, in order to change the angle of attack of the profile the angle of the oncoming flow is adjusted. Fluent provides an axial and normal force vector which needs to be converted into a lift and drag force referenced to the airfoil chord by means of the oncoming flow angle. This is performed using equations (4.14) and (4.15) where conventions are described in Figure 4.15.

$$L = Ncos(\alpha) - Asin(\alpha) \tag{4.14}$$

$$D = Nsin(\alpha) + Acos(\alpha) \tag{4.15}$$

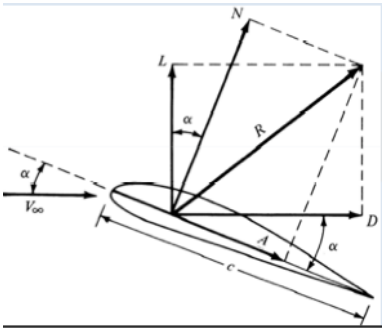


Figure 4.15: Diagram explaining conventions in equations (4.14) and (4.15)

4.4.1 Initial Conditions

To perform the simulations a number of initial approximations need to be made. These approximations are used as a guideline when creating, meshing and running the simulations. The boundary conditions used are chosen to mimic the conditions of the TC12 airfoil testing performed by Airbus. For the duration of this dissertation all simulations will be performed at a Reynolds number of 2.95 million. This coincides with the work done by Patzold (2008) and the availability of data for pressure distributions along the high lift device made possible by Airbus GmbH. Table 4.7 summarises the initial conditions.

Parameter	**Value**
Reynolds Number (based on chord length)	2.95 million
Mach Number	0.2
Air Properties	
Altitude	0 m (Sea Level)
Temperature	288.16 K
Density	1.225 kg/m^3
Pressure	0 Pa (gauge)
Kinematic Viscosity	1.789e-5 N.s/ m^3

Table 4.7: Initial conditions for CFD calculations

To find the boundary conditions a number of calculations need to be performed. The free stream velocity of the flow, based on Mach Number and Reynolds Number, is found using the ideal gas equation rearranged for solving the speed of sound, equation (4.16).

$$a = \sqrt{kRT} \tag{4.16}$$

where a is the speed of sound at given conditions, k is the heat capacity ratio for air (1.4), R is the ideal gas constant (287) and T is the temperature in Kelvin.

$a = \sqrt{1.4 * 287 * 288.16}$
$a = 340.26855 m/s$

Velocity is found using the Mach number relation. Equation (4.17):

$$V = Ma \tag{4.17}$$

where M is the free stream velocity and M is the Mach number.
$V = 0.2 * 340.26855$
$V = 68.05371 m/s$

Using the equation for Reynolds Number (equation (4.18)) the required chord length of the airfoil can be found.

$$Re = \frac{\rho V L}{\mu} \tag{4.18}$$

where Re is the Reynolds Number, ρ is the fluid density, L is the airfoil chord length and μ is the dynamic viscosity of the fluid.

$L = (Re * \mu)/(\rho * V)$
$L = (2.95e6 * 1.789e{-}5)/(1.225 * 68.05371)$
$L = 0.633059m$

An important consideration for boundary layer meshing on an airfoil is the height of the first cell. To calculate this, the law of the wall is used. Using the obtained results an effective sizing for the boundary layer can be found.[2] The skin friction of a plate of comparable length to the required airfoil length is used to obtain skin friction as follows:

$$C_f = 0.455log(Re)^{-2.58} \tag{4.19}$$

where C_f is skin friction coefficient and Re is chord Reynolds Number.

$C_f = 0.455log(2.95e6)^{-2.58}$
$C_f = 3.68e{-}3$

Shear stress of the plate is solved for using equation (4.20):

$$\tau_w = C_f 0.5 \rho U^2 \tag{4.20}$$

where τ_w is shear stress at the wall, ρ is fluid density and U is free stream velocity.

$\tau_w = 3.66e - 3 * \frac{1}{2} * 1.225 * 68.05731^2$
$\tau_w = 10.44N/m^2$

U^*: the friction velocity (or shear velocity is solved for). This is the shear stress is units of velocity as solved for in equation (4.21):

[2] Equation (4.19) is a modification of Prandtl's skin friction estimation for a flat plate done by (Schlichting, 2000), equation 21.16.

$$U^* = \sqrt{\frac{\tau_w}{\rho}} \tag{4.21}$$

$U^* = \sqrt{10.44/1.225}$
$U^* = 2.92m/s$

y^+ is initially given as an estimated value between 0 and the assumed maximum value it may achieve during simulation. For acceptable simulations of an airfoil the y^+ should fall between 0 and 5 according to the ANSYS user manual. For this calculation y^+ will be set at 1 for the flat plate approximation. This should be a good approximation to keep the y^+ value within the acceptable range during simulations of the full airfoil. Equation (4.22) is used to solve for y^+:

$$y = \frac{y^+ \mu}{U^* \rho} \tag{4.22}$$

where y is the distance from the wall, y^+ is the dimensionless wall distance.

$y = (1 * 1.1789e{-}5)/(2.92 * 1.225)$
$y = 5e{-}6m$

Finally the maximum size of the boundary layer is solved for using equation (4.23). This is used to determine the height of cells required to resolve the boundary layer or the airfoil. The equation is for a turbulent boundary layer and will be calculated for at the trailing edge where the boundary layer should be the largest. Using this assumption, the boundary layer mesh will account for the maximum boundary layer thickness and thus will resolve the boundary layer sufficiently along the entire chord length.

$$\delta = \frac{0.37x}{\sqrt[5]{Re_x}} \tag{4.23}$$

where δ is the length of the boundary layer at a given x location along a flat plate.

$\delta = (0.37 * 0.633059)/(\sqrt[5]{2.95e6})$
$\delta = 0.0119m$

Table 4.8 summarises the calculated boundary conditions.

Parameter	Value
Airfoil Chord	0.633059 m
Boundary Layer First Cell Height	5e-6 m
Boundary Layer Thickness	0.0119 m
Inlet Velocity	68.0571 m/s

Table 4.8: Summary of required boundary conditions from calculations

4.4.2 Solver Settings

The Fluent simulations for all configurations are set up with the same solver settings to maintain continuity across all simulations. The solver settings are explained in Table 4.9.

Condition	Value
Analysis Type	2D
Boundary	Pressure Far-Field
Mach Number	0.2
Gas	Ideal Gas (compressible)
Energy Equation	on
Pressure Velocity Coupling	
Scheme	SIMPLE
All formulations	Second Order

Table 4.9: Summary of solver settings used for Fluent validation simulations

Solution Controls

Convergence was monitored on the basis of the major residuals dropping below a certain criteria. The convergence criteria is summarised in table 4.10. Some solutions, particularly those using the SA turbulence model reached an oscillating convergence state where the solution oscillated between two values- this is referred to as *hanging residuals'* In this case the central value was taken as the solution. Solutions are considered converged if, firstly lift and drag residuals reach their convergence criteria, secondly if the continuity and velocity residuals reach their convergence or if neither set of criteria reaches convergence then the simulation terminates after the maximum number of iterations.

Criteria	Value
Maximum iterations	12 000
Continuity residual	$1e{-}6$
Velocity residual	$1e{-}6$
Lift residual	$1e{-}5$
Drag residual	$5e{-}5$

Table 4.10: Convergence criteria for Fluent simulations

4.4.3 Clean Configuration Validation

The TC12 profile in clean configuration is meshed and analysed in Fluent using the above calculated conditions. Meshing is done initially in ICEM and later in Ansys Mesher due to difficulties encountered with meshing more complex geometries in ICEM. Simulations are performed in Fluent and compared to the experimental data.

4.4.4 Meshing Strategy (Clean Configuration)

The general meshing strategy was to use a large far field domain comprised of a semi circular c-grid with the airfoil at the centre. The c-grid approach is used because, from the location of the flow entry (along the boundary) to the leading edge, of the airfoil there is a constant radius. This constant distance allows better simulation of free stream air when varying the angle of attack. The boundary layer and a portion of the downstream flow consisted of a mapped quad mesh, whilst the farfield consisted of free face elements which were a mix of tri and quad elements. The airfoil itself is set as a wall boundary condition.

Table 4.11 explains the exact size of the mesh domain. Figures 4.16 to 4.20 are referenced in the table to provide a thourough explanation of the sizing of each block within the mesh. The size of the boundary was selected based on recommendations from ANSYS online video tutorials. The mesh boundary layer values were all calculated in the previous section.

Region	**Figure**	**Section**	**Length (m)**	**Number of Nodes**	**Growth Rate**
Outer Block	4.16				
		A	5	145	
		B[3]	6.5	40	
		C	10	208	
Inner Block	4.17				
		A	0.666	45	
		B	0.286	40	1.3
		C	0.772	100	
		D	0.261	50	1.3
		E	0.590	85	1.05
		F	0.08	100	
		G	0.25	100	
		H	0.366	220	
Boundary Layer	4.18 & 4.19				
first cell height: *5e-6 m*		-	0.0119	50	1.1
Boundary Layer Trailing Edge	4.20				
		A	0.1	50	

Table 4.11: Summary of TC12 profile clean configuration blocking parameters for meshing

Mesh Outer Block

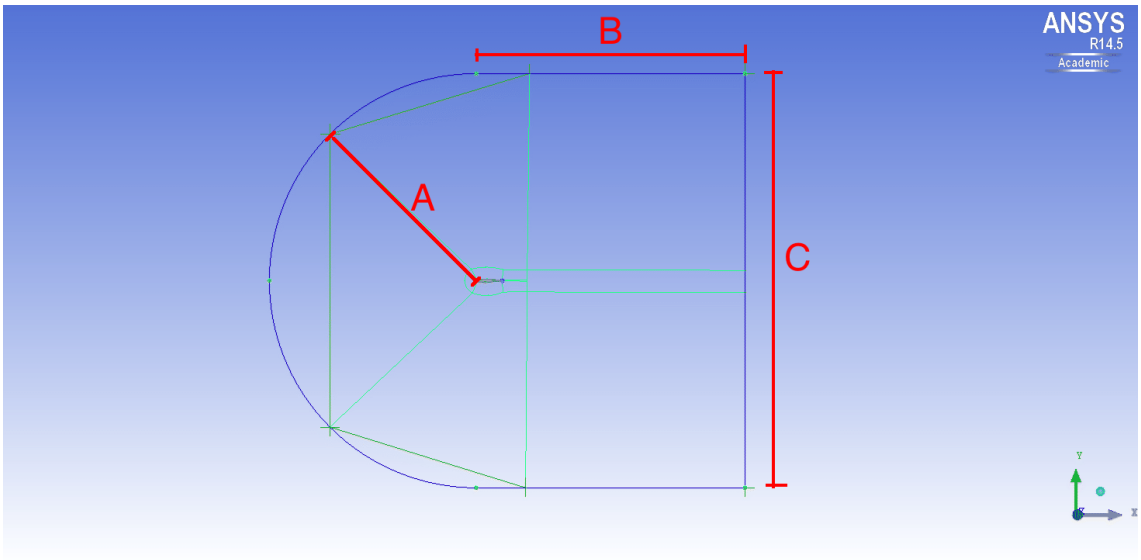


Figure 4.16: Initial blocking of TC12 profile clean configuration

Mesh Inner Block

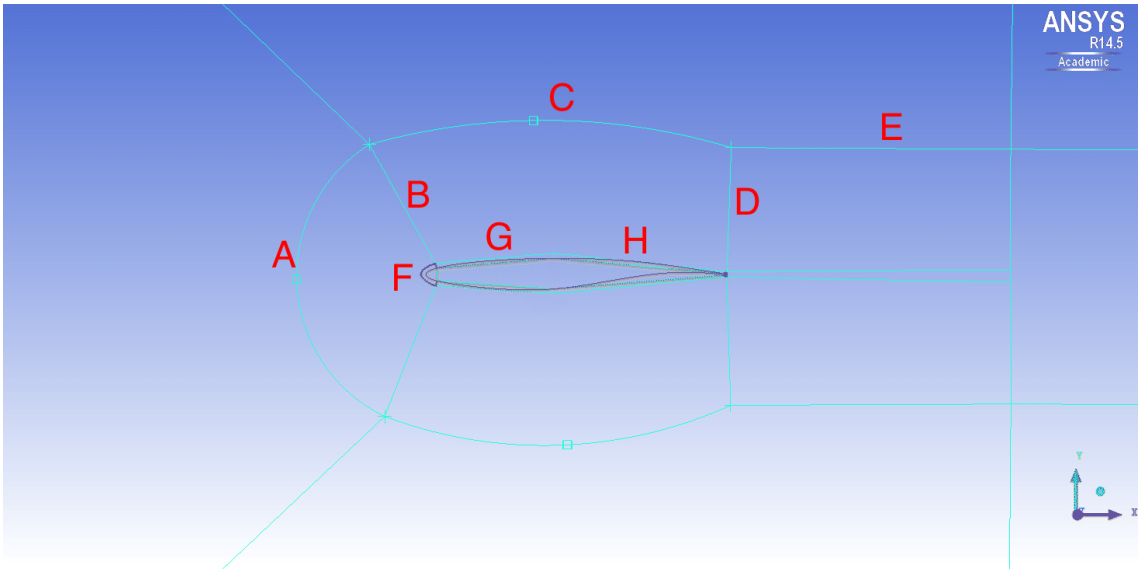


Figure 4.17: Close up of blocking of TC12 profile clean configuration mesh

Boundary Layer Mesh

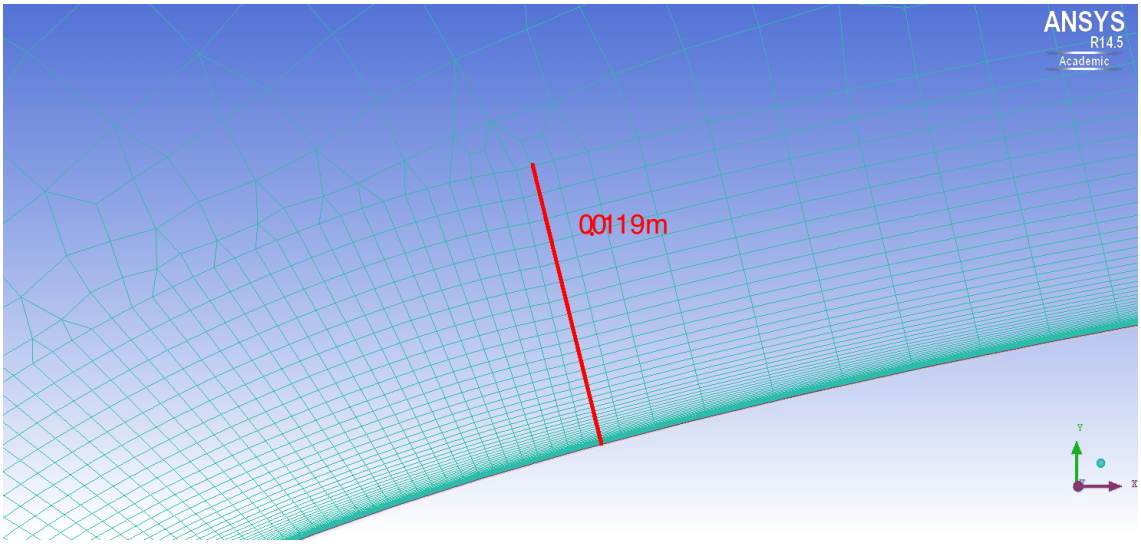


Figure 4.18: Boundary layer mesh of TC12 profile clean configuration

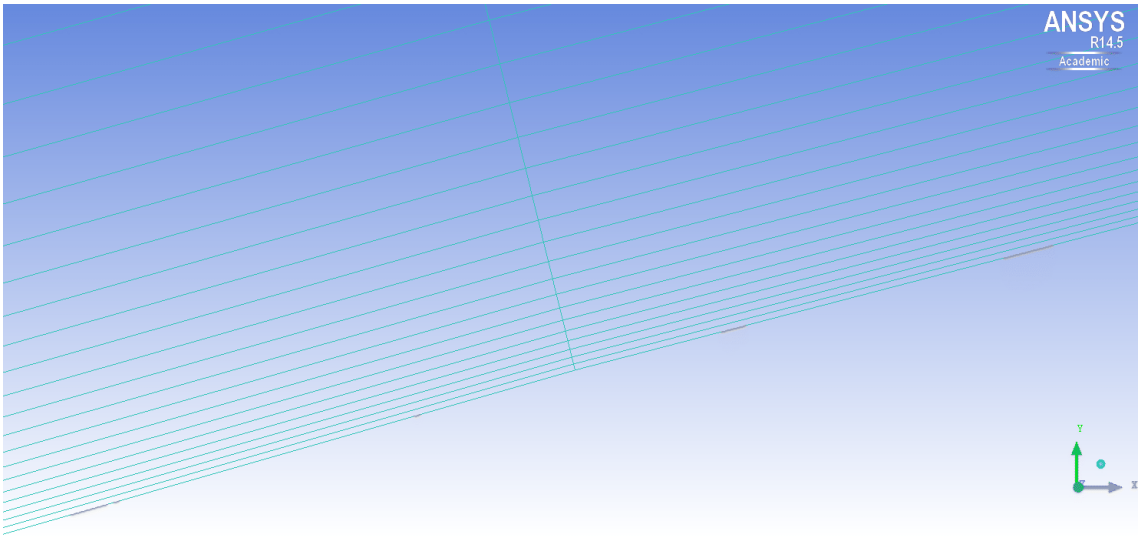


Figure 4.19: Boundary layer mesh close to surface of TC12 profile clean configuration

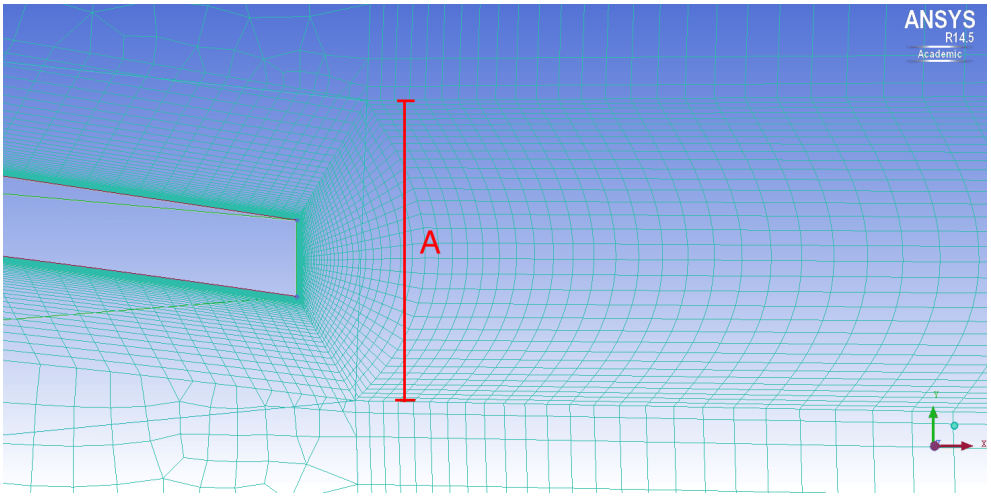


Figure 4.20: Boundary layer mesh at the trailing Edge of TC12 profile clean configuration

Final Mesh (Clean Configuration)

Using the aforementioned meshing strategies, a mesh was produced in ICEM. The mesh was smoothed at certain regions to adjust nodes with poor quality. This mesh would be used as an initial mesh for calculations and would be further refined within Fluent using the *mesh refinement by residuals* tools. Figure 4.21 and 4.22 show the final mesh in full view and zoomed in respectively.

Table 4.12 explains the number of nodes and elements at each major location on the mesh as well as their different types. The mesh has a quality over 0.35 for over 90 % of nodes.

Element Types	**Number of**
Line	1194
Tri	1402
Quad	100764
Element Parts	
Fluid	102166
Far Field	425
Airfoil	735
Trailing Edge	34
Total Elements	103360
Total Nodes	102062

Table 4.12: TC12 Clean Configuration Mesh Element Summary

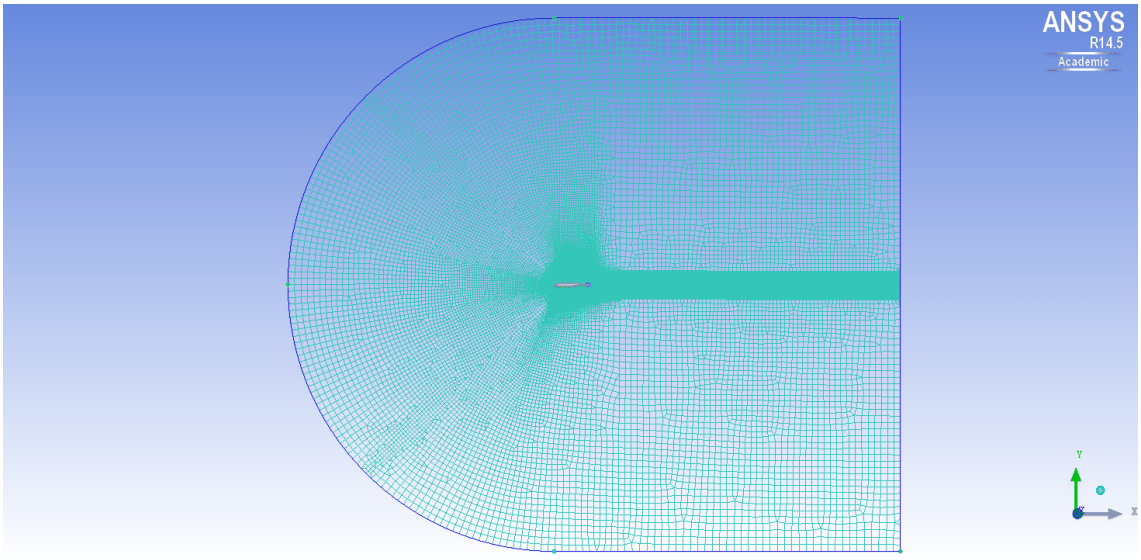


Figure 4.21: TC12 profile clean configuration airfoil mesh (full view)

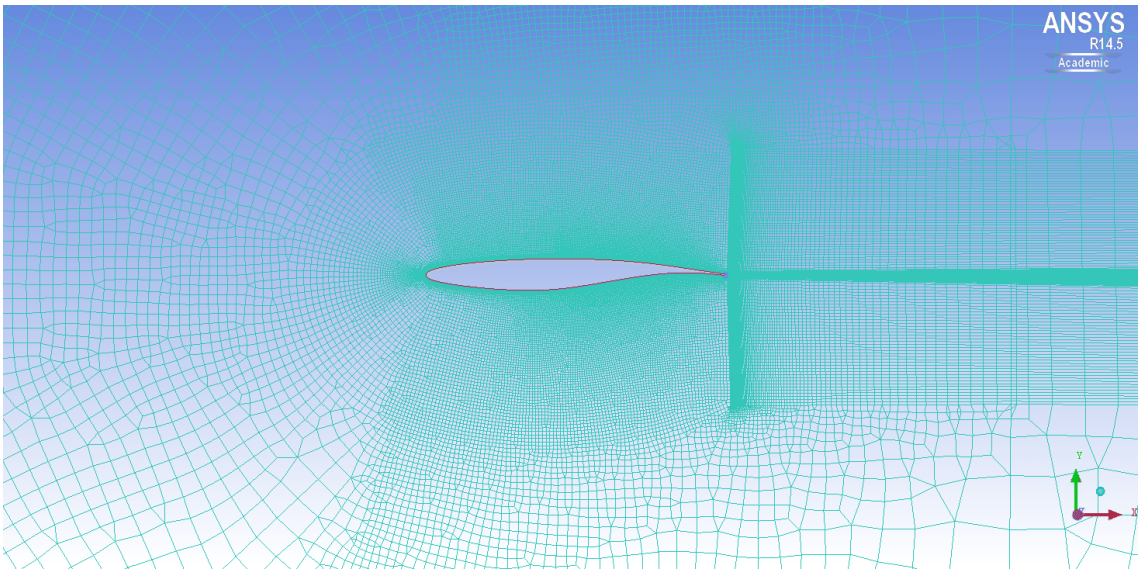


Figure 4.22: TC12 profile clean configuration airfoil mesh close Up on airfoil

Grid Convergence (Clean Configuration)

A grid convergence study was performed using the Spalart-Allmaras (SA) turbulence model at an angle of attack of 8.1051 degrees (to coincide with experimental results, see Figure 4.1). The resulting grid was then tested with other turbulence models.

In order to confirm that the resolution of the grid did not influence the results, grid adaptations were performed within Fluent. Fluent has an option to adapt a grid based on the gradient of residuals between cells. This is very helpful where, in some cases, cells are too large and data passed to adjacent cells is no longer accurate.

Table 4.13 shows the convergence of the final second order results for the grid with each adaptation step. The grid is considered converged when the residuals of drag (the absolute error between adaptation steps) fall below a factor of 1e-4. The adaptations show a change in drag, from step 1 to step 6, of 0.46% which can be considered negligible.

The error between the simulations and the experiments is also considered. As the adaptations are made the error is seen to change by a very negligible amount.

Adaptation Step	**Lift Coefficient**	**Error on Lift Coefficient**	**Drag Coefficient**	**Drag Coefficient Residuals**
1	1.1356	1.85%	0.019470	-
2	1.1354	1.83%	0.019613	7.34e-3
3	1.1352	1.81%	0.019690	3.93e-3
4	1.1345	1.74%	0.019570	6.09e-3
5	1.1345	1.74%	0.019556	7.15e-4
6	1.1346	1.76%	0.019561	2.56e-4

Table 4.13: Grid convergence study of the TC12 profile mesh in clean configuration

Figure 4.23 shows the mesh adaptations after the final adaptation step in the inflated area around the airfoil. This is where the primary adaptations occurred, farfield adaptations were negligible. Figure 4.24 shows the final adaptations of the mesh close to the boundary layer. Note the considerable refinement just off the surface at the leading edge used to capture high velocity flow in the vicinity.

The final number of nodes in the new mesh is 143504 nodes (41% increase). Compared to the change in computational error the grid convergence could have been avoided due to the increase in computational time required compared to the increase in accuracy achieved.

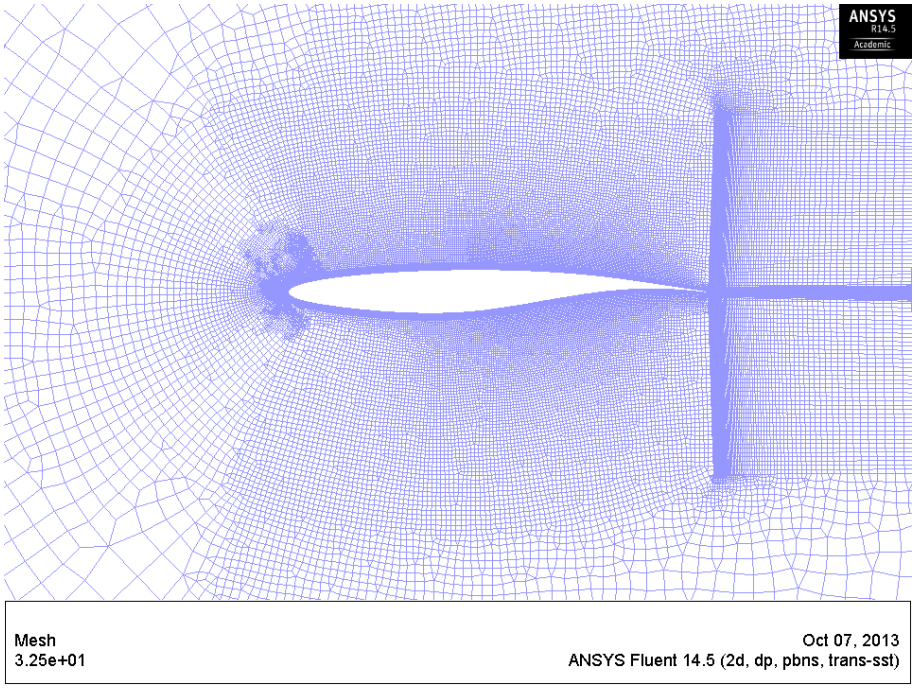


Figure 4.23: Mesh adaptations for TC12 profile clean configuration

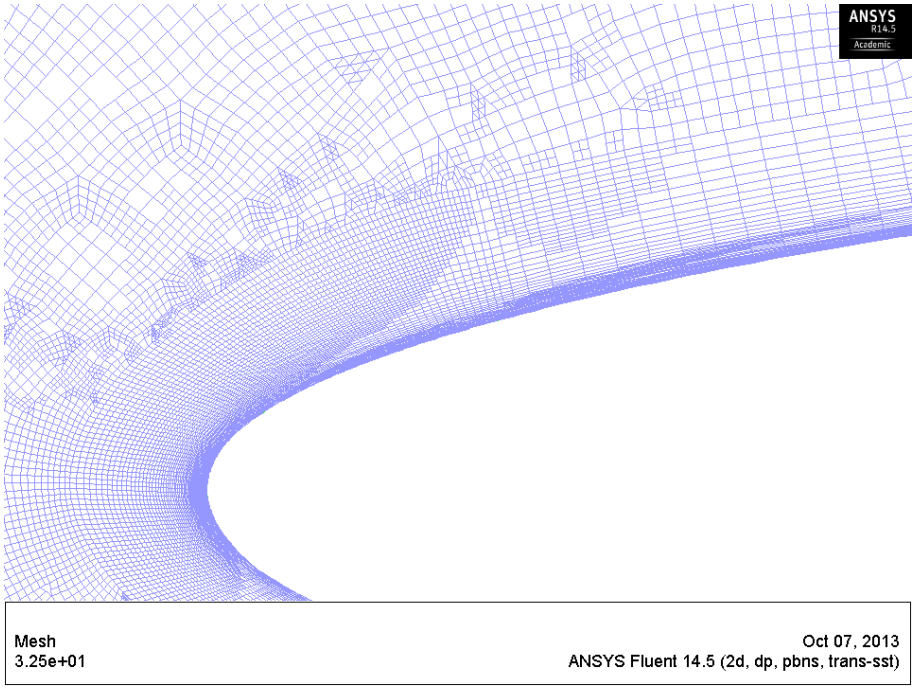


Figure 4.24: Mesh adaptations of TC12 profile clean configuration within the boundary layer at the leading edge

Selecting a Turbulence Model

A turbulence model is selected that best correlates the experimental to that of the simulations. Using the default turbulence models available in Fluent a number of turbulence models were tested with the previously produced grid. Table 4.14 summarises the errors in the various turbulence models when compared to experiments. All solutions were converged to a second order solution. Error was calculated as compared to experimental data (Figure 4.1).

Turbulence Model	**Lift Coefficient**	**Lift Coefficient Error (%)**	**Drag Coefficient**	**Drag Coefficient Error compared to SA**
Spalart-Almaras	1.1346	1.75	0.019561	-
k-ω with SST	1.1231	0.72	0.020182	3.17%
Transition SST	1.1229	0.6999	0.01995	1.99%
Transition k-kl-ω	1.1514	3.26	0.01867	4.55%

Table 4.14: Turbulence model selection for Fluent simulations for the TC12 profile clean configuration

According to literature the SA turbulence model is best suited for modelling external flow. The model is designed to use few computing resources due to its single equation nature. However, from table 4.14 it can be seen that for this case the Transition SST model provides the lowest error and the drag prediction is similar to that of the SA model. The k-ω model also provides a large error in drag when compared to the SA turbulence model- the reason for this is that the model, being a two equation model, tends to produce to much turbulence at stagnation points and areas with high velocity which can lead to increases in drag as seen. The Transition k-kl-ω turbulence model has the largest error in drag when compared to the SA turbulence model- this model is similar to that of the Transition SST model and thus also predicts drag poorly due to the same flow features. There is a correlation between the SA model and the Transition SST model.

The processing time of the SA and Transition SST simulations were not very different because of the simple geometry used; hence the Transition SST model is selected to simulate the TC12 profile in clean configuration.

4.4.5 Results (Clean Configuration)

The converged grid and selected turbulence model were used to perform additional Fluent simulations at a range of angles of attack to compare to the experimental data.

Residuals

Figure 4.25 shows the residuals for the finalised, converged grid, for the TC12 profile in clean configuration. The iterations being at 54 500 because Fluent was used previously to obtain the converged grid. Figure 4.26 shows the drag coefficient against the simulation iterations. The scaled residuals show a decreasing trend as they move towards the convergence criteria of 1e-6 whilst the drag residuals show that a steady value for drag is obtained during the simulation.

Convergence is obtained at 58 700 iterations which, when referenced from the starting iteration, leads to a convergence of a single simulation within 4 200 iterations.

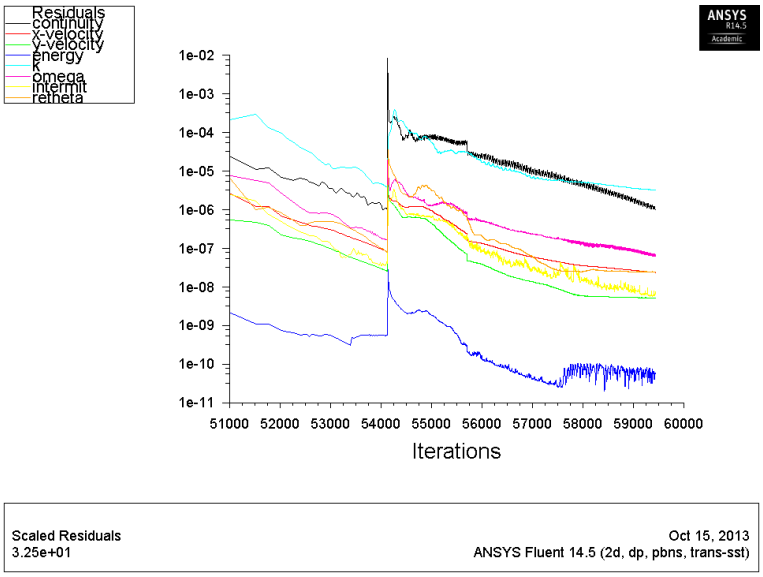


Figure 4.25: Second Order Convergence of Fluent Results for the TC12 Clean Airfoil at 8.1051 degrees

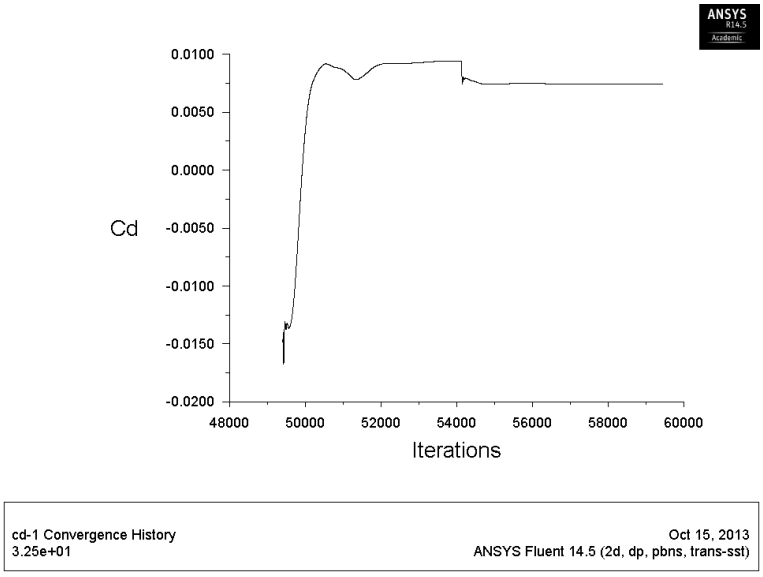


Figure 4.26: Coefficient of Drag convergence for the TC12 profile in clean configuration at 8.1051 degrees

Flow Features

Figure 4.27, which is a plot of velocity vectors, shows a separation bubble predicted at the leading edge of the airfoil (characterised by the reversed flow along the surface of the airfoil).

This separation bubble can be compared in the pressure distributions of the airfoil.

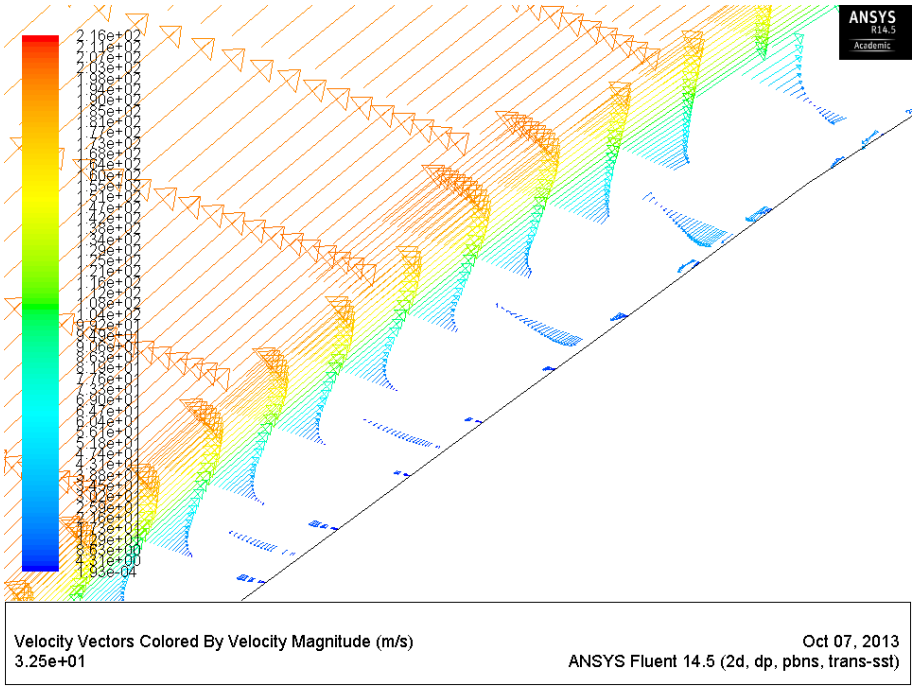


Figure 4.27: Separations at the leading edge of TC12 profile in clean configuration

Figures 4.28 to 4.29 show the lift and drag against angle of attack of the TC12 profile in clean configuration respectively.

Stall prediction of the TC12 profile in clean configuration is not accurate. Maximum lift is overpredicted by 7% and the stall angle is overpredicted by 28%. The trend according to experiments should be for a leading edge stall due to the bursting of a laminar separation bubble - this causes the sudden loss of lift seen in the experimental data at 8.611 degrees. Fluent predicts a slower trailing edge stall, as characterised by the mild decrease in lift at higher angle of attack due to the separation bubble not bursting. This behaviour of CFD to poorly predict stall is documented by Genc (2010) and results shown here follow similar trends. Fujii (2004) also notes this same trend for thin airfoils at high Reynolds numbers and states that a suitable solution could be to use a RANS/LES hybrid simulation.

The y^+ value along the surface of the airfoil is consistently below 2 for all angles of attack.

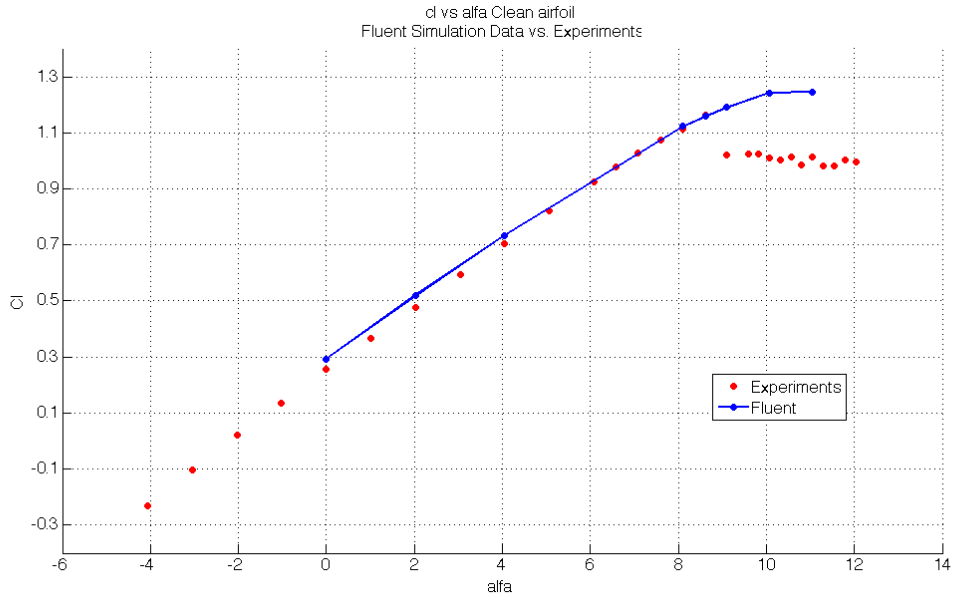


Figure 4.28: Cl vs. alfa for TC12 in clean configuration compared to experiments, Re 2.95 Million, transition-SST turbulence model

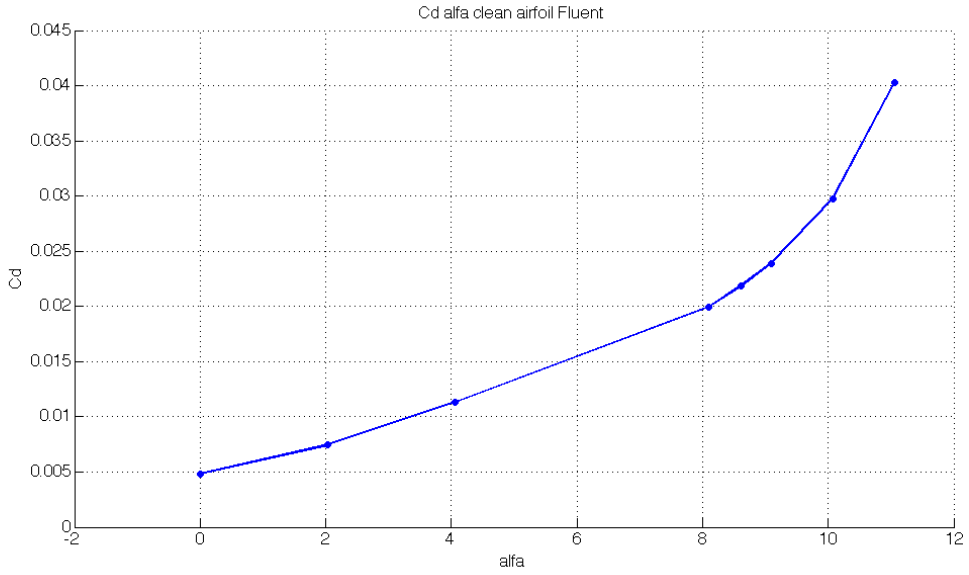


Figure 4.29: Cd vs. alfa for TC12 in clean configuration compared to experiments, Re= 2.95 Million, transition-SST turbulence model

Pressure Distributions

The pressure distribution along the airfoil is generated in Fluent as seen in Figure 4.30. There is qualitative agreement looking at the trends of the pressure distribution. Looking closely at the pressure peak in Figure 4.31 it becomes apparent that Fluent predicts a shorter separation

bubble with a lower pressure (more lift) than what is measured. It is also observed that the peak of the Cp curve is much higher than the experimental data (Figure 4.31). This inaccuracy could be related to the number of pressure taps used in the experimental set up where a rig with more pressure taps could resolve the peak at a higher location.

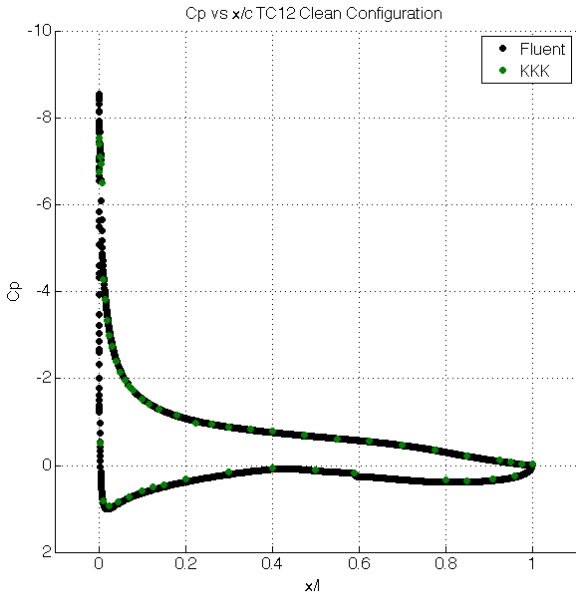


Figure 4.30: Pressure distributions of TC12 profile in clean configuration at 8.1 degrees, Fluent vs. Experiments

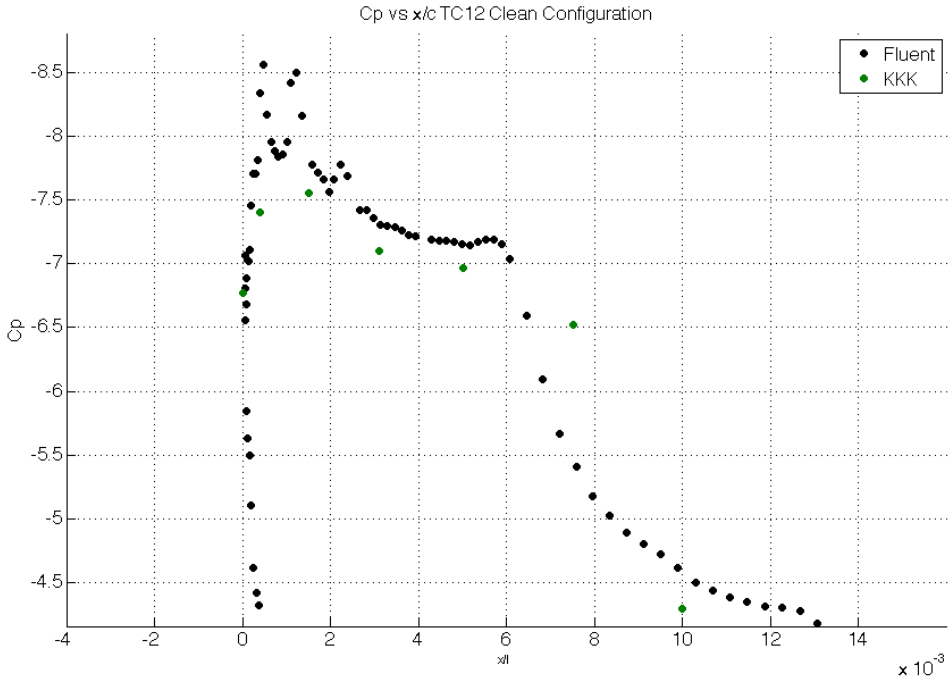


Figure 4.31: Pressure Distributions of TC12 profile in clean configuration zoomed in at separation bubble, Fluent vs. experiments

4.4.6 High Lift Configuration Validation

The TC12 profile in high lift configuration is meshed and analysed in Fluent using the same calculated conditions as the clean configuration profile. Meshing of the high lift configuration was performed in Ansys Meshing as the program made it easier to produce inflated boundary layers around the high lift airfoil. Due to the change in meshing tool there was no need to use blocking as was done in ICEM for the original clean airfoil mesh.[4]

4.4.7 Meshing Strategy (High Lift Configuration)

The mesh strategy was to emulate the mesh made for the clean airfoil. The domain size was kept consistent. Table 4.15 shows a summary of the mesh parameters used. The table references images for clarity.

[4]Because of the change in meshing software used the clean airfoil needed to be re-run at the reference angle with a new mesh created in the software. The results of this validation can be seen in appendix D.

Airfoil Part	Figure	First Cell Height (m)	Layers	Growth Rate	Max Cell Width (m)
Slat	4.32 & 4.33	5e-6	35	1.1	4e-4
Main body	4.34	5e-6	45	1.1	5e-4
Flap	4.35 & 4.36	5e-6	35	1.15	5e-4

Table 4.15: TC12 high lift configuration boundary layer mesh parameters

Mesh Outer Block

The outer block of the mesh domain is the same size as the block used for the clean configuration mesh. The length behind the airfoil is equivalent to 10 chord lengths.

Boundary Layer Mesh

The boundary layer was meshed using the parameters explained in table 4.15. Figures 4.32 to 4.36 show close up views of the important regions of the boundary layer mesh. The boundary layer is meshed with quad elements to maintain flow orthogonality with the airfoil walls, and to properly capture the boundary layer flows.

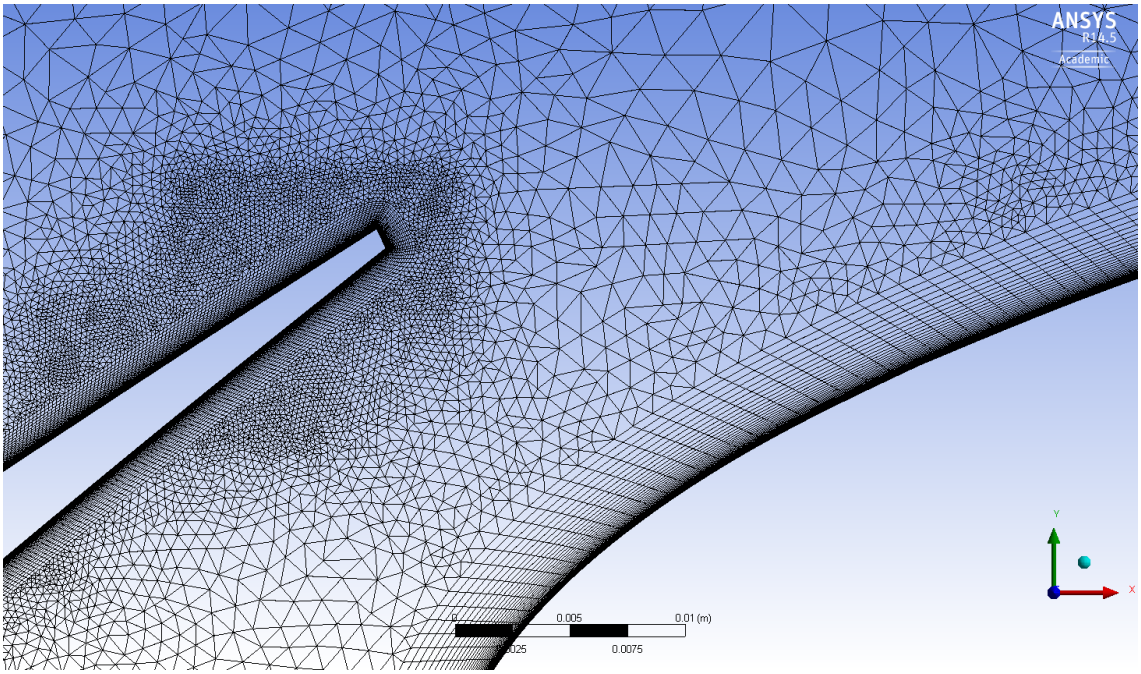


Figure 4.32: Mesh at the region between TC12 profile in high lift configuration, slat trailing edge and main element leading edge

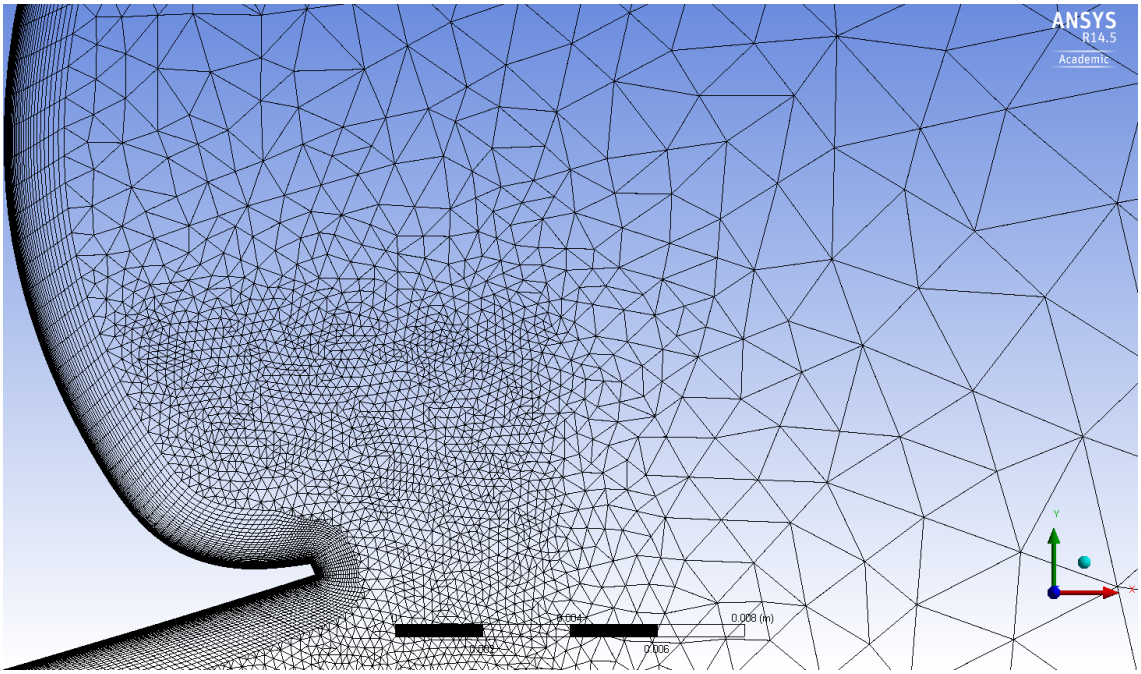


Figure 4.33: Mesh at the cove region of the slat TC12 profile high lift configuration

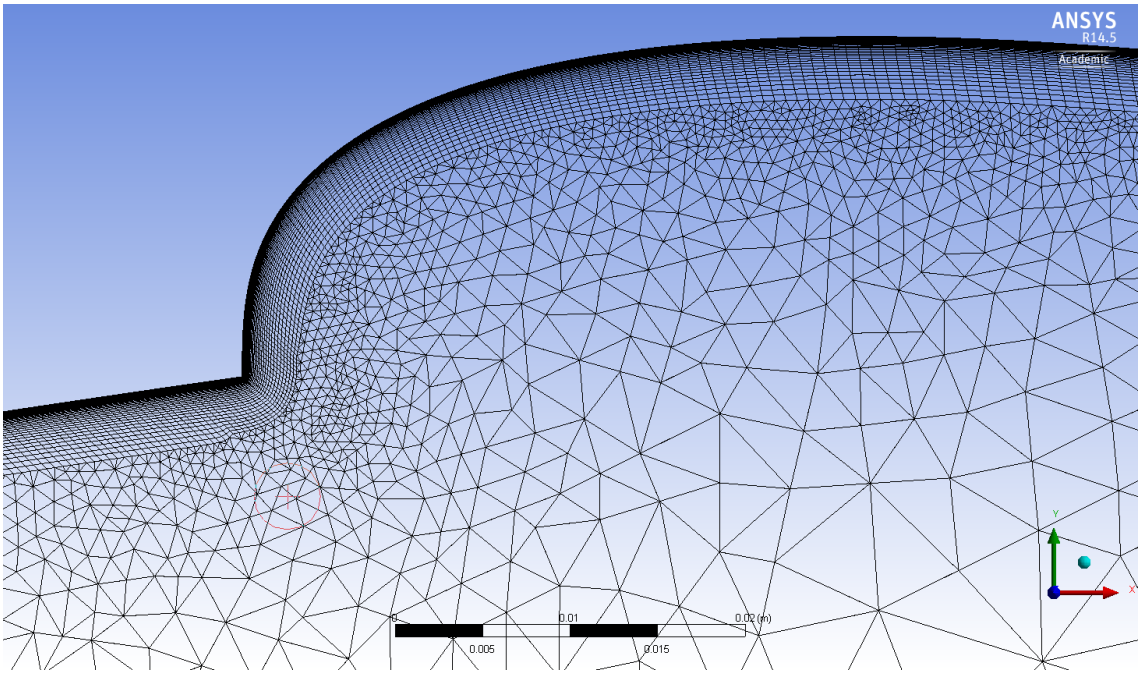


Figure 4.34: Mesh at the cove region of the main element TC12 profile in high lift configuration

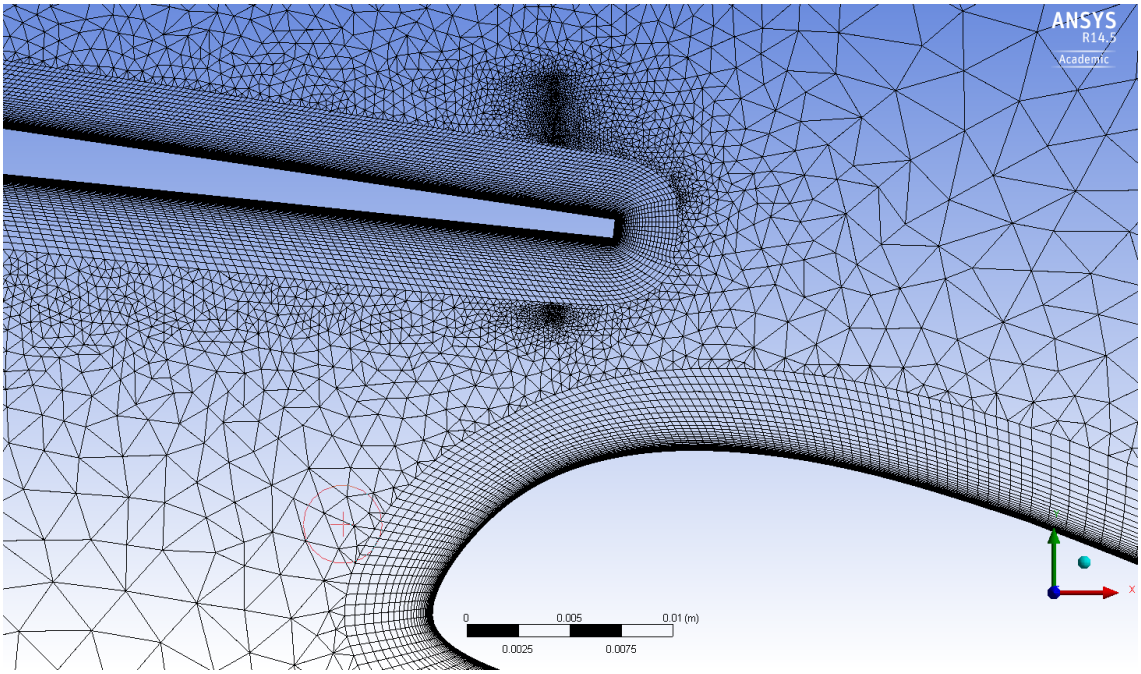


Figure 4.35: Mesh between the spoiler and the flap TC12 profile in high lift configuration

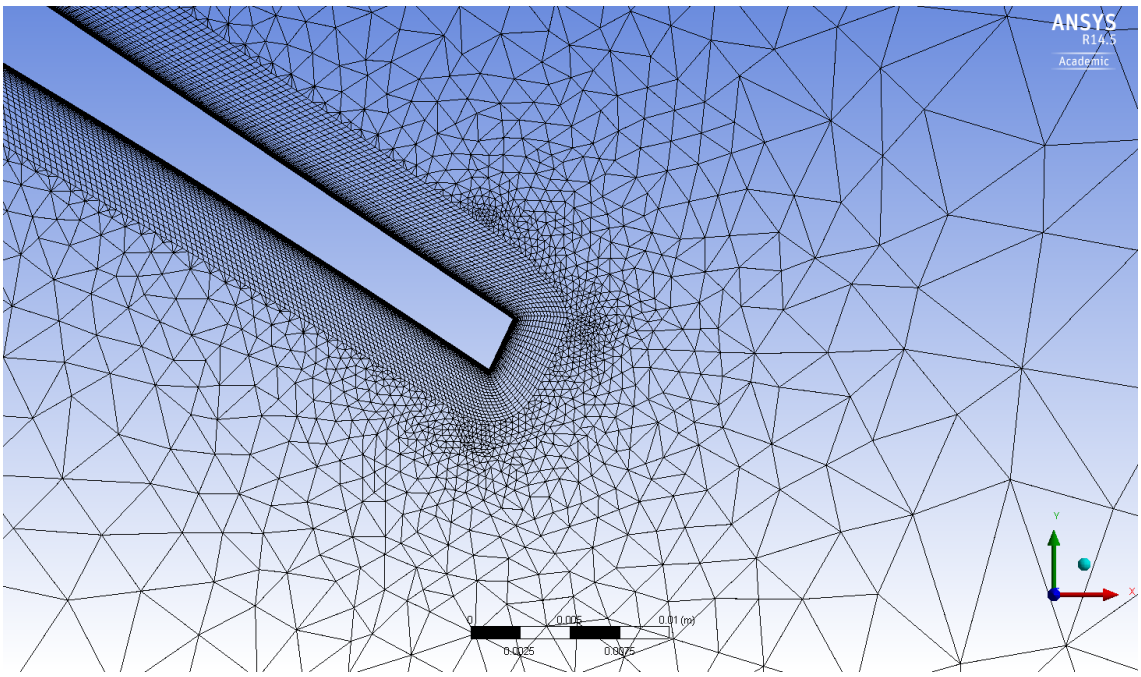


Figure 4.36: Close up of flap trailing edge mesh TC12 profile in high lift configuration

Final Mesh (High Lift Configuration)

Using the aforementioned meshing strategies a mesh was produced in ANSYS Mesher. The mesh was smoothed at certain regions to adjust nodes with poor quality. This mesh would be

used as an initial mesh for calculations and would be further refined during the grid convergence study. Figure 4.37 and 4.38 show the final mesh in full, and zoomed in respectively.

The mesh has a quality over 0.35 for over 90 % of nodes.

Table 4.16 shows the summary of the nodes and elements contained in the mesh and their numbers along the different bodies of the TC12 profile in high lift configuration.

Element Types	**Number of**
Line	4118
Tri	94808
Quad	148445
Element Parts	
Fluid	243253
Far Field	387
Slat	1176
Main	1786
Flap	769
Total Elements	247371
Total Nodes	207233

Table 4.16: Mesh node and element information for TC12 profile in high lift configuration

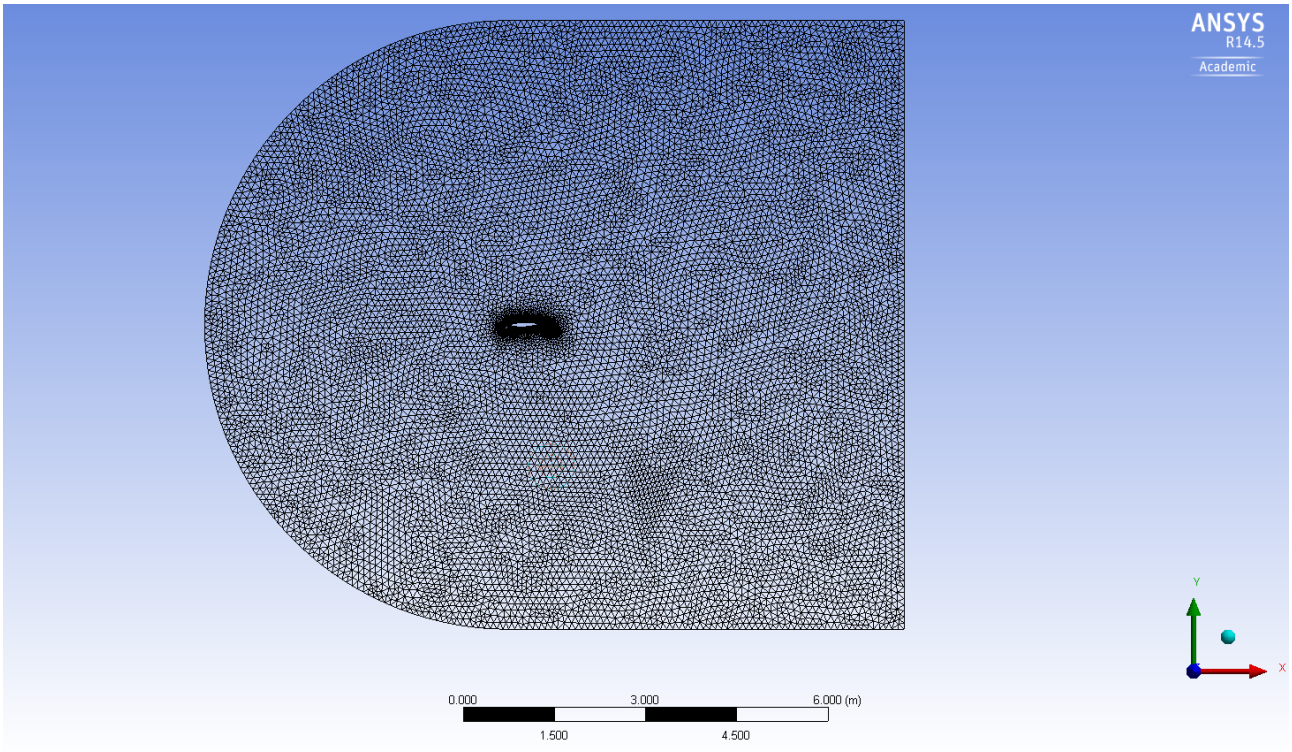


Figure 4.37: Mesh outer block for TC12 profile in high lift configuration

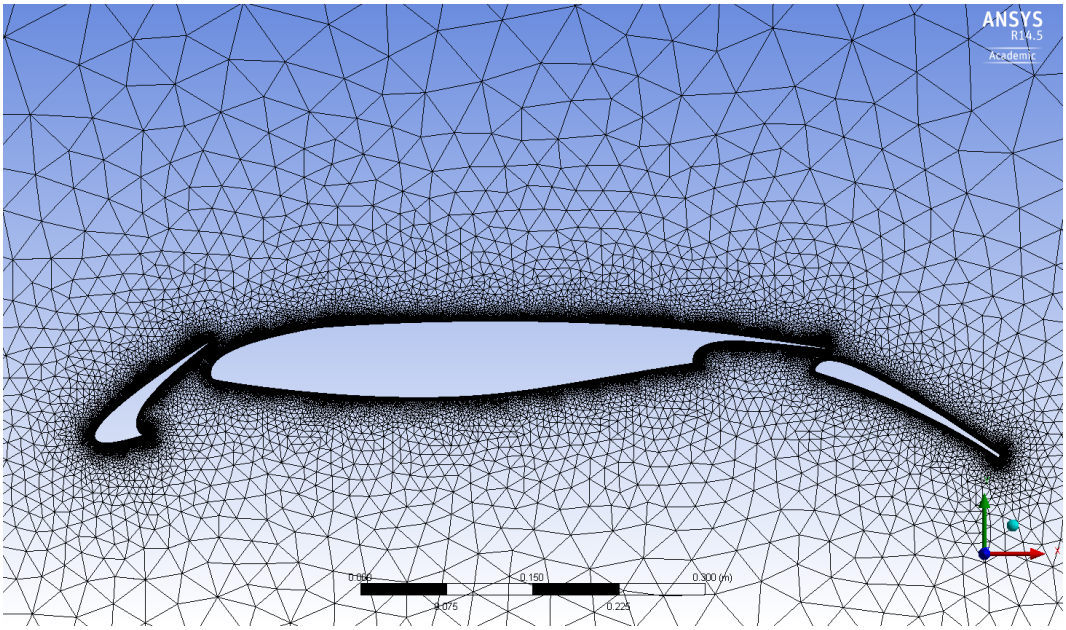


Figure 4.38: Mesh close up of airfoil for TC12 profile in high lift configuration

Grid Convergence (High Lift Configuration)

A Grid Convergence study was performed using the SA turbulence model at an angle of attack of 8.09 degrees (to coincide with experimental results, see Figure 4.2). The resulting grid was then tested with other turbulence models to find which model performs best for the given simulation. The grid convergence strategy is the same as that applied to the clean configuration mesh.

Table 4.17 shows the convergence of the final second order results for the grid with each adaptation step. The grid is considered converged when the drag residuals (the absolute error between adaptation steps) reaches a factor of 1e-4. In the case of the mesh for the high lift profile, grid convergence was much quicker than with the clean configuration mesh. This is due to the much higher cell count and the use of tri elements.

The error of each simulation compared to the experimental data is also shown. The error remains consistently at around 1.7 %. Thus showing that grid changes do not effect the results dramatically.

Adaptation Step	**Lift Coefficient**	**Error on Lift Coefficient**	**Drag Coefficient**	**Drag Coefficient Residuals**
1	2.8318	1.74%	0.068372	-
2	2.8320	1.76%	0.068322	7.31e-4

Table 4.17: Grid convergence study for TC12 profile in high lift configuration

Figure 4.39 shows the adaptations after the adaptation step in the area between the airfoil and the slat. This is where the primary adaptations occurred, farfield adaptations were negligible. Note the considerable refinement just off the surface at the leading edge used to capture high velocity flow in the vicinity. The adaptation required less steps as the grid for the high lift configuration already had almost double the number of elements in it than that of the mesh for the TC12 profile in clean configuration.

The final number of nodes in the new mesh is 207 233 nodes (4.7% increase).

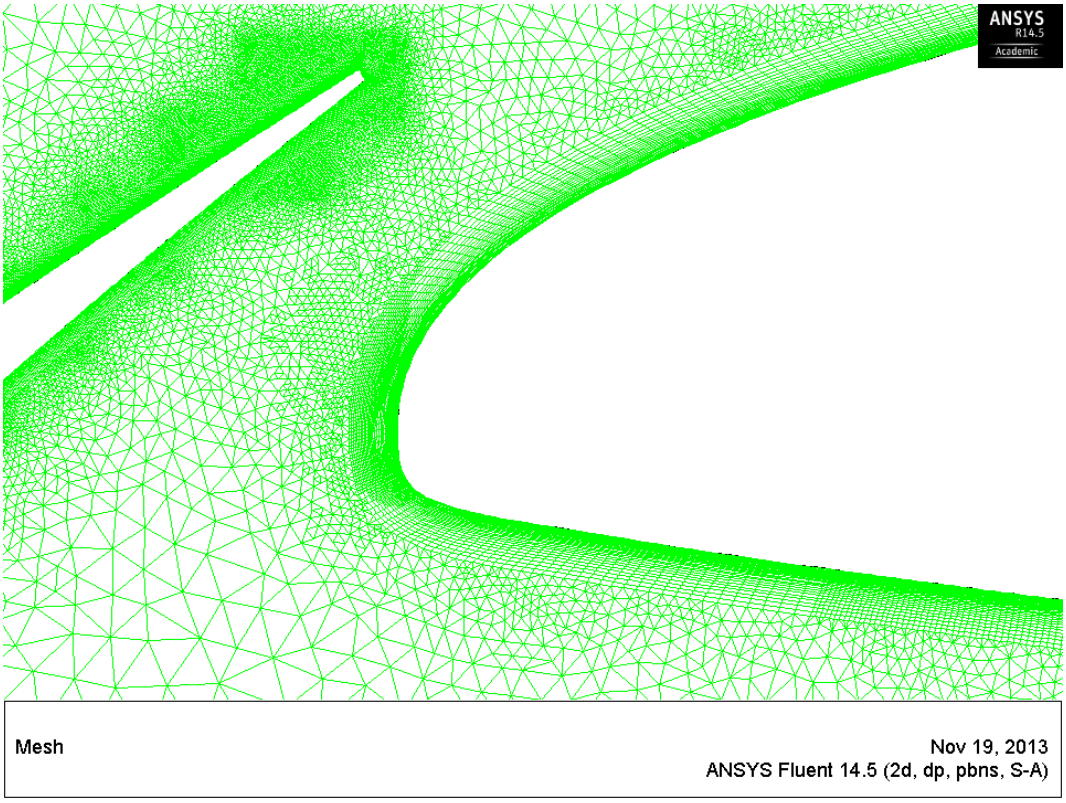


Figure 4.39: Adapted region of mesh for TC12 profile in high lift configuration

Selecting a Turbulence Model (High Lift Configuration)

As with the clean configuration a number of turbulence models were tested for the analysis of the TC12 profile in high lift configuration. Table 4.18 shows the lift and drag coefficients found at 8.091 degrees with various turbulence models and the errors associated with the calculations.

Turbulence Model	**Lift Coefficient**	**Lift Coefficient Error (%)**	**Drag Coefficient**	**Drag Coefficient Error compared to SA turbulence model**
Spalart-Almaras	2.8320	1.6547	0.068322	-
k-ω with SST	2.8337	1.2434	0.065803	3.68%
Transition SST	2.73145	3.2879	0.1264105	85%
Transition k-kl-ω	2.9546	3.26	0.0630155	7.77%

Table 4.18: Turbulence model selection TC12 profile in high lift configuration

As with the clean configuration turbulence model; the model with the lowest error was selected for testing. Since SA and k-omega SST both had similar errors when comparing lift against the experimental data; they were both selected as suitable turbulence models. The reason for the poor results of the Transition SST and Transition k-kl-omega in predicting drag is due to the

incorrect prediction of transition locations along the airfoil.

High Lift Configuration Results

SA Turbulence Model

Residuals

Figure 4.40 shows the set of residuals for the grid, Figure 4.41 shows the drag coefficient residuals. The same residual monitors are employed for the simulations of the TC12 profile in high lift configuration. Each simulation took about 7 500 iterations to converge. The figures begin at a high number of iterations because prior iterations are used to achieve the grid convergence.

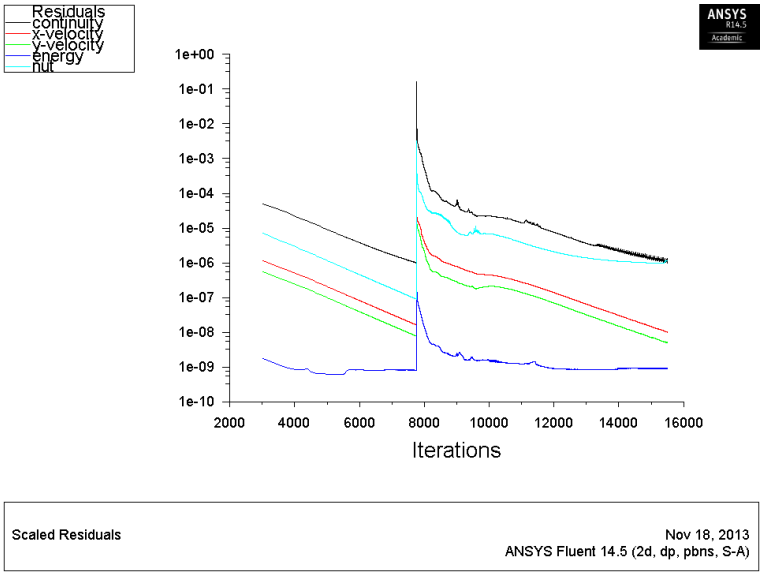


Figure 4.40: Scaled residuals for TC12 high lift configuration mesh, SA turbulence model

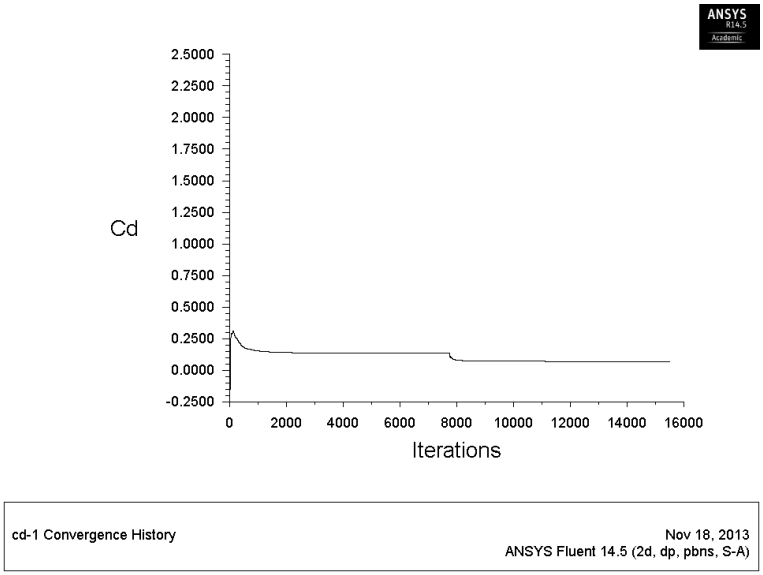


Figure 4.41: Convergence of drag coefficient residuals for TC12 high lift configuration mesh, SA turbulence model

Flow Features

Figure 4.42 shows the static pressure contours which highlight the low pressure areas at the leading edge of the main element and the flap as well as the high pressure areas at the main element and flap stagnation points.

Figure 4.43 shows the recirculations in the slat cove.

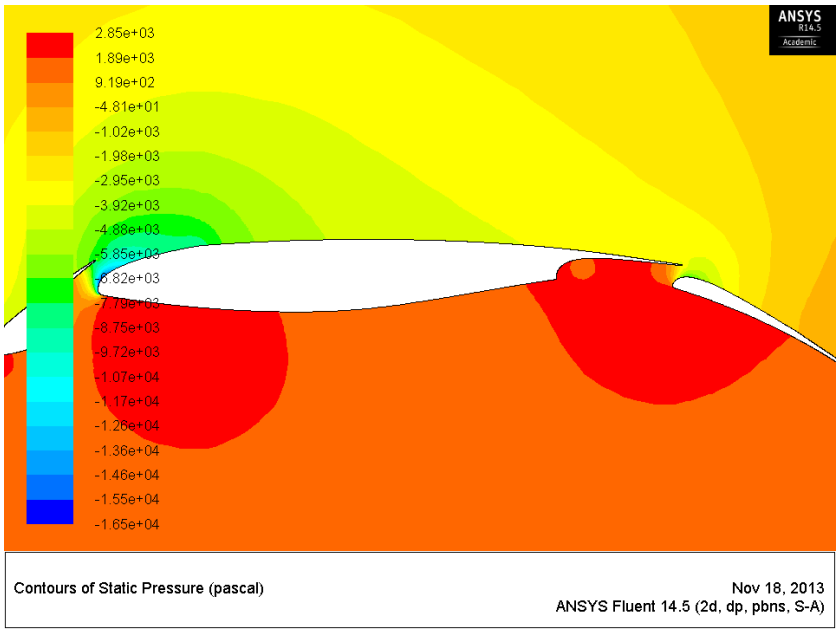


Figure 4.42: Pressure contours for TC12 profile in high lift configuration, SA turbulence model, 8.09 degree, Re 2.95 million

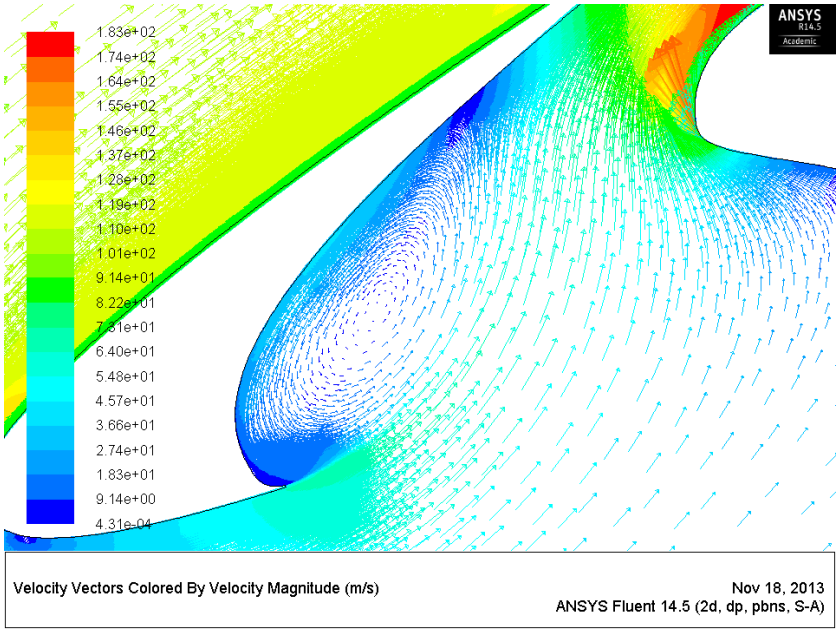


Figure 4.43: Recirculation at slat cove of TC12 profile in high lift configuration, SA turbulence model, 8.09 degrees, Re 2.95 million

k-omega SST Turbulence Model

Residuals

Simulations employing k-omega SST Turbulence Model was also performed. Using this turbulence model allowed for faster convergence than that of the SA turbulence model- typically within 150 iterations. Although the residuals (figure 4.44) did not fall below the convergence criteria, the drag convergence did reach a hanging bounded steady value as seen in figure 4.45. The value used for the lift and drag data was the averaged value of the peak amplitudes of the data. Further mesh adaptations would provide a better result with more sufficient convergence but the given results were seen to be sufficient for this section.

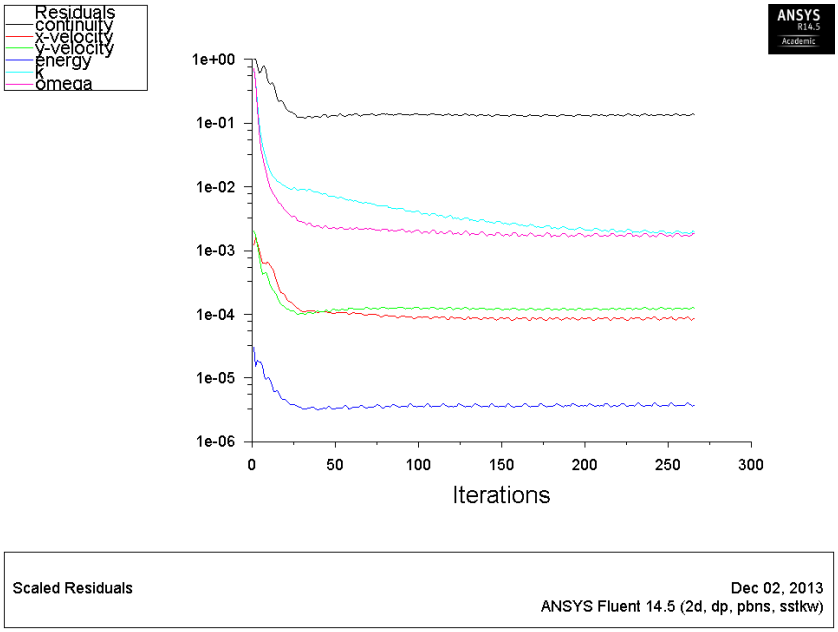


Figure 4.44: Scaled residuals of TC12 profile in high lift configuration, k-omega SST turbulence model, 8.09 degrees, Re 2.95 million

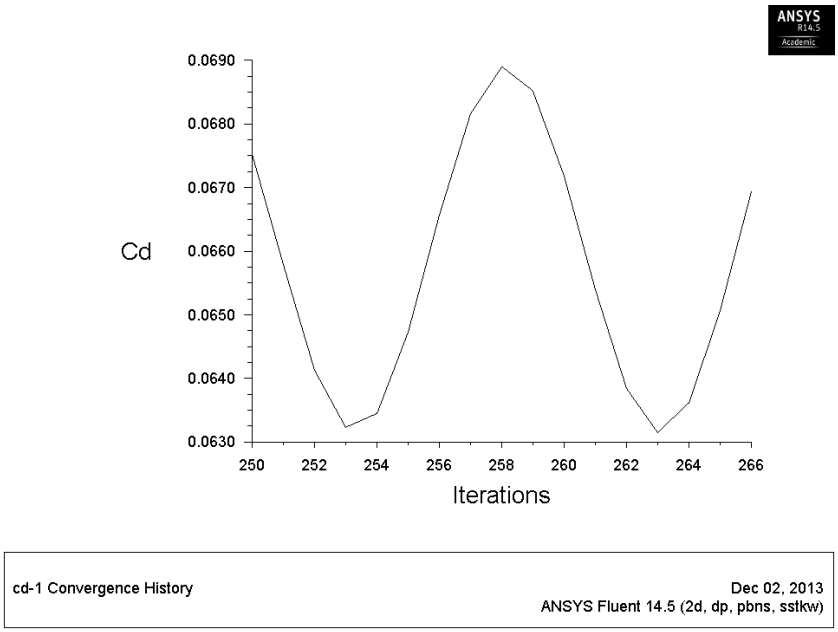


Figure 4.45: Excerpt of value of drag residuals for TC12 profile in high lift configuration, k-omega SST turbulence model, 8.09 degrees, Re 2.95 million

Flow Features

Figure 4.46 shows the static pressure contours which highlight the low pressure areas at the leading edge of the main element and the flap as well as the high pressure areas at the main element and flap stagnation points. These contours are very similar to those of the SA turbulence model.

Figure 4.47 shows the velocity contours of the model.

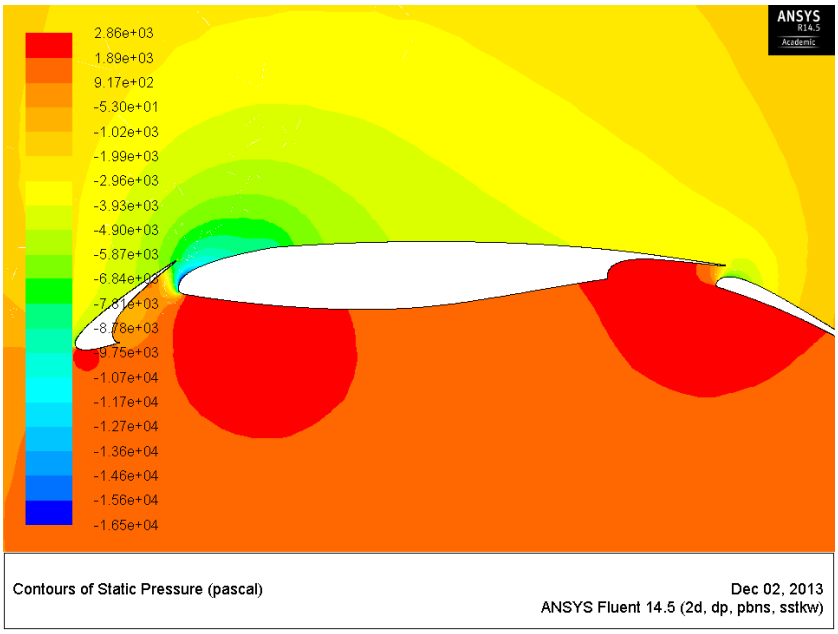


Figure 4.46: Pressure distribution for TC12 profile in high lift configuration, k-omega SST turbulence model, 8.09 degrees, Re 2.95 million

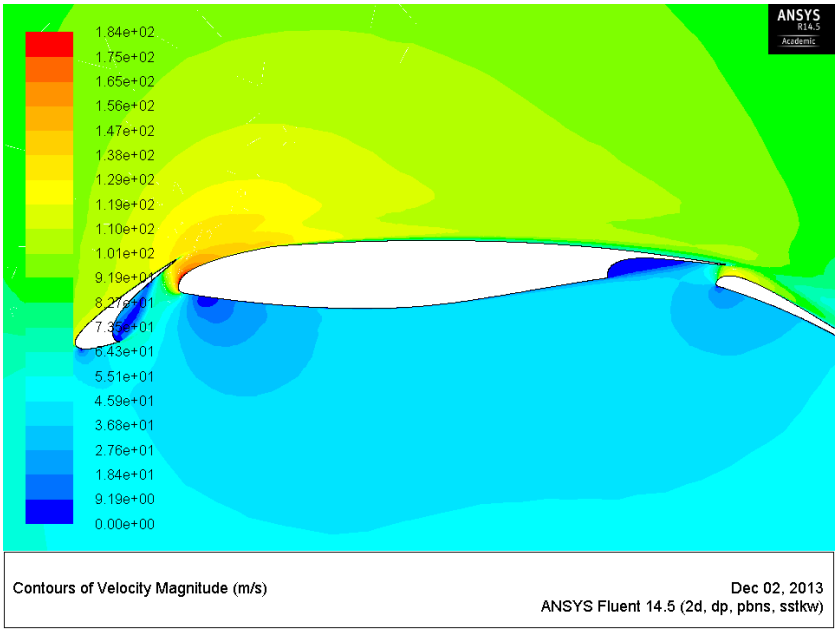


Figure 4.47: Velocity contours for TC12 profile in high lift configuration, k-omega SST turbulence model, 8.09 degrees, Re 2.95 million

4.4.8 Results (High Lift Configuration)

Figures 4.48 to 4.50 show the lift against angle of attack for the TC12 profile in high lift configuration. The data for the SA and k-omega SST turbulence models provide very similar results. In addition to the results, it was noted that data points at higher angles of attack, beyond those given in the results, did not converge, and were not included. For the SA turbulence model the maximum lift is underpredicted by 6.58% and the stall angle is overpredicted by 9.66%. The k-omega SST turbulence model shows an underprediction of maximum lift of 6.95% and the stall angle is also overpredicted by 9.66%.

Trends for lift prediction in results agree with those mentioned by (Rumsey and Ying, 2002) in which flow over a high lift airfoil is computed using a RANS code and the SA turbulence model. The result is also an underprediction of maximum lift.

Figure 4.50 shows the drag against angle of attack for the TC12 profile in high lift configuration. The SA turbulence model predicts slightly higher drag across the range of tested angles when compared to the k-omega SST turbulence model because of the different ways in which shear stress is handled by the two models, the latter using specific equations to calculate stress near bodies.

Maximum y^+ values for the simulations stayed below a value of 2 for all simulated angles of attack.

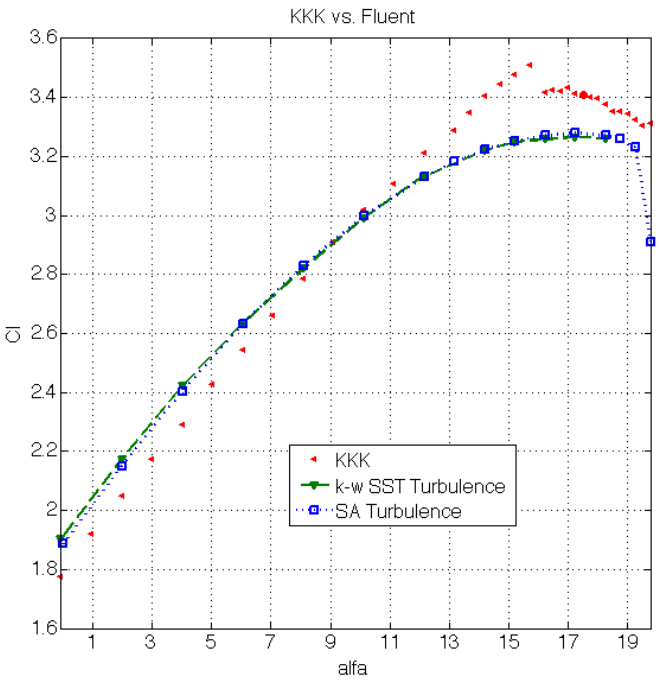


Figure 4.48: Cl vs. alfa for TC12 profile in high lift configuration, Re 2.95 million vs. KKK windtunnel data

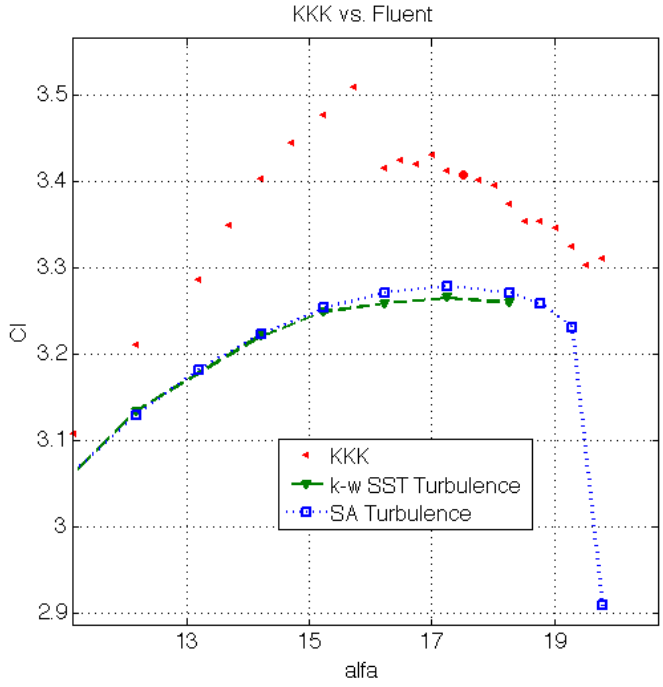


Figure 4.49: Cl vs. alfa showing stall for TC12 profile in high lift configuration, Re 2.95 million vs. KKK windtunnel data

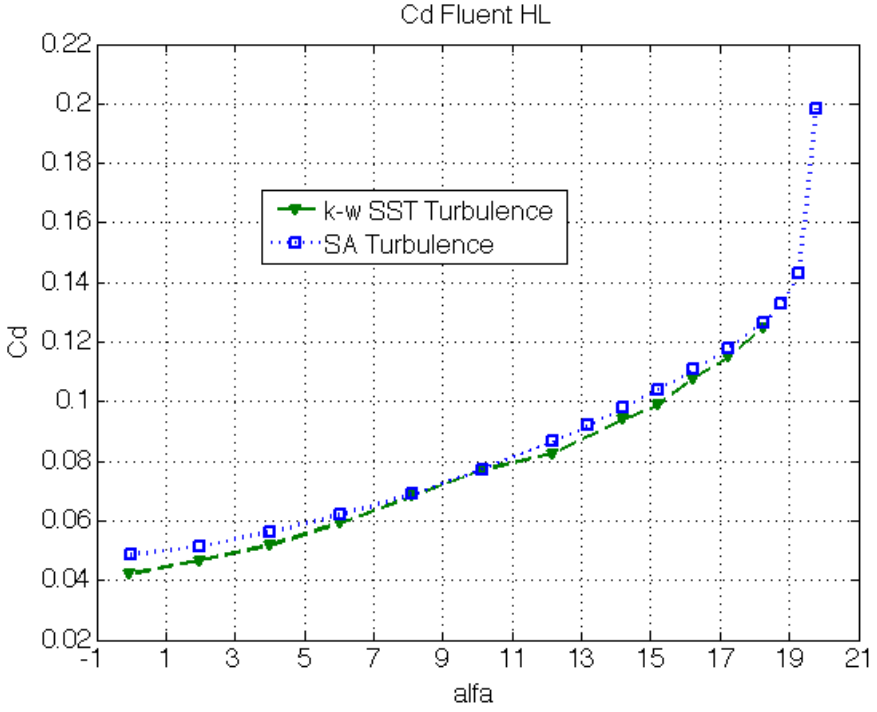


Figure 4.50: Cd vs. alfa for TC12 profile in high lift configuration, Re 2.95 million

Pressure Distributions SA Turbulence Model High Lift

Figure 4.51 to 4.53 show the pressure distributions of the simulations of the TC12 profile in high lift configuration when compared to the experimental data at an angle of attack of 8.11 degrees using the SA turbulence model. At this angle of attack the computational data agrees very well with the experiments at the main element and the slat, predicting, with subjective accuracy, the pressure along the elements. There is, however, a discrepancy at the region of the slat where pressure along the upper surface is over predicted. This discrepency implies that the velocity of air at the leading edge of the flap is higher in the computations than in the experiments. This error is related to the way in which the turbulence model handles the high velocity flow at the extreme curvature of the slat leading edge. The higher velocity flow causes an overall increase in lift generated by the slat.

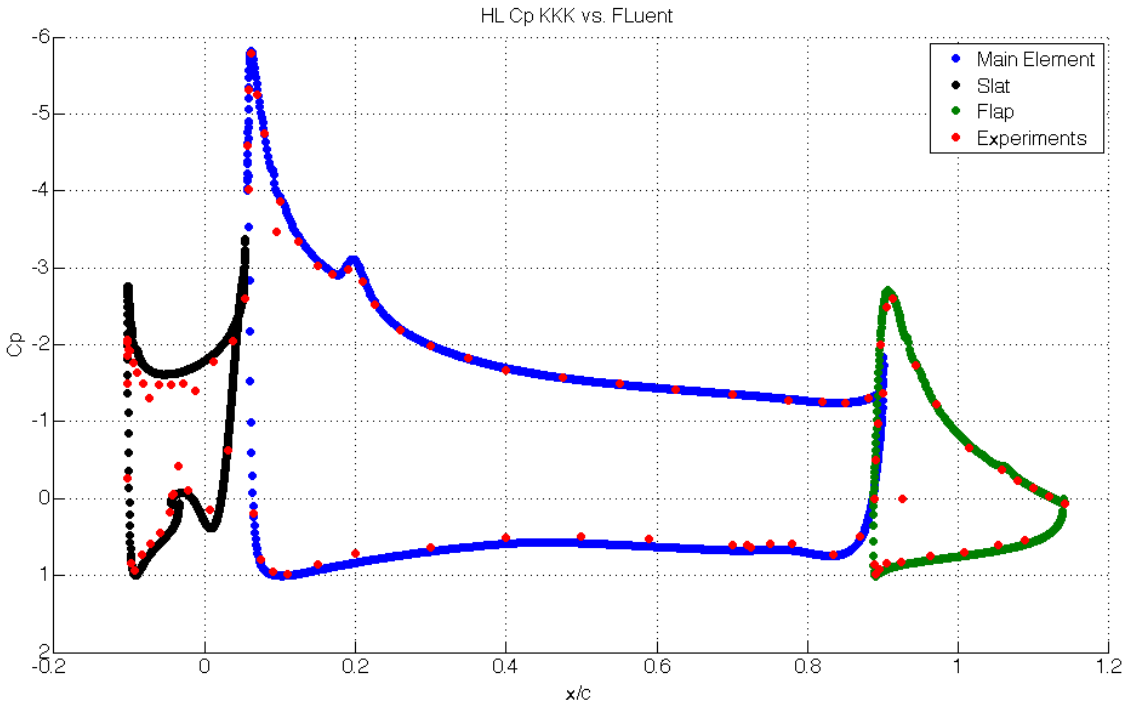


Figure 4.51: Pressure distribution for TC12 profile in high lift configuration, SA Turbulence Model vs. Windtunnel Data, 8.09 degrees, Re 2.95 Million

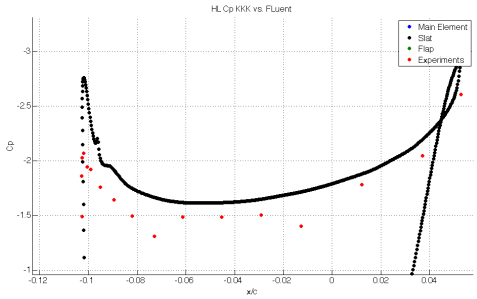


Figure 4.52: Pressure distribution at slat for TC12 profile in high lift configuration, SA turbulence model vs. windtunnel data, 8.09 degrees Re 2.95 million

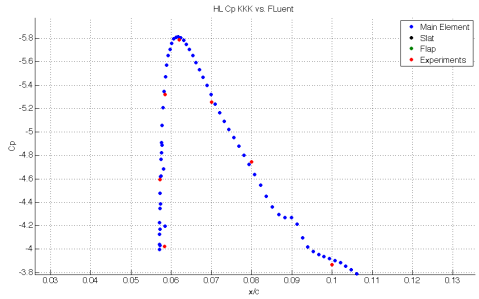


Figure 4.53: Pressure distribution peak for TC12 profile in high lift configuration, SA turbulence model vs. windtunnel data, 8.09 degrees Re 2.95 million

Pressure Distributions k-omega SST Turbulence Model High Lift

Figure 4.54 to 4.56 show the pressure distributions of the simulations of the TC12 profile in high lift configuration when compared to the experimental data at an angle of attack of 8.11 degrees using the k-omega SST turbulence model. When compared to the SA turbulence model not much difference is seen between the two sets of predictions. Both models overpredict slat pressure.

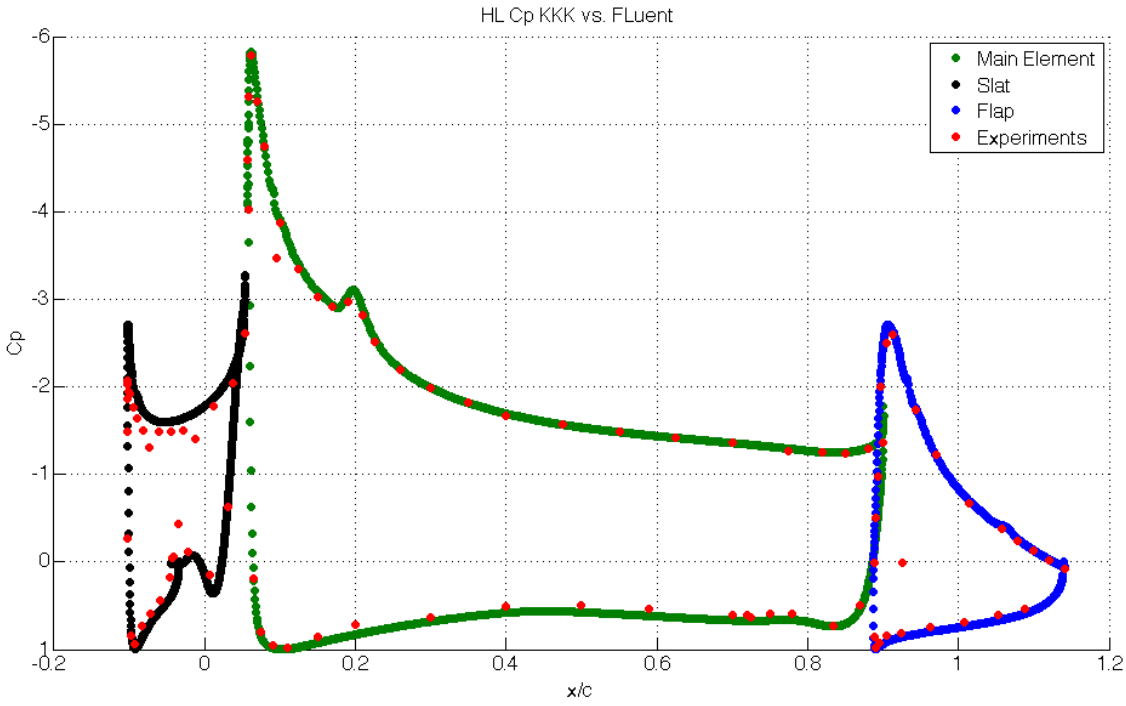


Figure 4.54: Pressure distribution for TC12 profile in high lift configuration, k-omega SST turbulence model, 8.09 degrees, Re 2.95 million

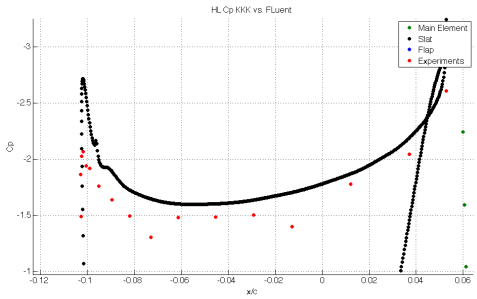


Figure 4.55: Pressure Distribution at slat for TC12 profile in high lift configuration, k-omega SST turbulence model vs. windtunnel data, 8.09 degrees, Re 2.95 million

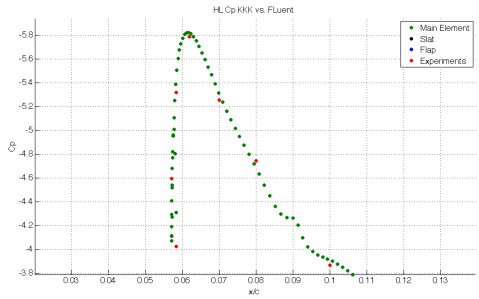


Figure 4.56: Pressure peak at slat for TC12 profile in high lift configuration, k-omega SST turbulence model vs. windtunnel data, 8.09 degrees, Re 2.95 million

4.5 Conclusion

Simulated data presented here is validated against experimental data as effectively as is possible with the given tools, time and computational constraints. The data presented in this section is from here on referred to as the 'baseline configuration' data. The data from the simulations will be used to draw comparisons from future simulations using the same aerodynamic tools and settings.

MSES predicted the lift against angle of attack of the TC12 profile in clean configuration very accurately, even being able to predict the stall angle quite accurately at a Reynolds number of 2.94 million. The pressure distribution of the TC12 profile in high lift configuration was predicted with reasonable accuracy at a matched lift coefficient value. There is however some inconsistency with pressure predictions at the slat due to coarse gridding required in that region. Results of lift against angle of attack were not able to predict stall due to issues of non convergence.

The ESDU method predicted the zero lift angle of attack very accurately but the maximum lift coefficient value was predicted quite poorly. Suggestions were explored on how to modify the methods to be able to use them to predict aerodynamic behaviour of modified geometries, but it was concluded that the methods are too reliant on a very accurate data bank to be modified with any success.

ANSYS Fluent was used to predict aerodynamic performance of the TC12 profile in clean and high lift configuration. Boundary and initial conditions were derived from the testing conditions used to produce the experimental data of the airfoil profiles. Airfoils were meshed in ANSYS Mesher and the RANS equations solved in Fluent based on the derived boundary conditions. Mesh independence was confirmed by gradually increasing mesh density and observing the effect on the results of lift and drag. Lift coefficient against angle of attack was compared to experimental data. Errors were noted in the type of stall behaviour observed for both profiles (a gradual trailing edge instead of a sharp leading edge stall as seen in experiments).

5 Aerodynamic Investigation 1

The first approach to aerodynamically optimise the TC12 profile for landing configuration is a 'zero order' optimisation approach. This process involves optimising the TC12 flap, by means of implementing the novel concept, in isolation (avoiding any effects of the slat and main element of the high lift system). XFOIL is used within a Genetic Algorithm to optimise the flap of the TC12 high lift profile in isolation. This is the first of two unique optimisation methods and data produced by this method is compared to the baseline data.

In this chapter the optimisation procedure is explained. This includes the MATLAB Genetic Algorithm Toolbox which runs the optimisation algorithm (*Global Optimization Toolbox*, 2014), and XFOIL which acts as the aerodynamic solver for each individual configuration produced. Upon successful validation of the tools, the optimisation process is explained in detail. Converged results are analysed and the best solution is selected. The optimised flap is incorporated into the full high lift system and analysed in MSES and Fluent. Solutions are compared to the baseline results. Results from Fluent deemed the optimisation unsuccessful from an aerodynamic point of view due to losses not accounted for along the main element.

5.1 Flap Optimisation Routine

The flap optimisation selected is one in which the aforementioned novel concept is optimised, via a numerical optimisation, in order to achieve a solution geometry which performs aerodynamically better than the baseline geometry.

Figure 5.1 shows the system diagram of the optimisation. The three components of the flow chart are explained in the three sections that follow. In the diagram *GA* is the MATLAB Genetic Algorithm (section 5.1.1) which handles the optimisation procedure, *Geom* is the Geometry Function (section 5.1.2) which creates new geomtries, *XFoil* is the program XFOIL[5] (herein referred to as the Aerodynamic Solver (section 5.1.3) which is used to analyse the geometries and *Fit* is the multi-objective Objective Function (section 5.1.4) used to determine the feasibility of analysed solutions. The solutions are fed back into the MATLAB Genetic Algorithm where new populations are created and solutions trends monitored. Upon convergence the GA stops and the set of most optimised solutions is provided.

[5] An interactive panel code used for analysing subsonic airfoils, (*XFOIL Subsonic Airfoil Development System*, 2013)

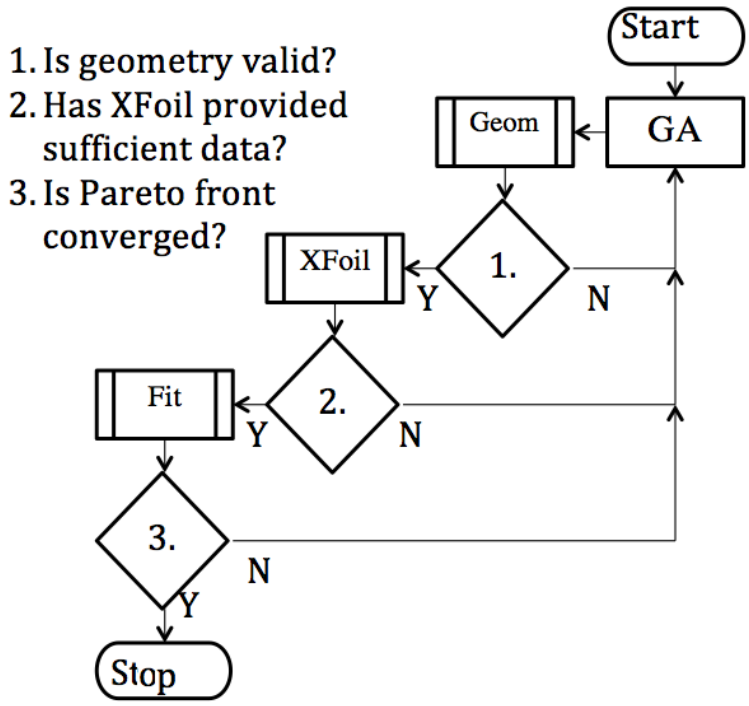


Figure 5.1: System diagram of the optimisation routine

Upon successful completion of the validation of the tools as seen in appendix E the MATLAB Genetic Algorithm tool was implemented to solve the problem as posed.

5.1.1 Genetic Algorithm

For this optimisation the MATLAB genetic algorithm provides the design variables to the first of the three modules and in return receives the output variables. The GA calls the function as a black box with specific generations. The first generation has a semi-random spread across the design space to attempt to sparsely cover all possible design directions. Subsequent generations are produced using a set of genetic mutations and then run by the GA. The GA recreates a fitness landscape of n dimensions where n is the number of design variables. Each population tends closer to the global minimum and when the distance between populations falls below the convergence criteria the solution is produced.

5.1.2 Geometry Function

The geometry function takes the four design variables and generates a geometry from them. This geometry is checked for any errors and if successful it is passed to the next module (the aerodynamic solver). If unsuccessful, the aerodynamic solver and objective function are avoided and a very large number is returned to the GA.

The flap extension is designed to extend out of the leading edge of the flap. During cruise the flap extension will be stored within the flap itself. Figure 5.2 shows the function input variables and a sample output geometry of the TC12 flap leading edge with modifications. Only the

leading edge of the TC12 flap is shown for clarity. The four variables were chosen to minimise the number of parameters required for the optimisation yet to provide sufficient variables to create unique geometries that fulfil the specification of the flap extension concept.

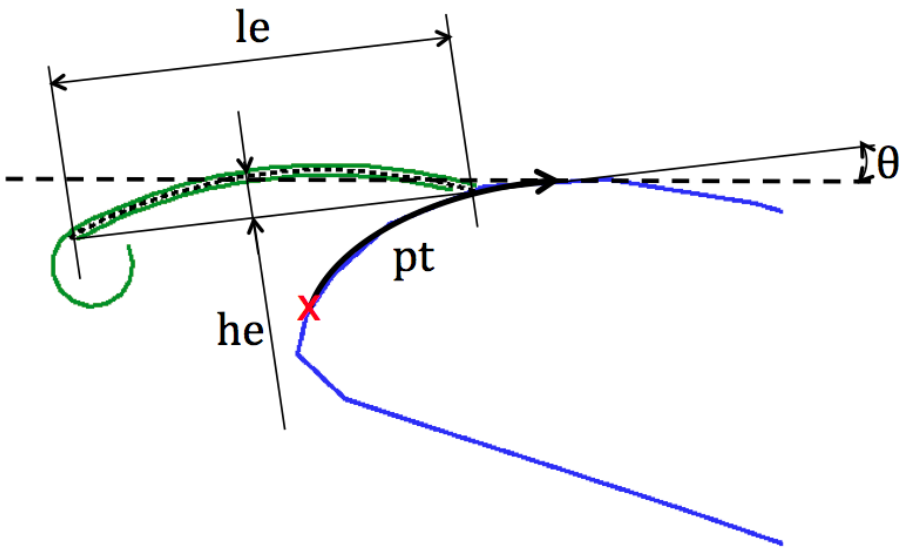


Figure 5.2: Selected design variables for optimisation

Where *le* is the length of the flap extension, θ is the angle from horizontal that the flap extension is directed downwards, *he* is the height above the flap extension length at which the maximum camber occurs (this point is at exactly 50% of the length), *pt* is a point along the leading edge of the flap at which the flap extension centreline extends from.

Design Space Constraints

To obtain a feasible solution the design space needs to be constrained within a certain region. Constraints arise from design requirements and need to be handled accordingly. Figure 5.3 shows graphically the implicit constraints that are calculated based on the input variables. The diameter of the leading edge ball and the thickness of the flap is based on the designed implemented by F. and Fullmer (1947).

The kinematic design requirement for the retracted position of the flap extension is shown in the figure as the red dotted line, the extension and retraction of the concept follows a circular arc of motion. Any concepts generated by the geometry tool that are not able to fulfil the kinematic constraints are automatically rejected.

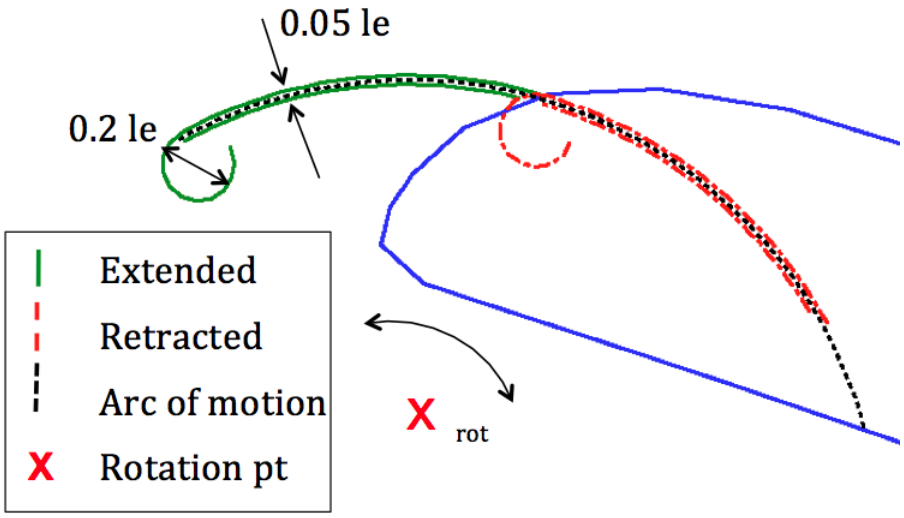


Figure 5.3: Constrained optimisation variables

Variables are constrained using feasible regions that a wide variety of configurations can be tested but also to minimise the design variables to known feasible values. Variable constraints are selected as:

$$
\begin{aligned}
0 < \mathbf{he} < 0.025 \\
0 < \mathbf{le} < 0.07 \\
0 < \mathbf{al} < 50 \\
5 < \mathbf{pt} < 40
\end{aligned}
$$

5.1.3 Aerodynamic Solver

XFOIL is used to solve the aerodynamic solution of each new configuration generated by the geometry function. XFOIL cannot solve airfoils where there are sharp changes in continuity (high panel angles), thus the geometry as seen in figure 5.2 is splined to provide continuity and better convergence. A similar approach is performed by Thomson (1996). The spline acts as a simulated steady shear layer produced by separations which can be approximated as a steady wall. XFOIL is programmed to run off a script that is generated by MATLAB prior to calling the aerodynamic solver and is unique for each configuration. The script tells XFOIL to:

- Turn off XFOIL graphics options.
- Load current airfoil configuration.
- Apply three filtering steps to remove any major discontinuities on the airfoil geometry.
- Repanel airfoil to account for poor geometry creation (160 panels).
- Change simulation Reynolds number to 2.95 million.

- Change maximum iterations per angle of attack to 100.
- Start polar accumulation for the data points that follow.
- Collect lift a drag data for a series of angles of attack and write to file.
- Save and exit.

Solutions are read by the MATLAB code and then subsequently analysed using the objective function. If the MATLAB function finds no data or incomplete data for the given airfoil that data point is discarded.

5.1.4 Objective Function

Equation (5.1) is the problem being solved by the GA. The problem is to minimise the objective function using real numbers as input. Equations (5.2) - (5.4) are the three objective functions to be solved for. Namely: *maximising the maximum lift coefficient*, *maximising the maximum lift to drag ratio* and *maximising the stall angle*. These three figures are chosen because:

- Maximum lift is a problem for current single slotted flap systems as per Rudolph (1996b).
- Lift drag ratios are a good figure of merit when incorporating drag into the objective function the ratio is a key component in measuring total range of an aircraft. There are also increased benefits of higher L/D (Meredith, 1993) for aircraft.
- Higher stall angles lead to more protection of the high lift system near stall. Higher stall angles lead to higher maximum lift coefficients.

Equation (5.5) represents the input variables for optimisation. Input variables are explained in the next chapter on Design Constraints.

$$min(\mathbf{F}_{obj}(x)), (x \in \mathbb{R}) \tag{5.1}$$

$$\mathbf{F}_{obj1}(\mathbf{x}) = -C_{L_{max}} \tag{5.2}$$

$$\mathbf{F}_{obj2}(\mathbf{x}) = -\frac{L}{D}_{max} \tag{5.3}$$

$$\mathbf{F}_{obj3}(\mathbf{x}) = -\alpha_{stall} \tag{5.4}$$

$$\mathbf{x} = \begin{Bmatrix} he \\ le \\ al \\ pt \end{Bmatrix} \tag{5.5}$$

5.2 Solution

The optimisation converged after the *average distance between populations* residual dropped below 0.0001. This occurred after *106 generations* with a total of *6 418 function evaluations*. On a Core 2 Duo machine with 8Gb RAM- this equated to about three days of processing time.

Figure 5.4 shows the Pareto front of converged solutions. The Pareto front is a surface of optimum points that corresponds to optimum solutions of individual criteria.

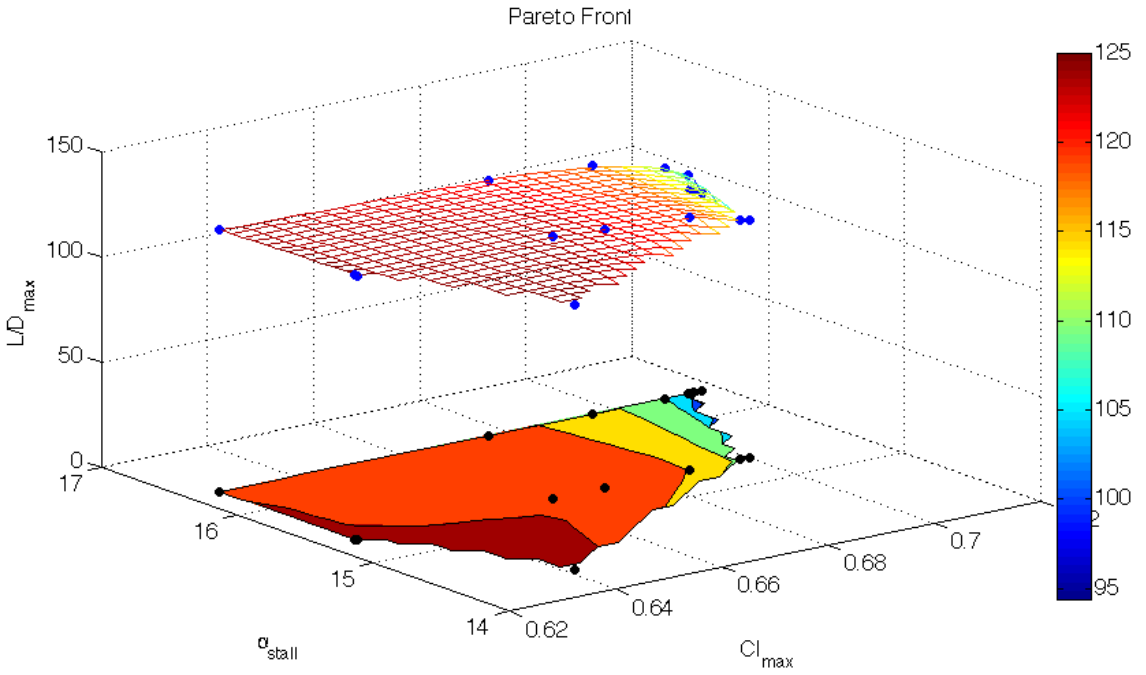


Figure 5.4: Pareto front of optimised solutions

The optimised solution selected is from the central region of the pareto front and is a good tradeoff of the three selected objective functions. The final solution has the following input variables:

he: 0.0055
le: 0.053
al: 19.28
pt: 22.99

Figure 5.5 shows the solution selected front the pareto front. The pareto front shows a series of data that is more favourable than the results when run in XFOIL alone without filtering. The airfoils analysed by XFOIL within the GA are thinned out slightly because of the filtering step. This provides a more robust set of results to the GA. The method of optimisation is still effective as trends amongst configurations still hold. The geometric approximation sent to the

XFOIL calculation, named 'Xfoil', can be seen in the figure.

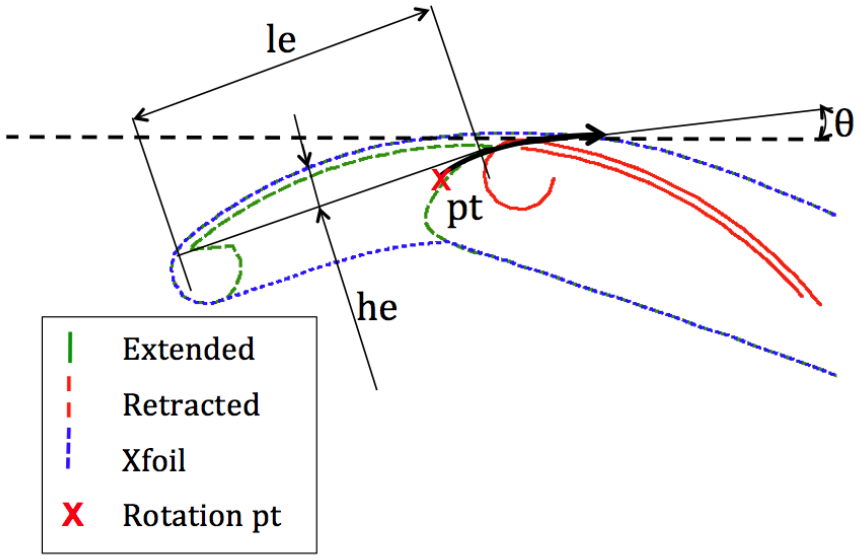


Figure 5.5: Geometry of solution of zero order flap optimisation

5.2.1 XFoil Result

Figure 5.6 and 5.7 show the coefficient of lift and drag against angle of attack (respectively) for the optimised TC12 flap compared to the baseline flap. These figures are for the flap alone and do not include effects of the full high lift system. The reason for the negative angle of attack in the figures is because the zero angle of attack is taken as the setting angle of the flap for landing (see fig. 3.3 for clarification if required).

The optimised airfoil provides a higher maximum lift coefficient and lower drag at high angles of attack. Stall angle increases from -12 degrees to -10 degrees (*16.7% increase*), maximum lift coefficient increases from 0.5426 to 0.6045 (*11.4% increase*) and maximum lift drag ratio increases from 94.8 to 107.4 (*13.3% increase*).

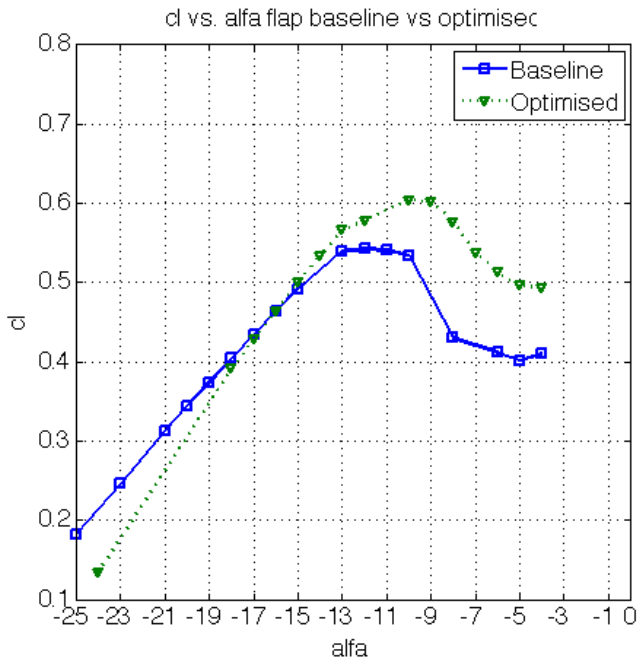


Figure 5.6: Cl vs. alfa of TC12 flap optimised solution vs baseline in XFOIL

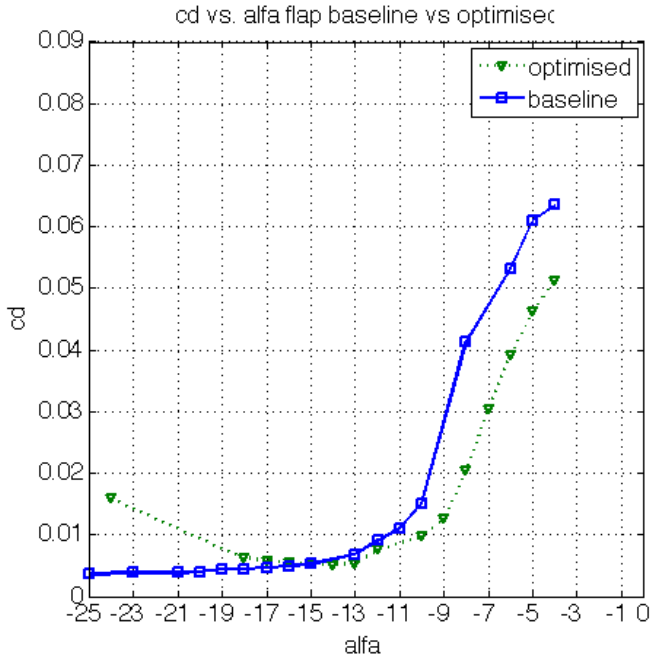


Figure 5.7: Cd vs. alfa of TC12 flap optimised solution vs baseline in XFOIL

5.2.2 MSES Result

MSES is used to determine the characteristics of the zero order optimised flap when implemented into the full high lift system. The same gridding parameters as used in the validation

are implemented for the analysis of the zero order optimised solution. The grid across the flap is seen in figure 5.8, the grid upstream of the flap is the same as in the Validation section.

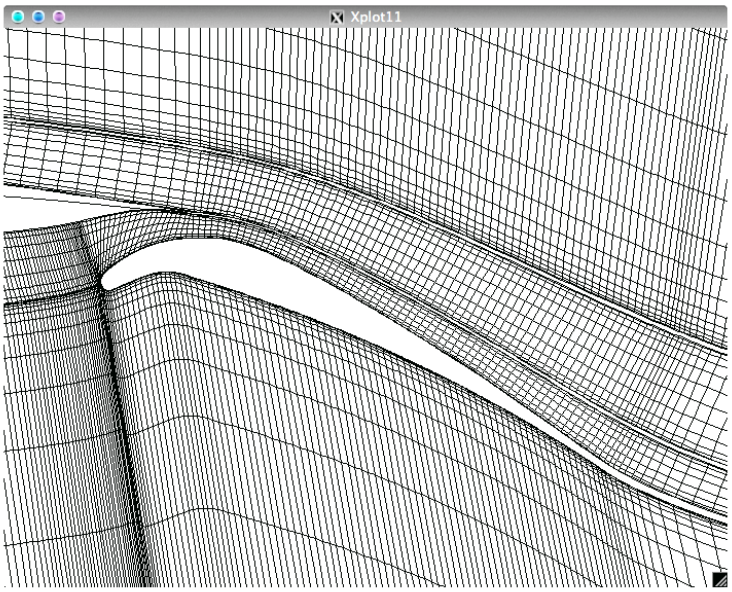


Figure 5.8: Gridding at the flap for the zero order optimised extension

Figure 5.9 and 5.10 show the lift and drag against angle of attack for the zero order optimised system compared to the baseline solution. According to the figures the optimised concept performs best at lower angles of attack, providing decreased drag and increased lift between 0 and 6 degrees. At angles of attack beyond 6 degrees the new configuration is found to be less favourable than the baseline because as the angle of attack increases past a critical value the flap is more susceptible to separation due to increased camber. This increased camber causes a loss of lift at the trailing edge of the flap causing the flap extension to be the primary source of lift at the trailing edge. This causes an overall decrease in performance in this region.

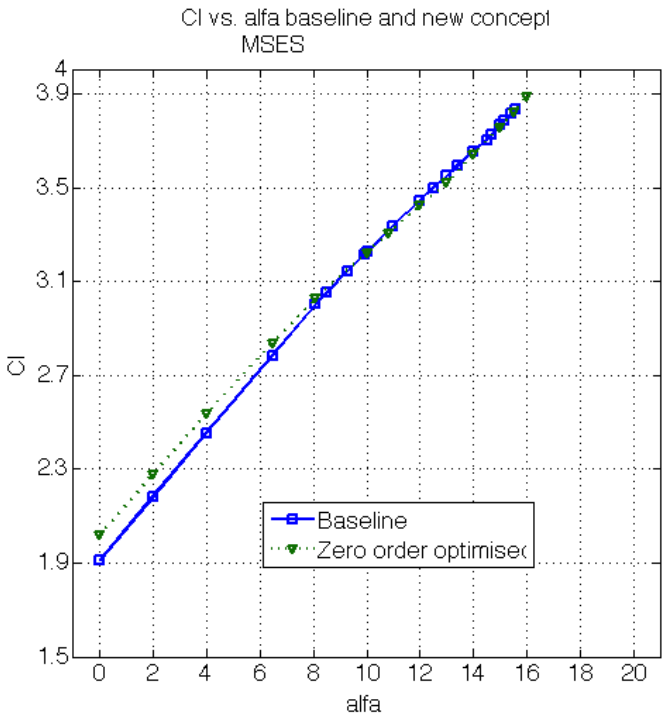


Figure 5.9: Cl vs. alfa of TC12 profile in high lift configuration optimised solution vs baseline in MSES

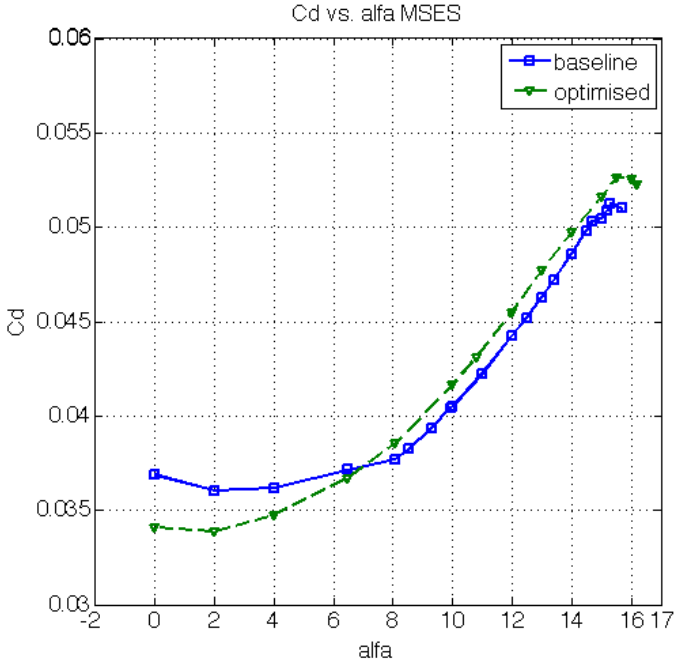


Figure 5.10: Cd vs. alfa of TC12 profile in high lift configuration optimised solution vs baseline in MSES

In figure 5.11 the pressure distribution across the full high lift system for both the optimised and baseline configuration analysed in MSES at the same angle of attack is shown. From this figure it can be seen that upstream of the flap, the slat and leading edge of the main element have a decreased static pressure (increase in lift) along the upper surface. Figure 5.12 shows the effect of the modifications to the flap alone by means of looking more closely at the same pressure distribution, a slightly lower pressure peak is shown but there is a large lift generating region along the flap extension which thus increases local lift across the flap alone. The lower pressure peak is due to an overall lower velocity at in the vicinity x/c 0.9. At a Cp value of -1.4 an inflection point is seen on the pressure distribution. This is the point where the flap extension attaches to the flap of the TC12 profile. Due to a discontinuous geometry there is a discontinuity in the pressure distribution.

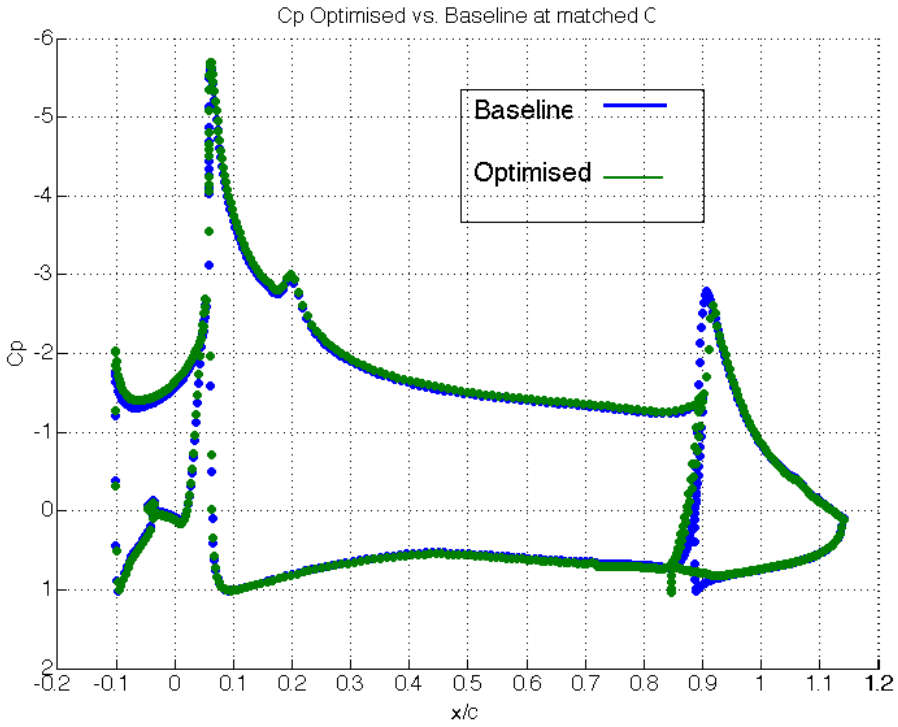


Figure 5.11: Pressure distribution of TC12 profile in high lift configuration optimised solution vs. baseline in MSES, baseline matched Cl, Re 2.95 Million

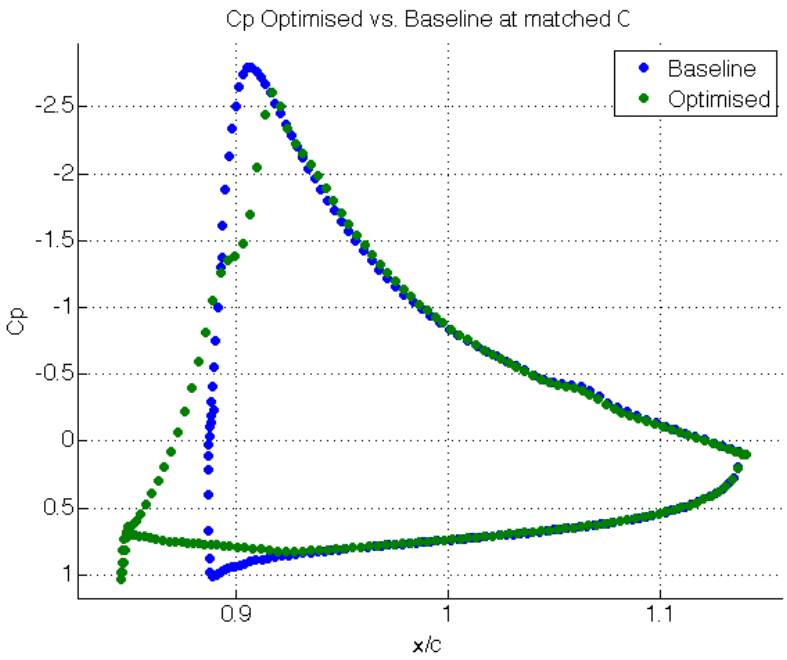


Figure 5.12: Pressure distribution of TC12 high lift configuration flap at 8.09 degrees optimised solution vs. baseline in MSES, baseline matched Cl, Re 2.95 million

5.2.3 Fluent Result

ANSYS Fluent is used to analyse a more realistically representative geometry of the zero order optimised extension when implemented into the high lift system.

The same gridding guidelines are used as established in the Validation section. Likewise the same conditions and settings are also used. The only change in this regard is a modification of the mesh at the area near the leading edge of the flap. This modified region is seen in figure 5.13. The flap and extension has 35 mesh layers within the boundary layer. The final mesh has 277 888 nodes and 317461 elements.

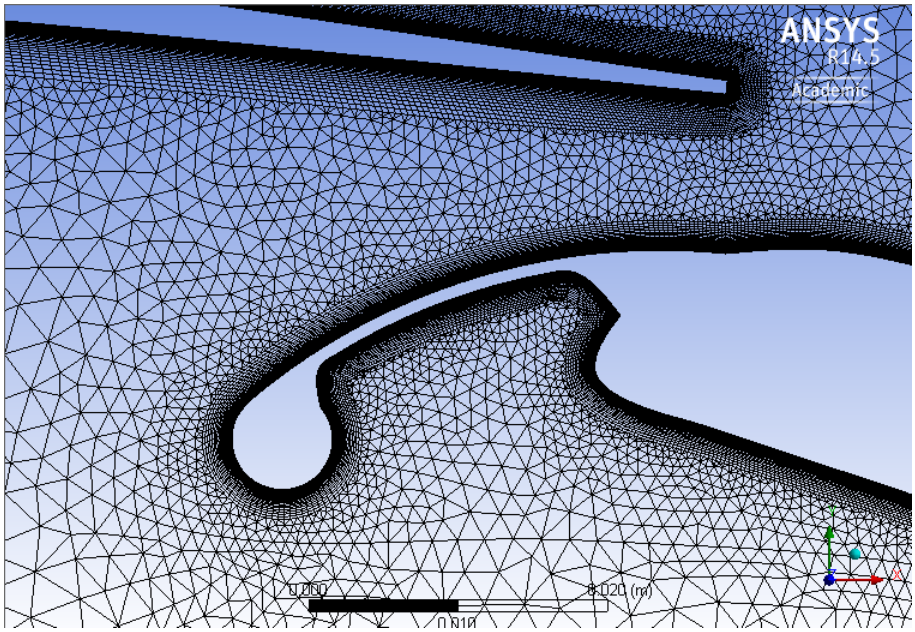


Figure 5.13: Mesh at the leading edge of the TC12 flap showing the implementation of the new concept

Figure 5.14 shows the lift against angle of attack for the zero order optimised concept against the baseline data in ANSYS Fluent. The optimised concept produces less lift than the baseline solution for all angles of attack. By looking at the stall point in figure 5.15 it is seen that the optimised concept has a lower stall angle and lower maximum lift coefficient. This is quantified as a decrease of maximum lift of 2.1% and a decrease in stall angle of 5.9%. The loss of lift near stall is attributed to the very high camber caused by the flap extension in conjunction with the flap of the TC12 profile. At higher angles of attack the increased local camber of the flap is more prone to separation. This separation causes the flap to stall earlier than it normally would, reducing circulation around the full system causing the decrease in stall observed.

Figure 5.16 shows the drag against angle of attack for the zero order optimised concept against the baseline data in ANSYS Fluent. Drag matches quite closely but upon close inspection the optimised solution produces higher drag at all angles of attack before stall. After stall the zero order optimised concept fairs better by producing less drag.

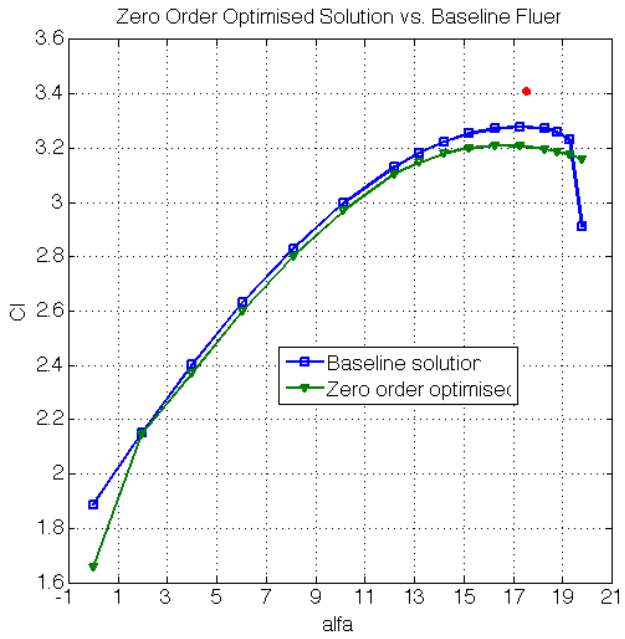


Figure 5.14: Cl vs. alfa of TC12 high lift configuration zero order optimised solution vs. baseline in Fluent SA turbulence model, Re 2.95 Million

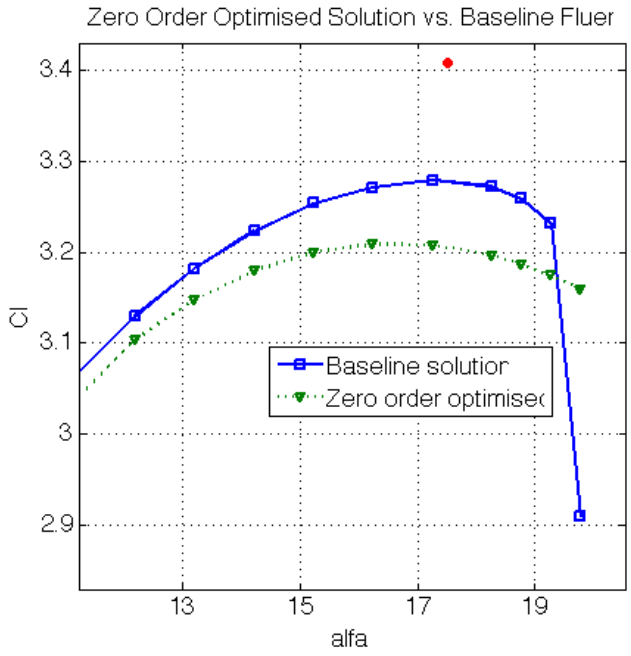


Figure 5.15: Cl vs. alfa of TC12 high lift configuration at stall zero order optimised solution vs. baseline in Fluent SA turbulence model, Re 2.95 Million

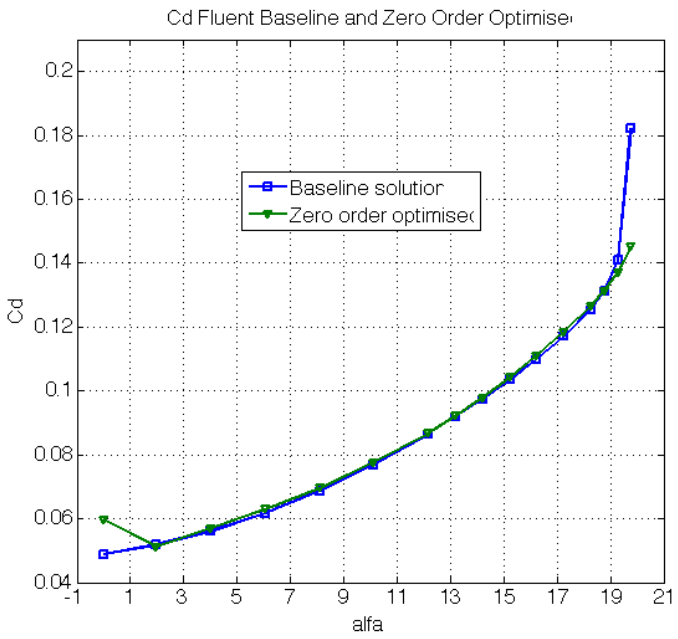


Figure 5.16: Cd vs. alfa of TC12 high lift configuration zero order optimised solution vs. baseline in Fluent SA turbulence model, Re 2.95 Million

Figure 5.17 shows the pressure distribution of the zero order optimised concept compared to the validated results of the TC12 profile. Unlike in MSES there is no change in pressure upstream of the new concept. The pressure distribution is qualitatively similar for both the optimised concept and the baseline solution, this leads a conclusion that the optimised concept has not increased circulation around the entire system. Figure 5.18 shows the pressure distribution on the flap alone showing, once again, a decreased pressure peak but an increased lifting area along the flap extension. The pressure distribution along the flap extension at about x/c 0.9 shows a sudden change in pressure. This is because, at the inflection point, there is a junction between where flap extension and the flap itself where the geometry is not continuous.

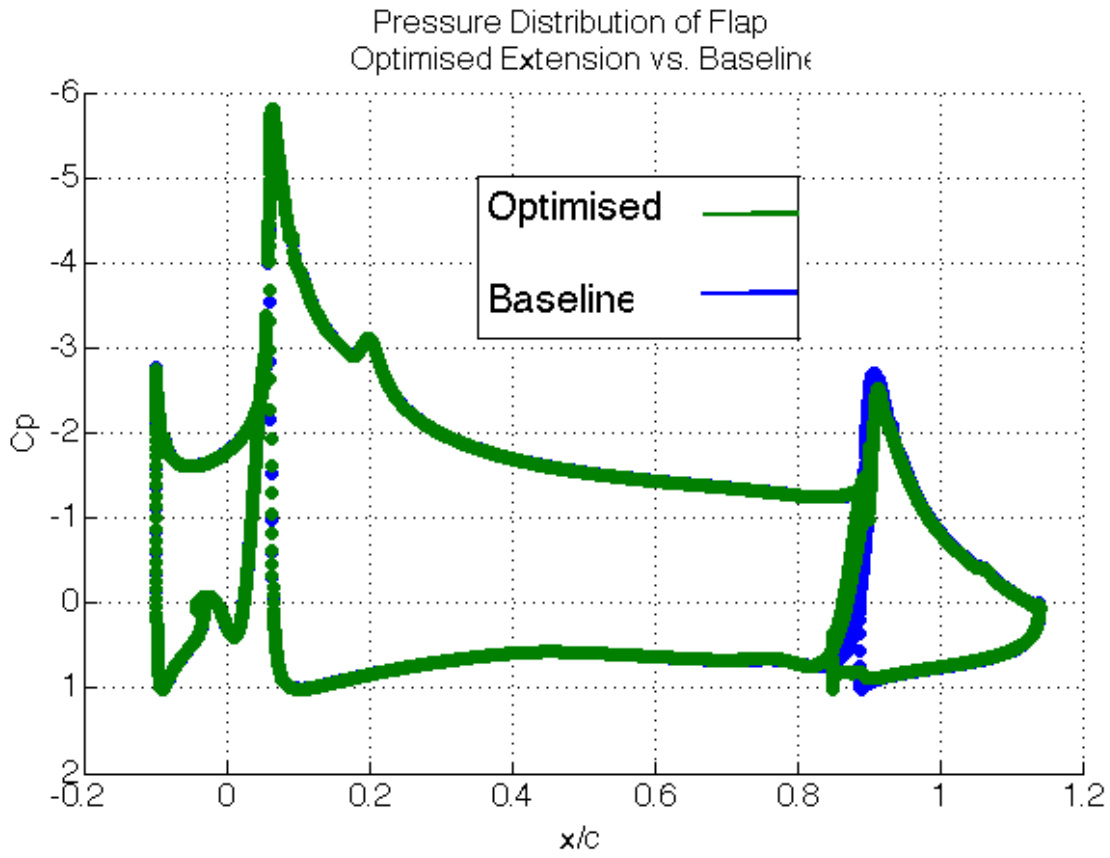


Figure 5.17: Pressure distribution of tc12 high lift configuration optimised solution vs. baseline in Fluent SA turbulence model, 8.09 degrees, Re 2.95 million

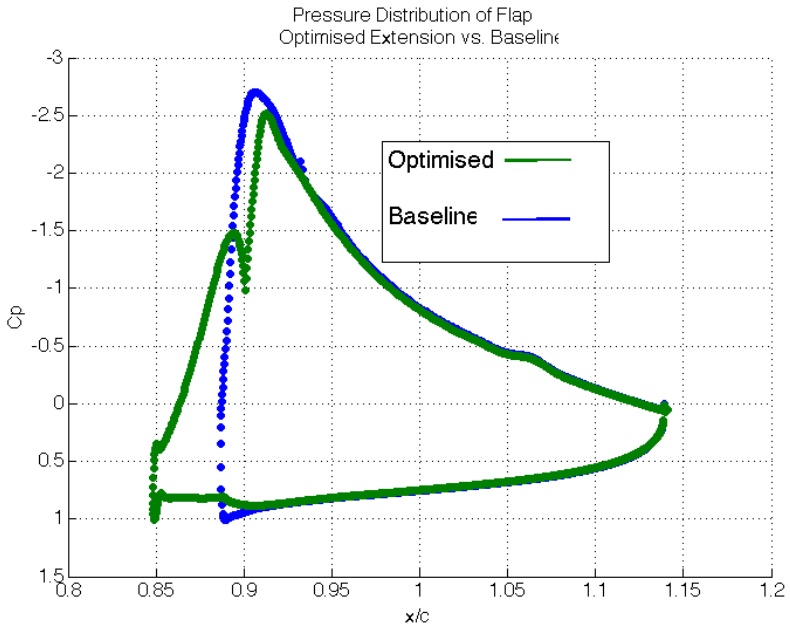


Figure 5.18: Pressure distribution at flap of TC12 high lift configuration optimised solution vs. baseline in Fluent SA turbulence model, 8.09 degrees, Re 2.95 million

The optimised concept, as analysed in ANSYS Fluent showed a slight decrease in lift within the linear region of the lift curve slope and a decrease in stall angle and maximum lift produced. There is a large local increase in lift at the flap, proving that the optimisation method was successful.

However, the Coanda effect is observed within the flow field of the trailing edge underneath the spoiler cove (figure 5.19). The Coanda effect is the tendency of a fluid jet to be attracted to a nearby surface. In this case, the fluid flow from the pressure side of the main element airfoil, which would normally be part of a freestream flow, over the leading edge of the flap of the TC12 profile now has the tendency to be attracted to the geometry of the flap extension due to its inclusion within the flow field. The flow attracted to the flap extension has to accelerate along the curved surface, causing a low pressure suction (lifting) region along the flap extension. This suction reduces the recirculation region within the spoiler cove causing a decrease in pressure with span at the trailing edge of the main element (figure 5.20). The overall effect is a net loss of lift along the main element airfoil due to a change is the pressure difference between the upper and lower surfaces.

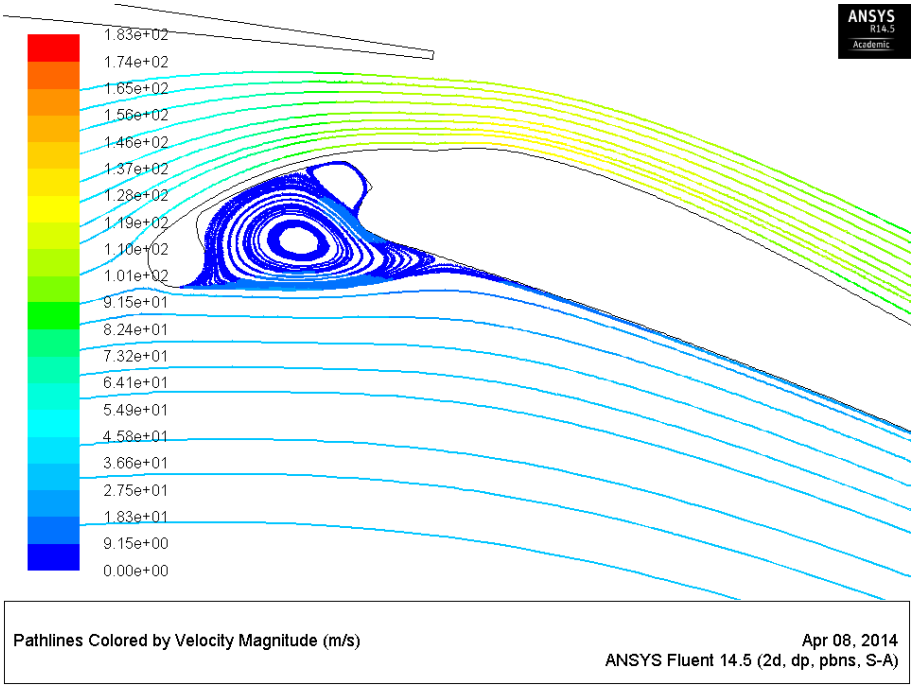


Figure 5.19: Streamlines around trailing edge of zero order optimised flap extension showing the Coanda effect

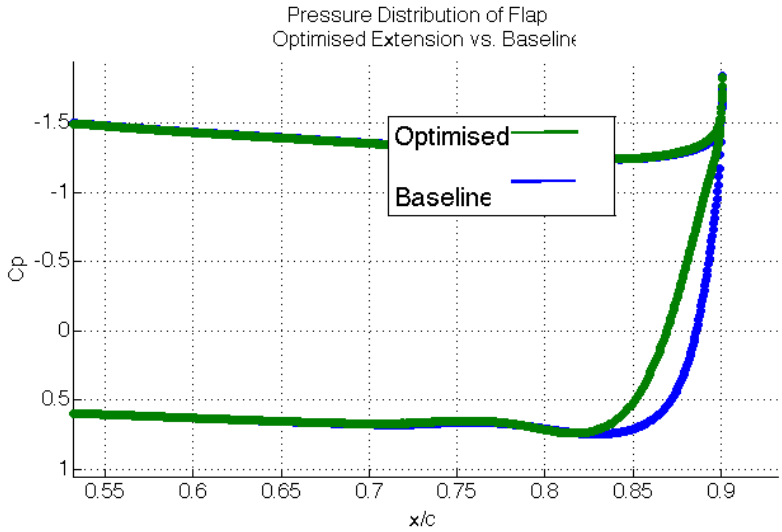


Figure 5.20: Pressure coefficient along span at the trailing edge of the main element of the TC12 profile comparing zero order optimised solution to the baseline

5.3 Smoothed Geometry

Using the zero order flap optimisation solution as a baseline the geometry of the solution was modified slightly in order to attempt to increase the performance of the concept without having to run a new optimisation. In figure 5.18 it is identified that the discontinuous pressure peak is an area which can be fixed easily by making the junction between the flap and the extension

continuous. The geometry is modified and then subsequently meshed and analysed as before (mesh of the concept seen in figure 5.21). The mesh has 278 410 nodes and 318 025 elements.

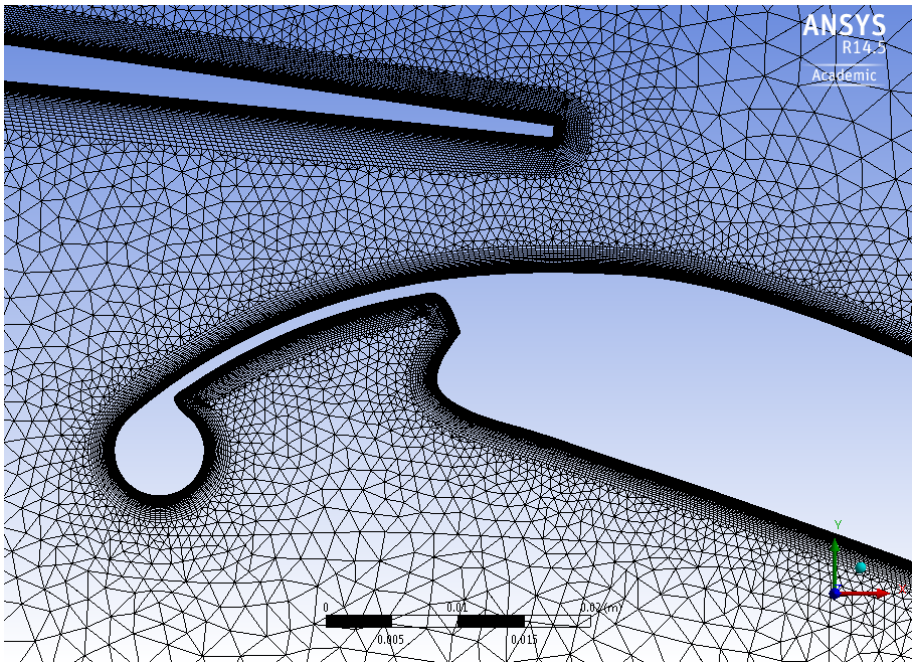


Figure 5.21: Mesh at the leading edge of the TC12 flap showing the meshing around the smoothed concept

The geometry is tested at an angle of attack of 8.09 degrees, in order to compare it with the baseline solution. Lift and drag of the smoothed geometry are:

Cl: 2.8209 (0.3% worse than baseline)

Cd: 0.0678 (1.5% better than baseline)

The pressure distribution of the full system and the flap alone (in figures 5.22 and 5.23) show the same trends as before where not much change has occurred at the main element and slat. The *kink* in the pressure distribution is averted but the peak pressure is lower than that of the original zero order optimised concept.

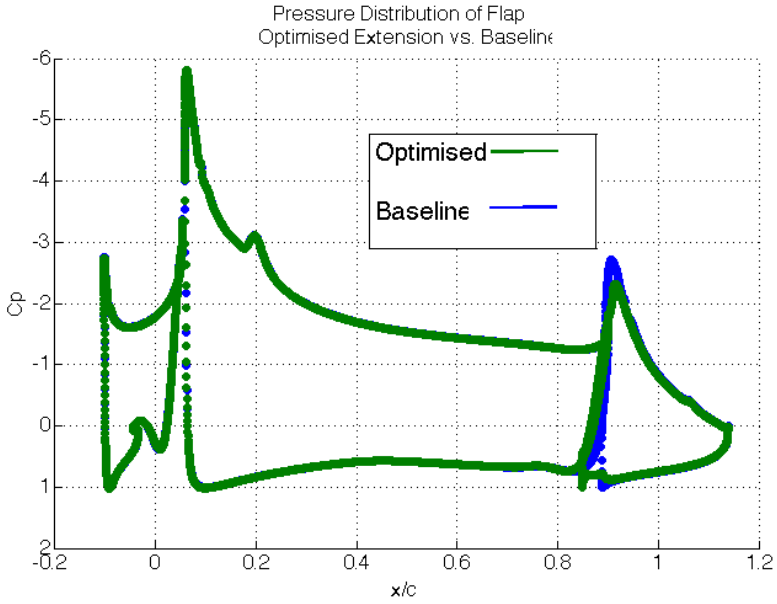


Figure 5.22: Pressure distribution of TC12 high lift configuration optimised solution with smoothed geometry vs. baseline at 8.09 degrees in Fluent, SA turbulence model, Re 2.95 Million

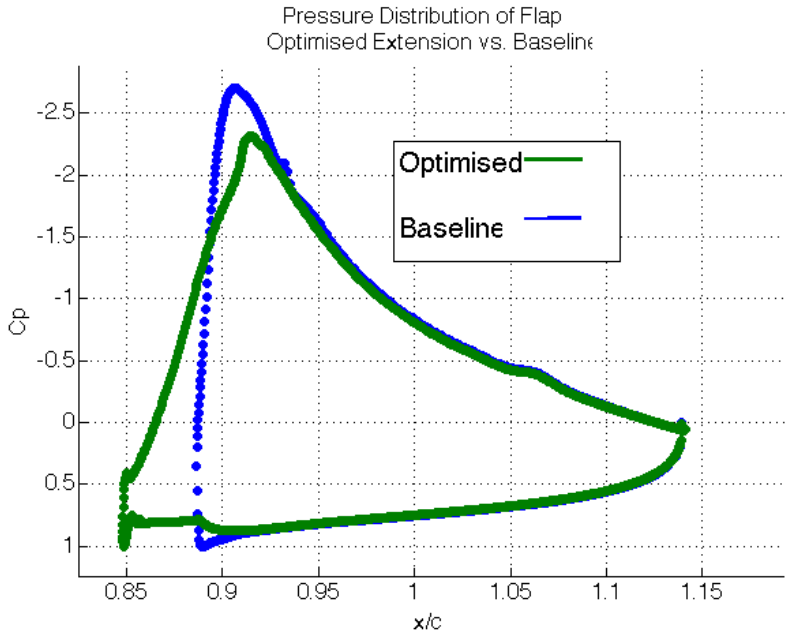


Figure 5.23: Pressure distribution of TC12 high lift configuration optimised solution with smoothed geometry vs. baseline at 8.09 degrees in Fluent, SA turbulence model, Re 2.95 Million

The smoothed version of the concept performs marginally better than unsmoothed concept at an angle of attack of 8.09 degrees. The smoothing was a success in this regard but does provide a geometry that is not feasible based on the proposed kinematics of the concept. The concept

still fares worse aerodynamically than the baseline TC12 concept and thus it is not pursued further.

5.4 Slotted Geometry

A second modification is performed to observe its efect on the zero order optimised solution. A slot is added to the optimised solution in an attempt to increase the velocity of the flow in the region of the leading edge of the flap. This solution should be able to minimise the pressure loss at the leading edge of the TC12 flap by making use of the slot effect (Smith, 1975). The size of the slot is the same as the thickness of the spoiler.

The same gridding guidelines are used as established in the Validation section. Likewise the same conditions and settings are also used. The only change in this regard is a modification of the mesh at the flap and the extension. This modified region is seen in figure 5.24. The flap and extension has 19 mesh layers within the boundary layer and the flap has 25 layers in the boundary layer mesh. The reason for the low number of elements is because the geometry tended to *crush* the elements of the mesh when more layers were used due to the proximity of the two elements to each other. The final mesh has 306 196 nodes and 397 203 elements.

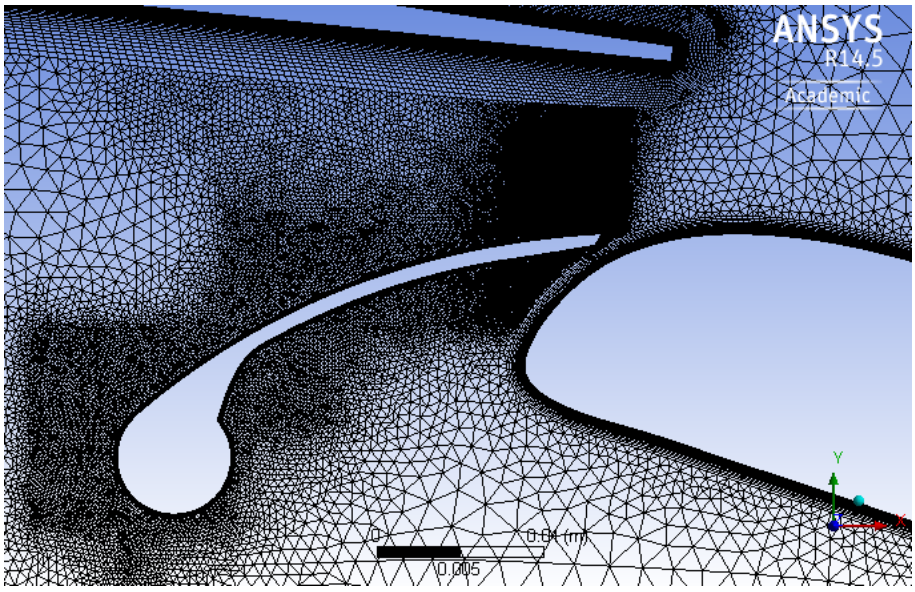


Figure 5.24: Mesh at the leading edge of the TC12 flap showing the meshing around the slotted concept

The geometry is tested at an angle of attack of 8.09 degrees to compare it with the baseline solution. Lift and drag of the slotted geometry are:

Cl: 2.8015 (1% worse than baseline)

Cd: 0.0687 (0.2% better than baseline)

Figure 5.25 shows the pressure distribution of the slotted geometry compared to that of the baseline TC12 high lift configuration. By looking closely at the flap pressure distribution in figure 5.26 it can be seen that the optimised solution still has a lower pressure peak than the baseline- thus the slow was not effective. Figure 5.27 shows the large recirculations as well as a separation bubble on the leading edge of the flap which stop the freestream flow from behaving as it would in the baseline concept.

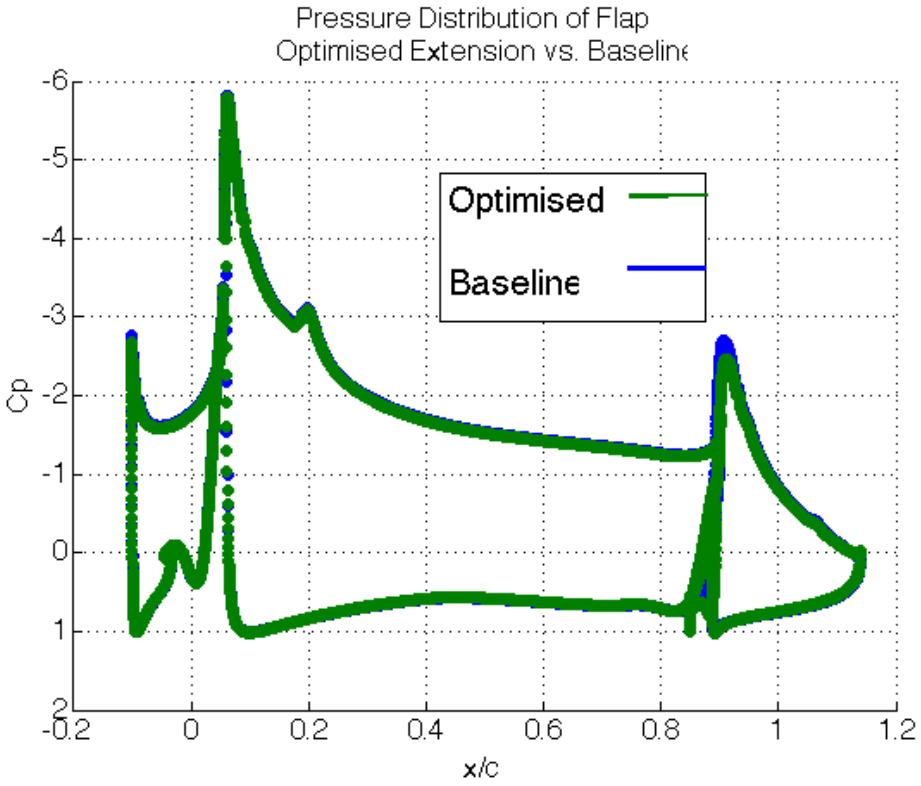


Figure 5.25: Pressure distribution of TC12 high lift configuration optimised solution with slot vs. baseline at 8.09 degrees in Fluent, SA turbulence model, Re 2.95 Million

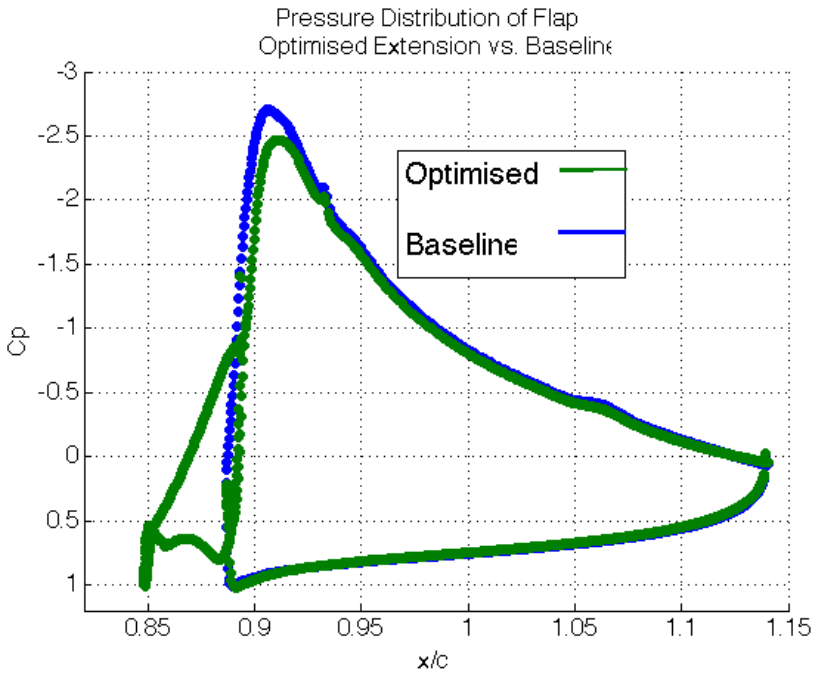


Figure 5.26: Pressure distribution of TC12 high lift configuration optimised solution with slot (flap alone) at 8.09 degrees vs. baseline in Fluent, SA turbulence model, Re 2.95 Million

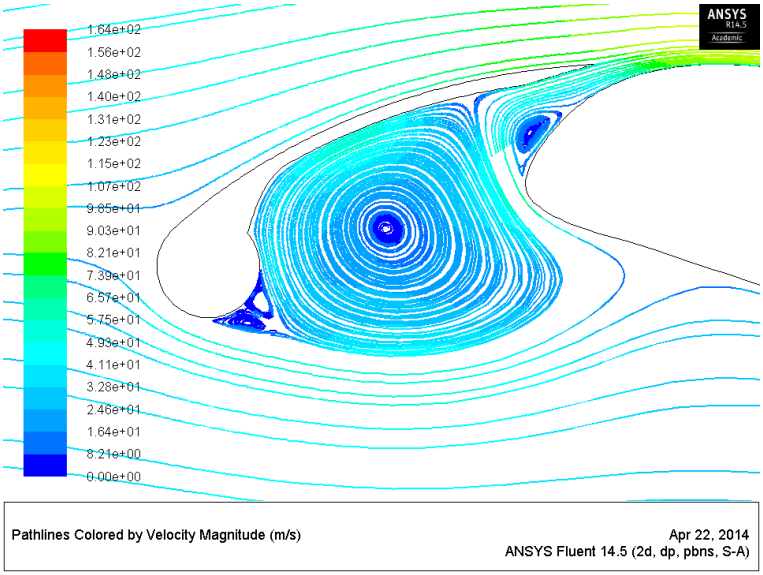


Figure 5.27: Recirculation regions on new concept extension with slot

The effect of recirculations on the slotted geometry shows that, for this slot configuration, the concept is infeasible due to the presence of many complex recirculations in the vicinity of the slot. Overall there is a decrease in performance when compared to the baseline.

5.5 Findings

An optimisation by means of using a zero order approach was explained, XFOIL was used to solve for an objective function which was optimised using a Genetic Algorithm within MATLAB. The flap, in isolation, was shown to have increased performance by means of implementing the flap extension concept. Large increases in maximum lift and stall point were observed.

Verification of the optimisation was performed in MSES and ANSYS Fluent to compare the optimised solution with the validated CFD. For this the new concept was implemented into the full high lift system and analysed. The flap extension concept was seen to increase lift at the trailing edge of the TC12 profile in high lift configuration. The geometric impingement of the flap extension on the flow field showed that, in the vicinity of the spoiler cove, the Coanda effect caused decreases in pressure at the recirculation region and at the flap extension providing decreased lift from the high lift system. Premature stall was observed due to increased flap camber providing early onset of separation at the trailing edge.

Finally, there was an attempt to improve on the optimised solution by implementing two new design modifications, namely a slotted geometry and a smoothed geometry. Both of these modifications provided a better understanding of the flow field around the flap extension concept but did not increase performance over that of the baseline solution.

6 Aerodynamic Investigation 2

The second approach to aerodynamically optimise the TC12 profile for landing configuration is, once again, to implement the novel concept on the leading edge of the TC12 flap as before. This optimisation is performed using ANSYS Workbench which has a number of built in optimisation tools. The optimisation tool selected is the ANSYS DesignXplorer Multi Objective Genetic Algorithm (MOGA) tool. This second optimisation will highlight the differences in the two optimisation methods used. Data produced by this method is compared to the baseline data and that of the first aerodynamic investigation.

In this chapter the ANSYS DesignXplorer optimisation tool is explained. The procedure of the optimisation involves solely using the solutions of CFD simulations as input to the optimisation tool. The optimisation tool did not converge due to time constraints so the best available solution was explored. This solution was seen to be ineffective when compared to the baseline calculations.

6.1 Optimisation Routine

Figure 6.1 shows a system diagram for the ANSYS Workbench Direct Optimisation. In the diagram *MOGA* is the optimisation tool (section 6.1.1), *Geom* is the geometry creation tool (section 6.1.2), *Mesh* is the Ansys Mesher (section 6.1.3) and *Fluent* is ANSYS Fluent the aerodynamic solver (section 6.1.4). The modules pass information to eachother in serial. Each module is described in its own section following on from here.

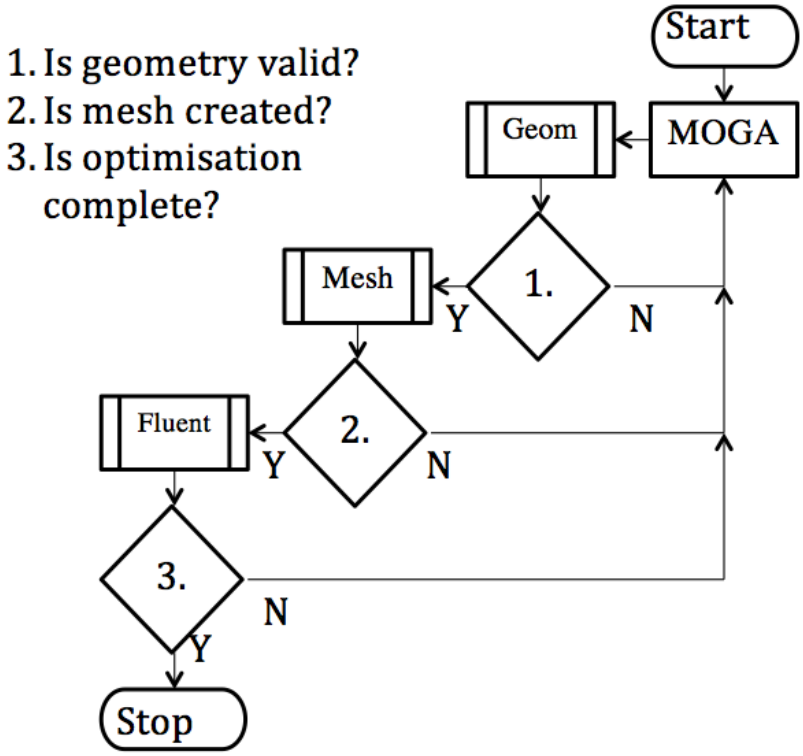


Figure 6.1: System diagram of MOGA optimisation in Ansys DesignXplorer

6.1.1 Multi Objective Genetic Algorithm

DesignXplorer is a tool within ANSYS Workbench that uses response surfaces and direct optimisation to efficiently explore a solution space. The tool relies on the parameterisation and linking of various ANSYS workbench modules together. Each module within workbench allows for parameterisation of input and output variables making the setting up of optimisations straightforward.

For this particular optimisation the Ansys DesignerXplorer MOGA optimisation method was selected because of the authors familiarity with Genetic Algorithms as a tool for optimisations.

Objective Function

The objective function used for the DesignXplorer optimisation was the same function suggested by Brezillon et al. (2008) who used C_L^3/C_D^2 to successfully optimise 2D high lift airfoils by means of computational geometric optimisations. Equation (6.1) states the problem- a maximisation of the objective function. Equation (6.2) states the objective function. The inclusion of the value *0.00000001* is a workaround used to prevent division by zero because the initial state of the solution is for each point to be zero. Equation (6.3) states the input variables to the problem.

$$max(\mathbf{F}_{obj}(x)), (x \in \mathbb{R}) \tag{6.1}$$

$$\mathbf{F}_{obj}(\mathbf{x}) = \frac{C_L^3}{C_D^2 + 0.00000001} \tag{6.2}$$

$$\mathbf{x} = \begin{Bmatrix} le \\ he \\ th \\ \theta \\ ca \end{Bmatrix} \tag{6.3}$$

Design Constraints

The design space is selected to provide a similar space to that of the zero order optimisation method's constraints. The author also manually checked a number of feasible configurations because the geometry tool had a tendency to cease functioning when certain geometries were tested. After some time a relatively good set of constraints for the parameters was found.

$$\begin{gathered} 0.0015 < \mathbf{th} < 0.004 \\ 0.0015 < \mathbf{he} < 0.006 \\ 120 < \mathbf{ca} < 160 \\ 0.02 < \mathbf{le} < 0.06 \\ 144 < \theta < 177 \end{gathered}$$

6.1.2 Geometry Tool

The geometry was parametrised into five input variables. The leading edge ball (as used in the zero order optimisation approach figure 5.2) was not used for the DesignXplorer optimisation due to the high drag seen just behind this region. The geometry producing tool used is ANSYS DesignModeler, a 2D and 3D CAD tool which allows users to prepare models for meshing. The TC12 profile in high lift configuration is statically placed within its fluid region and the parameterised flap extension is removed, and boundary conditions placed on the geometry surfaces.

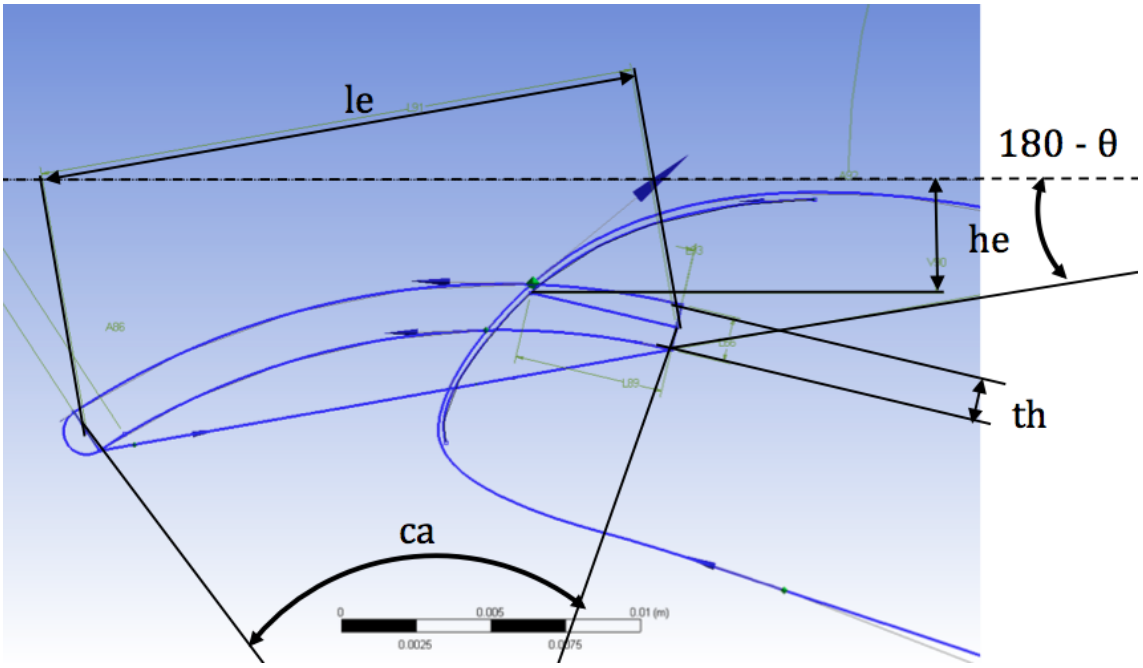


Figure 6.2: Parameterisation of flap extension concept in DesignXplorer

where *le* is length, *he* is the vertical drop from the line along *y=0*, *th* is the thickness of the flap extension, *ca* is the camber of the flap extension and θ is the angle of attack of the flap concept.

6.1.3 Meshing Tool

The meshes used within the DesignXplorer optimisation are automatically updated to conform to eachother using the settings applied during setup this is because the geometry is sent to the meshing tool (ANSYS Mesher). Figure 6.3 shows an example of one such mesh generated for a configuration within the DesignXplorer optimisation. The number of elements in the boundary layer had to be reduced because meshes with more boundary layer elements generated negative volumes in the extension cove on the lower surface of the flap extension. A compromise was made and 35 layers were used to mesh the boundary layer of the flap and flap extension (figure 6.4). The height of the boundary layer mesh on the flap is still conformal to the required height based on calculations in the Validation section. An example of one such final mesh had 198418 nodes and 227689 elements. This number will fluctuate based on the differing geometries automatically created.

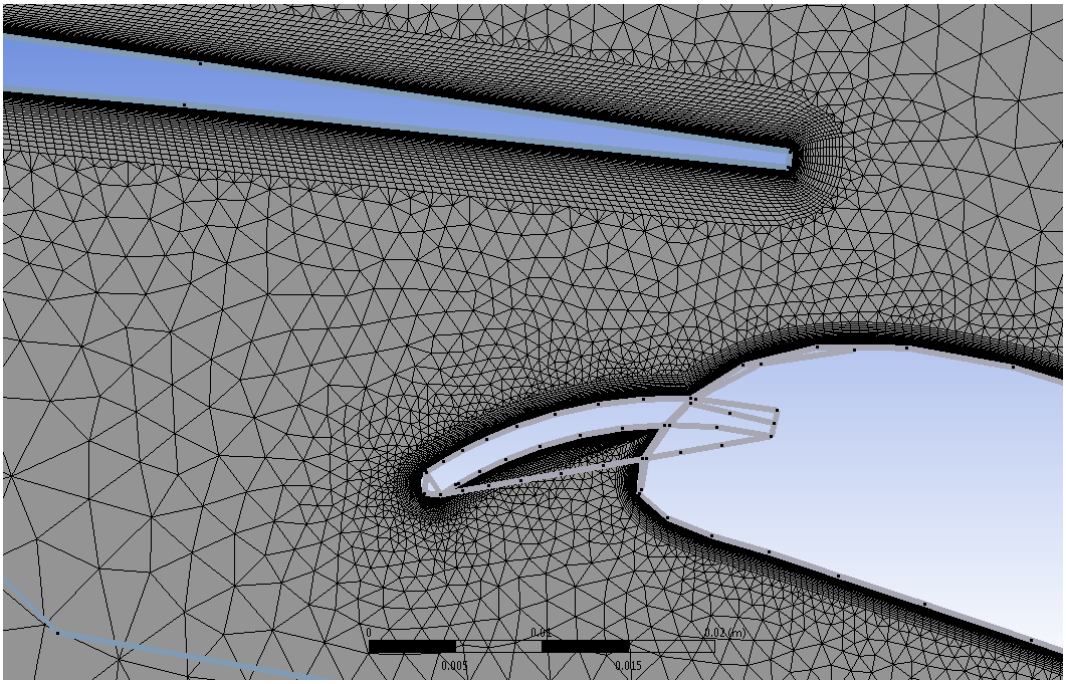


Figure 6.3: Example of an automatically generated mesh for DesignXplorer optimisation of TC12 high lift profile

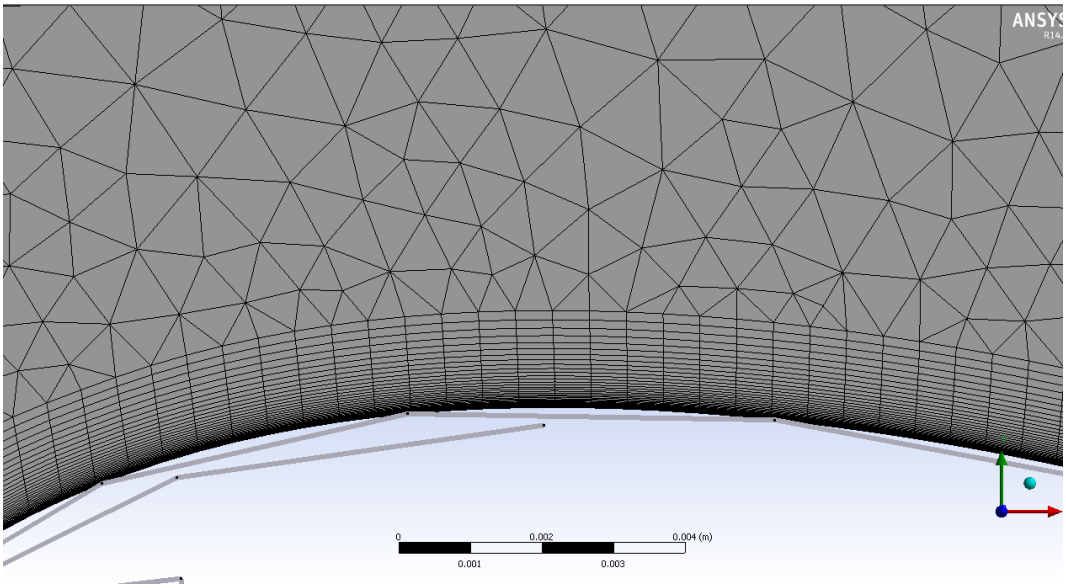


Figure 6.4: Boundary layer sizing of mesh for DesignXplorer optimisation of TC12 high lift profile

6.1.4 Aerodynamic Solver

The aerodynamic solver used is ANSYS Fluent, solver settings are conformal to those used for the validation of the TC12 high lift profile. Convergence criteria is also the same. Fluent automatically imports the mesh generated by the meshing tool and solves a RANS simulation at an

angle of attack of 8.09 degrees and a velocity of Mach 0.2. The angle of attack is fixed to, once again, coincide with available data. This angle is the threshold at which high lift computations become hard to predict (*AIAA CFD High Lift Prediction Workshop*, 2014) but, with no other pressure data for validation, it is the only available option. The validation from the previous section also showed acceptable agreement at this angle thus there are no foreseeable errors at this angle of attack.

The lift and drag coefficients are exported to DesignXplorer where the MOGA then solves the objective function and generates the optimisation populations.

6.2 Solution

The final solution given by the DesignModeler optimisation is not yet converged. The optimisation was set to perform 15 optimisation iterations with 30 samples per iteration. The initial sample set was set to 80 points. The total number of design points was 457 of which 61 of those failed due to impossible geometries being generated by the parametrised geometry creation tool.

Figure 6.5 is the convergence history of the optimisation tool. This plots the objective function against the number of points per optimisation. Each spike and subsequent decrease of the objective function represents a single generation. After roughly 200 points the function maximum value jumps to a new steady value, it is impossible to say (without additional function evaluations) whether or not the function would converge to the given point or to a new, more optimum, point.

The solution to the optimisation of the TC12 profile in high lift configuration by means of running the ANSYS DesignXplorer optimisation tool is, from here on, referred to as the *'DesignXplorer optimised solution'*.

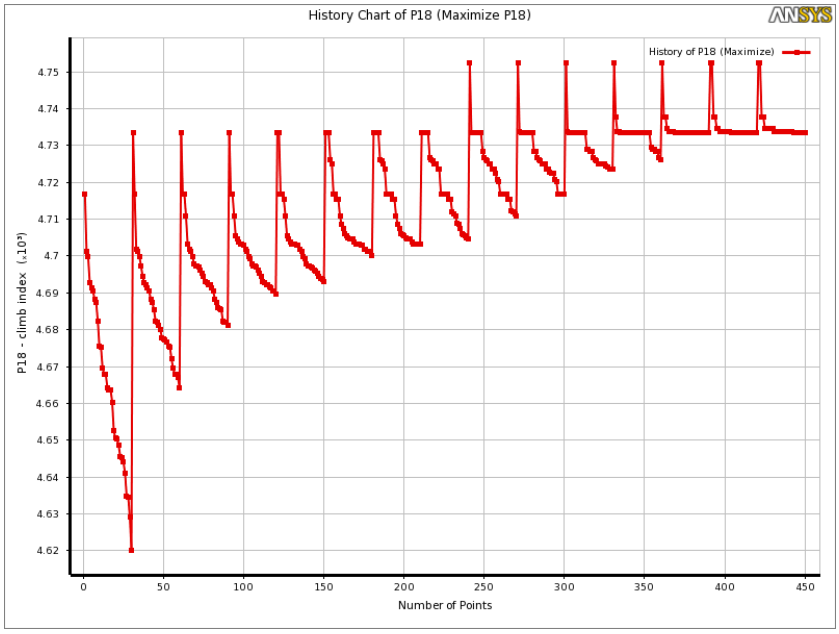


Figure 6.5: Convergence history of DesignXplorer MOGA optimisation of TC12 profile

Running on an Intel Xeon processor with four cores and 16Gb RAM the optimisation took roughly 40 minutes per design point for a total run time of about 10 days. As a comparison, the zero order optimisation had a total of 6418 design points. Based on this figure it would take about 175 days (or 6 months) for the optimisation to converge. Because of the long estimated processing time it was not feasible to obtain a fully converged solution.

ANSYS DesignXplorer conducts a sensitivity analysis based on the design points analysed. This allows the author to see which parameters most and least affect the objective function. The sensitivities (seen in figure 6.6) have the convention that a positive sensitivity indicates that an increase in that input increases the output whilst negative sensitivities indicates that an increase in that input decreases that output. The sensitivity chart indicates that lift increases as camber and position (green and yellow bars respectively) are decreased, whilst drag increases with the same set of parameters. The chart also indicates that as thickness increases so does lift and drag. These parameters are contradictory and most certainly non linear. This implies that a solution within the design space needs to be found that increases lift more than it increases drag.

The sentitivity of the objective function, however, shows that primarily for an increase in angle there is an increase in the function.

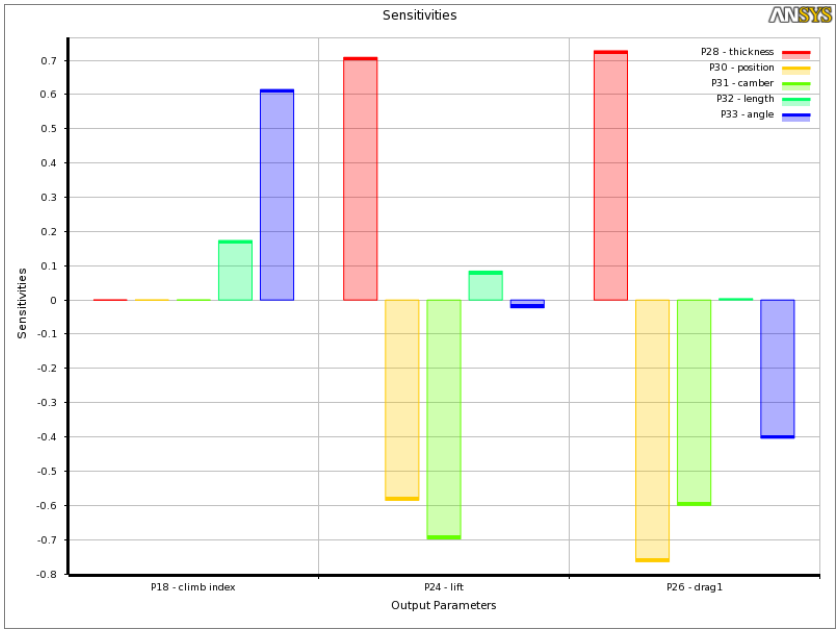


Figure 6.6: Sensitivity analysis of input parameters to output parameters of DesignXplorer MOGA optimisation of TC12 profile

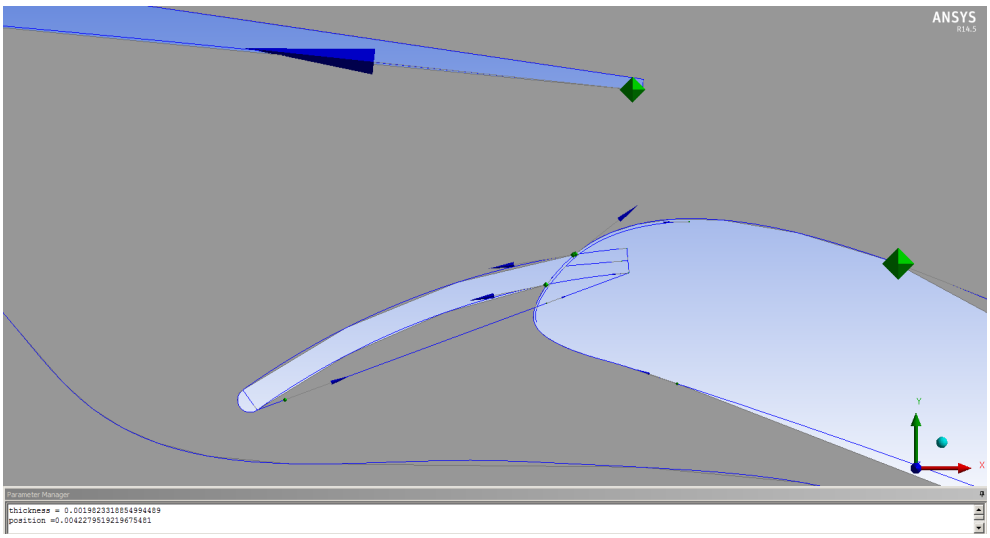


Figure 6.7: Geometry of DesignXplorer MOGA optimised solution

The geometry of the final solution is seen in figure 6.7. The optimisation using DesignXplorer could not account for the kinematics of the system using the parameterisation within the geometry tool. This is apparent in the solution as, clearly, the optimised flap extension for this case will not be able to retract along its curve. Nevertheless the solution is still analysed further. The mesh generated by the meshing tool is seen in figure 6.8 and follows the same parameters as highlighted before.

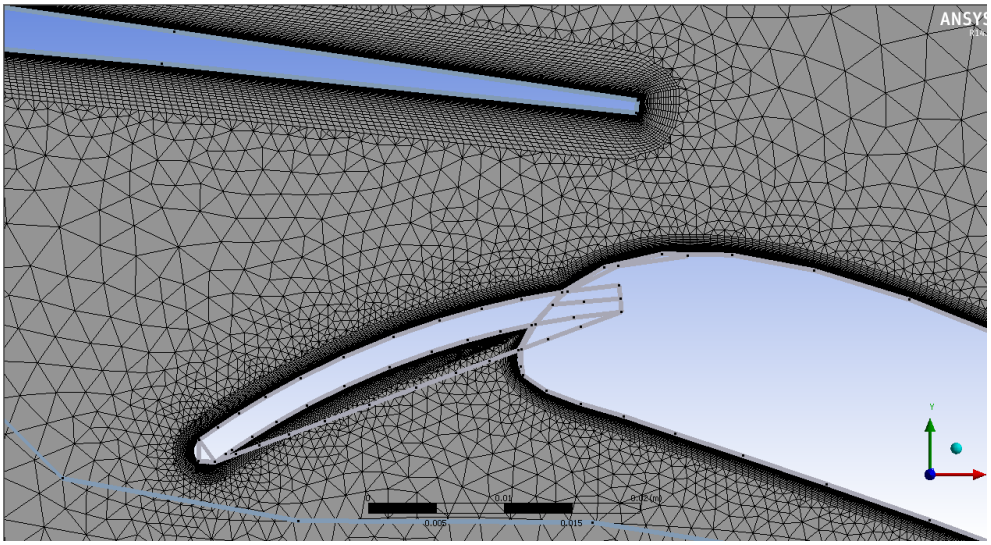


Figure 6.8: Mesh of DesignXplorer MOGA optimised solution

Lift performance of the optimised concept closely matches that of the baseline TC12 profile in high lift configuration. Figure 6.9 and 6.10 show the lift against angle of attack and stall region of the same data respectively. The DesignXplorer optimised solution performs better than the zero order optimised solution. The stall angle is the same as the baseline and maximum lift is decreased by 0.244%. Drag (as shown in figure 6.11) is also marginally increased with increasing angle of attack, at an angle of 8.09 degrees drag is increased by 0.3644%.

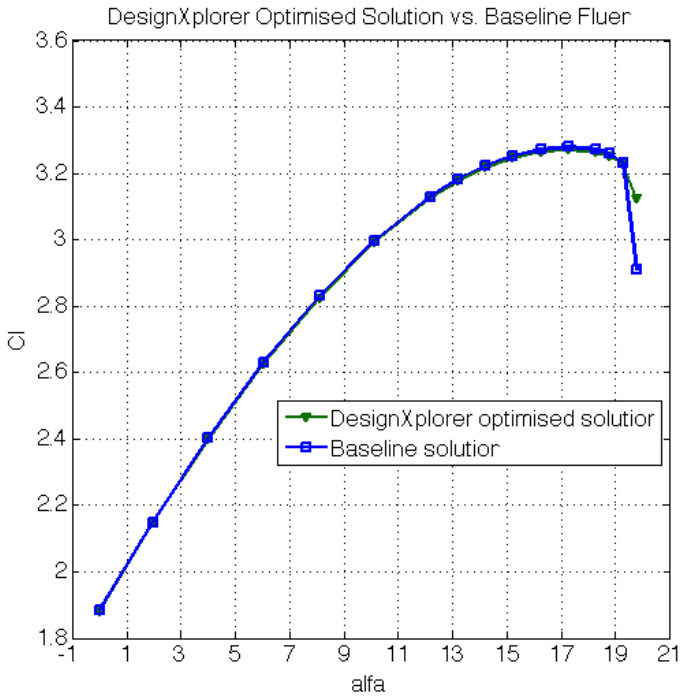


Figure 6.9: Cl vs. alfa of TC12 profil in high lift configuration DesignXplorer optimised solution vs. baseline in fluent sa turbulence model, Re 2.95 million

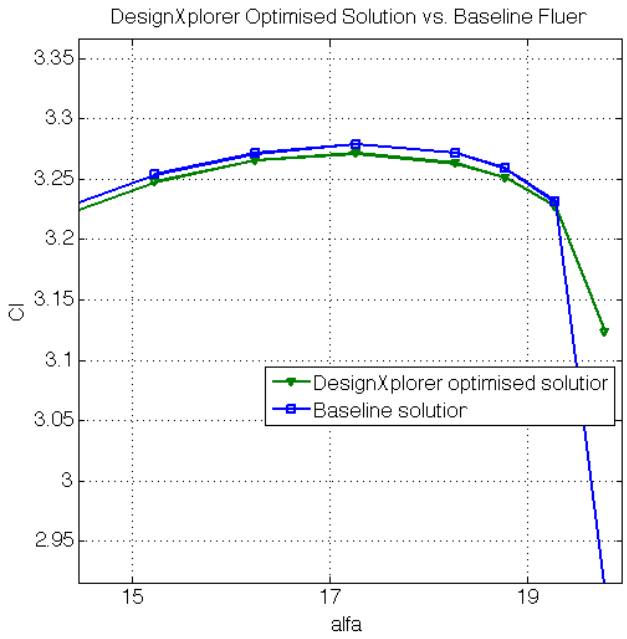


Figure 6.10: Cl vs. alfa at stall of TC12 profile in high lift configuration DesignXplorer optimised solution vs. baseline in Fluent, SA turbulence model, Re 2.95 million

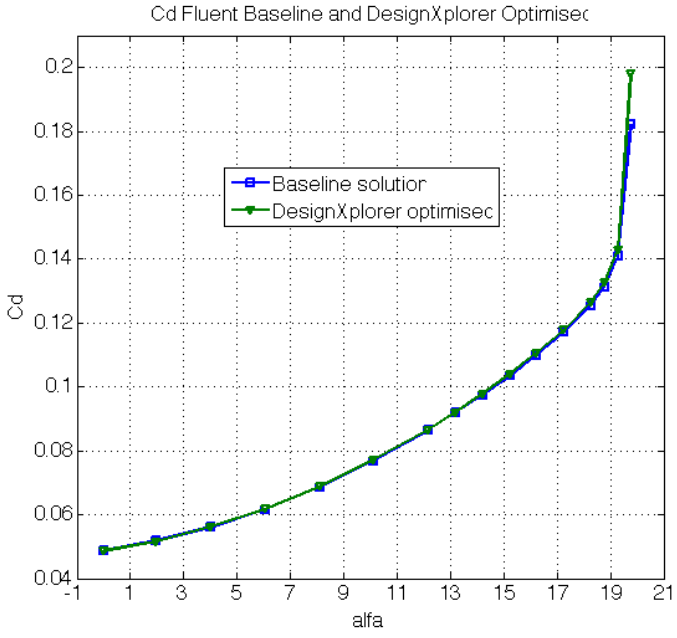


Figure 6.11: Cd vs. alfa of TC12 profile in high lift configuration DesignXplorer optimised solution vs. baseline in Fluent SA turbulence model, Re 2.95 million

Figure 6.12 shows the overall pressure distribution against non-dimensionalised chord length for

the DesignXplorer optimised concept. At the main element and slat there is negligible change between the optimised and baseline configurations.

By looking at the flap in isolation (figure 6.13) the increase in lift due to the flap extensions implementation becomes apparent- this is seen as an area integration within the small region between x/c 0.85 and 0.9. This region represents an increase in lift at this location due to the presence of the flap extension. The pressure peak at a C_p -2.5 is slightly lower on the optimised concept. This is due lower flow velocity on the upper surface of the flap where, in the baseline concept, there would be increased velocity along the flap leading edge due to high curvature. The implementation of the concept allows for decreased flap curvature and thus slightly decreased flow velocity.
Overall the optimised flap in isolation produces more lift than the baseline. There is, however, an overall negligible loss of lift in the system because of the pressure losses at the main element as can be seen by the 'missing' region of pressure in figure 6.14.

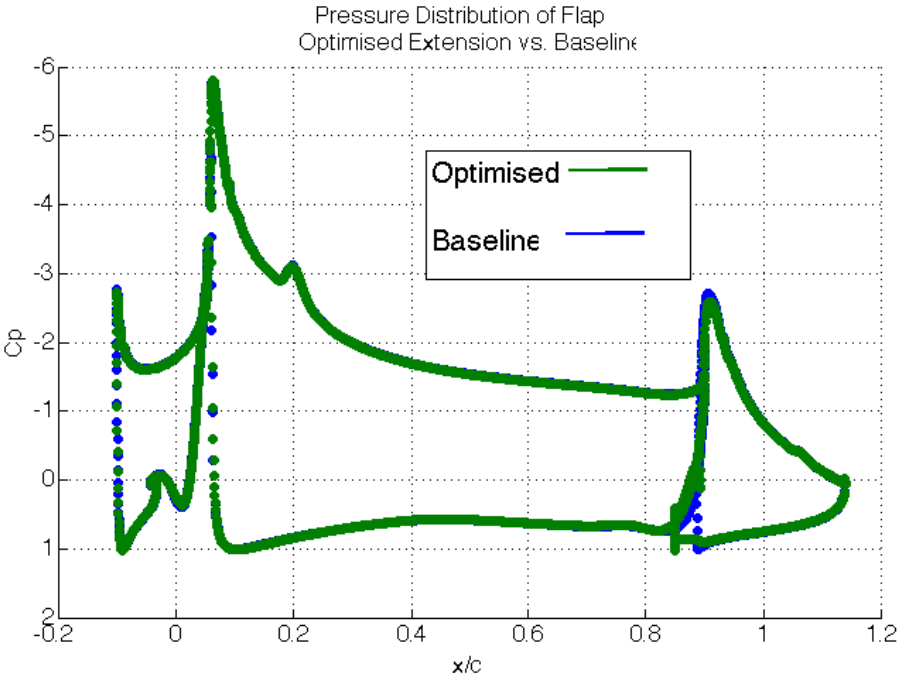


Figure 6.12: Pressure distribution of TC12 high lift configuration at 8.09 degrees DesignXplorer optimised solution vs. baseline in Fluent, Re 2.95 million, SA turbulence model

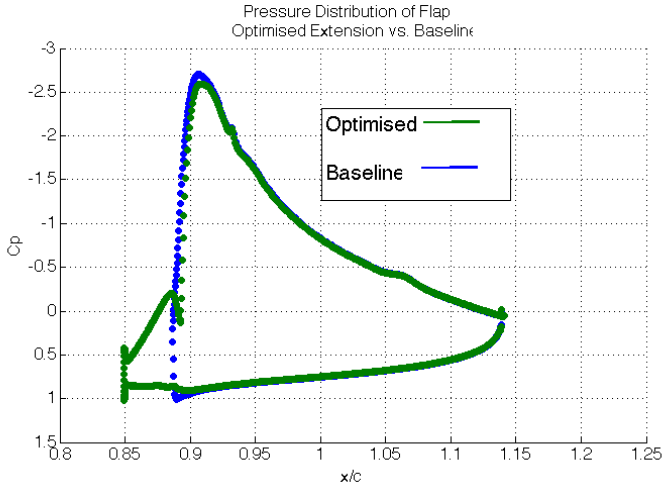


Figure 6.13: Pressure distribution of TC12 high lift configuration flap at 8.09 degrees DesignXplorer optimised solution vs. baseline in Fluent, Re 2.95 million, SA turbulence model

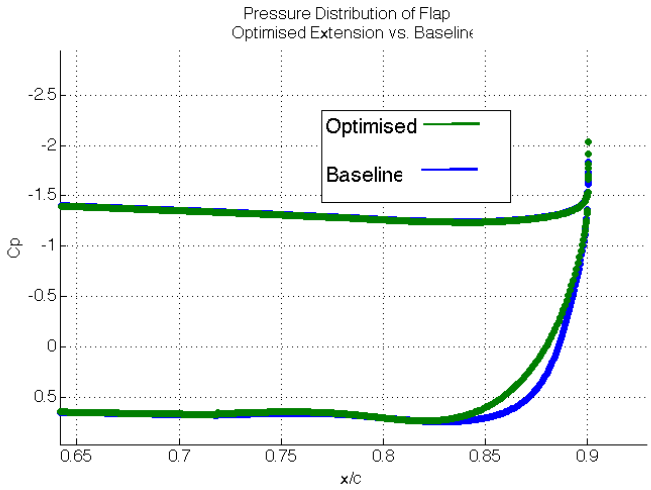


Figure 6.14: Pressure distribution of TC12 high lift configuration main element at 8.09 degrees DesignXplorer optimised solution vs. baseline in Fluent, Re 2.95 million, SA turbulence model

The streamlines showing velocity magnitude in the vicinity of the optimised concept show a shift in the size of the recirculation region when compared to the baseline solution. There is also a new recirculation region underneath the flap extension.

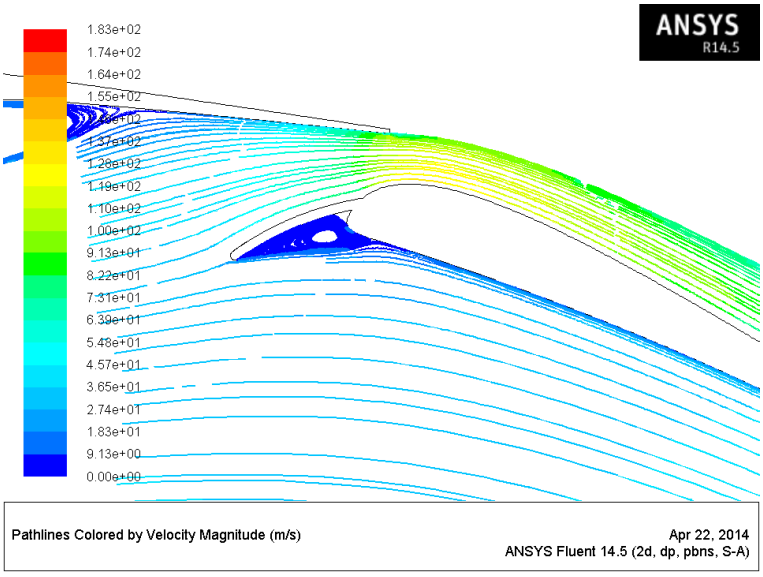


Figure 6.15: Streamlines showing recirculation region of the DesignXplorer optimised concept

6.3 Findings

The DesignXplorer MOGA optimisation tool achieved a considerably different solution to that of the zero order optimised solution. The optimisation may not have fully converged and the time to final convergence cannot be estimated but the solution still performs better than that of the previous optimisation method.

In isolation the flap alone performs better than the baseline TC12 profile flap. This is because the implemented flap extension concept provides more camber and surface area to the flap which increases lift locally.

Compared to the zero order optimised solution, the solution to the DesignXplorer optimised flap is not affected by the Coanda effect as greatly because of the physical size and position of the new design does not impinge on the freestream flow, within the spoiler cove, as greatly as before.

The overall system shows negligible losses of lift caused by the flap concept affecting the pressure on the main element airfoil decreasing lift slightly. Although the isolated concept does improve performance an additional step in the optimisation procedure could be to move the flap (with attached novel concept) outwards and to then optimise the gap and overlap parameter. Gap and overlap parameter optimisation is fairly common within high lift design and could be easily implemented within a CFD optimisation (Soulat et al., 2012) but is outside the scope of this dissertation.

7 Aeroacoustic Investigation

An aeroacoustic investigation is performed to quantify the sound produced by the TC12 profile in high lift configuration. The investigation extends to a comparison whereby the sound produced by the ANSYS DesignXplorer optimised solution (the best performing of the two aerodynamic investigations) is analysed and compared to the sound produced by the baseline solution.

In this chapter ANSYS Fluent is used to solve a series of CAA simulations. ANSYS Fluent has a number of different methods of calculating acoustics, the one employed in this study was the FWH solver built into Fluent. Acoustic simulations are solved based on time dependent fluctuations solved using a transient formulation. Two different types of simulations were performed, one using the SA turbulence model and another using the DES turbulence model. Once the baseline results are found they are compared to results of acoustic simulations of the flap extension optimised with ANSYS DesignXplorer.

7.1 Initial Conditions

As with the CFD simulations the initial conditions for the CAA simulations remain the same, these a shown in table 7.1.

Parameter	*Value*
Reynolds Number	2.95 million
Mach Number	0.2
Air Properties	
Altitude	0 m (Sea Level)
Temperature	288.16 K
Density	1.225 kg/m^3
Pressure	0 Pa (gauge)
Kinematic Viscosity	1.789e-5 N.s/ m^3

Table 7.1: Initial conditions for CAA simulations

Boundary conditions for the CAA simulations also still hold true to those calculated for the CFD simulations, thus the same boundary conditions. Changes will arise from the condition that the simulations are to be transient.

The time step (Δt) set in Fluent is independent of the frequency (f) needed to be resolved because ANSYS Fluent uses a fully implicit time stepping formulation. The recommended procedure by ANSYS is to set the required time step at least one order of magnitude smaller than the smallest required time constant in the system.

The Courant-Friedrichs-Lewy (CFL) condition (equation (7.1)) can be used as a measure of the required order of magnitudes for frequency resolution

$$C = \frac{U\Delta t}{\Delta x} \tag{7.1}$$

where C is the non-dimensional Courant number, U is the freestream velocity, Δt is the minimum time step and Δx is the length scale which, in this case, is the minimum cell length.

Minimum cell length is that given in the boundary layer as 0.0004m. According to the ANSYS guidelines a user should aim to resolve a Courant number between 20-40 within post processing to achieve acceptable resolution of length scales.

$40 = (68.0571 * \Delta t)/0.0004$
$\Delta t = 0.000235s$

Rounding and dropping the solution by one order of magnitude provides a final timestep of:

$\Delta t = 2.5e{-}5s$

This time step is kept constant for all the simulations within the fixed time stepping method.

7.2 Solver Settings

The Fluent simulations for all configurations are set up with the same solver settings to maintain continuity across all simulations. The solver settings are explained in Table 7.2. Each simulation is done using as many second order properties as possible. The DES turbulence model sets the *Transient Formulation* to the bounded version automatically due to the mathematical formulations of the model.

Each model is given 6000 time steps in which to converge the initial transient simulation. After initial convergence the acoustic solver is turned on and 1 000 time steps are used to solve the acoustic solution. The 1 000 times steps are equivalent to a simulation time of 0.025s and are deemed sufficient time to account for a single set of vortices shed by the TC12 profile in high lift configuration. This assumption is confirmed by looking at the fluctuating values of the variables during this time.

During the acoustic simulations the acoustic signals were computed *on-the-fly* by the Fluent acoustic solver which employs the FWH equations to the transient data. Acoustic reference pressure was 2e-5 Pa. Convergence criteria for SA and DES turbulence was set to a maximum of 20 and 30 iterations respectively to allow for sufficient convergence of time steps.

Condition	**Value (SA Turbulence)**	**Value (DES Turbulence)**
Analysis Type	2D	2D
Boundary	Pressure Far-Field	Pressure Far-Field
Mach Number	0.2	0.2
Angle of attack	8.09 degrees	8.09 degrees
Gas	Ideal Gas (compressible)	Ideal Gas (compressible)
Energy Equation	on	on
Pressure Velocity Coupling	SIMPLE	SIMPLE
Spatial Discretization		
Gradient	Least Squares Cell Based	Least Squares Cell Based
Pressure	Standard	Standard
Density	Second Order Upwind	Second Order Upwind
Momentum	Second Order Upwind	Bounded Central Differencing
Modified Turbulent Viscosity	Second Order Upwind	Second Order Upwind
Energy	Second Order Upwind	Second Order Upwind
Transient Formulation	Second Order Implicit	Bounded Second Order Implicit
Convergence Criteria		
Number of Time Steps	6000	6000
Number of time steps for acoustics on	1 000	1 000
Time Step Size	2.5e-5 s	2.5e-5 s
Maximum number of iterations	20	30

Table 7.2: Summary of solver settings used for Fluent CAA simulations

7.3 Mesh Set up

The FWH acoustic solver in Fluent requires an integration region around the area of interest to be able to solve the FWH analogy using the time dependant data. To achieve this the mesh is split into two regions, separated by an integration source surface (figure 7.1). The integration region needs to be sufficiently close to the airfoil to capture the unsteady fluctuations but sufficiently far away to not capture 'noisy' signals. The approach selected was to use a constant vorticity (ω) region around a first order transient response which corresponded to a vorticity of $\omega = 100/s$. This surface looked visually similar to those used in literature. At the leading edge the surface is very close to the slat (figure 7.2) and at the trailing edge the surface expands further away from the airfoil body on the upper surface (figure 7.3). The surface extends some distance beyond the chord length to capture additional vortical structures presumed to be located in these areas.

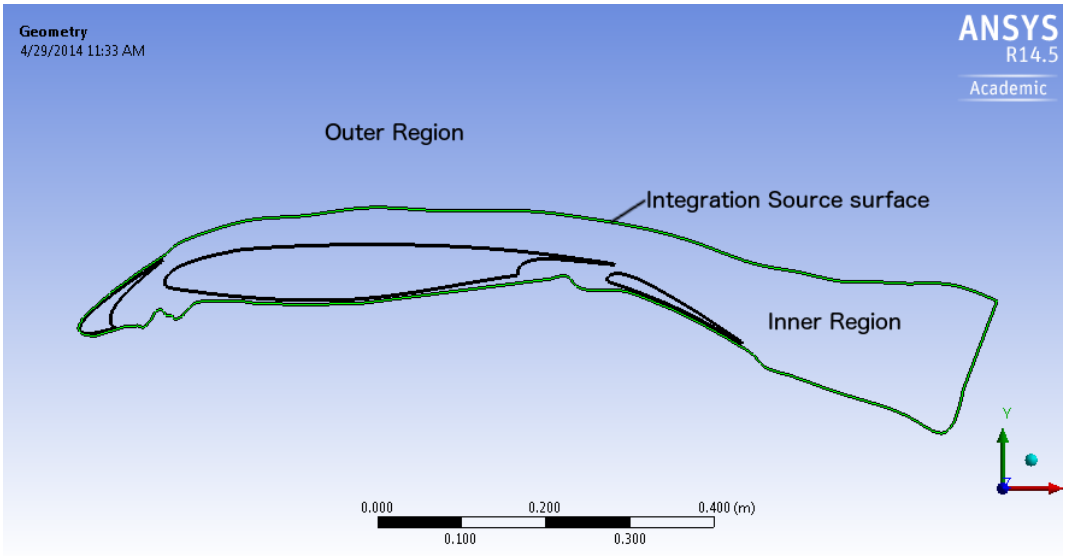


Figure 7.1: Integration region around TC12 profile in high lift configuration for acoustic calculations

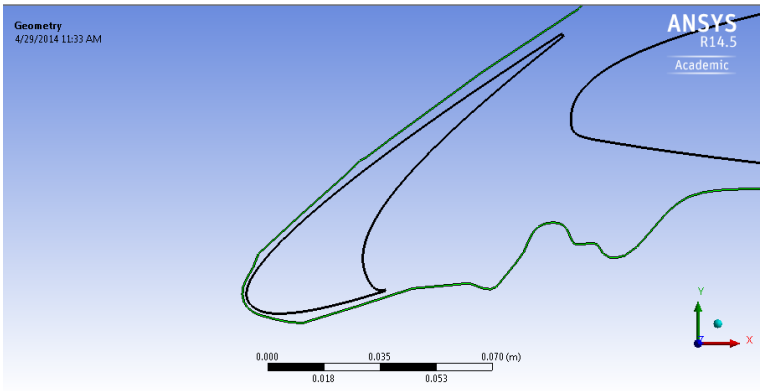


Figure 7.2: Integration region around TC12 profile in high lift configuration for acoustic calculations at slat

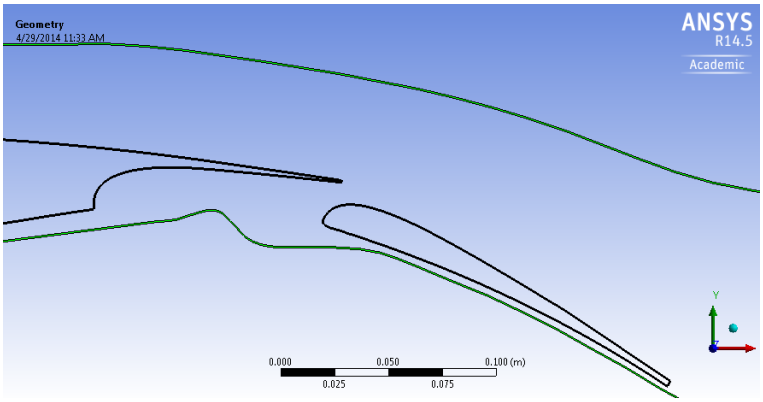


Figure 7.3: Integration region around TC12 profile in high lift configuration for acoustic calculations at flap

7.4 SA Based Acoustic Simulations

Acoustic simulations were run using the same SA turbulence models as were employed in the steady calculations. The first simulation was run using the same mesh used for steady calculations on the TC12 profile in high lift configuration (247 371 nodes, 207 233 elements). Images of this mesh can be seen in figures 4.32 - 4.36. The only addition is that of the integration region.

Results from the initial mesh were not very convincing and the mesh was refined based on the gradient of vorticity. The refinement region is shown in figure 7.4. The refined mesh has 842 996 nodes (241% increase).

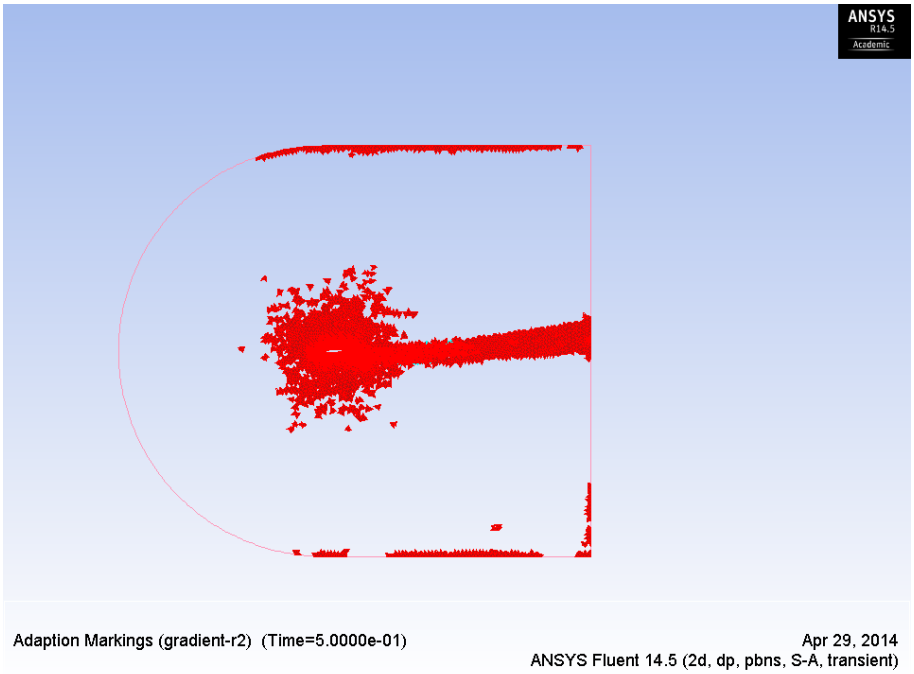


Figure 7.4: Mesh refinements for SA turblence model acoustic simulations

7.4.1 Solution

Upon completion of the simulation the data from the unsteady calculations are used to produce the directivity plot which shows P'_{RMS} with the leading edge of the airfoil located at the centre of the polar plot. Directivity is measured along a circle that is located 3.9m away from the centre of the mesh close to the extremities. The directivity of the simulations for both meshes is presented in figure 7.5. Directivity in acoustics is a measure of the radiation pattern from a particular source indicating the amount of energy radiated in particular directions.

The directivity plots of the TC12 profile in high lift configuration when using the SA turbulence model shows two main lobes extending upwards from the upper surface and a slightly smaller lobe extending downwards from the lower surface. There is also a minor lobe extending aft from the trailing edge. Refinements in the mesh smoothed data in all regions baring a region towards the leading edge which has additional noise introduced.

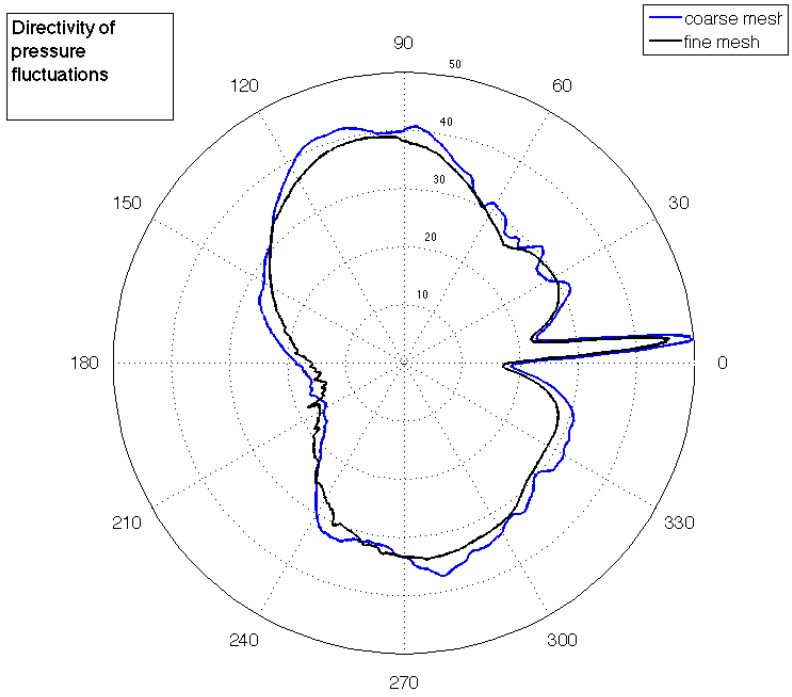


Figure 7.5: Directivity of sound for the TC12 profile in high lift configuration at 8.09 degrees angle of attack using the SA turbulence model

The sound spectrum is shown in figure 7.6, this is the sound pressure level (in Decibels) against frequency (in Hz). Sound is calculated for the concept at a receiver located 3.9m below the airfoil (still within the mesh region) by means of the FWH acoustic analogy integrated around the region seen in figure 7.1. This shows the sound pressure level against frequencies within the normal range of human hearing for the two meshes. Apart from a decreasing trend in data there is no consistency between the two sets of results.

The reason for the poor results is that the SA turbulence model does not account for turbulent length scales accurately and does miss key portions of data required to measure acoustic signals. The data presented in the figure may very well be just noise.

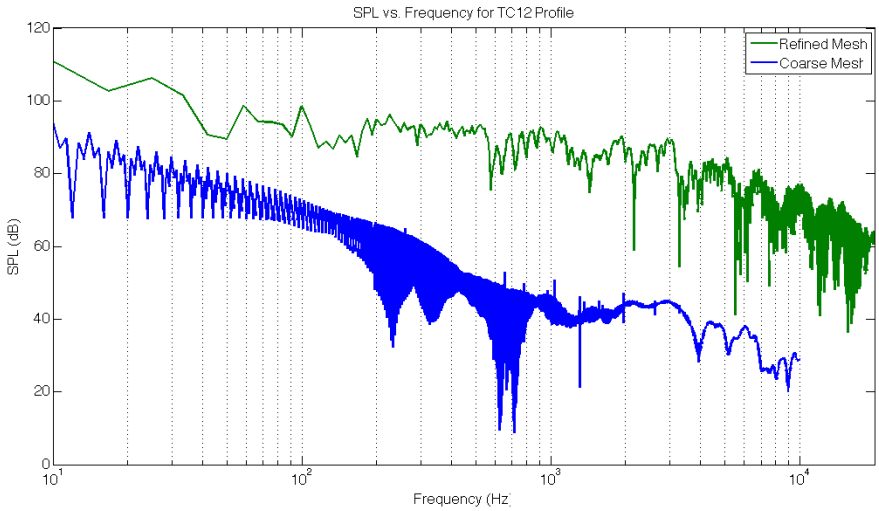


Figure 7.6: Sound spectrum for the TC12 profile in high lift configuration at 8.09 degrees angle of attack using the SA turbulence model

7.5 DES Based Acoustic Simulations

The DES turbulence model is a RANS/LES hybrid model which employs RANS turbulence formulations near walls and LES formulations away from walls where turbulent length scales are greater and less computationally expensive to simulate. In Fluent the DES formulation automatically resolves the length scales for the user so the user is not required to specify different regions for RANS and LES calculations respectively. The DES formulation should resolve the necessary turbulence length scales required for successful calculation of acoustic signals.

Acoustic simulations using the DES turbulence model are performed on the TC12 profile in high lift configuration. The initial conditions and solver settings explained in this chapter are used for the solutions. The mesh used for calculations is the same as the one used in the calculation of the SA turbulence model acoustic simulations.

Convergence

The DES simulation is converged using the criteria given in table 7.2. The acoustic signals are only resolved once the solution reaches a relatively steady state (1 000 iterations of acoustics after 6 000 discarded iterations). The fluctuation of drag for the 1 000 time steps used to calculate the acoustic signals for the TC12 profile, in high lift configuration, is shown in figure 7.7. The data shows fluctuation of the drag about a drag coefficient value of about 0.0635. Since the drag is fluctuating around a single point it can be concluded here that the solution is acceptable for resolving acoustic signals.

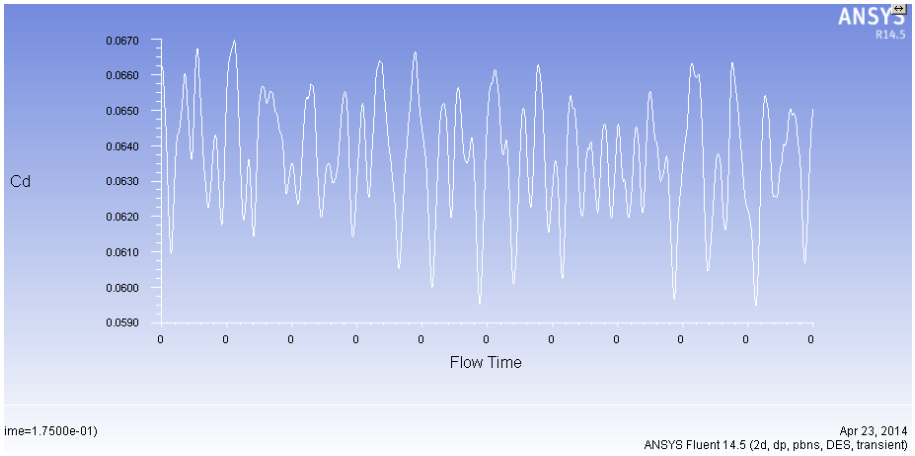


Figure 7.7: Fluctuation of drag during last 1 000 iterations of the TC12 profile in high lift configuration at 8.09 degrees angle of attack using the DES turbulence model

To determine whether the transient simulation is sufficiently converged the cell based Courant number contour is checked (as per recommendation by ANSYS). The contours of cell Courant number (figure 7.8) show that at the trailing edge of the TC12 profile there is only a very small region that shows a Courant number over 30. This figure falls within the recommendations made by ANSYS and thus concludes that the solution is converged.

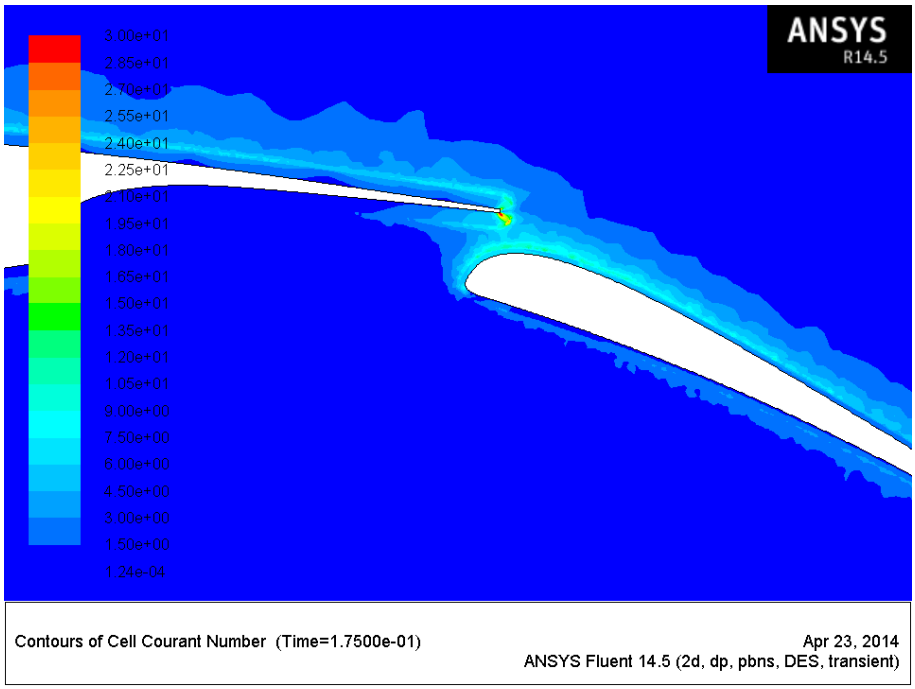


Figure 7.8: Courant numbers at each cell at the trailing edge of the TC12 profile in high lift configuration at 8.09 degrees angle of attack using the DES turbulence model

7.5.1 Solution

Vorticity is used as a measure of noise and can give a good indication of the fluctuating vortices produced in contact with bodies. Figure 7.9 shows vorticity contours between 0 - 1 000/s at the trailing edge of the TC12 airfoil in high lift configuration. The contours show that regions within the boundary layer are highly rotational. Of particular interest is the large, unsteady, shear layer within the cove region underneath the spoiler.

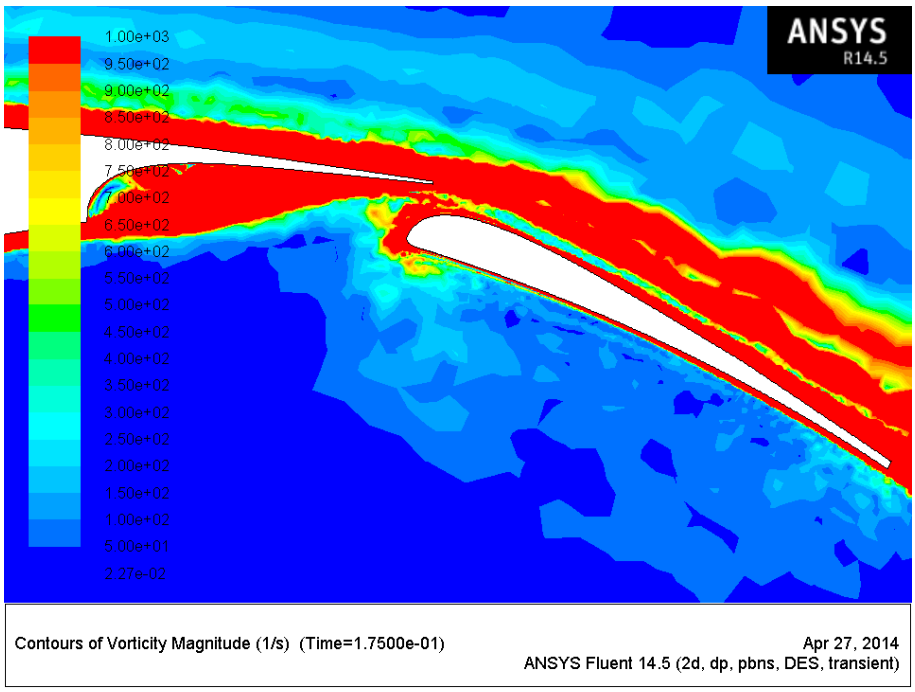


Figure 7.9: Vorticity between 0 - 1 000 near the trailing edge of the TC12 profile in high lift configuration at 8.09 degrees angle of attack using the DES turbulence model

Directivity (figure 7.10) follows the same trend as the directivity found for using the SA turbulence model. This shows consistency between the pressure fluctuations predicted by the two turbulence models.

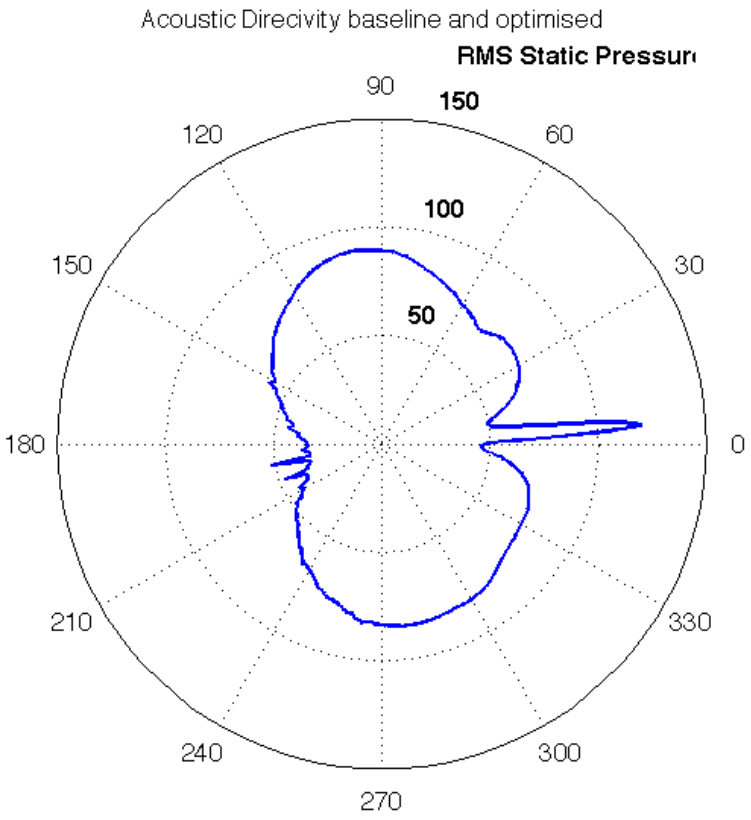


Figure 7.10: Directivity of sound for the TC12 profile in high lift configuration at 8.09 degrees angle of attack using the DES turbulence model

The full sound spectrum for the TC12 profile in high lift configuration is presented in figure 7.11. The data presented here is more akin to that found in literature and follows similar trends. Data is filtered using the Savitzky-Golay filtering tool in MATLAB. The filtering tool is a digital filter which smoothes data using local cubic approximations in small regions. A caveat of this filter is that initially (at low frequencies) the filtered data clearly does not follow the data trend very accurately due to the lack of signal noise (few data points to work with) within the data.

The sound spectrum as predicted using the DES turbulence model shows a peak in sound pressure levels at a frequency of about 1 000Hz. The peak is at about 80dB. This value would be greater in a full 3D configuration due to additional noise source locations along a span.

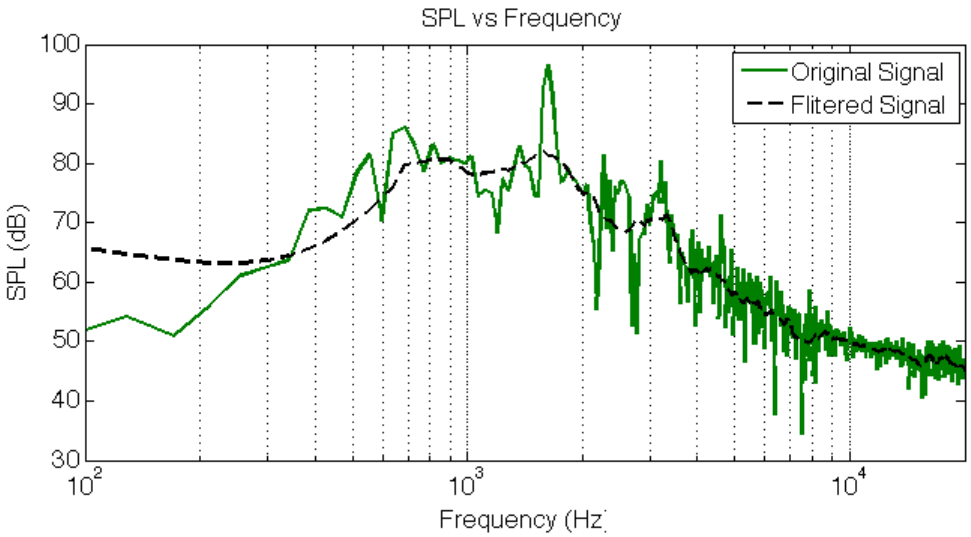


Figure 7.11: Sound spectrum for the TC12 profile in high lift configuration at 8.09 degrees angle of attack using the DES turbulence model

7.6 Acoustics of the DesignXplorer Solution

Acoustic simulations are performed on the DesignXplorer optimised solution of the TC12 profile in high lift configuration. This simulation is performed to compare the noise generated by the baseline configuration against that generated by the new concept.

Figure 7.12 is the vorticity magnitude around the new concept between 0 and 1 000/s. The boundary layer of the flow around the TC12 profile in high lift configuration is highly rotational, showing excessive high vorticity magnitudes in this region. The vorticity contours of the DesignXplorer optimised concept and the baseline solution are overlayed onto eachother as seen in figure 7.13. The black regions in this diagram show areas where there is a difference in vorticity magnitude between the two simulations. It is observed that the high vortical region (>1 000/s) within the shear layer, that bounds the recirculation region, within the spoiler cove (not entirely visible), is minimised by the effect of the novel concept on the flow field.

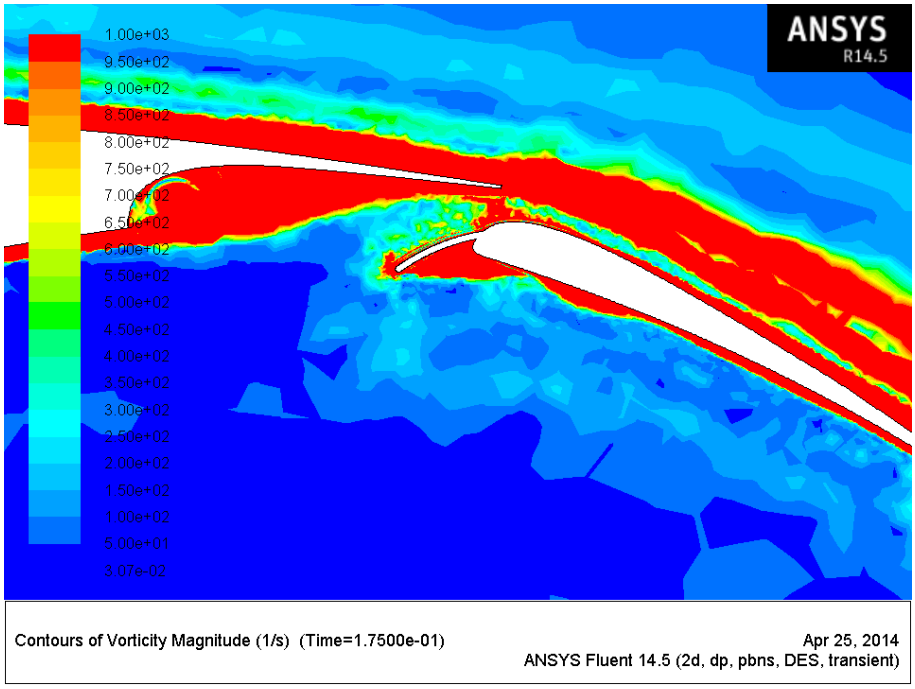


Figure 7.12: Vorticity between 0 - 1 000 near the trailing edge of the DesignXplorer optimised TC12 profile in high lift configuration at 8.09 degrees angle of attack using the DES turbulence model

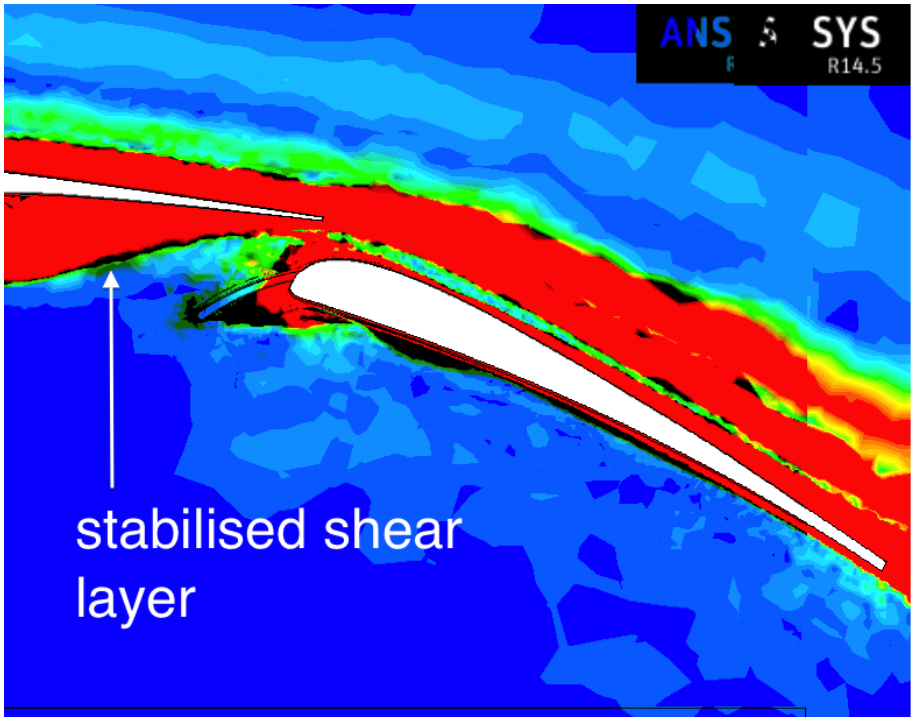


Figure 7.13: Vorticity between 0 - 1 000 near the trailing edge comparing the TC12 profile in high lift configuration compared to the DesignXplorer optimised solution at 8.09 degrees angle of attack using the DES turbulence model

Directivity plots of the two concepts against eachother (figure 7.14) show the same trends throughout 360 degrees. As directivity is a measure of where sound is radiated from this shows that the new concept has no major effects on the locations from where sound is radiated.

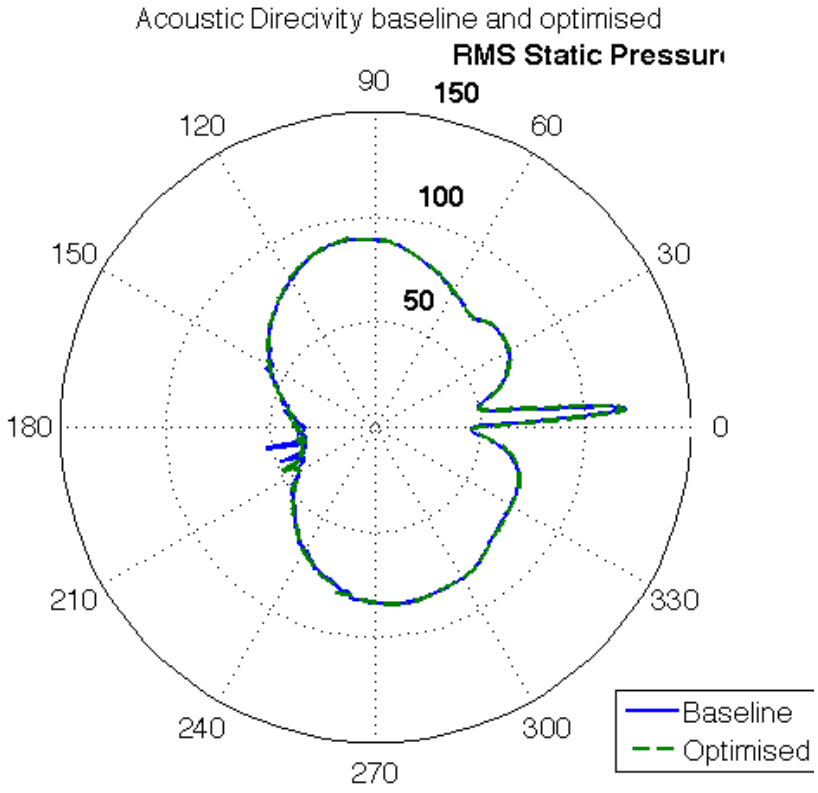


Figure 7.14: Directivity of sound for the optimised TC12 profile in high lift configuration against the baseline at 8.09 degrees angle of attack using the DES turbulence model

The sound spectrum for the DesignXplorer optimised solution is presented in figure 7.15. The data is also filtered using the Savitzky-Golay filter in MATLAB. Compared to the baseline solution the acoustic signals for this simulation appear to be more noisy at frequencies beyond 1 000Hz. The peak of the data at 1 000Hz is a lot *flatter* than that of the baseline.

Figure 7.16 compares the filtered acoustic data of the baseline to that of the DesignXplorer optimised solution. It is uncertain whether the filtered data between 100 and 500 Hz is entirely accurate due to the errors noted within the filtering tool. Data in the mid frequency range seems to correlate quite well. Where the baseline data has more peaks and troughs between 1 000 and 4 000 Hz the DesignXplorer optimised solution provides a more steady response which follows the same trend. From 6 000 to 20 000 Hz the DesignXplorer optimised solution appears to decrease the sound pressure level by about 10dB across this range.

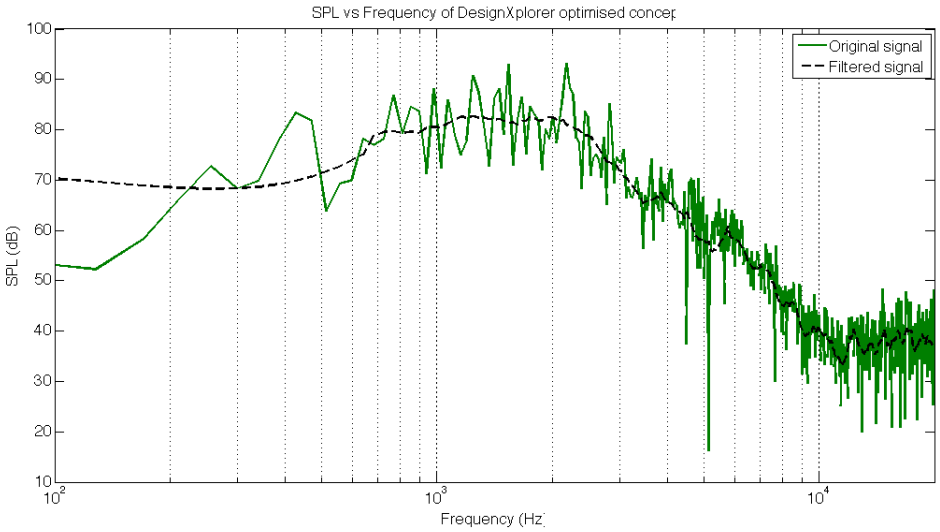


Figure 7.15: Sound spectrum for the optimised TC12 profile in high lift configuration against the baseline at 8.09 degrees angle of attack using the DES turbulence model

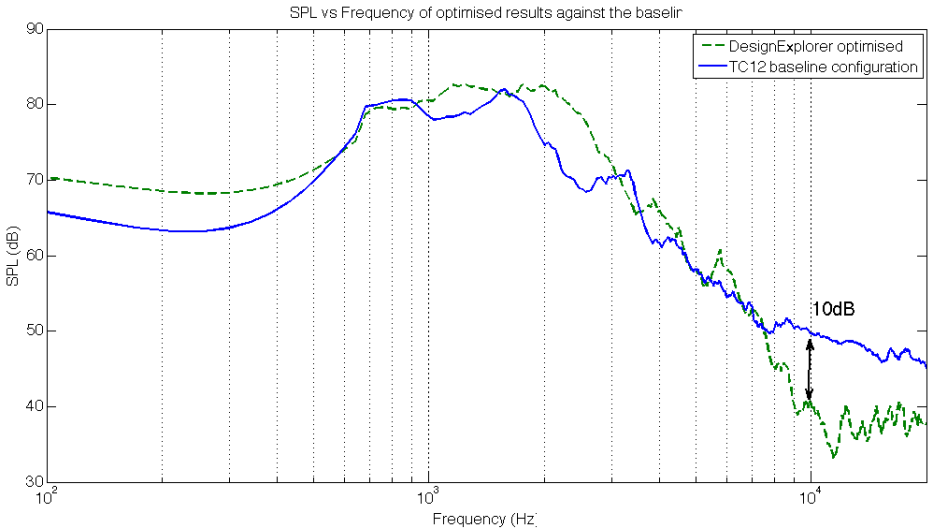


Figure 7.16: Filtered sound spectrum for the optimised TC12 profile in high lift configuration against the baseline at 8.09 degrees angle of attack using the DES turbulence model

7.7 Findings

Acoustic simulations of the TC12 profile were run. Simulations using the SA turbulence model were not successful. The simulations performed using the SA turbulence model highlight the flaws in using a completely RANS based turbulence model to simulate acoustics. Results did not correspond to literature very well and were deemed to be unhelpful due to poor trends.

After employing the RANS/LES formulation by means of the DES turbulence model in 2D a better set of results was obtained that was more consistent with data from literature (Dobrzynski et al., 1998; Zhang, 2010). A comparison was made between acoustic results of the TC12 profile in high lift configuration and the DesignXplorer optimised solution. By implementing the flap extension on the high lift profile the flow field at the trailing edge was modified. This modification brought stability to the shear layer within the spoiler cove shown by a decreased area of highly vortical flow within the cove. Highly vortical flow is a primary noise generating mechanism, by reducing the amount of vortical flow within the region of the spoiler cove the overall noise generated could be reduced. This reduction is vortical flow and additional flow stability led to a decrease of high frequency noise of approximately 10dB.

8 Design Investigation

UPON completion of the primary investigations in aerodynamics and aeroacoustics an ancillary design investigation is to be performed. By following the MDO procedures suggested by Isikveren (2010) and Mistree and Stonis (1994) and utilised by Mamo (2010) the author decided it would be best to have a forward look into the implementation of the flap extension. The design recommendation thus becomes an initial technical feasibility study for the flap extension concept. The optimisations, as performed prior to this, might suffice for noise and aerodynamic criteria but the mechanical design as such is not completely ready for deployment or manufacture. This section aids in evolving the design to bring it a step closer to a final design. After this section it would be advisable to redesign and re-optimise the concept flap in order to produce a second iteration solution.

The recommendation procedure is multi faceted and involves a number of steps. Firstly a number of concepts are brainstormed based on the geometry of the flap. The predesign concepts are compared by means of a Down Selection Process (DSP) to determine which concept will be most likely to succeed as a finished product.

8.1 Predesign Concepts

The following section shows the brainstormed concepts. For all concepts the pink lines show the stowed (cruise) positions and the blue lines show the deployed (high lift) positions.

Vitale Baseline Concept

This concept is the one derived by Vitale (2010) which was deemed to be the best actuation method for the flap, a concept sketch is shown in Fig. 8.1. After initial problems with using a Kruger flap a redesign was required and this concept was thought up. It is said that the actuation mechanism will not be hindered because the area behind the main element (cove) is a drainpipe which is effectively a dead zone. The concept would be deployed in a maximum lift production position for take off and a maximum noise reduction position for landing. It is possible that the actuation pipe would cause additional noise similar to the aeroacoustic rod-airfoil test case. The concept scoring for this concept is available in appendix F.1.

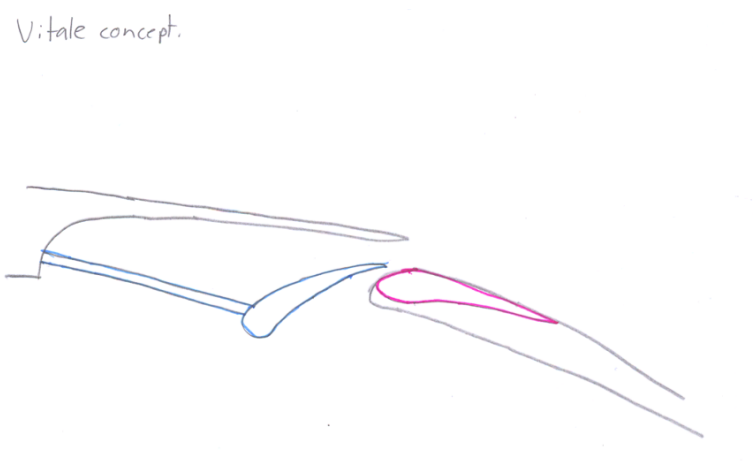


Figure 8.1: Vitale predesign concept

Betz Track

The Betz track is a solution to any additional power requirements that may be required by additional actuation methods, seen in Fig. 8.2. The concept flap extends with a lagging track so that when the flap is is fully extended landing position the concept flap is in the correct position for optimised effects. The concept also includes a cover to close any gap that may form between the concept flap and the flap, this closed gap decreases any additional noise from cavities. The concept scoring for this concept is available in appendix F.2.

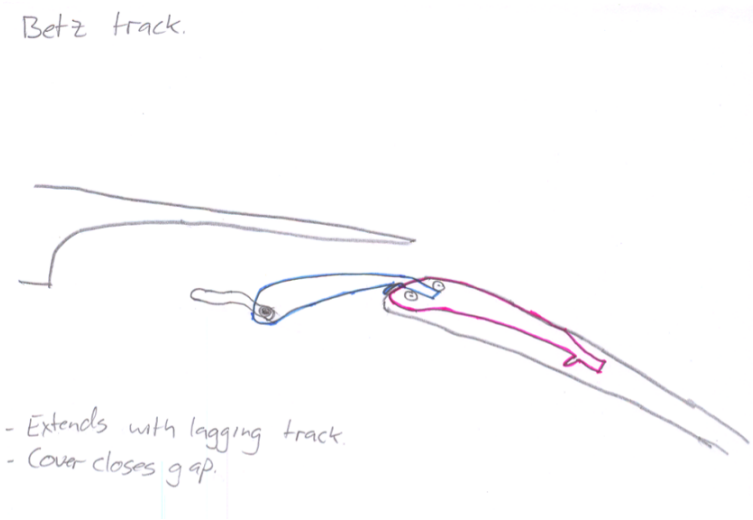


Figure 8.2: Betz track predesign concept

Kruger (unpowered)

Initially, the concept flap was considered to be a Kruger deployed flap. Kruger flaps are generally hinged at the pressure side of the leading edge of a wing. This would have been acceptable if

the concept flap was not moved to the suction side of the leading edge. This concept (Fig. 8.3) modifies the entire flap deployment method by hinging the entire primary flap onto the concept flap which is hinged to a lagging track. For actuation the flap would move outwards until the concept flap reaches the end of the track. once this occurs the flap will rotate clockwise into its final position. This actuation saves considerably on weight of additional structures required. The concept scoring for this concept is available in appendix F.3.

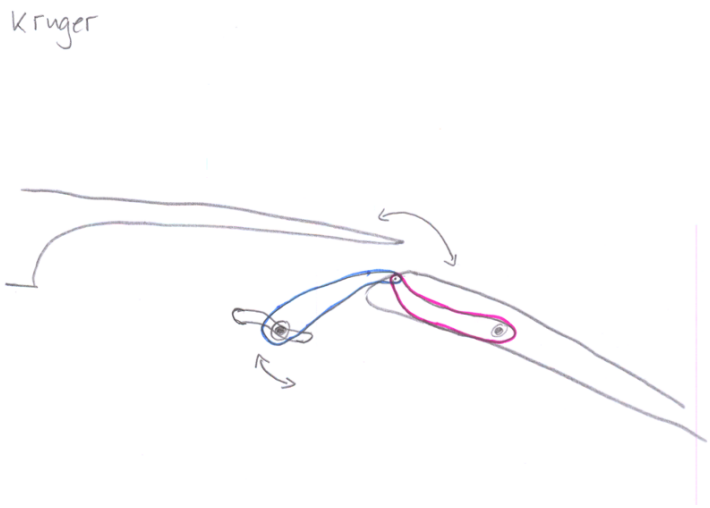


Figure 8.3: Unpowered Krueger flap predesign concept

Powered Betz Track

The unpowered Betz Track relies on a passive means of actuation. The logical progression is to add an additional gearbox to the torque tube actuation system which can be used to deploy the Betz flap (Fig. 8.4). This minimises any additional external structures that are required by the unpowered version- instead all structures are housed inside the flap track fairings allowing an increase in aerodynamic efficiency and decrease in noise. The concept scoring for this concept is available in appendix F.4.

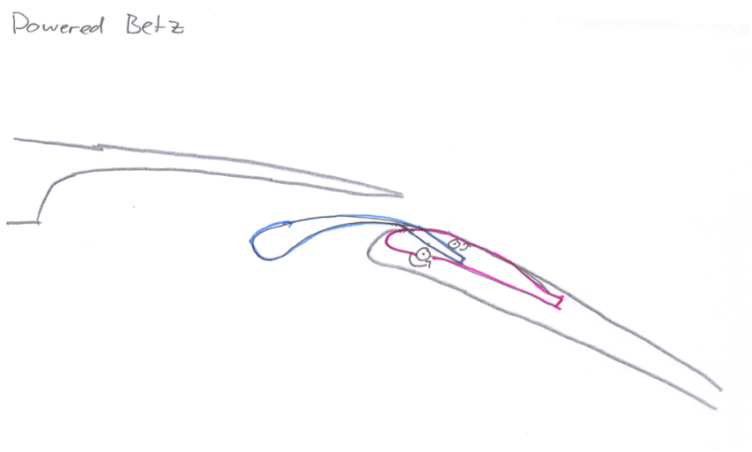


Figure 8.4: Powered Betz predesign concept

Fixed Position

The idea for this concept is to have the simplest concept flap possible and to see what effect it will have on the entire system (Fig. 8.5). A fixed position concept flap means that, by using a numerical geometric optimisation, the shape can be made to fulfil all performance criteria and not be constrained by the geometry of the main flap. This does however cause an issue with stowage as there will be space lost within the wing that can be used for fuel storage. The concept scoring for this concept is available in appendix F.5.

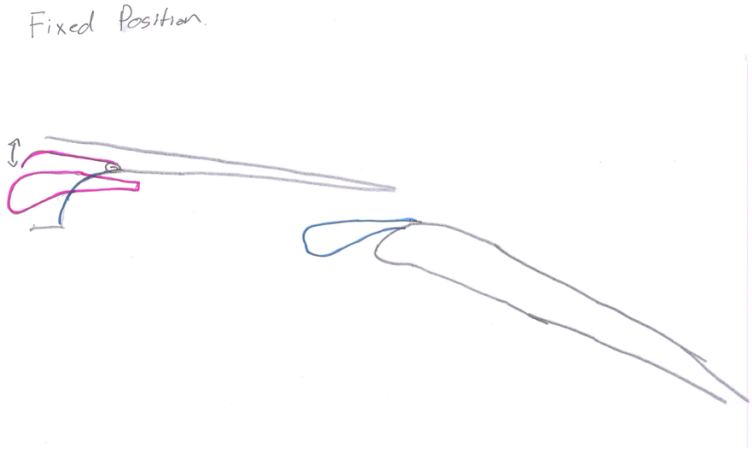


Figure 8.5: Fixed position predesign concept

Bullnose

A Bullnose Kruger flap is a very common leading edge device and in particular can be used in a number of different positions for take off or landing. The modified concept flap bullnose (Fig. 8.6) will however be based on the lagging track like the Betz flap but will instead incorporate a variable camber extension which whould be able to provide different operating points for take off or landing. The system is generally lighter than a full leading edge device but is complex due to the mechanisms involved. Furthermore it is well known that bullnose kruger flap design is

complex and involves much trial and error in windtunnels to achieve a working geometry. The concept scoring for this concept is available in appendix F.6.

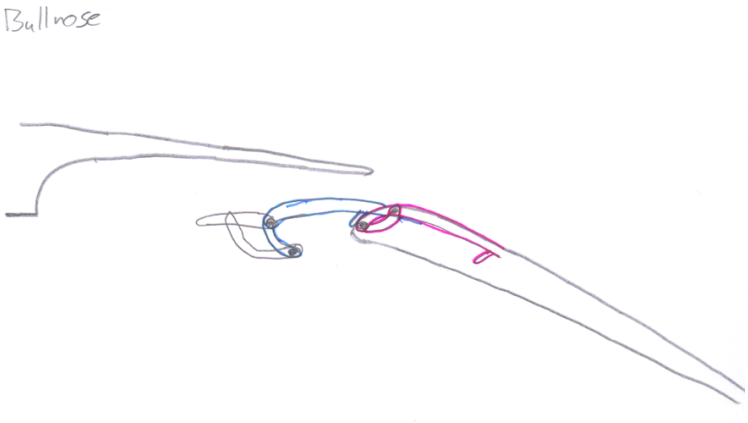


Figure 8.6: Bullnose predesign concept

8.2 Concept Down Selection

Down selection is performed in order to narrow down all the brainstormed concepts by means of a multi criteria decision matrix. Each concept is compared to each other concept and a weighting is applied to the scores in order to minimise problems that can occur when making decisions on a purely subjective basis. The criteria is split into individual disciplines with each discipline having its own individual set of criteria.

Tables 8.1 and 8.2 show the disciplines selected by the author by which each concept will be evaluated. Each discipline is split into a series of individual criteria related to that particular discipline.

Criteria	**Reasoning**
Aerodynamics	
C_{Lmax} *improvement*	Does the concept have a benefit to maximum lift?
L/D Improvement	Does the concept increase aerodynamic efficiency?
Stall Progression	As α increases how will stall progress? Adversely (sudden stall) or slowly?
Trim	Is it foreseen that the concept will unnecessarily increase the overall pitching moments of the profile?
Aerodynamic Noise	
Cove Noise	Does the concept produce noise by having cove regions (similar to landing gear wells)?
Separation Noise	At operating point will the concept have significant separation which will increase noise?
Noise from Supporting Structures	Are there extra external structures which may produce aerodynamic noise?
Kinematic Systems	
Actuation	How is the mechanical operation of the system?
Power Required	Does the actuation system require additional power to run?
Simplicity	Are there many or few parts?
Proven Technology	Is the concept actuation based on a pre existing technology?
Motion	Is the motion of the deployment conventional?
Structure	
Weight	Does the structure add too much weight?
Easy Integration	Is there any sort of possible retrofit capability to the concept?
Additional Structures	Are there extra structures that need to be added for the concept to work?

Table 8.1: Down Selection Process disciplines and criteria part 1

Criteria	**Reasoning**
Optimisation	
Room for Optimisation	Is the concept able to be further optimised by means of numerical optimisation?
Number of Variables	Are there many variables/constraints to account for in an optimisation of the concept?
Flexibility of Design	Would a large redesign completely change the concept?
Cost	
System Complexity	A more complex system is more costly due to having many parts, long assembly and manufacturing time etc.
Maintenance	Is the system easy to maintain?
Certification Time	Is it foreseen that the system will take a long time to certify?
Design Cost	Is the design sufficiently complex that it will be costly to design in detail?
Reliability	
Complete System Loss	If the entire system is lost will the aircraft still be able to complete its mission?
Actuation Jam	Will an actuation jam cause further damage, can normal operation continue?
Redundancy	Is there a back up plan in case of primary system failure?
Structural Damage	Will structural damage be adverse to the system operation?
Manufacturing	
Easy Installation	Is the system easy to install?
Materials	Does the system make use of many varied materials which will be hard to source?
Number of Parts	Is the part count foreseen to be high?

Table 8.2: Down Selection Process disciplines and criteria part 2

Each discipline with its subcategories is compared with a baseline. In the case of the comparison a plus will imply the item is better than the datum whilst a minus will imply a concept is worse than the datum (figure 8.7 is an example of part of the DSP process). A total for each criteria is added to become the 'Score' and then the concept is totalled using equation (8.1) to equate the 'normalised score'. The discipline is then totalled using the same equation to achieve the normalised score for the baseline concept.

	Vitale Concept	Betz Track	Kruger	Powered Betz	Fixed Position	Bullnose
Aerodynamics						
CLmax improvement		+	-	+	+	+
L/D improvement		S	-	S	+	-
Stall progression		+	+	+	+	-
Trim (moments)		S	S	S	+	-
Score	0.00	2.00	-1.00	2.00	4.00	-2.00
Normalised Score	**0.33**	0.67	0.17	0.67	1.00	0.00

Figure 8.7: Example of DSP selection

$$R_{ij} = \frac{S_{ij} - S_j^{min}}{S_j^{max} - S_j^{min}} \tag{8.1}$$

where R_{ij} represents the normalised attribute rating for alternative i with respect to comparison j, S_j^{min} and S_j^{max} are the lowest and the highest possible values of the ratings respectively. The spreadsheets used for this comparison can be seen in appendix F from figure 8.1 - 8.6
After all DSP comparisons are made the data is weighted. Each generalised criteria is given a dominant weight and a designers intuition weighting is also given. Weighting factors are seen in figure F.7. Each table in figures F.8 - F.10 represents one of the baseline concepts (bolded), one of the spreadsheets from the DSP process. And each cell in these tables represents the sum product of the normalised scores with the weights for each scenario.

The data from figures F.8 - F.10 is averaged by scenario[6], then the scenarios are averaged by concept (see figure F.11. This solution is then plotted on a histogram (figure 8.8).

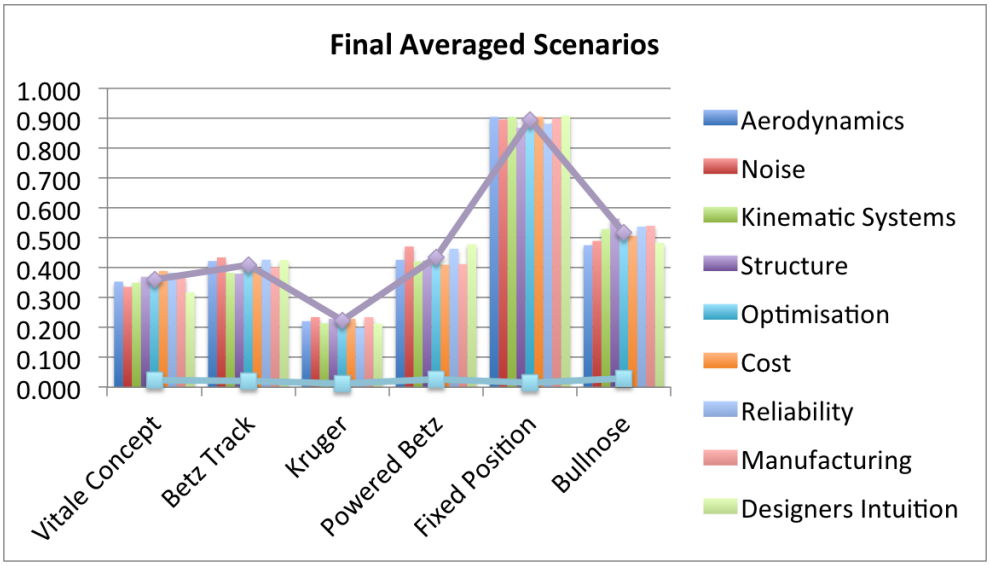


Figure 8.8: Results of concept DSP

[6]eg. for scenario 1 (aerodynamics), all occurrences of the Vitale concept are averaged and placed in the *Final Averaged Scenarios* table in the row for Vitale concept and the column for aerodynamics

The results of the DSP clearly shows that the fixed position concept is the most successful concept and should be investigated further. A risk assessment should still be done to evaluate the design and implementation risks of each concept to confirm whether the DSP selected concept is the most effective. This will be outside the scope of this project.

8.3 Conclusion

By performing an MDO using the DSP process a subjective process of selecting a concept is made inherently more objective by removing uncertainty and doubt from the decision maker. The *Fixed Position* concept is selected as the most likely concept to succeed based on the DSP. A primary reason for this is due to the flexibility of the concept by definition. The concept has no moving parts thus it wins for any manufacturing, cost or reliability screening processes. A risk assessment may yield this concept to be unfeasible due to its impingement on existing structures.

9 Conclusion

9.1 Summary and Conclusions

A Novel concept for a high lift device is investigated, by means of computational studies, to increase aerodynamic performance and decrease aerodynamically generated noise of the TC12 profile in high lift configuration. Based on comparative results of two optimisation methods it was possible to maintain status quo for aerodynamic performance by means of a negligible change in lift and drag production. Aeroacoustic results showed that the implementation of the novel concept decreased high frequency noise by about 10dB.

The TC12 research profile, provided by Airbus GmbH, is presented along with experimental data for the lift coefficient against angle of attack for the profile. This data is validated by the author using two experimental tools, MSES and ANSYS Fluent as well as a semi-empirical method by ESDU. The results of MSES agree very well against those of the TC12 profile in clean configuration by discrepancies are seen when using the code to simulate the TC12 profile in high lift configuration. One notable issue being that stall is not predicted. Results from Fluent agree well with experimental data at angles of attack below stall. Fluent predicts incorrect stall behaviour for the TC12 profile in both clean and high lift configuration- a gradual trailing edge stall is predicted whilst a sharp leading edge stall should be predicted. The ESDU method predicts lift coefficient at zero angle of attack well but maximum lift coefficient is over predicted. These results were thus referred to as the baseline results.

A novel concept is suggested that will improve aerodynamic performance of the TC12 profile in high lift configuration. Two sets of aerodynamic investigations are performed with the aim of improving aerodynamic performance of the profile.

In the first aerodynamic investigation, a zero order optimisation process is used to increase aerodynamic performance. The zero order approach used a simplified method to optimise the TC12 profile flap in isolation of the rest of the high lift system. This optimisation showed a *proof of concept* that the suggested flap extension did increase aerodynamic performance of the airfoil in isolation. The optimisation process was successful on a system level. When the optimised solution was implemented into the full system and analysed in MSES and Fluent results showed that the flap extension implemented into the high lift system decreased the stall angle and maximum lift coefficient. The Coanda effect was observed due to the inclusion of the flap extension in the vicinity of the spoiler cove. The flow was attracted to the flap extension increasing velocity along the extension thus increasing lift here. Simultaneously the recirculation region within the spoiler cove was decreased thus decreasing pressure along span at the main element. Overall the effects caused a decrease in the total lift produced by the profile.

The second aerodynamic investigation implements ANSYS DesignXplorer as a different optimisation method. This was used to increase aerodynamic performance of the TC12 profile in high lift configuration. Due to limitations in computing time the results of the simulation were not converged but should show a trend towards convergence. The optimised results showed lift and drag against angle of attack to follow similar trends to that of the baseline.

Acoustic simulations using two types of turbulence models were tested. The SA turbulence model was tested and results instantly disregarded since they did not follow trends. Results

of the acoustic simulations using the DES turbulence model were much more favourable. The Sound Pressure Level response of the DesignXplorer optimised concept was compared to the TC12 profile in high lift configuration. The simulations showed that the optimised solution caused a reduction in higher frequency tones of up to 10dB. This figure is of major relevance as the FP-7 framework calls for a reduction of noise of 10dB by the year 2020. The reduction of noise is due to the impingement of the flap concept on the flow field at the slat cove which stabilises the fluctuating shear layer reducing noise in this vicinity. This result shows that there is room for further investigation of the concept as a noise reduction device.

Finally, some predesign concepts are examined, in a design investigation, using a Down Selection Process to apply objective evaluation to the subjective approach of finding a more realisable solution of the concept flap extension. A *fixed concept* is seen to work best because of the improvements it has over other concepts with minimisation of parts, costs and maintenance. The results of the DSP need further work to achieve a workable solution.

9.2 Recommendations for Future Work

Work done in this dissertation uncovered a number of new research areas that can be further expanded upon.

Experimental Studies

The lift and drag data from the simulations performed should be confirmed by means of experimental wind tunnel testing. Windtunnel testing could be conducted following the procedure of Wolkensinger (2008) using the facilities available at the University of the Witwatersrand. This particular model can be modified to include interchangeable geometries for the validation of various flap leading edge concepts. Pressure taps should be used to measure lift and hot wire anemometers or similar method used to measure drag.

Acoustic signals should be resolved following the procedure suggested by Reboul and Dala (2012) to calculate estimated farfield noise generated by the conventional and optimised TC12 airfoil in high lift configuration.

Using these two experimental studies will aid in finding the shortfalls of the computational studies and allow for a better understanding of the computational results. Visualisation of the spoiler cove by means of Particle image velocimetry can help to understand the noise generating mechanisms of that region of the airfoil.

Aerodynamic Optimisations

This work uncovered that the flap extension concept was not successfully implemented within two different optimisation strategies. A third optimisation study could be employed- the mesh deformation tools within ANSYS Fluent.

The zero order optimisation study revealed that the flap extension concept worked well on the flap in isolation from the rest of the system. The flap extension concept could be employed as a leading edge device. It is recommended that fundamental research on rudimentary configurations of the flap extension be carried out using a series of NACA airfoils as the baseline.

The DesignXplorer optimisation did not converge. A better approach to this optimisation could be to use more relaxed convergence criteria or more powerful computing resources. This could be investigated further.

Computational Aeroacoustics

Additional computational work should be done on the aeroacoustic data of the TC12 profile. Different turbulence models should be tested as well as full span 3D models to see the effect of span on the acoustic results.

A modification of an empirical method such as the code NREL could be one way to computationally validate the data obtained in this study.

Computational Aeroacoustic Optimisations

A more elaborate piece of future work could be to do an aeroacoustic optimisation of the flap extension implemented on the TC12 profile so minimise aerodynamic noise. To optimise the concept the minimisation of SPL at a specific frequency (or range of frequencies) could be set as the objective function. This is currently not feasible since, on current hardware, each transient simulation took 20 hours for the aeroacoustic simulations. This was based on a calculation of 10 seconds per timestep with 7000 timesteps required for the baseline mesh of around 220000 nodes. If an estimated 1000 generations are required for optimisation convergence this leads to an optimisation time of 2.28 years.

By using the acoustic data of the TIMPAN project, modifications can be made to airfoil profiles to see how fundamental modifications affect the sound generated by the profiles after modification.

References

AIAA CFD High Lift Prediction Workshop (2014). [Online]. http://hiliftpw.larc.nasa.gov/index.html (Accessed 10 April 2014).

Angland, D. (2008). *Aerodynamics and Aeroacoustics of Flap Side-Edges*, PhD thesis, University of Southampton.

ANSYS Fluent online user guide (2013). [Online]. http://www.arc.vt.edu/ansys_help/flu_ug/flu_ug_sec_acoustics_sources.html (Accessed 18 February 2014).

ANSYS Fluent online user guide Large Eddy Simulation (LES) Model (2013). [Online]. http://www.arc.vt.edu/ansys_help/flu_th/flu_th_sec_turb_les.html (Accessed 21 October 2013).

Bizzarrini, N., Grasso, F. and Coiro, D. P. (2011). Numerical Optimization for High Efficiency , Low Noise Airfoils, *29th AIAA Applied Aerodynamics Conference, 27-30 June 2011, Honolulu, HI, USA, AIAA*, pp. 1–16.

Brezillon, J., Dwight, R. and Wild, J. (2008). Numerical Aerodynamic Optimisation Of 3D High-lift Configurations, *26th International Congress Of The Aeronautical Sciences*, pp. 1–11.

Brooks, P., Thomas, A. and Schlinker, B. (1983). Progress in rotor broadband noise research., *Vertica* **7**(4): 287–307.

Brooks, T., Pope, D. and Marcolini, M. (1989). Airfoil self-noise and prediction, nasa reference publication, *Technical Report 1218*, National Aeronautics and Space Administration.

Busquin, P. (2001). *European Aeronautics : a vision for 2020 : meeting society's needs and winning global leadership*, Luxembourg, European Commission.

Campbell, J. P. (1964). Airframe noise studies on wings with deployed high-lift devicesstatus of vstol research and development in the united states, *AIAA* (97-106).

Casalino, D., Diozzi, F., Sannino, R. and Paonessa, A. (2008). Aircraft noise reduction technologies: A bibliographic review, *Aerospace Science and Technology* **12**: 1–17.

Chen, H., Zhang, Y., Zhang, W. and Fu, S. (2012). GA Optimization Design of Multi-Element Airfoil, *Seventh International Conference on Computational Fluid Dynamics (ICCFD7)*, pp. 1–6.

Choudhari, M., Khorrami, M. and Lockard, D. (2012). Slat cove noise: 30p30n 3-element, simplified high-lift configuration (modified slat), *Category 7 of BANC-II Workshop*.

Dobrzynski, W. (2008). Almost 40 Years of Airframe Noise Research What did we achieve?, number May, pp. 1–37.

Dobrzynski, W., Nagakura, L., Gehlhar, B. and Buschbaum, A. (1998). Airframe noise studies on wings with deployed high-lift devices, *AIAA* (98-2337).

Duddy, R. (1949). High lift devices and their uses, *Journal of the Aeronautical Society* **53**(465): 859–900.

EASN : Aeronautical Research and Technology Areas (2013). [Online]. http://www.easn.net/research-technology-areas/1/#5 (Accessed 21 February 2013).

ESDU 85033: Increments in Aerofoil Maximum Lift Coefficient due to Deployment of Various High Lift Devices (1992). IHS-Groups UK- based subsidiary, Technical Indexes Ltd.

European High Lift Programme II (2006). [Online]. http://ec.europa.eu/research/transport/projects/items/eurolift_ii_en.htm (Accessed 25 February 2013).

F., F. and Fullmer, J. (1947). Two-dimensional wind-tunnel investigation of the naca 64 1-012 airfoil equipped with two types of leading-edge flap, *Technical Report 1277*, National Advisory Council for Aeronautics.

Fed (1996a). *Federal Aviation Regulations: Part 23 Airworthiness Standards: Normal, Utility, Acrobatic and Commuter Category Airplanes*.

Fed (1996b). *Federal Aviation Regulations: Part 25 Airworthiness Standards: Transport Category Airplanes*.

Ffowcs-Williams, J. E. and Hawking, D. L. (1969). Sound generation by turbulence and surfaces in arbitrary motion., *Philosophical Transactions of the Royal Society of London* **A342**: 264–321.

Fujii, K. (2004). Progress and Future Prospects of CFD in Aerospace: Observations From 30 Years Research, *24th International Congress Of The Aeronautical Sciences*.

Genc, M. (2010). Numerical Simulation of Flow over a Thin Airfoil at High Reynolds Number using a Transition Model, *Proceedings of the Institute of Mechanical Engineers, Part C: Journal of Mechanical Engineering Science*.

Gibson, J. S. (1974). Non-engine aerodynamic noise investigation of a large aircraft, nasa contractor report, *Technical Report CR-2378*, National Aeronautics and Space Administration.

Global Optimization Toolbox (2014). [Online]. http://www.mathworks.com/products/global-optimization/ (Accessed 16 April 2013).

Hansen, H. and Szabo, I. (1998). Investigation of stall characteristics of an a3xx relevant airfoil up to high reynolds numbers in the technology program hak 2, *DaimlerChrysler Aerospace Airbus GmbH* .

Herr, M. (2012). Efficient and Airworthy Passive and Active Airframe Noise Control Strategies, *VKI Lecture Airframe Noise Reduction*, pp. 1–77.

Hirschberg, S. R. . A. (2004). *An Introduction to Acoustics*, Eindhoven University of Technology.

Isikveren, D. A. (2010). Pre-concept techniques, University Lecture.

Kania, W., Gnarowski, W., Stalewski, W., Galpin, S., Goraj, Z. and Figat, M. (n.d.). Aerodynamic Study Of A Novel Trailing-edge Flap Concept Of A High-lift Transport Configuration, pp. 1–10.

Kita, D. (Feb. 1985). Mechanical high lift systems, *Technical report*, Grumman Aerodynamics Lecture Series, Grumman Aerospace Corporation.

Kuo, B. C. and Sarigul-Klijn, N. (2012). Conceptual study of micro-tab device in airframe noise reduction: (ii) 3d computation, *Aerospace Science and Technology* **17**(1): 32 – 39.
URL: *http://www.sciencedirect.com/science/article/pii/S127096381100040X*

Lighthill, M. J. (1952). On sound generated aerodynamically. i. general theory, *Proceeds of the Royal Society. London* **A211**: 564–587.

Lighthill, M. J. (1954). On sound generated aerodynamically. ii. turbulence as a source of sound, *Proceeds of the Royal Society. London* **A222**: 1–32.

Mamo, T. (2010). *Initial Technical Feasibility Study of an Innovative Leading Edge High-Lift Device*, Master's thesis, University of the West of England, Bristol.

Mason, W. H. (2007). High-lift aerodynamics, [Online]. http://www.scribd.com/doc/85164491/PAV-highLift-mason (Accessed 28 February 2013).

Mason, W. H. (2010). Transonic aerodynamics of airfoils and wngs, [Online]. http://www.dept.aoe.vt.edu/~mason/Mason_f/ConfigAeroTransonics.pdf (Accessed 24 June 2013).

Meredith, P. (1993). Viscous phenomena affecting high-lift systems and suggestions for future cfd development, *AGARD CP-515*.

Mistree, F., L. K. and Stonis, L. (1994). Selection in the conceptual design of aircraft, *AIAA-94-4382-CP*.

Modification De La Forme Dun Profil (1980). University Lecture.

MSES Multi-element Airfoil Design/Analysis Software (2013). [Online]. http://acdl.mit.edu/research.html (Accessed 12 February 2013).

Nebenfuhr, B. (2012). *Aerodynamic and Aeroacoustic Analysis of a Multi-Element Airfoil using Hybrid RANS/LES Modeling Approaches*, PhD thesis, Chalmers University Of Technology, Sweden.

NREL AirFoil Noise (2006). [Online]. http://wind.nrel.gov/designcodes/simulators/NAFNoise/ (Accessed 18 April 2013).

OPtimisation for low Environmental Noise impact (2009). [Online]. http://www.cdti.es/recursos/doc/eventosCDTI/Aerodays2011/6E3.pdf (Accessed 6 March 2013).

Orszag, S. A. (1970). Analytical theories of turbulence, *Journal of Fluid Mechanics* **41**.

Patzold, J. (2008). *Numerical optimisation of a three-element high-lift aerofoil*, Master's thesis, University of the West of England, Bristol.

Prandtl, L. and Tietjens, O. G. (1957). *Applied Hydro- and Aeromechanics*, Dover, New York.

Reboul, F. and Dala, L. (2012). Acoustic Measurements in a Low-Speed Wind Tunnel, Type Gttingen, *AIAA Journal* **50**: 2277–2281.

Reckzeh, D. (2003). Aerodynamic Design of the High-Lift-Wing for a Megaliner Aircraft, *Aerospace Science and Technology*, number 7(2), pp. 107–119.

Reckzeh, D. (2004). Aerodynamic Design Of Airbus High-lift Wings In A Multidisciplinary Environment, *European Congress on Computational Methods in Applied Sciences and Engineering ECCOMAS 2004*, number July, pp. 1–19.

Reckzeh, D. (2008). Aerodynamic Design Of The A400m High-lift System, *26th International Congress Of The Aeronautical Sciences*.

Rudolph, K. C. (1996a). High-Lift Systems on Commercial Subsonic Airliners, *NASA CR 4746* (September).

Rudolph, P. K. C. (1996b). High-lift systems on commercial subsonic airliners, nasa contractor report, *Technical Report 4746*, National Aeronautics and Space Administration.

Rumsey, C., Lee-Rausch, E. and Watson, R. (2003). Three-dimensional effects in multi-element high lift computations, *Computers & Fluids* **32**: 631–657.

Rumsey, C. and Ying, S. (2002). Prediction of high lift: review of present cfd capability, *Progress in Aerospace Sciences* **38**: 145–180.

SADE Public Web Site (2009). [Online]. http://www.sade-project.eu/about.html (Accessed 6 March 2013).

Schlichting, H. (2000). *Boundary-Layer Theory, 8th Edition*, Springer.

Seifert, J. (2012). A review of the Magnus effect in aeronautics, *Progress in Aerospace Sciences* **55**: 17–45.

Shang, J. and Huang, P. (2014). Surface plasma actuators modeling for flow control, *Progress in Aerospace Sciences* **67**(0): 29 – 50.

Sijtsma, P. and Stoker, R. (2004). Determination of absolute contributions of aircraft noise components using fly-over array measurements, *Technical Report NLR-TP-2004-167*, National Aerospace Laboratory NLR.

Singer, A., Lockard, D. and Brentner, K. (1999). Computational aeroacoustic analysis of slat trailing-edge flow, *5th AIAA/CEAS Aeroacoustics Conference*, number 99-1802.

Smith, A. (1975). High-Lift Aerodynamics 37th Wright Brothers Lecture, *Journal of Aircraft* **12**(6): 501–530.

Soulat, L., Dridi, W., Moreau, S. and Fosso-Pouangue, A. (2012). Multi-Objective Optimization of a High-Lift Airfoil, *28th International Congress Of The Aeronautical Sciences*, pp. 1–11.

Technologies to IMProve Airframe Noise (2013). [Online]. http://www.xnoise.eu/about-x-noise/projects/generation-2-projects/TIMPAN/ (Accessed 6 March 2013).

The ADHF "advanced dropped hinge flap" patented by Airbus onboard the A350 XWB (2013). [Online]. http://bloga350.blogspot.com/2013/08/the-adhf-advanced-dropped-hinge-flap.html (Accessed 30 March 2014).

Thiede, P. (2001). EUROLIFT - advanced high lift aerodynamics for transport aircraft, *Air and Space EUrope* **3**(3/4): 105–108.

Thomson, K. (1996). *Aerodynamics of kruger flap equipped airfoils*, Master's thesis, Queen's University.

VALidation and Improvement of Airframe Noise prediction Tools (2009). [Online]. http://www.cimne.com/websasp/valiant/default.asp?id=plan (Accessed 6 March 2013).

Van Dam, C. (2002). The aerodynamic design of multi-element high-lift systems for transport airplanes, *Progress in Aerospace Sciences* **38**(2): 101–144.

Vitale, N. (2010). *Implementation of high lift concept on the leading edge of a flap, b.eng individual project*, Master's thesis, University of the West of England, Bristol.

Wagner, C., Huttl, T. and Sagaut, P. (2007). *Large-Eddy Simulation for Acoustics*, Cambridge University Press.

Wild, J. (2008). International Journal of Computational Fluid Dynamics Multi-objective constrained optimisation in aerodynamic design of high-lift systems, *International Journal of Computational Fluid Dynamics* **22**(March 2008): 153–168.

Wolkensinger, C. (2008). *Experimental analysis of the airbus tc12 high-lift profile in the uwe low speed wind tunnel*, Master's thesis, University of the West of England, Bristol.

XFOIL Subsonic Airfoil Development System (2013). [Online]. http://web.mit.edu/drela/Public/web/xfoil/ (Accessed 22 March 2013).

Zhang, X. (2010). Airframe noise: High lift device noise, *Encyclopedia of Aerospace Engineering* .

10 Appendix

A ESDU Tables

Figure A.1 - A.5 are copies of the tables from ESDU 85033 used to find values for the ESDU validation.

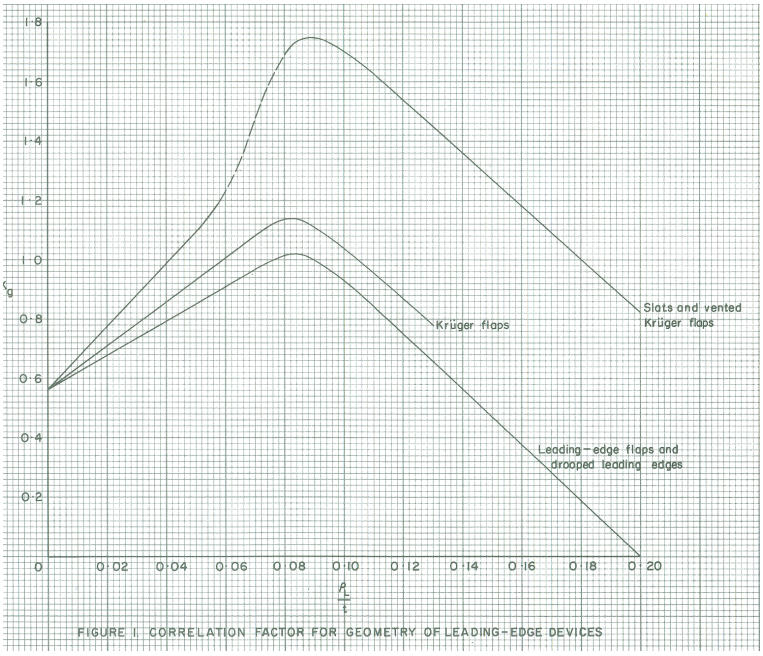


Figure A.1: Figure 1 from ESDU 85033

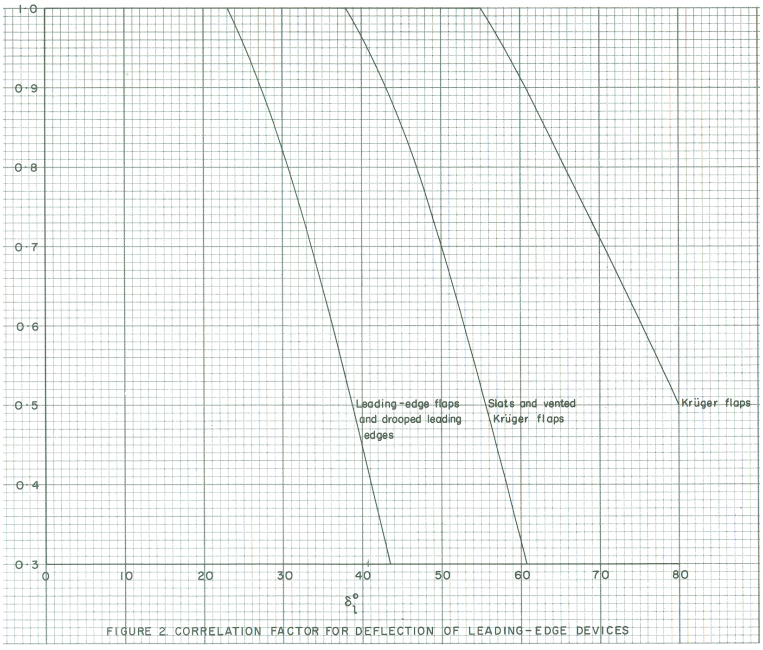


Figure A.2: Figure 2 from ESDU 85033

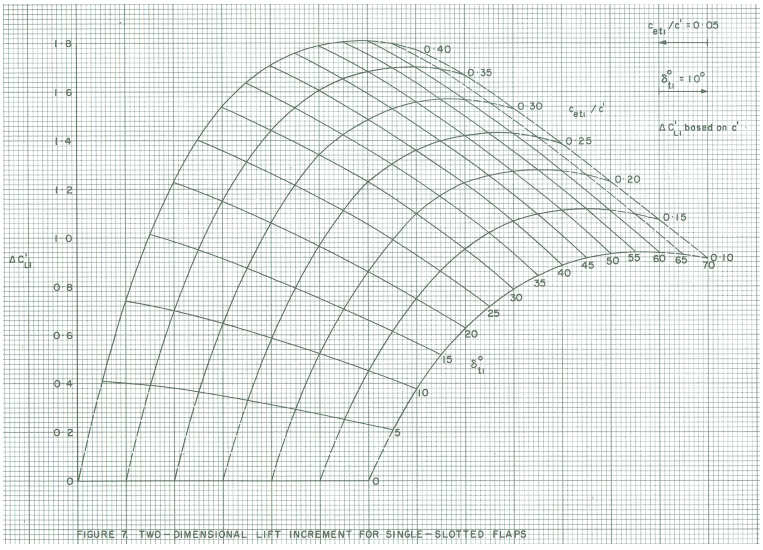


Figure A.3: Figure 7 from ESDU 85033

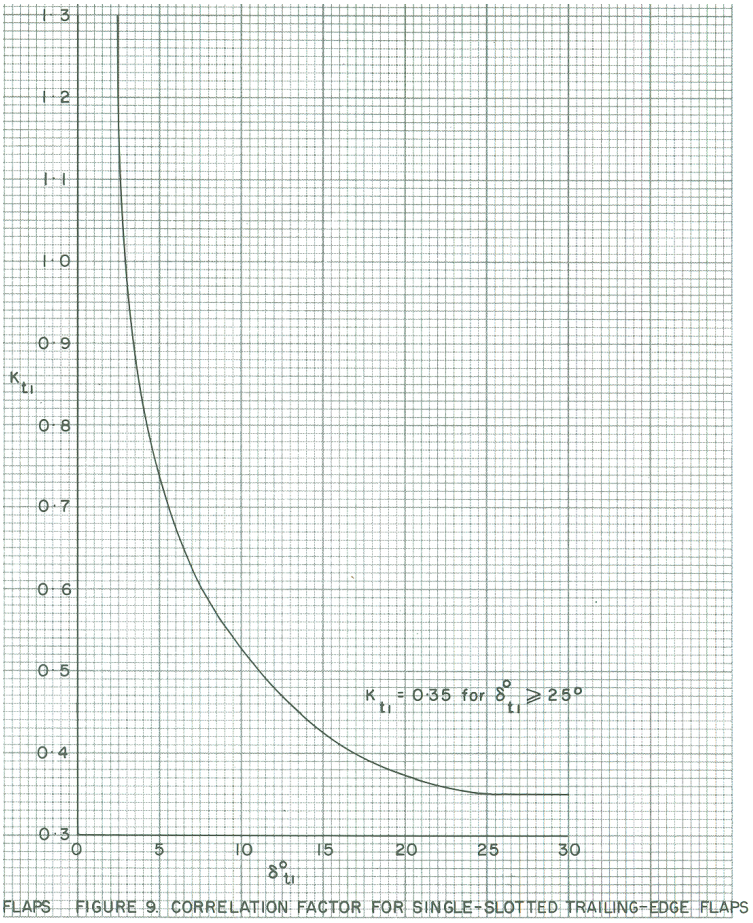


Figure A.4: Figure 9 from ESDU 85033

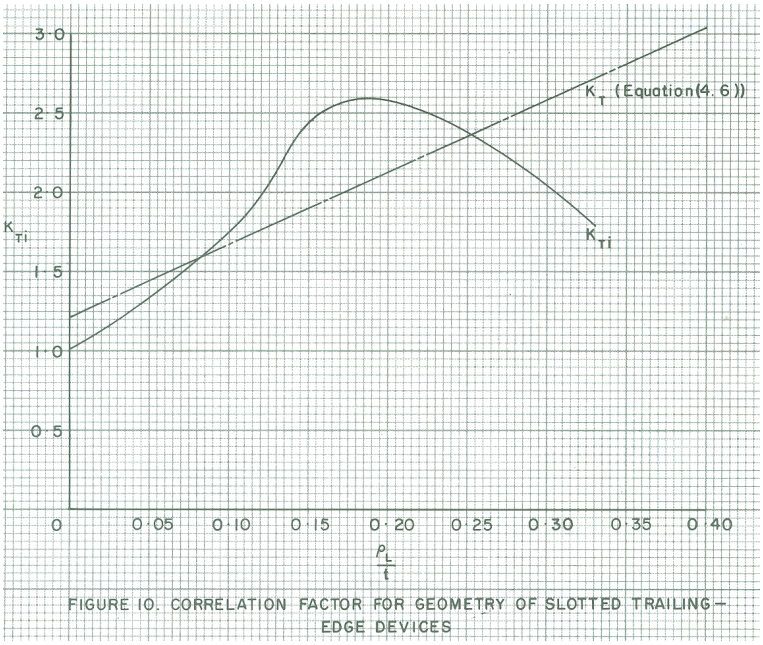


Figure A.5: Figure 10 from ESDU 85033

B MSES Grids

Figures B.1 to B.5 show various aspects of the streamline grid used to calculate the aerodynamic forces on the TC12 profile in high lift configuration. Unlike with RANS equations; MSES uses a series of steady Euler equations coupled with a separate set of integral formulations for the boundary layer calculations. This negates the need for a highly resolved boundary layer mesh.

In figure B.1 note that the grid is slanted. This is done by the grid generator to account for the angle of attack setting for the particular simulation- in this case an angle of 8.09 degrees is shown.

Stagnation points are seen in figures B.3 and B.5. These are calculated by the grid generator and are related to the angle of attack.

In figures B.3 and B.4 an ungrided area is seen at the cove regions of the airfoil; this is an input from the user to simulate the recirculation zone where highly vortical flows are encountered. These flow features cannot be resolved by the MSES solvers and as a result are excluded from the calculation.

MSES solves a series of panels along the airfoil element bodies across the generated streamlines. The panelling of the elements is seen in figures B.6 to B.8. Panelling is performed subjectively to provide a good converged solution. It was observed that the solver was very sensitive to fine panelling along the slat and thus a coarser panelling approach needed to be pursued for that element (fig. B.6).

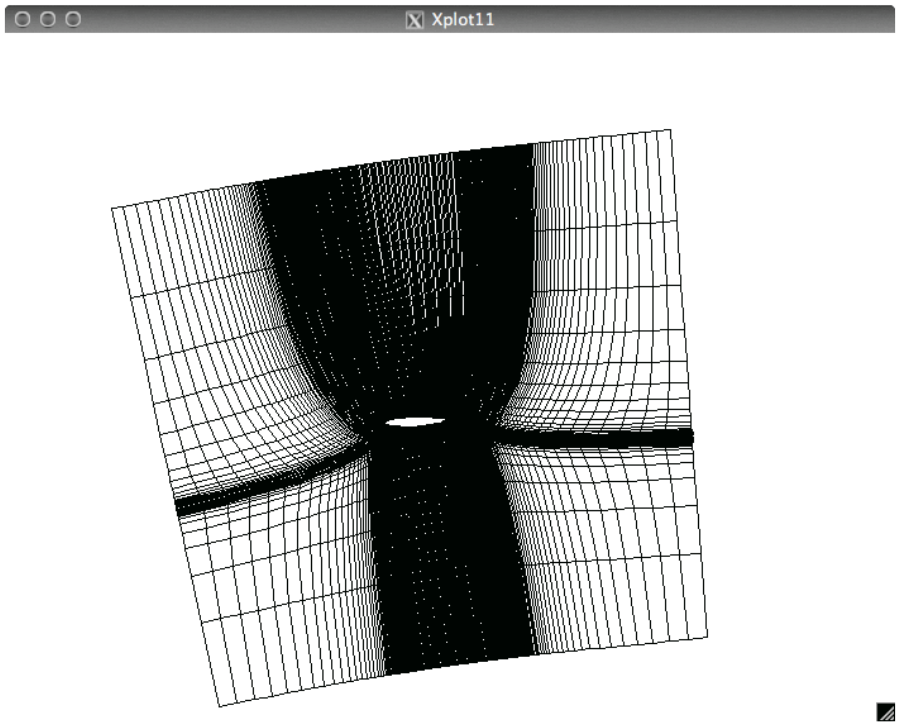


Figure B.1: Full view of grid for the TC12 profile in high lift configuration in MSES

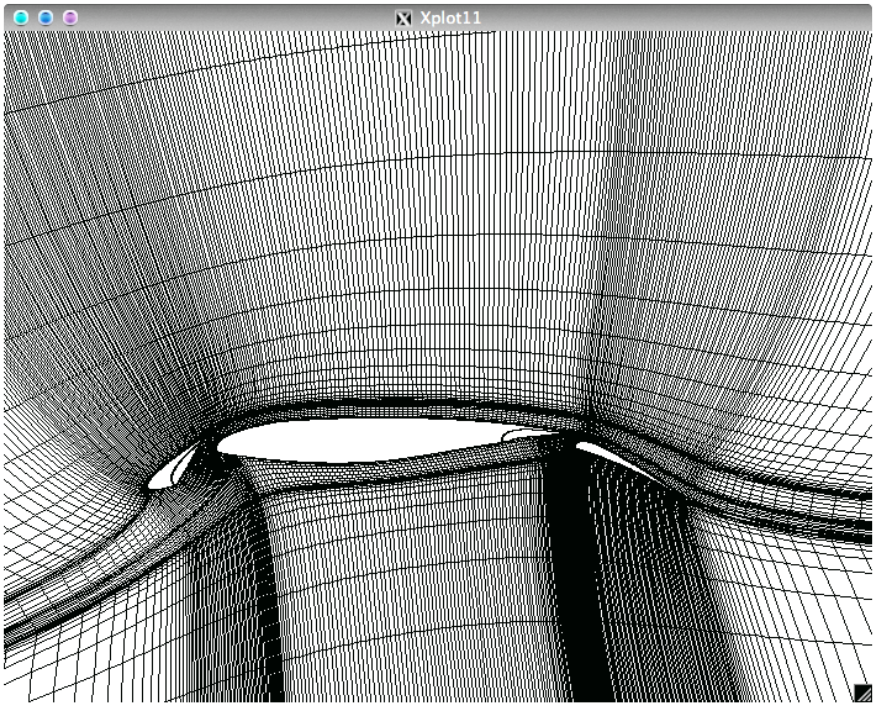


Figure B.2: View of grid close to airfoil for the TC12 in profile high lift configuration in MSES

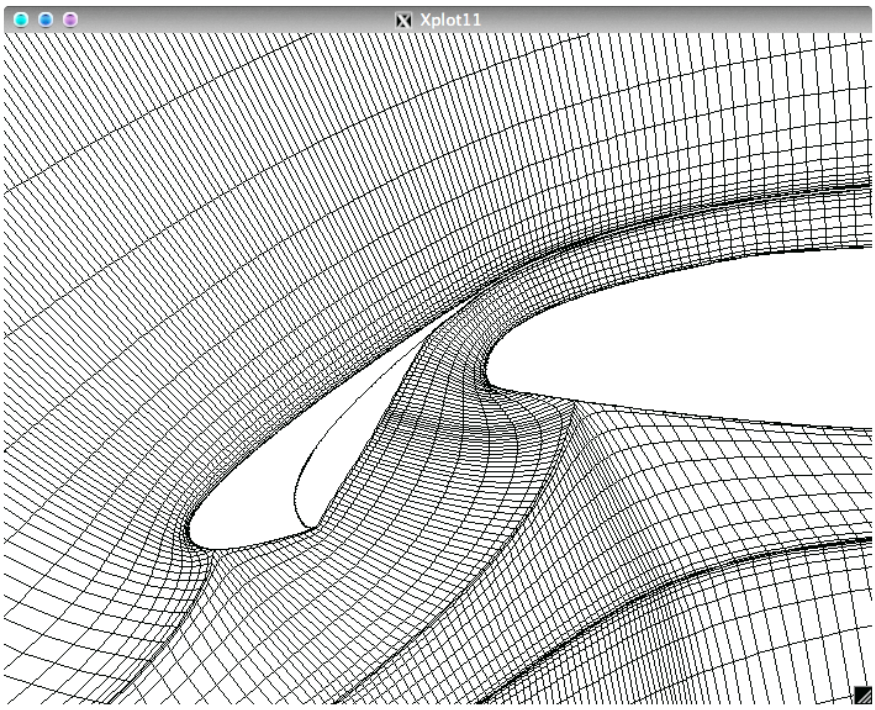


Figure B.3: Grid at slat cove for the TC12 profile high lift configuration in MSES

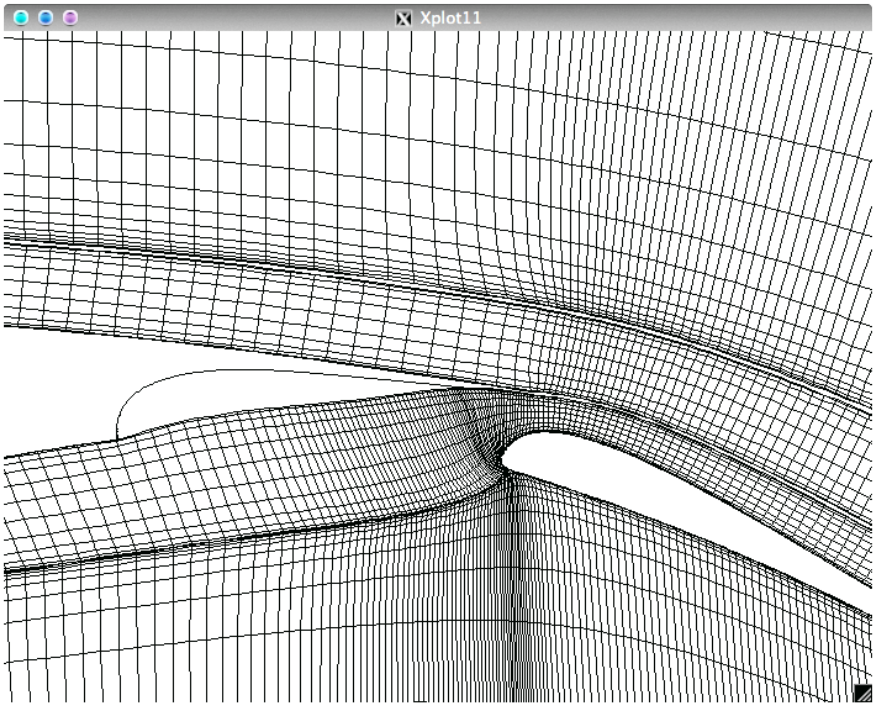


Figure B.4: Grid at spoiler cove for the TC12 profile high lift configuration in MSES

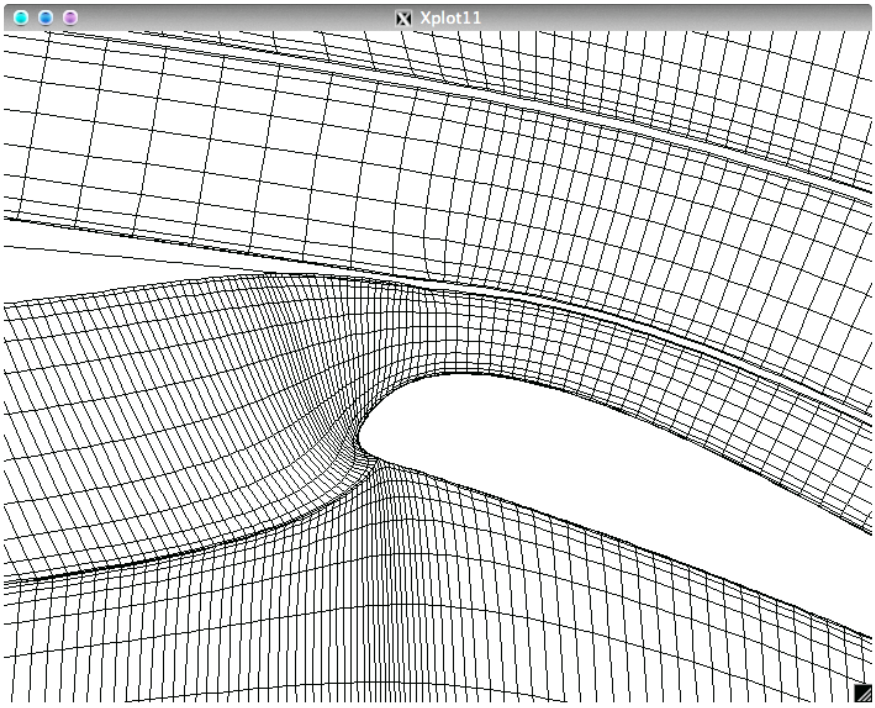


Figure B.5: Grid at leading edge of flap for the TC12 profile in high lift configuration in MSES

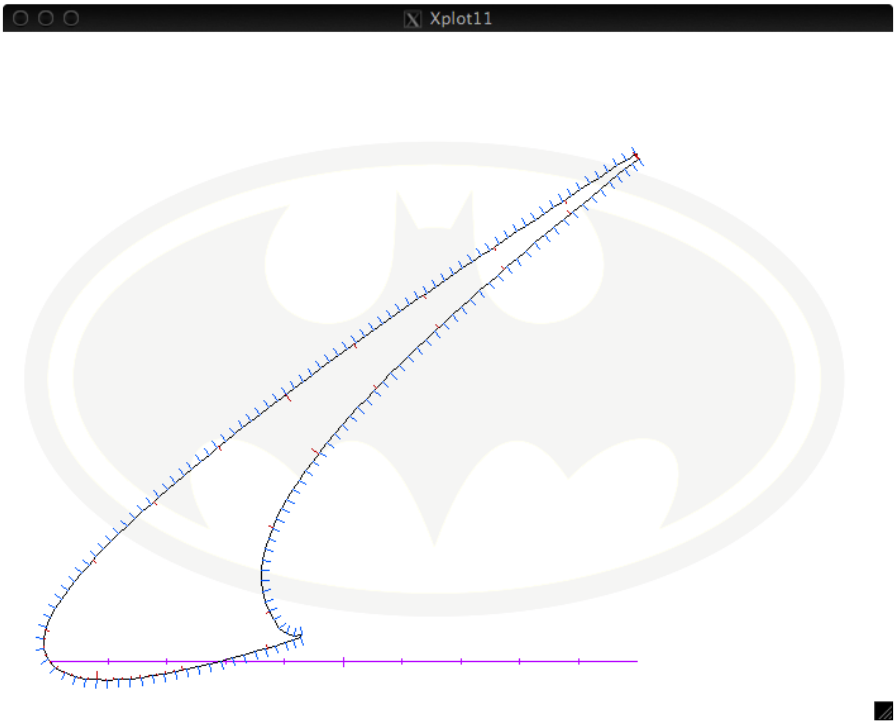


Figure B.6: Slat panelling for the TC12 profile in high lift configuration in MSES

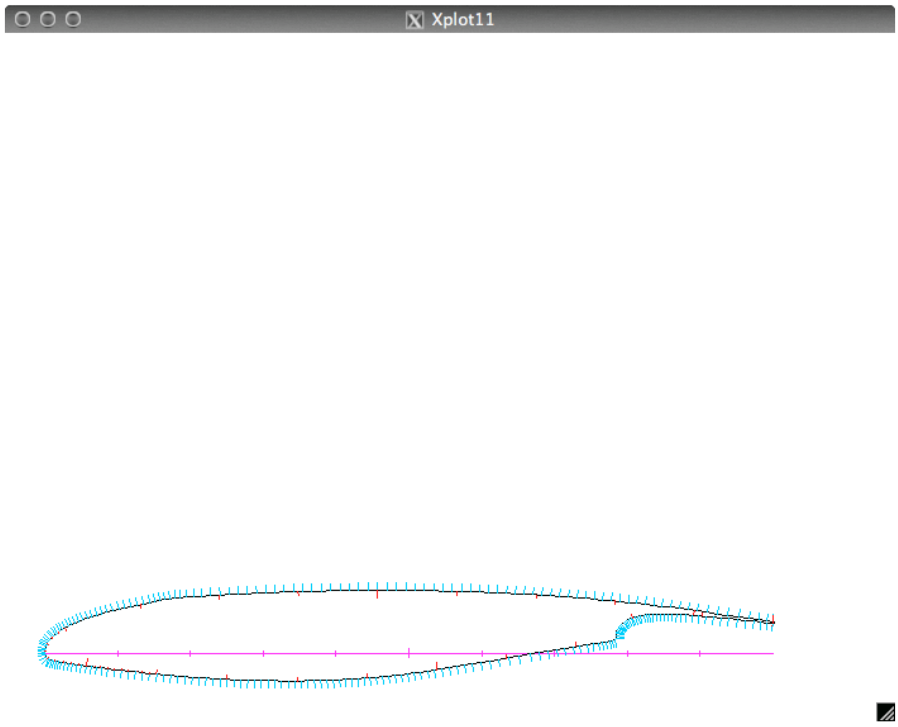


Figure B.7: Main element panelling for the TC12 profile in high lift configuration in MSES

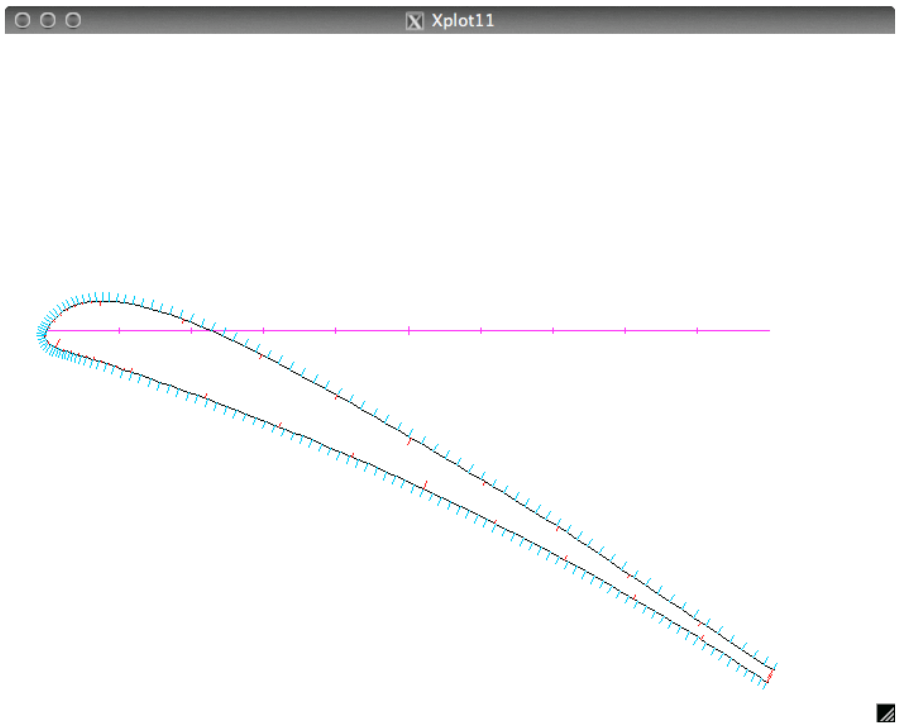


Figure B.8: Flap panelling for the TC12 profile high lift configuration in MSES

C Additional MSES Results

Figures C.1 - C.5 show comparisons of the results obtained with MSES compared to the wind tunnel data for the range of Reynolds numbers shown.

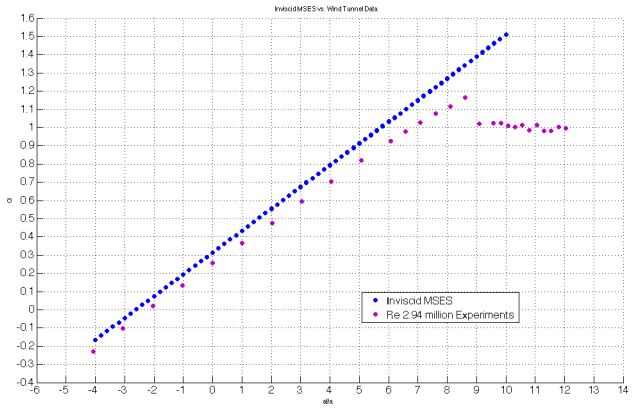


Figure C.1: Cl vs. alfa for TC12 profile in clean configuration, inviscid, MSES

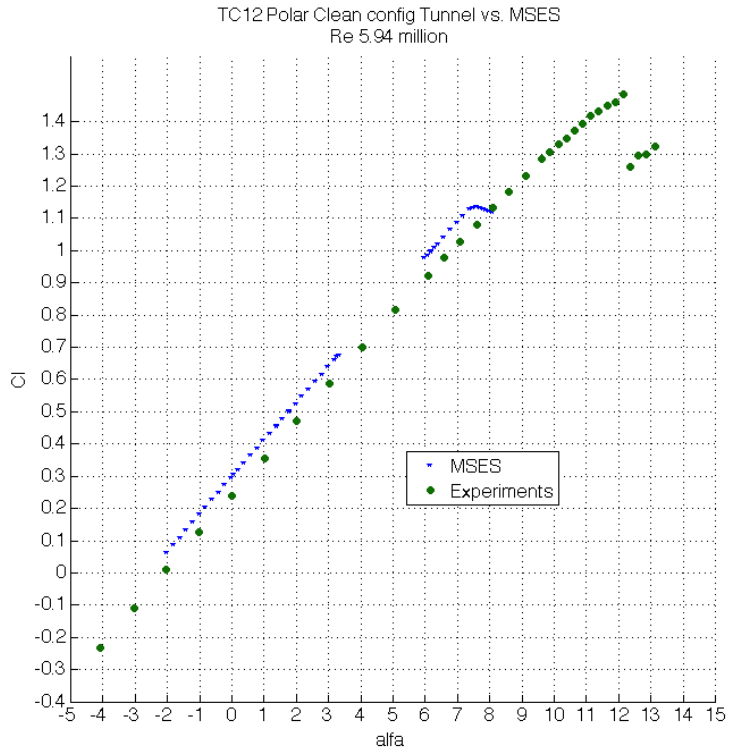


Figure C.2: Cl vs. alfa for TC12 profile in clean configuration, Re 5.94 million, MSES

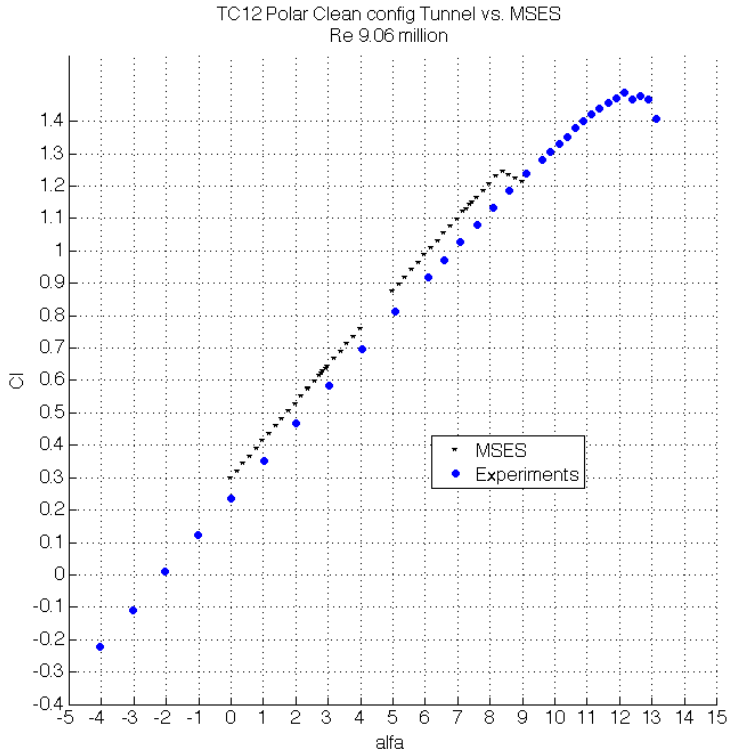


Figure C.3: Cl vs. alfa for TC12 profile in clean configuration, Re 9.06 million, MSES

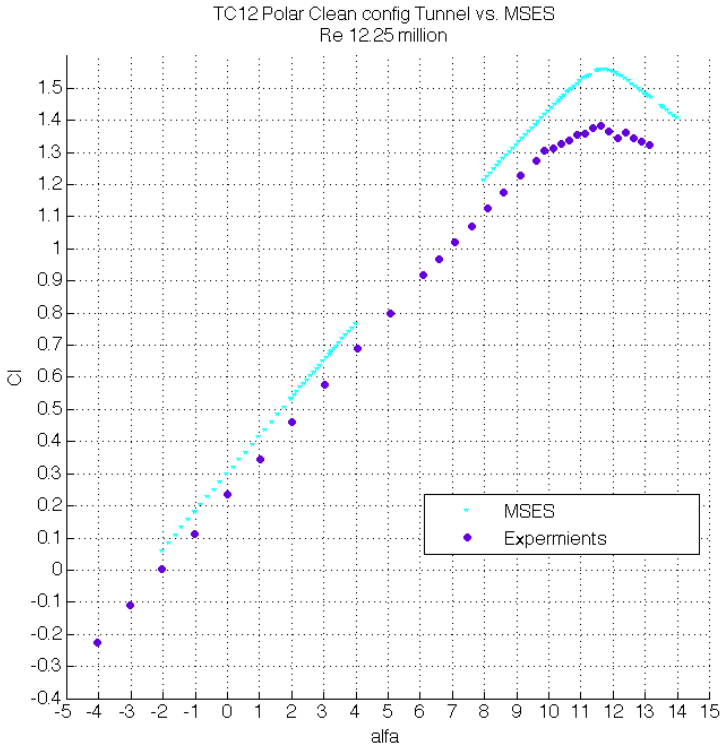


Figure C.4: Cl vs.alfa for TC12 profile in clean configuration, Re 12.25 million, MSES

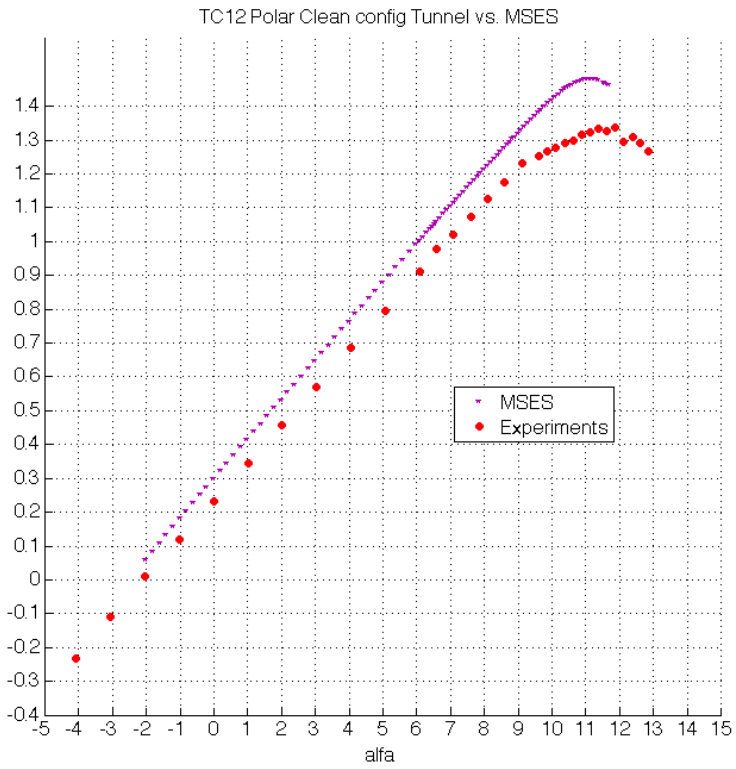


Figure C.5: Cl vs. alfa for TC12 profile in clean configuration, Re 14.44 million, MSES

D Clean Airfoil Mesh in Ansys Mesher

Figure D.1 to D.4 show the meshes created in Ansys Mesher that were used to confirm mesh independence when using a different meshing tool.

Table D.1 shows the breakdown of the elements used in the mesh.

Element Types	**Number of**
Line	2969
Tri	38315
Quad	116190
Element Parts	
Fluid	154505
Far Field	387
Airfoil	2582
Total Elements	157474
Total Nodes	136832

Table D.1: Mesh information for tri mesh of TC12 profile in clean configuration, ANSYS mesher

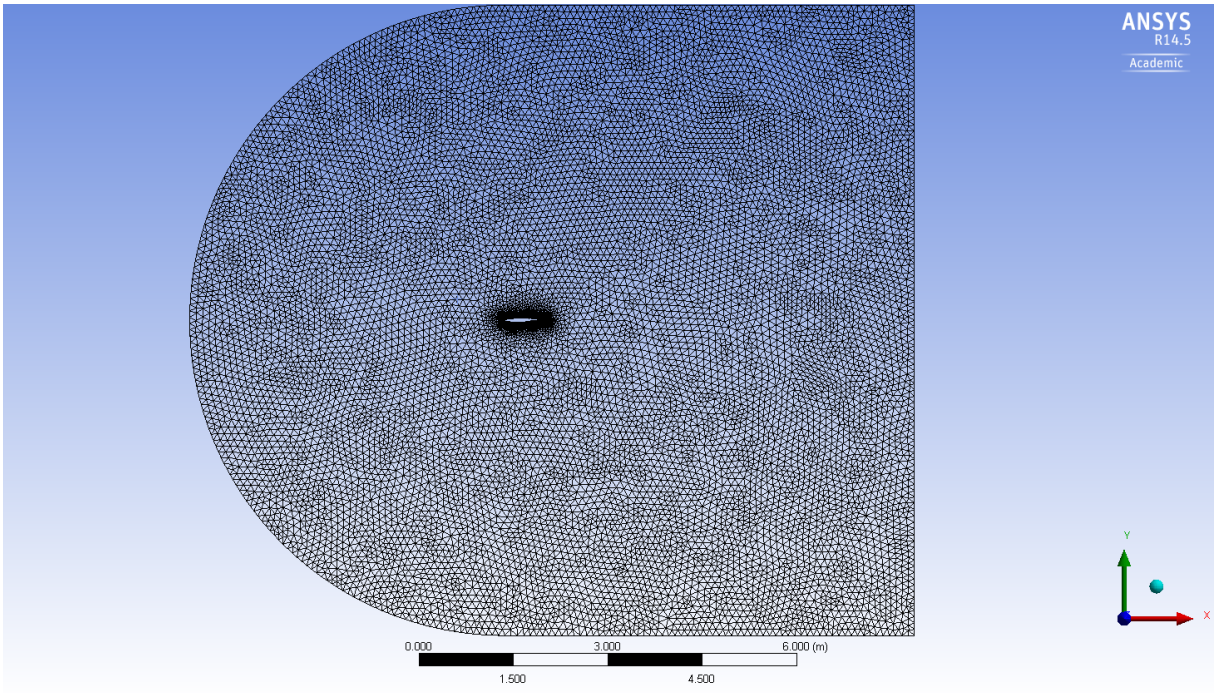


Figure D.1: Mesh for the TC12 profile clean configuration in ANSYS mesher

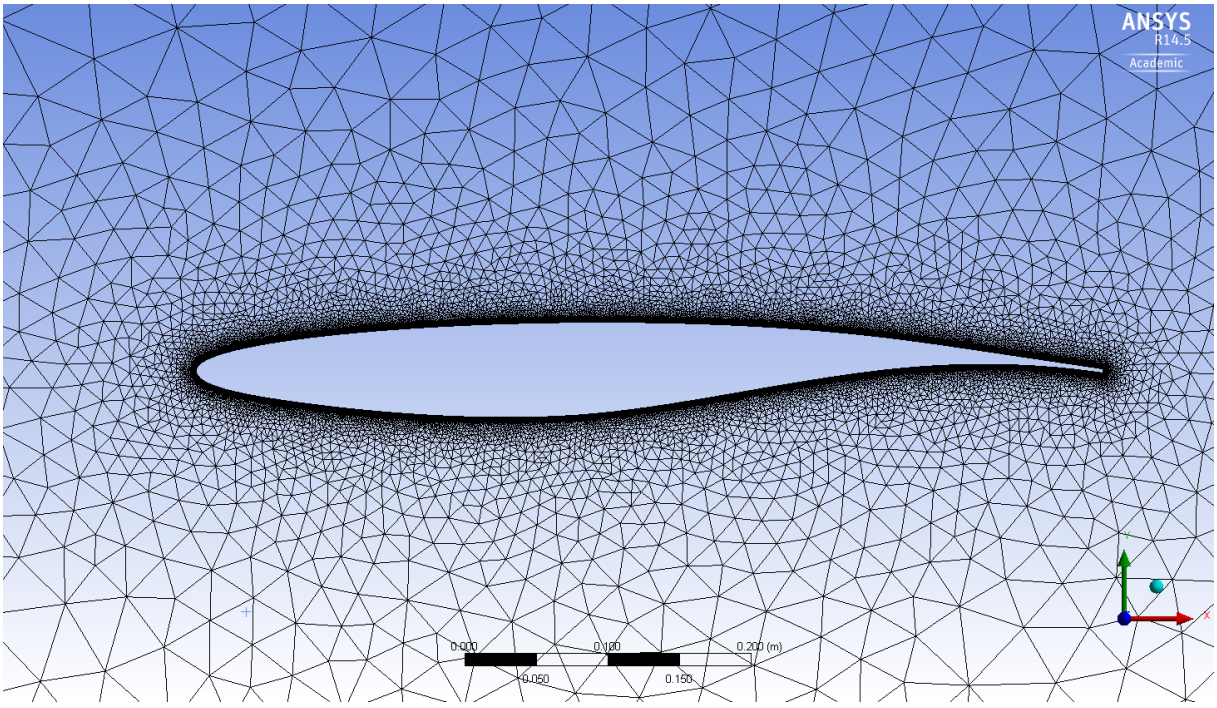


Figure D.2: Mesh for the TC12 profile in clean configuration, ANSYS mesher (zoomed in)

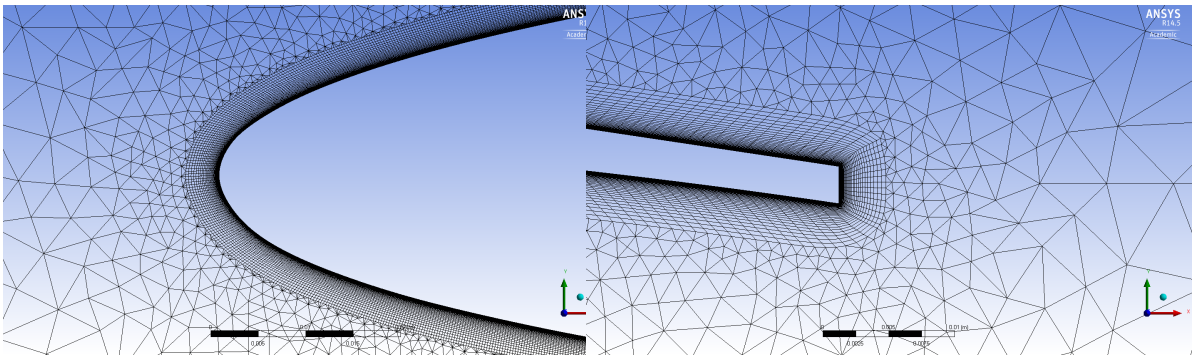


Figure D.3: Mesh for TC12 profile clean configuration leading edge, ANSYS mesher

Figure D.4: Mesh for TC12 profile clean configuration trailing edge, ANSYS mesher

Table D.2 shows the values obtained by the tri mesh and compares them to the values obtained in the validation section. The differences between these meshes are negligible. From this it can be concluded that the new mesh strategy can be used for the high lift configuration with negligible difference to current results.

Cl	Cl difference	Cd	Cd difference	Cm	Cm difference
1.13462	1.0392%	0.02017	1.108%	0.08957	2.0267%

Table D.2: Discrepancies between quad mesh and tri mesh for TC12 profile in clean configuration

E Validation of Tools for Zero Order Optimisation

E.1 MATLAB Genetic Algorithm Toolbox

Validation is performed on the optimisation toolbox as well as on the solver settings for a single point optimisation. For validation the GA solver is used to find the angle of attack at which to lift to drag ratio is the highest, for a fixed Mach and Reynolds number, for the flap of the TC12 profile. If the solver finds the correct solution it can be concluded that the MATLAB Genetic Algorithm optimises for a single point optimum sufficiently well. Multiple objective optimisation validation is almost impossible according to Wild (2008) due to the lack of experimental data available for systematic changes of various geometric parameters.

Validation Problem

$$min(\mathbf{F}_{obj}(x)), (x \in \mathbb{R}) \tag{E.1}$$

Validation Design Variables

$$\mathbf{F}_{obj}(x) = -C_L \tag{E.2}$$

$$x = \alpha \tag{E.3}$$

E.2 Validation Solutions

The solution is converged when the objective function converges to a tolerance of 0.0001. Figure E.1 shows the convergence of the solution as the generations proceed. The solution is well converged.

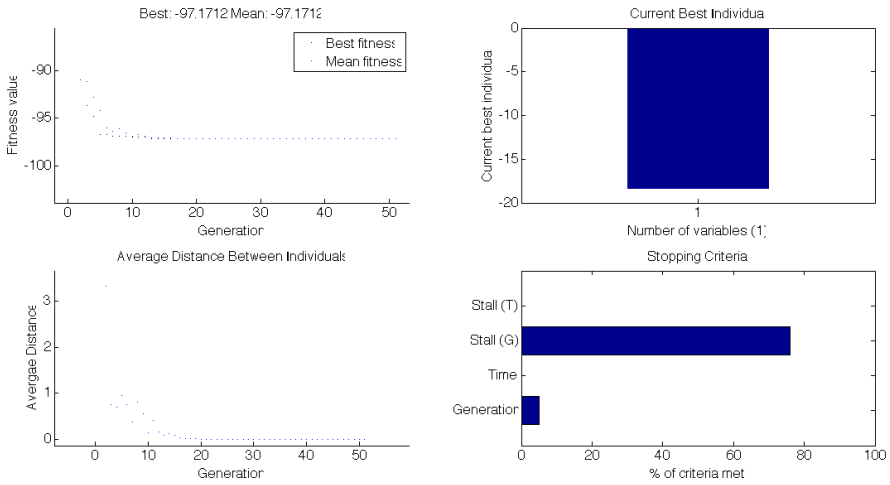


Figure E.1: GA results for toolbox validation

The GA provides a sufficient solution finding stall at -12.7 degrees (local coordinates based on zero angle being the flap setting angle). Given the problem posed, the tool was deemed valid for optimisations.

F Down Selection Process Data

Figures F.1 to F.6 are the resulting raw data of the Down Selection Process. Each figure has a baseline concept to which each of the other concepts is compared based on the given criteria. Selection is subjective.

	Vitale Concept	Betz Track	Kruger	Powered Betz	Fixed Position	Bullnose
Aerodynamics						
CLmax improvement		+	-	+	+	+
L/D improvement		S	-	S	+	-
Stall progression		+	+	+	+	-
Trim (moments)		S	S	S	+	-
Score	0.00	2.00	-1.00	2.00	4.00	-2.00
Normalised Score	**0.33**	0.67	0.17	0.67	1.00	0.00
Noise						
Cove Noise	S	S	S	S	-	-
Separation Noise	S	+	+	+	+	+
Noise from supporting structures	S	+	+	+	+	+
Score	0.00	2.00	2.00	2.00	1.00	1.00
Normalised Score	**0.00**	1.00	1.00	1.00	0.50	0.50
Kinematic Systems						
Actuation		+	+	+	+	S
Power required		S	+	-	+	+
Simplicity		-	+	S	+	-
Proven technology		-	+	+	S	+
Motion		-	-	+	+	+
Score	0.00	-2.00	3.00	2.00	4.00	2.00
Normalised Score	**0.33**	0.00	0.83	0.67	1.00	0.67
Structure						
Weight		S	S	-	+	+
Easy integration into existing system		-	+	S	+	+
Additional structures		-	+	+	+	S
Score	0.00	-2.00	2.00	0.00	3.00	2.00
Normalised Score	**0.40**	0.00	0.80	0.40	1.00	0.80
Optimisation						
Room for optimisation		S	+	S	+	+
Number of variables		-	S	+	+	+
Flexibility of design		S	S	S	+	+
Score	0.00	-1.00	1.00	1.00	3.00	3.00
Normalised Score	**0.25**	0.00	0.50	0.50	1.00	1.00
Cost						
System complexity		-	+	+	+	S
Maintenance		-	+	S	+	+
Certification time		S	S	S	+	S
Design Cost		S	S	S	S	+
Score	0.00	-2.00	2.00	1.00	3.00	2.00
Normalised Score	**0.40**	0.00	0.80	0.60	1.00	0.80
Reliability						
Complete system lost		S	-	S	+	+
Actuation jam		+	-	+	+	S
Redundancy		S	S	S	+	-
Structural Damage		+	-	+	+	+
Score	0.00	2.00	-3.00	2.00	4.00	1.00
Normalised Score	**0.43**	0.71	0.00	0.71	1.00	0.57
Manufacturing						
Easy Installation		-	S	-	+	S
Materials		S	S	S	S	S
Number of parts		-	+	+	+	S
Score	0.00	-2.00	1.00	0.00	2.00	0.00
Normalised Score	**0.50**	0.00	0.75	0.50	1.00	0.50

Figure F.1: Comparison criterion Vitale baseline

1	Betz Track	Vitale Concept	Kruger	Powered Betz	Fixed Position	Bullnose
Aerodynamics						
CLmax improvement		-	S	S	+	+
L/D improvement		-	-	S	+	-
Stall progression		S	+	-	+	-
Trim (moments)		S	S	S	+	-
Score	0.00	-2.00	0.00	-1.00	4.00	-2.00
Normalised Score	**0.33**	0.00	0.33	0.17	1.00	0.00
Noise						
Cove Noise		-	S	-	+	-
Separation Noise		-	S	S	S	S
Noise from supporting structures		-	S	+	+	+
Score	0.00	-3.00	0.00	0.00	2.00	0.00
Normalised Score	**0.60**	0.00	0.60	0.60	1.00	0.60
Kinematic Systems						
Actuation		S	-	-	+	+
Power required		-	-	-	+	+
Simplicity		+	-	-	+	S
Proven technology		-	+	S	+	+
Motion		+	-	+	+	+
Score	0.00	0.00	-3.00	-2.00	5.00	4.00
Normalised Score	**0.38**	0.38	0.00	0.13	1.00	0.88
Structure						
Weight		+	+	-	+	+
Easy integration into existing system		+	S	+	+	+
Additional structures		+	S	+	+	S
Score	0.00	3.00	1.00	1.00	3.00	2.00
Normalised Score	**0.00**	1.00	0.33	0.33	1.00	0.67
Optimisation						
Room for optimisation		S	S	-	S	+
Number of variables		+	S	S	+	-
Flexibility of design		-	S	S	S	S
Score	0.00	0.00	0.00	-1.00	1.00	0.00
Normalised Score	**0.50**	0.50	0.50	0.00	1.00	0.50
Cost						
System complexity		+	+	-	+	S
Maintenance		+	+	-	+	+
Certification time		S	S	-	+	S
Design Cost		S	-	-	+	-
Score	0.00	2.00	1.00	-4.00	4.00	0.00
Normalised Score	**0.50**	0.75	0.63	0.00	1.00	0.50
Reliability						
Complete system lost		S	-	+	-	S
Actuation jam		-	-	+	+	+
Redundancy		+	S	-	+	S
Structural Damage		+	-	S	+	+
Score	0.00	1.00	-3.00	1.00	2.00	2.00
Normalised Score	**0.60**	0.80	0.00	0.80	1.00	1.00
Manufacturing						
Easy Installation		+	S	+	+	+
Materials		S	S	S	S	S
Number of parts		+	+	S	+	+
Score	0.00	2.00	1.00	1.00	2.00	2.00
Normalised Score	**0.00**	1.00	0.50	0.50	1.00	1.00

Figure F.2: Comparison criterion Betz baseline

	Kruger	Vitale Concept	Betz Track	Powered Betz	Fixed Position	Bullnose
Aerodynamics						
CLmax improvement		S	+	+	+	+
L/D improvement		+	+	+	+	S
Stall progression		S	S	S	+	-
Trim (moments)		S	S	S	+	-
Score	0.00	1.00	2.00	2.00	4.00	-1.00
Normalised Score	**0.20**	0.40	0.60	0.60	1.00	0.00
Noise						
Cove Noise		-	S	S	+	-
Separation Noise		+	S	S	S	S
Noise from supporting structures		-	+	+	+	S
Score	0.00	-1.00	1.00	1.00	2.00	-1.00
Normalised Score	**0.33**	0.00	0.67	0.67	1.00	0.00
Kinematic Systems						
Actuation		+	+	+	+	+
Power required		S	+	-	+	+
Simplicity		+	-	+	+	+
Proven technology		-	-	-	+	S
Motion		-	+	+	+	+
Score	0.00	0.00	1.00	1.00	5.00	4.00
Normalised Score	**0.00**	0.00	0.20	0.20	1.00	0.80
Structure						
Weight		+	S	-	+	+
Easy integration into existing system		S	S	S	+	+
Additional structures		S	S	+	-	S
Score	0.00	1.00	0.00	0.00	1.00	2.00
Normalised Score	**0.00**	0.50	0.00	0.00	0.50	1.00
Optimisation						
Room for optimisation		S	S	-	+	S
Number of variables		+	S	S	+	-
Flexibility of design		+	+	+	+	+
Score	0.00	2.00	1.00	0.00	3.00	0.00
Normalised Score	**0.00**	0.67	0.33	0.00	1.00	0.00
Cost						
System complexity		+	S	+	+	S
Maintenance		S	-	-	+	S
Certification time		S	S	S	+	S
Design Cost		+	S	S	+	S
Score	0.00	2.00	-1.00	0.00	4.00	0.00
Normalised Score	**0.20**	0.60	0.00	0.20	1.00	0.20
Reliability						
Complete system lost		+	+	+	-	+
Actuation jam		+	+	+	+	S
Redundancy		S	+	S	+	S
Structural Damage		+	+	+	-	+
Score	0.00	3.00	4.00	3.00	0.00	2.00
Normalised Score	**0.00**	0.75	1.00	0.75	0.00	0.50
Manufacturing						
Easy Installation		S	S	S	+	+
Materials		-	+	-	S	+
Number of parts		+	S	S	+	-
Score	0.00	0.00	1.00	-1.00	2.00	1.00
Normalised Score	**0.33**	0.33	0.67	0.00	1.00	0.67

Figure F.3: Comparison criterion Krueger baseline

	Powered Betz	Vitale Concept	Betz Track	Kruger	Fixed Position	Bullnose
Aerodynamics						
CLmax improvement		S	S	-	+	+
L/D improvement		-	+	-	+	-
Stall progression		S	-	-	+	-
Trim (moments)		S	S	S	+	-
Score	0.00	-1.00	0.00	-3.00	4.00	-2.00
Normalised Score	**0.43**	0.29	0.43	0.00	1.00	0.14
Noise						
Cove Noise		+	+	-	+	-
Separation Noise		-	S	S	S	S
Noise from supporting structures		-	-	-	+	-
Score	0.00	-1.00	0.00	-2.00	2.00	-2.00
Normalised Score	**0.50**	0.25	0.50	0.00	1.00	0.00
Kinematic Systems						
Actuation		-	-	S	+	-
Power required		+	+	+	+	+
Simplicity		+	+	-	+	+
Proven technology		S	S	+	+	+
Motion		S	-	-	-	-
Score	0.00	1.00	0.00	0.00	3.00	1.00
Normalised Score	**0.00**	0.33	0.00	0.00	1.00	0.33
Structure						
Weight		S	+	+	+	+
Easy integration into existing system		S	S	-	S	+
Additional structures		S	-	S	-	+
Score	0.00	0.00	0.00	0.00	0.00	3.00
Normalised Score	**0.00**	0.00	0.00	0.00	0.00	1.00
Optimisation						
Room for optimisation		+	S	-	+	S
Number of variables		+	S	S	+	-
Flexibility of design		+	+	-	S	+
Score	0.00	3.00	1.00	-2.00	2.00	0.00
Normalised Score	**0.40**	1.00	0.60	0.00	0.80	0.40
Cost						
System complexity		+	S	-	+	S
Maintenance		S	+	S	+	+
Certification time		S	S	-	+	S
Design Cost		+	S	-	+	S
Score	0.00	2.00	1.00	-3.00	4.00	1.00
Normalised Score	**0.43**	0.71	0.57	0.00	1.00	0.57
Reliability						
Complete system lost		S	-	-	-	S
Actuation jam		-	-	-	+	-
Redundancy		S	S	-	+	-
Structural Damage		S	S	S	+	S
Score	0.00	-1.00	-2.00	-3.00	2.00	-2.00
Normalised Score	**0.60**	0.40	0.20	0.00	1.00	0.20
Manufacturing						
Easy Installation		S	S	S	+	+
Materials		S	S	-	S	+
Number of parts		+	+	S	+	+
Score	0.00	1.00	1.00	-1.00	2.00	3.00
Normalised Score	**0.25**	0.50	0.50	0.00	0.75	1.00

Figure F.4: Comparison criterion Powered Betz baseline

	Fixed Position	Vitale Concept	Betz Track	Kruger	Powered Betz	Bullnose
Aerodynamics						
CLmax improvement		-	S	-	-	+
L/D improvement		-	-	-	-	-
Stall progression		-	S	-	-	-
Trim (moments)		-	S	-	-	-
Score	0.00	-4.00	-1.00	-4.00	-4.00	-2.00
Normalised Score	**1.00**	0.00	0.75	0.00	0.00	0.50
Noise						
Cove Noise		-	S	-	S	-
Separation Noise		S	S	S	S	S
Noise from supporting structures		-	-	-	S	-
Score	0.00	-2.00	-1.00	-2.00	0.00	-2.00
Normalised Score	**1.00**	0.00	0.50	0.00	1.00	0.00
Kinematic Systems						
Actuation		S	-	-	S	-
Power required		-	S	-	-	S
Simplicity		-	-	-	S	-
Proven technology		S	S	+	S	+
Motion		-	-	-	S	-
Score	0.00	-3.00	-3.00	-3.00	-1.00	-2.00
Normalised Score	**1.00**	0.00	0.00	0.00	0.67	0.33
Structure						
Weight		-	-	-	-	S
Easy integration into existing system		S	S	-	S	S
Additional structures		S	S	S	S	S
Score	0.00	-1.00	-1.00	-2.00	-1.00	0.00
Normalised Score	**1.00**	0.50	0.50	0.00	0.50	1.00
Optimisation						
Room for optimisation		+	-	S	S	+
Number of variables		-	-	-	-	S
Flexibility of design		-	-	+	S	+
Score	0.00	-1.00	-3.00	0.00	-1.00	2.00
Normalised Score	**0.60**	0.40	0.00	0.60	0.40	1.00
Cost						
System complexity		-	-	-	-	-
Maintenance		-	-	-	-	-
Certification time		S	S	S	S	S
Design Cost		-	-	-	-	-
Score	0.00	-3.00	-3.00	-3.00	-3.00	-3.00
Normalised Score	**1.00**	0.00	0.00	0.00	0.00	0.00
Reliability						
Complete system lost		+	+	-	+	+
Actuation jam		-	-	-	-	-
Redundancy		S	S	-	-	S
Structural Damage		-	-	-	-	S
Score	0.00	-1.00	-1.00	-4.00	-2.00	0.00
Normalised Score	**1.00**	0.75	0.75	0.00	0.50	1.00
Manufacturing						
Easy Installation		-	S	-	-	S
Materials		-	-	-	-	S
Number of parts		-	-	-	-	-
Score	0.00	-3.00	-2.00	-3.00	-3.00	-1.00
Normalised Score	**1.00**	0.00	0.33	0.00	0.00	0.67

Figure F.5: Comparison criterion Fixed baseline

	Bullnose	Vitale Concept	Betz Track	Kruger	Powered Betz	Fixed Position
Aerodynamics						
CLmax improvement		-	-	-	-	+
L/D improvement		+	+	+	+	+
Stall progression		+	+	+	+	+
Trim (moments)		+	+	+	+	+
Score	0.00	2.00	2.00	2.00	2.00	4.00
Normalised Score	**0.00**	0.50	0.50	0.50	0.50	1.00
Noise						
Cove Noise		+	+	-	+	+
Separation Noise		S	S	S	S	S
Noise from supporting structures		-	S	S	+	+
Score	0.00	0.00	1.00	-1.00	2.00	2.00
Normalised Score	**0.33**	0.33	0.67	0.00	1.00	1.00
Kinematic Systems						
Actuation		-	-	-	+	+
Power required		-	S	-	-	+
Simplicity		S	+	-	-	+
Proven technology		-	-	S	-	S
Motion		+	+	-	+	S
Score	0.00	-2.00	0.00	-4.00	-1.00	3.00
Normalised Score	**0.57**	0.29	0.57	0.00	0.43	1.00
Structure						
Weight		-	-	-	-	-
Easy integration into existing system		S	S	S	S	+
Additional structures		-	S	S	+	-
Score	0.00	-2.00	-1.00	-1.00	0.00	-1.00
Normalised Score	**1.00**	0.00	0.50	0.50	1.00	0.50
Optimisation						
Room for optimisation		-	S	S	S	S
Number of variables		+	+	S	+	+
Flexibility of design		-	S	-	-	-
Score	0.00	-1.00	1.00	-1.00	0.00	0.00
Normalised Score	**0.50**	0.00	1.00	0.00	0.50	0.50
Cost						
System complexity		+	+	S	+	+
Maintenance		+	+	S	S	+
Certification time		S	S	S	S	S
Design Cost		+	+	-	-	+
Score	0.00	3.00	3.00	-1.00	0.00	3.00
Normalised Score	**0.25**	1.00	1.00	0.00	0.25	1.00
Reliability						
Complete system lost		-	S	-	S	-
Actuation jam		-	-	-	+	+
Redundancy		S	S	S	S	+
Structural Damage		-	-	-	S	-
Score	0.00	-3.00	-2.00	-3.00	1.00	0.00
Normalised Score	**0.75**	0.00	0.25	0.00	1.00	0.75
Manufacturing						
Easy Installation		S	S	-	S	S
Materials		S	S	S	S	+
Number of parts		-	+	+	S	+
Score	0.00	-1.00	1.00	0.00	0.00	2.00
Normalised Score	**0.33**	0.00	0.67	0.33	0.33	1.00

Figure F.6: Comparison criterion Bullnose baseline

Figure F.7 shows the ranking of a series of scenarios which are weighted according to one of the selected criteria. The final scenario is a designers intuition which weights criteria according to the intuition of the author.

	Scenario Number								
	1	2	3	4	5	6	7	8	9
Aerodynamics	0.222	0.111	0.111	0.111	0.111	0.111	0.111	0.111	0.146
Noise	0.111	0.222	0.111	0.111	0.111	0.111	0.111	0.111	0.200
Kinematics	0.111	0.111	0.222	0.111	0.111	0.111	0.111	0.111	0.195
Structures	0.111	0.111	0.111	0.222	0.111	0.111	0.111	0.111	0.100
Optimisation	0.111	0.111	0.111	0.111	0.222	0.111	0.111	0.111	0.045
Cost	0.111	0.111	0.111	0.111	0.111	0.222	0.111	0.111	0.089
Reliability	0.111	0.111	0.111	0.111	0.111	0.111	0.222	0.111	0.135
Manufacturing	0.111	0.111	0.111	0.111	0.111	0.111	0.111	0.222	0.090
Weighted Sum	1.000	1.000	1.000	1.000	1.000	1.000	1.000	1.000	1.000

1 Aerodynamics weighted
2 Noise weighted
3 Kinematics weighted
4 Structures weighted
5 Optimisation weighted
6 Cost weighter
7 Reliability weighted
8 Manufacturing weighted
9 Designers intuition

Figure F.7: Scenario weightings

Figure F.8 to F.10 show the final weightings of each concept after weights are applied.

	Scenario Number								
	1	2	3	4	5	6	7	8	9
Vitale Concept	0.331	0.294	0.331	0.338	0.322	0.338	0.342	0.349	0.303
Betz Track	0.339	0.376	0.265	0.265	0.265	0.265	0.344	0.265	0.394
Kruger	0.557	0.650	0.631	0.628	0.594	0.628	0.539	0.622	0.628
Powered Betz	0.635	0.672	0.635	0.605	0.616	0.628	0.640	0.616	0.685
Fixed Position	0.944	0.889	0.944	0.944	0.944	0.944	0.944	0.944	0.900
Bullnose	0.538	0.593	0.612	0.626	0.649	0.626	0.601	0.593	0.548

	Scenario Number								
	1	2	3	4	5	6	7	8	9
Betz Track	0.360	0.390	0.365	0.323	0.379	0.379	0.390	0.323	0.390
Vitale Concept	0.492	0.492	0.533	0.603	0.547	0.575	0.581	0.603	0.460
Kruger	0.358	0.388	0.321	0.358	0.377	0.391	0.321	0.377	0.325
Powered Betz	0.299	0.347	0.294	0.318	0.281	0.281	0.369	0.336	0.355
Fixed Position	1.000	1.000	1.000	1.000	1.000	1.000	1.000	1.000	1.000
Bullnose	0.571	0.638	0.669	0.645	0.627	0.627	0.682	0.682	0.649

Figure F.8: Scenario weightings for Vitale Concept and Betz Track

	Scenario Number								
	1	2	3	4	5	6	7	8	9
Kruger	0.141	0.156	0.119	0.119	0.119	0.141	0.119	0.156	0.144
Vitale Concept	0.406	0.361	0.361	0.417	0.435	0.428	0.444	0.398	0.323
Betz Track	0.452	0.459	0.407	0.385	0.422	0.385	0.496	0.459	0.470
Powered Betz	0.335	0.343	0.291	0.269	0.269	0.291	0.352	0.269	0.379
Fixed Position	0.833	0.833	0.833	0.778	0.833	0.833	0.722	0.833	0.815
Bullnose	0.352	0.352	0.441	0.463	0.352	0.374	0.407	0.426	0.401

	Scenario Number								
	1	2	3	4	5	6	7	8	9
Powered Betz	0.337	0.345	0.290	0.290	0.334	0.337	0.356	0.317	0.322
Vitale Concept	0.419	0.415	0.424	0.387	0.498	0.466	0.431	0.443	0.364
Betz Track	0.359	0.367	0.311	0.311	0.378	0.375	0.333	0.367	0.312
Kruger	0.000	0.000	0.000	0.000	0.000	0.000	0.000	0.000	0.000
Fixed Position	0.839	0.839	0.839	0.728	0.817	0.839	0.839	0.811	0.869
Bullnose	0.421	0.405	0.442	0.516	0.450	0.469	0.428	0.516	0.372

Figure F.9: Scenario weightings for Krueger and Powered Betz

	Scenario Number								
	1	2	3	4	5	6	7	8	9
Fixed Position	0.956	0.956	0.956	0.956	0.911	0.956	0.956	0.956	0.982
Vitale Concept	0.183	0.183	0.183	0.239	0.228	0.183	0.267	0.183	0.169
Betz Track	0.398	0.370	0.315	0.370	0.315	0.315	0.398	0.352	0.391
Kruger	0.067	0.067	0.067	0.067	0.133	0.067	0.067	0.067	0.027
Powered Betz	0.341	0.452	0.415	0.396	0.385	0.341	0.396	0.341	0.466
Bullnose	0.556	0.500	0.537	0.611	0.611	0.500	0.611	0.574	0.478

	Scenario Number								
	1	2	3	4	5	6	7	8	9
Bullnose	0.415	0.452	0.479	0.526	0.471	0.443	0.499	0.452	0.454
Vitale Concept	0.291	0.272	0.267	0.235	0.235	0.347	0.235	0.235	0.284
Betz Track	0.628	0.647	0.636	0.628	0.684	0.684	0.601	0.647	0.596
Kruger	0.204	0.148	0.148	0.204	0.148	0.148	0.148	0.185	0.153
Powered Betz	0.612	0.668	0.604	0.668	0.612	0.585	0.668	0.594	0.666
Fixed Position	0.861	0.861	0.861	0.806	0.806	0.861	0.833	0.861	0.894

Figure F.10: Scenario weightings for Fixed Position and Bullnose

Figure F.11 shows the averaged results of the Down Selection Process.

	Final Averaged Scenarios					
	Aerodynamics	**Noise**	**Kinematic Systems**	**Structure**	**Optimisation**	
Vitale Concept	0.354	0.336	0.350	0.370	0.378	
Betz Track	0.423	0.435	0.383	0.380	0.407	
Kruger	0.221	0.235	0.214	0.229	0.229	
Powered Betz	0.427	0.471	0.422	0.424	0.416	
Fixed Position	0.906	0.896	0.906	0.869	0.885	
Bullnose	0.475	0.490	0.530	0.565	0.527	
	Cost	**Reliability**	**Manufacturing**	**Designers Intuition**	**Average**	**Standard Deviation**
	0.390	0.383	0.369	0.317	0.361	**0.023**
	0.400	0.427	0.402	0.425	0.409	**0.020**
	0.229	0.199	0.234	0.213	0.223	**0.012**
	0.410	0.464	0.412	0.479	0.436	**0.027**
	0.906	0.882	0.901	0.910	0.896	**0.014**
	0.507	0.538	0.541	0.484	0.517	**0.030**

Figure F.11: Averaged results of the Down Selection Process